Sorption-Based Heat and Mass Exchangers for Humidity Control Systems

By
Seyed Mohammadali Rahnama

M.Sc., University of Tehran, 2013
B.Sc., University of Tehran, 2011

Thesis Submitted in Partial Fulfillment of the
Requirements for the Degree of
Doctor of Philosophy

in the
School of Mechatronic Systems Engineering
Faculty of Applied Sciences

SIMON FRASER UNIVERSITY
Fall 2022

Declaration of Committee

Name:	**Seyed Mohammadali Rahnama**
Degree:	**Doctor of Philosophy**
Title:	**Sorption-Based Heat and Mass Exchangers for Humidity Control Systems**
Committee:	**Chair: Mohammad Narimani** Lecturer, Mechatronic Systems Engineering
	Majid Bahrami Supervisor Professor, Mechatronic Systems Engineering
	Bonnie L. Gray Committee Member Professor, Engineering Science
	Sami Khan Committee Member Assistant Professor, Sustainable Energy Engineering
	Taco Niet Examiner Associate Professor, Sustainable Energy Engineering
	Andrew Rowe External Examiner Professor, Mechanical Engineering University of Victoria

Abstract

In northern latitudes during the cold season, adding a dehumidification system can raise the total energy consumption of greenhouses by 80%. Developing an efficient dehumidification system for greenhouses is a necessity in order to reduce its energy consumption and emissions, e.g., greenhouse gas (GHG) emissions. One alternative solution to already existing systems are sorption-based systems. One of the main advantages of using a desiccant system is that the required heat for desorption could be supplied by low-grade energy sources and is a clean technology, which operates without the use of refrigerants. But, in the absence of such a heat source their performance will drop. In this thesis, a new isothermal sorption-based heat and mass exchanger (IsoHMX) as an alternative dehumidification system is proposed to increase water uptake (the amount of adsorbed water) and significantly reduce input energy. The novel concept is based on delivering the released heat of adsorption from the high humidity stream to the desorption part of the system where the drier air stream is being processed. This heat delivery results in an ideal isothermal condition during the adsorption/desorption process, which means cooler adsorption and warmer desorption processes. This will significantly improve the sorption kinetics in both the adsorption and desorption processes. As part of this research, a proof-of-concept test set up for the proposed IsoHMX is designed and built. The performance of the system was measured under different inlet conditions and substrate material. Furthermore, a numerical and a closed-form analytical model are developed and verified with the experimental data. Both models showed very good agreement with the experimental results. With the help of the closed-form analytical solution an optimized design of the IsoHMX was found using multi-objective genetic algorithm to maximize moisture removal capacity (MRC) and the dehumidification coefficient of performance (DCOP). This study showed that the optimized design is independent of the inlet temperature and relative humidity. In the end, the performance of the optimized IsoHMX is compared to a commercial desiccant wheel. The results showed that IsoHMX is more energy efficient, i.e., it has a higher DCOP and the desiccant wheel has higher MRC.

Keywords: adsorption; dehumidification coefficient of performance (DCOP); moisture removal capacity (MRC); multi-objective optimization; analytical modeling

Dedication

To my mother, sister, my brother
and my friends Amir, Erfan and Ali
for their love, support and encouragement.

Acknowledgements

I would like to express my deep gratitude towards the many great people who made accomplishing this dissertation possible and enjoyable for me.

First, I'd like to express my deepest appreciation to my Senior Supervisor at Simon Fraser University (SFU), Dr. Majid Bahrami, for his support and guidance throughout my PhD studies. He has had a remarkable impact on my presentation and communication skills which are priceless, and I always would be thankful for that.

I'd like to express my gratitude to my supervisory committee members, Dr. Bonnie L. Gray and Dr. Sami Khan, for their insightful comments and encouragement. Also, I'd like to thank my examining committee members, Dr. Nedjib Djilali and Dr. Taco Niet for their valuable time reading this thesis and helping me to refine it.

Moreover, I'd like to express my gratitude to Drs. Maryam Khajehpour, Claire McCague, Postdoctoral Fellows, and Dr. Martin Cermak, Dr. Ecem Cerrah PhD graduate, Ryutaro Tatsumi, Haowen (Peter) Li Co-op students at the Laboratory for Alternative Energy Conversion (LAEC), for providing me with their technical support and expert guidance on various aspects of the project.

I'd like to specially thank my close friend and lab partner, Reza Abadi, for always helping me with different aspects of this project.

Finally, I would like to express my gratitude to my family, who always supported me in all stages of my personal life and professional career.

Table of Contents

List of Tables

List of Figures

Nomenclature

c_p	Specific heat capacity (J/kg.K)
H	Channel height (m)
h	Convective heat transfer coefficient(w/m^2.K)
h_{ad}	Enthalpy of adsorption (J/kg)
h_m	Convective mass transfer coefficient (m/s)
k	Thermal conductivity (W/m.K)
L	Length of channel(m)
Nu	Nusselt number (-)
P	Pressure (Pa)
T	Temperature (K)
t	Time (s)
u	Air velocity (m/s)
W	Uptake of desiccant (kg/kg)
x	Axial direction (m)
y	Radial direction (m)

Greek parameters

ρ	Density (kg/m^3)
δ	Thickness (m)
ω	Humidity ratio (kg/kg)

Subscript

a	Air
avg	Averaged

d	Desiccant
HX	Heat exchanger
HTF	Heat transfer fluid
in	Inlet air
lam	Laminar
out	Outlet air
p	Process
q	Isoflux
r	Regeneration
ref	Reference
s	Substrate
sat	Saturation
T	Isothermal
tur	Turbulent

Abbreviations

DC-HX	Desiccant coated heat exchanger
DCOP	Dehumidification coefficient of performance
DW	Desiccant wheel
ERV	Enthalpy recovery ventilator
HR	Humidity ratio
HTF	Heat transfer fluid
HX	Heat exchanger

GA	Genetic Algorithm
MRC	Moisture removal capacity
MRC^*	Moisture removal capacity per frontal surface area
NCG	Non-condensable gases
RH	Relative humidity

Executive summary

Motivation

Humidity control is one of the key functions of heating, ventilating, and air conditioning (HVAC) systems. Humidity has significant impact on human life, e.g., human comfort and health in buildings, the growth rate and plant health in greenhouses. This study is focused on greenhouse dehumidification; however, the results can be applied to other applications. In northern latitudes during the cold season, adding a dehumidification system can raise the total energy consumption of greenhouses by up to 80%. Currently, most greenhouses use venting for dehumidification, i.e., opening vents near or on the roof of greenhouses, which lead to a significant loss of energy and an excessive need for heating during the cold season. Data collected in France and the United Kingdom shows that venting-heating can account for 20% of the overall yearly energy consumption of a greenhouse with tomato crops and a relative humidity set point of 85%. In addition to energy consumption, excessive humidity combined with condensation can lead to fungal diseases, leaf necrosis, and soft and thin leaves, all of which indicates the importance of maintaining a desired humidity level in greenhouses. Therefore, developing an efficient dehumidification system for greenhouses is a necessity in order to reduce the energy consumption and emissions of greenhouses.

Greenhouse dehumidification systems, can be categorized in three groups:

1- Mechanical refrigeration dehumidification, such as heat pumps: Some modern greenhouses use heat pumps to condense extra humidity instead of venting. Heat pumps offer a high coefficient of performance (COP), values as high as 10 have been reported. However, heat pumps involve challenges, such as: a high initial cost, the cost of electricity (operation costs), maintenance issues, Ozone Depletion Potential (ODP) and Global Warming Potential (GWP) for the refrigerants used in vapor compression systems and carbon footprint of the used electricity.

2- Air-to-air heat exchangers, such as heat recovery ventilators: Air-to-air heat exchangers recover exhausted heat through venting. Such systems are simple and inexpensive. Experimental results indicate that heat exchangers could control relative humidity (RH)

satisfactorily during the cold and mild seasons. The overall efficiency of these systems has been reported between 60-90%. The major challenges with heat recovery systems are condensation and frost formation. In cold climates, such as Canada and Northern Europe (below −10 °C), frost often forms inside the heat recovery ventilation/energy recovery ventilation (/HRVs/ERVs) and would negatively impact the performance of the exchangers and can block the air flow channels.

3- Sorption-based systems, such as desiccant wheels and coated heat exchangers: A desiccant-based (sorption-based) dehumidification system has been widely studied in our lab. Desiccant-based systems have two main processes, adsorption and desorption. During the adsorption process, humidity is adsorbed from the air stream to a desiccant, which generates heat due to physical sorption. During the desorption process, which requires heat, humidity is desorbed from the desiccant material to the exhaust air stream. One of the main advantages of using a desiccant system is that the required heat for desorption could be supplied by low-grade energy sources, with temperatures less than 80◦C. This low-grade heat could be provided using waste heat or renewable energy sources, e.g., solar heat. It is also a clean technology, which operates without the use of refrigerants. The dehumidification coefficient of performance (DCOP) of desiccants wheels has been reported to be between 0.1-2.

Objectives

This study aims to investigate and develop a new improved sorption-based system, which works under isothermal condition (named isothermal heat and mass exchanger (IsoHMX)) as an alternative dehumidification system to increase the water uptake, i.e., the amount of water that is adsorbed during adsorption, and significantly reduce the input energy. The novel concept is based on delivering the released heat of adsorption from the high humidity stream to the desorption part of the system, where the drier air stream is being processed. This heat delivery results in an ideal isothermal condition during the adsorption/desorption process, which results in cooler adsorption and warmer desorption processes. This will significantly improve the sorption kinetics in both adsorption and desorption processes.

As part of this research, a proof-of-concept test set up for the proposed IsoHMX is built, aluminum and acrylic are considered for building the heat/mass exchanger and their performance are compared. IsoHMX design is optimized using a new heat/mass transfer model that is also a part of this PhD program and the performance of the optimized IsoHMX is compared to a commercial desiccant wheel (DW).

Methodology

To achieve the objective of this program, a systematic approach is undertaken. Figure 1 shows the roadmap of the research program. The following highlights the milestones and the steps of the proposed methodology:

- Establish performance metrics for dehumidification systems to enable benchmarking of desiccant wheel (DW) and other dehumification systems against the proposed dehumidification system (IsoHMX). The performance metrics, includes the moisture removal capacity (MRC) and the dehumidification coefficient of performance (DCOP).
- Develop an analytical model to investigate the heat and mass transfer and predict the performance IsoHMX that will ultimately be used for design optimization after validation against experimental data. This will include development of a suite of new compact and accurate analytical models to predict performance under various operating parameters, e.g., desiccant and air temperature, air relative humidity, desiccant uptake and the inlet velocity for the IsoHMX;
- Design and build a test bed to assess the IsoHMX's performance;
- Characterize various substrates in terms of thermal conductivity and thermal diffusivity;
- Characterize a number of sorption composites to select a suitable sorption composite and to determine the effect of composition on the performance of IsoHMX;
- Test the proposed IsoHMX proof-of-concept under various operating conditions;
- Validate the proposed analytical and numerical models with the experimental data;

- Perform a parametric study and multi objective optimization to improve the IsoHMX's design; and
- Compare the performance of the optimized IsoHMX with the desiccant wheel in a greenhouse under a range of operating conditions.

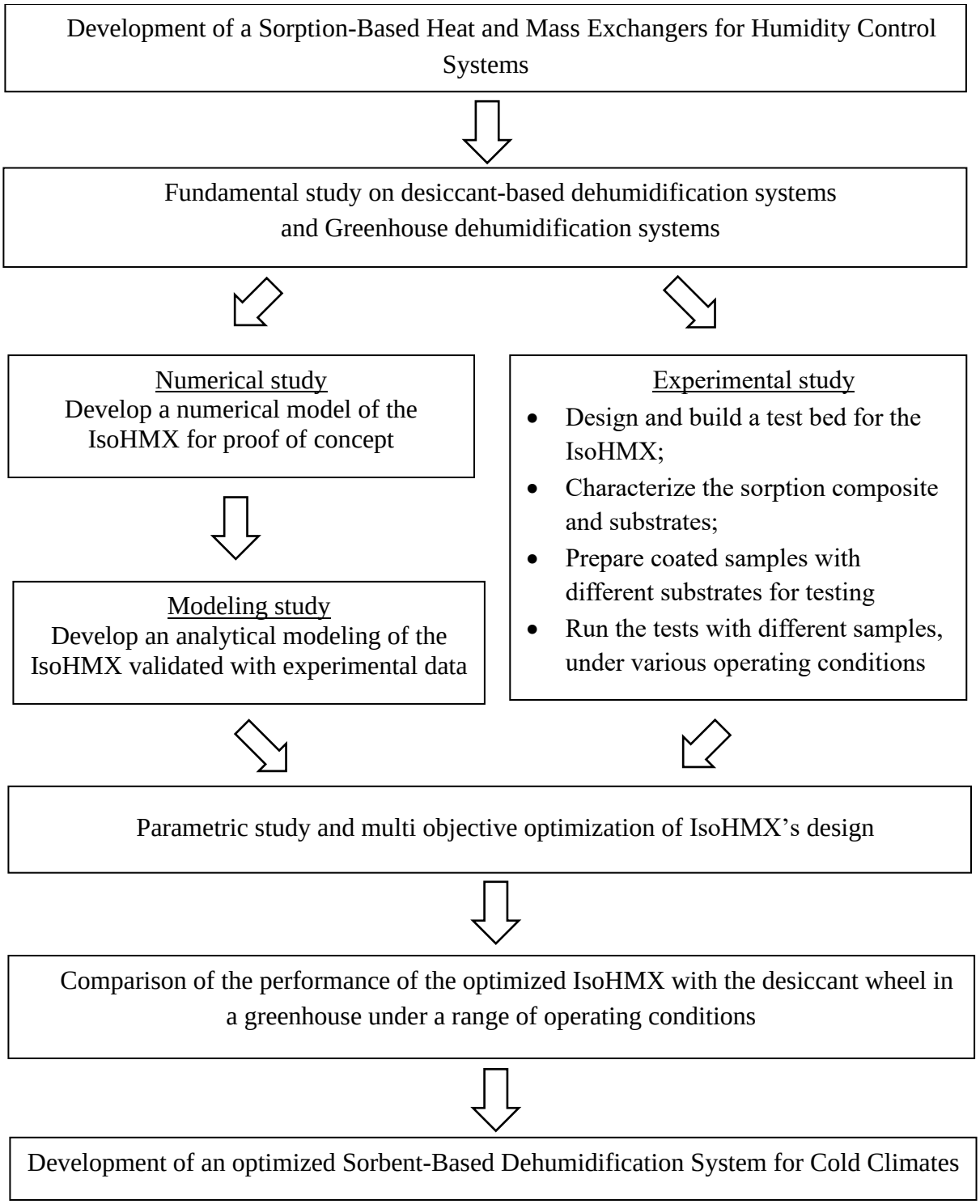

Figure 1. Scope and deliverables of the present research project

Contributions

The contributions of this research project are highlighted below:

1. Developed a novel concept and a proof-of-concept for IsoHMX, i.e., a new heat delivery design through a conductive substrate. IsoHMX requires no extra components and/or parasitic power and maintenance. The only pertinent work in the literature is limited to an elaborate heat delivery system by water inside a coated heat exchanger that requires parasitic power (a pump) and adds complexity and notable cost.
    - Determined the effect of the substrate material on the performance of sorption-based dehumification systems, through the experimental study using the custom build test bed.
    - A considerable increase in DCOP in cold climate was achieved
2. Developed the first analytical solution for IsoHMX with no simplification regarding the derivatives of the uptake with respect to humidity ratio and temperature. For simplification, previous studies used average value for mentioned derivatives.
    - A closed-form analytical solution for real time control was developed to predict the performance of the IsoHMX under various operating conditions. [submitted, Applied Thermal Engineering]
    - Optimized design of the IsoHMX using the closed-form solution, through a multi objective genetic algorithm. [Provisional patent is being filed.]
3. Developed an analytical model to predict the performance of a desiccant coated heat exchanger. [submitted, Applied Thermal Engineering]
    - Developed an analytical model to predict MRC and DCOP through a compact closed-form equation which can be used for real time control system and optimization.

1 Introduction:

Introducing a dehumidification system with low energy consumption, environmentally friendly, and suitable for cold climates for the greenhouse is the objective of this research project. In the current study, a novel sorption-based humidity control system with the mentioned properties is introduced. The results of the study could be extended to other applications as well and greenhouse was chosen as a case study which could benefit a lot from an efficient dehumidification system. Humidity control is one of the key functions of heating, ventilating and air conditioning (HVAC) systems. It can directly affect human comfort and health in buildings, the growth rate and plant health in greenhouses, and corrosion of computer parts in data centers.

Relative humidity (RH) plays a vital role in human thermal comfort. More importantly, high humidity in buildings can result in fungal growth that can lead to respiratory diseases. Humidity control is more important in cold northern climates, where people spend most of the cold season indoors. As such, Northern Canada, Alaska and Greenland have the highest rate of respiratory infections in infants [1]. In northern climates, energy saving strategies recommendations are for airtight building construction, which results in insufficient fresh air ventilation. An insufficient ventilation rate (~20 m^3/h) leads to a rise in humidity and mold growth [2]–[4]. In a study in Nunavut (Northern Canada), this was reported to be the main cause of respiratory infections [5]. The minimum required ventilation rate could be calculated based on the American Society of Heating, Refrigerating, and Air-conditioning Engineers (ASHRAE's) Standards, e.g., 75 m^3/h for a 70 m^2 single bedroom apartment [6]. As important as the ventilation of residential buildings is in cold climates, this study focused on the ventilation of greenhouses in such climates; however, the results can also be applied to the ventilation of residential buildings.

As it was mentioned, the focused of the current study is on the greenhouses but results could be extended to other applications as well, e.g., residential and commercial buildings. A considerable part of the Canadian economy is from the agriculture and food sectors [7], i.e., they are almost 5% of the total Canadian Gross Domestic Product [8]. In Canada, greenhouse temperature and humidity are controlled by systems that mainly depend on fossil fuels and have a significant operating cost. In 2005, the Canadian greenhouse industry costs were approximately $260 million,

i.e., this was 12% of their total revenue [9]. On the other hand, climate control is one of the key features in greenhouse food production [10]. Climatic parameters, include humidity, temperature, concentration of CO_2, and supplemental lighting. Reaching the optimum climatic parameters results in an increase in both crop quality and yield. Humidity control also plays a vital role in crop health; low humidity leads to reduced stem lengths and leaf sizes [11], while excessive humidity along with condensation can lead to fungal diseases, leaf necrosis, and soft and thin leaves [12]–[14]. Several studies were performed on climate control and finding the optimum greenhouse climatic parameters [15]–[20]. It was concluded that humidity is the most challenging climatic parameter to control in greenhouses. Relative humidity, which varies with air temperature and transpiration, should be maintained at a constant level.

Thus, there is an absolute need for developing controllable efficient greenhouse dehumidification systems that run using non-payable or low-cost sources, e.g., low-grade heat, geothermal, and solar [21], [22].

First, a quick overview of the different types of moisture control technologies in the greenhouse is provided in section 1.1, and then more detail on the novel moisture removal system is provided in section 1.2. Then at chapter 2, experimental study of the proposed system is explained, followed by analytical and numerical model explained in chapter 2. Then, the optimized design of the system is found in chapter 4, and its performance is compared to a commercial desiccant wheel at chapter 5.

1.1 Key technologies for moisture removal in greenhouses

In this section key technologies for moisture removal in greenhouses is introduced.

1.1.1 Venting

Venting (ventilation) which is achieved by opening vents near or on the roof of greenhouses [10] is the commonly used and the simplest method for dehumidification in greenhouses [23], [24]. Natural or passive ventilation is the opening of vents without the use of a fan [25], and when a fan is used, ventilation is referred to as “forced” [26]. During the cold season, venting leads to significant heat loss and an increase in heating costs. Data collected in France and the United Kingdom show that venting-heating can account for 20% of the overall energy consumption of a

greenhouse per year for tomato crops, and a relative humidity set point of 85% [12]. Maslak and Nimmermark [27] and Campen and Bot [28] reported that ventilation is responsible for 20–30% of the thermal energy used for climate control of greenhouses.

1.1.2 Mechanical refrigeration systems

Due to their high coefficient of performance, i.e., a COP of 10 [29], heat pumps are the typically used mechanical refrigeration system used in greenhouses [23]. Also, the heat which is removed during condensation can be used to reduce the overall energy consumption of the system [30], see Figure 2. Heat pumps are more beneficial in closed greenhouses, as they are able to control CO_2 and humidity levels [31], [32]. Han et al. [33], [34] compared three dehumidification systems, i.e., a heat pump, forced ventilation, and an air-to-air heat exchanger in a commercial tomato greenhouse in Saskatchewan, Canada. They concluded that the heat pump consumes less energy than the other two systems. However, there are challenges associated with heat pumps. This includes: a high initial cost [33], the cost of electricity (operation costs), maintenance issues [33], the Ozone Depletion Potential (ODP) and the GWP of the refrigerants used in the vapor compression systems. Moreover, Campen et al. [13] concluded that if heat pumps are not used for space heating, they are not economical for greenhouse dehumidification.

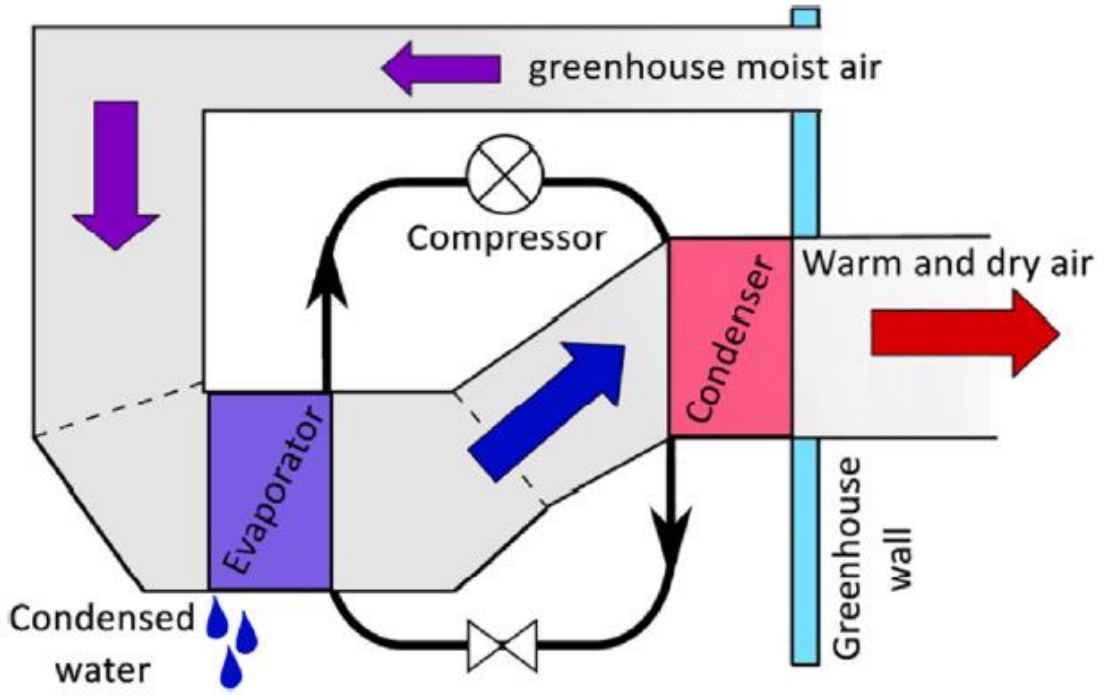

Figure 2. Airflow in a heat pump dehumidifier [12]

1.1.3 Air-to-air exchanger

Air-to-air heat exchangers recover exhausted heat through venting. This system is simple and inexpensive and has an overall efficiency of 60-90% [35], [36]. The majority of the studies that considered air-to-air heat exchangers for dehumidifying greenhouses, concluded that this system is the most efficient approach, especially during cold seasons. Campen et al. [13] and De Hallaux and Gauthier [37] concluded that this system could reduce the energy consumption of the greenhouse, but it depends on the effectiveness and energy consumption of the heat exchanger. Han et al. [38] studied this system in a greenhouse located in Saskatoon, Canada. They concluded that this system is beneficial during cold and mild weather conditions, but it was less effective during summer. The major challenges with these systems are condensation and frost formation [39]. Although this system works better in cold and mild condition, but in climates such that found in Canada and Northern Europe (below −5 °C), frost often forms inside the heat recover exchangers (HRVs) and would negatively impact the performance of the exchangers [40].

1.1.4 Desiccant-based dehumidification systems

Desiccant-based systems have two main processes, adsorption (or absorption for liquid-based systems) and desorption. During the adsorption process, humidity is adsorbed from the air stream (the air inside the greenhouse) to a desiccant, which generates heat due to physical sorption. In the desorption process, which requires heat, humidity is desorbed from the desiccant material to the exhaust air stream (outside air), as shown in Figure 3. Based on the sorbent material, there are two desiccant system types, i.e., liquid-based and solid-based. One of the main advantages of using a desiccant system is that the required heat for desorption, could be supplied by low-grade energy sources [11] with temperatures of less than 80◦C. This low-grade heat could be provided using waste heat or renewable energy sources, e.g., solar [41]. It is also a clean technology, i.e., uses no Ozone Depletion Potential (ODP) and Global Warming Potential (GWP) refrigerants. The dehumidification coefficient of performance (DCOP) of desiccant wheels has been reported to be between 0.1-2 [42][43]. These advantages have made desiccant-based dehumidification systems attractive for studies with different applications, e.g., residential buildings [44] and more recently, greenhouses [23].

Most greenhouse dehumidification-related studies focus on liquid desiccant dehumidifiers. In a number of studies, it was reported that liquid desiccant dehumidifiers were able to perform satisfactorily [45]–[47], while in other studies, they reported that these systems were only able to reduce the dehumidification load by 30–50% [48], [49]. Other challenges of using this system are: the complexity of the system and the high cost of the installation [13].

Solid desiccants are highly porous materials, and the typically used ones are: activated silica gel, zeolite, and titanium silicates [50]. Solid desiccants are environmentally-friendly, non-flammable, non-corrosive, not chemically reactive with moist air, and less expensive compared to liquid desiccants [51], [52]. There are various existing solid desiccant dehumidification systems, e.g., packed column of pellets, desiccant material coated on fibrous paper forming desiccant wheels [53]. Packed columns are inexpensive but have high pressure drop, desiccant wheel is a good alternative to packed beds as it has low pressure drop [54]. Desiccant wheel is the most common solid based desiccant system. The main source of desiccant wheel’s energy consumption is the regeneration heat. In dehumidification of an indoor space, both indoor air and outdoor air can be

use as the regeneration air [55]–[57]. Using indoor or outdoor air as the regeneration air has a direct effect on performance of the wheel as it determines the required regeneration temperature[58], [59]. The previous studies to improve desiccant wheel's performance as the most common solid based desiccant system, are briefly explained in the following two paragraphs:

The following paragraph gives an over view about the previous studies on the systems with the outdoor air as the regenerations air; Caliskan et al.[60] integrated the desiccant wheel with a heat recovery wheel and an evaporative air cooler. This system showed good energy performance. Chen et al. [61] studied a desiccant evaporative combined chilled air/chilled water system. 60 °C regeneration temperature for moderate and 70 °C for high humidity climate was recommended. Ren et al.[62] combined the desiccant wheel with a thermal energy storage unit and a photovoltaic thermal collector. It was concluded that both photovoltaic and energy storage unit can be used as the regeneration heat source. Liu et al. [63] developed a two-stage desiccant wheel system which the regeneration heat is provided by a solar thermal collector and a photovoltaic power generation device. The results showed that increasing the regeneration air temperature by 10 °C will lead to 0.9 to 2.7 g/kg increase in the dehumidification capacity of the system. Zhou [64] studied a desiccant wheel combined with a solar collector and results showed 50% improvement in the power consumption of the system.

The following paragraph gives an over view about the previous studies on the systems with indoor air as the regenerations air; Ukai et al. [65] studied performance of a desiccant wheel in hot humid climate with indoor air as the regeneration air. The results indicated that the supply air condition also plays an important role in the energy performance of the system. Fong and Lee [66] studied the desiccant wheel combined with a heat exchanger with indoor air as the regeneration air. It was concluded that the wheel requires higher rotational speed while working with heat exchanger and no regeneration heat, compared to a case with regeneration heat. Kabeel et al. [67] numerically studied desiccant wheel combined with a phase change material (PCM) heat storage system and a solar air collector. Results showed that the electric energy consumption of the system could be decrease up to 90%. Shahzad et al. [68] experimentally studied a desiccant wheel integrated with a heat recovery wheel and an evaporative cooler. The result showed 60–65% increase in coefficient of performance (COP). Tian et al. [69] experimentally studied a desiccant wheel combined with a

heat pump. In the proposed system the return air was used for regeneration and the system showed a better performance compared to conventional dehumidification systems. Habib et al. [70] simulated a desiccant with return air as the regeneration air. Result of the simulation showed COP of 1.52 for the system. Asadi et al. [71] studied a two-stage desiccant cooling system with different regeneration configurations. The proposed system used both indoor and outdoor air as the regeneration air. It was concluded that there is an optimum regeneration temperature for each configuration.

Solid desiccant based dehumidification systems are mostly used for air conditioning applications in high humidity climates [72] and there are few studies on the solid desiccant application in the greenhouse [23]. Sultan et al. [51], [73] studied a solid desiccant system with various desiccant materials in the greenhouse and analyzed the water uptake. It was reported that an activated carbon fiber (ACF) and an activated carbon powder (ACP) can perform successfully at an RH higher than 40% and 60%, respectively, and silica gel can perform well under all RH ranges. The performance of a solid desiccant dehumidifier in agricultural product storage was studied by Mahmood et al. [74]. They reported a higher COP value at a low regeneration temperature and a longer dehumidification time for a high relative humidity value. Rjibi et al. [75] simulated a desiccant wheel in a greenhouse and concluded that raising the regeneration temperature from 60 to 90°C reduces the moisture content of the air drastically, i.e., from 4.3 to 0.7 g/kg. A desiccant-coated heat exchanger (DC-HX) has been introduced recently and has been the subject of many studies; Saeed and Al-Alili [76] reviewed the modeling and experimental studies of the DC-HXs, and Vivekh et al [77] presented a summary of the DC-HX's developments in a review paper. Amani et al. [78] studied a new FAM-Z02 DC-HX that was used for dehumidification in a greenhouse and reported that its performance was satisfactory.

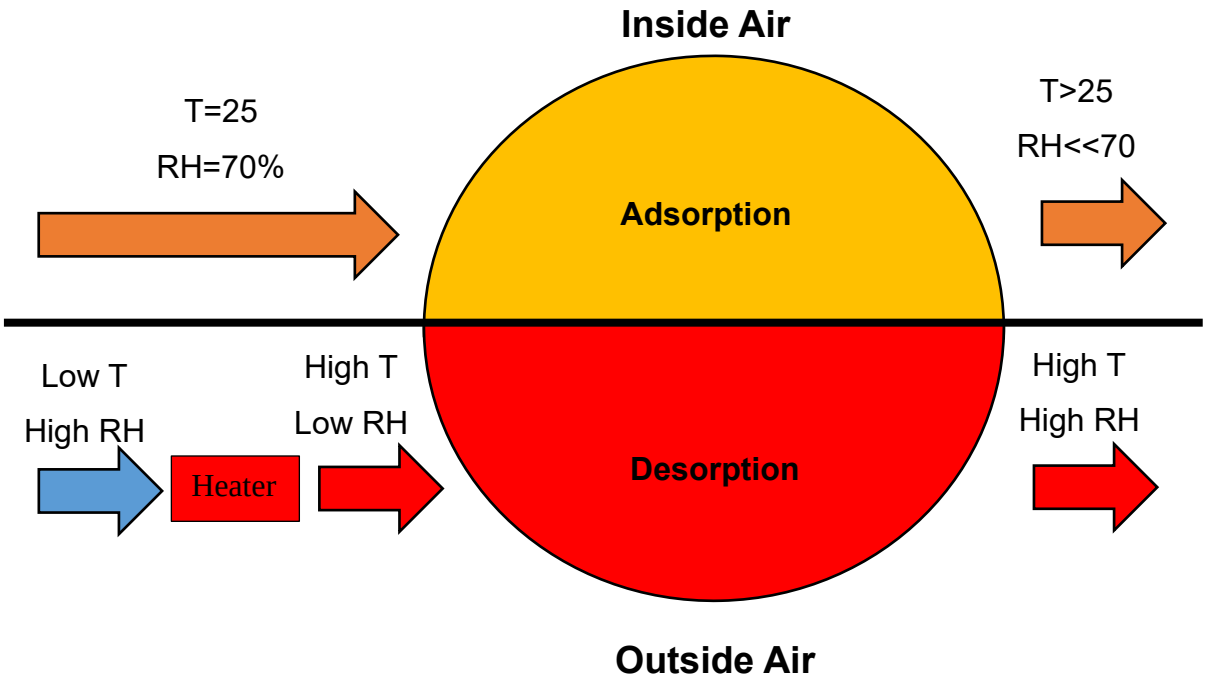

Figure 3. Adsorption desorption cycle using a desiccant wheel in greenhouse in cold climate

1.3 The isothermal heat and mass exchanger (ISOHMX)

In this section, the novel moisture removal system for greenhouses is introduced. First, the general idea, and then the thermodynamic cycle of the system is explained.

Greenhouse dehumidification using a desiccant-based system in a cold climate faces a major challenge: as the outside air's (regeneration air) temperature is very low (Figure 3), using this air as regeneration stream will lead to a very low moisture removal capacity (MRC), i.e., amount of removed water in an hour (kg/hr). To increase the MRC, cold air should be heated up before desorption, but it will lead to a huge waste of energy as this hot air is exhausted to the outside of the greenhouse. A solution to this heat loss is using a heat exchanger to recover some of the lost heat. But. this will result in condensation and frost issues in cold climates, which is the focused climate of this study.

The general idea behind this new design is to deliver heat from the adsorption to the desorption section so that there would be isothermal adsorption and desorption areas. This delivery of heat benefits the system in two ways:

- The hotter adsorption section will result in better desorption; and
- The cooler adsorption section will increase water uptake.

This delivery of heat could be achieved by either choosing a desiccant wheel with a conductive substrate (existing desiccant wheels use nonconductive material as the substate, e.g., paper) or an air-to-air heat exchanger coated with desiccant on both sides, see Figure 4. As it was mentioned, adsorption/desorption is a cyclic phenomenon and sorption material should be introduced to two different streams in the known intervals. In desiccant wheel this will be achieved by rotation the wheel and introducing the sorption material to the both streams, as shown in Figure 3. In coated heat exchanger there is a need for additional system to exchange the streams between channels in a known interval.

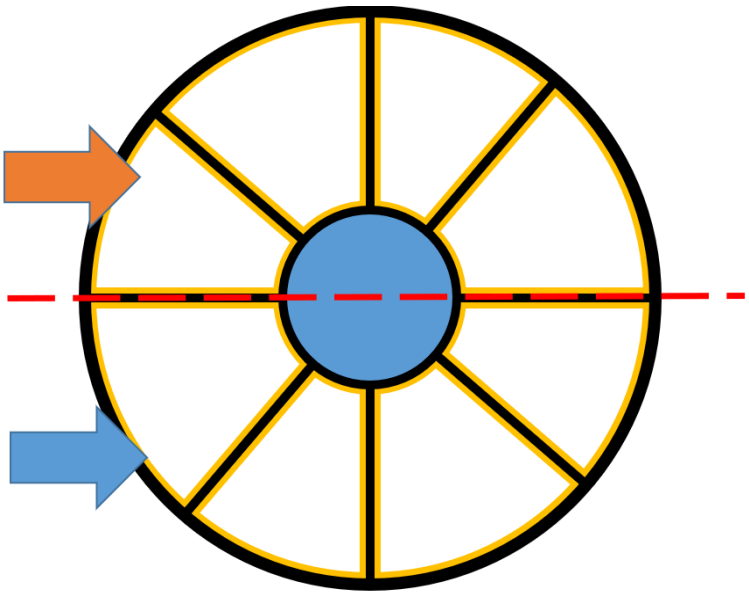

a)

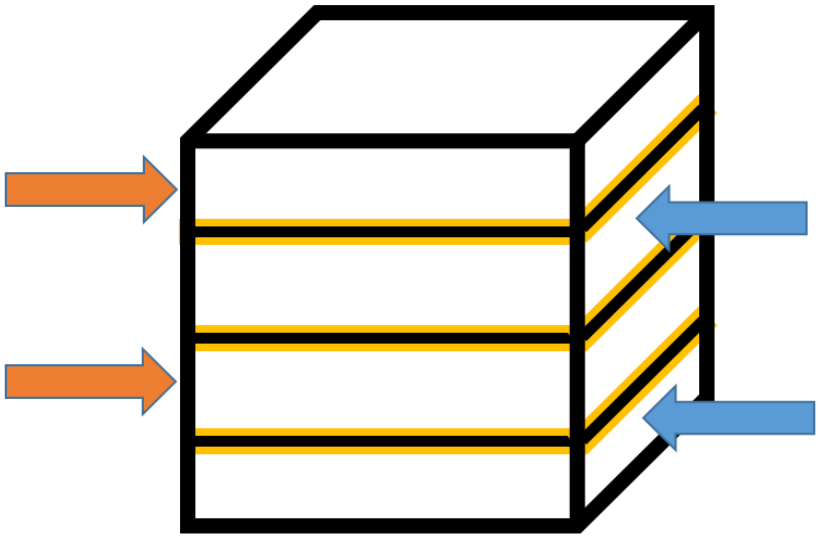

b)

Figure 4. Two concept designs for a solid desiccant dehumidification system with conductive substrate. Yellow lines indicate coatings: a) specially-designed desiccant wheel with a conductive substrate; and b) a desiccant-coated air-to-air exchanger

1.3.1 The thermodynamic cycle of the ISOHMX

After introducing the concept and general idea of the IsoHMX, the thermodynamic cycle of the system on explained in the following section.

A parallel flow version of desiccant-coated air-to-air exchanger, IsoHMX, (Figure 4-b) is chosen for the modeling and experimental study. A 2D schematic of the mentioned geometry is illustrated in Figure 5; two parallel air channels separated by a double-sided coated substrate.

The IsoHMX cycle consists of two half cycles, i.e., adsorption and desorption. Two different streams of air pass through the channels and are switched after each half cycle time, i.e., a hot and humid stream (25°C, 70% RH) flows through one channel and a cold and dry stream (5°C, RH lower than 70%) through the other one in one half cycle and vice versa in the other half. It should be noted that the term "dry air" is understood to be air with a low humidity ratio or moisture content; thus, 5°C and 70% RH is a dry air stream.

The thermodynamic cycle of the system is explained in the following:

The orientation of hot and cold streams at the beginning of a cycle is assumed to follow Figure 5, i.e., a hot and humid stream through the top channel and a cold and dry stream through the bottom one. The mass transfer mechanism in an IsoHMX is basically the same as any other desiccant-based system; At the beginning of the cycle, the upper channel's desiccant layer is dry. As the hot humid air passes over the desiccant layer, the layer adsorbs moisture from the air. On the other hand, the bottom desiccant layer is wet so as the cold dry passes over it, it desorbs moisture to the air. At the end of the first half cycle, the top channels' desiccant is wet and the bottom one is dry. So, in the second half cycle, the cold dry air passes through the top channel and the hot humid air through the bottom one.

Heat transfer in the IsoHMX consists of heat transfer in five regions: (Figure 5)

1- Top air channel: Convective heat transfer with the desiccant layer. The direction of heat transfer is from the air to the desiccant as the hot air passes through the channel and vice versa when introduced to the cold air stream;
2- Top desiccant layer: Convective heat transfer with the air and conductive heat transfer with the substrate. Also, there is a heat generation source/sink due to adsorption/desorption;

3- Substrate: Conductive heat transfer with the top and bottom desiccant layer;

4- Bottom desiccant layer: Convective heat transfer with the air and conductive heat transfer with the substrate. Also, there is a heat generation source/sink due to adsorption/desorption.

5- Bottom air channel: Convective heat transfer with a desiccant layer.

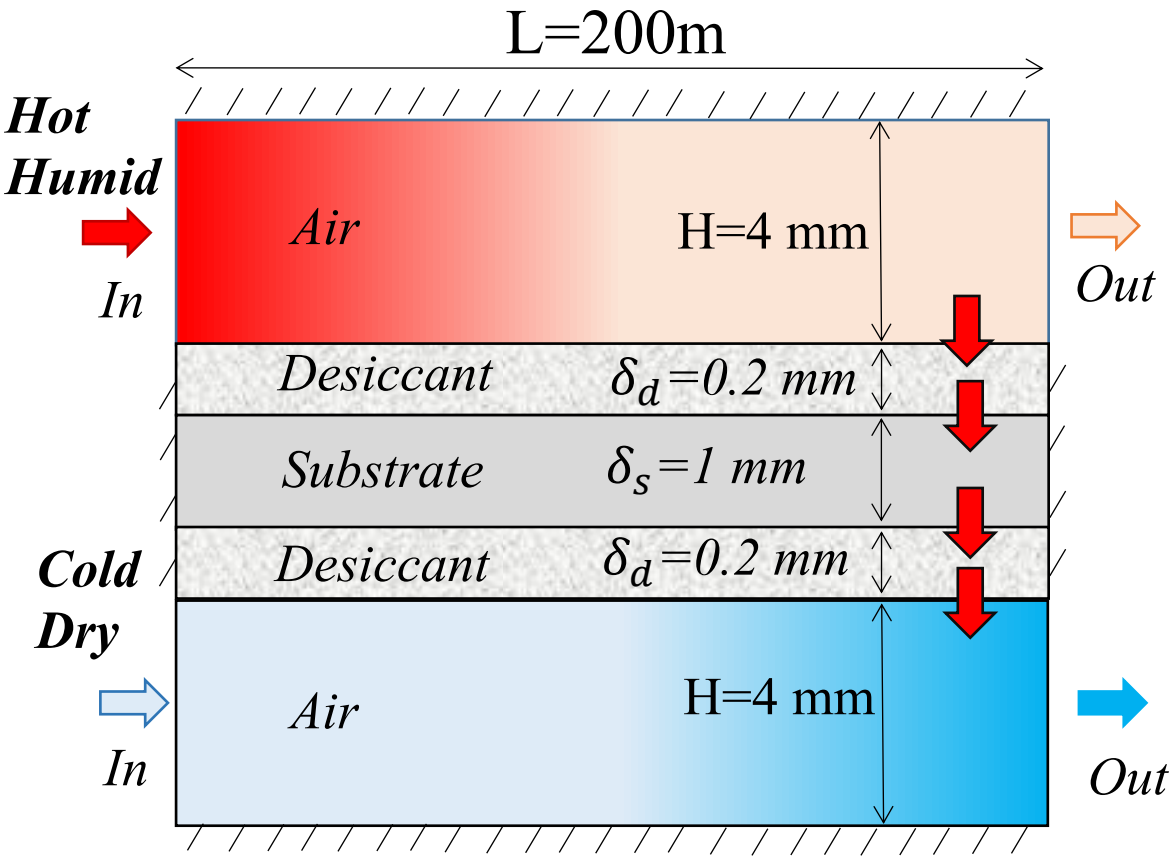

Figure 5. Schematic of a parallel flow IsoHMX with two air channels at the top and bottom and a double side coated substrate.

Heat transfer direction is shown with red arrows: From top air stream to desiccant layer through convection, from top desiccant layer to the substrate through conduction, through substrate to the bottom channel through condition, and from bottom desiccant layer to the bottom air stream through convection.

1.3.1.1 Performance metrics

To evaluate the performance of the IsoHMX, the commonly-used MRC and the DCOP parameters are used in this study. The time-averaged moisture removal during the adsorption process, the MRC (g/hr), can be calculated as follows [79]:

$$MRC = \frac{3600*1000}{t_{cycle/2}} \int_0^{t_{cycle/2}} \dot{m}_{\mathrm{a}} \, (\omega_{a,out} - \omega_{a,in}) dt \quad (1)$$

It should be noted that to calculate the amount of water that is adsorbed/desorbed during one cycle, the MRC's unit should be changed to the SI format, i.e., kg/s, then multiplied by the cycle time ($2\ t_{cycle/2}$) . In the current study, as MRC is depending on the size of the system, new definition of MRC, i.e., MRC*, is introduced, which is MRC per frontal surface area:

$$MRC^* = \frac{MRC}{Surface\ of\ the\ frontal\ area} \quad (2)$$

The DCOP is the ratio of the latent heat removed during the adsorption process ($\dot{Q}_{lat}$) over the input energy, i.e., heater power ($\dot{Q}_{reg}$), and electrical power input of the fan ($\dot{Q}_{fan}$). The DCOP can be computed using the following equation [80]:

$$DCOP = \frac{\dot{Q}_{lat}}{\dot{Q}_{reg}+\dot{Q}_{fan}} \approx \frac{\dot{Q}_{lat}}{\dot{Q}_{reg}} \quad (3)$$

Considering the trivial power consumption of the fan, in the absence of a heater, which is the case for the IsoHMX, the DCOP is going to be a massive number. To be more accurate, it should be noted that as it was explained earlier, the hot stream which resembles the inside air of the greenhouse will be cooler and drier after passing through the IsoHMX. This air should be heated up to the inlet temperature, i.e., 25°C, in order to maintain the greenhouse's temperature at a constant temperature. The time average amount power that is needed to heat up this return air, is considered as heater power ($\dot{Q}_{reg}$) to calculate the DCOP for the IsoHMX, i.e., $DCOP_{IsoHMX}$, see Section 0:

$$DCOP_{IsoHMX} = \frac{\dot{Q}_{lat}}{\dot{Q}_{reg}} = \frac{\frac{1}{t_{cycle/2}} \int_0^{t_{cycle/2}} h_{fg} \dot{m}_{ads} dt}{\frac{1}{t_{cycle/2}} \int_0^{t_{cycle/2}} \dot{m}_{air} c_{p,a} (T_{a,in} - T_{a,out}) dt} \quad (4)$$

1.4 Research motivation

A dehumidification system with low energy consumption, environmentally friendly, and suitable for cold climates is the outcome of this research project. We strongly believe that the cold climate countries and specifically Canada, at the forefront of environmental leadership in North America, implementing this idea can effectively reduce the fuel consumption, and minimize greenhouse gases and carbon emissions in greenhouses. This project is part of a Natural Sciences and Engineering Research Council of Canada (NSERC) College-University Idea to Innovation (Cu-I2I) Grant collaboration project on reducing energy consumption of greenhouses between Simon Fraser University, Kwantlen Polytechnic University, CORE Energy Recovery Solutions Inc., and Argus Technologies Ltd.

1.5 Research objectives

This study aims to investigate and develop a new improved sorption-based system, which works under isothermal condition (named isothermal heat and mass exchanger (IsoHMX)) as an alternative dehumidification system to increase the water uptake, i.e., the amount of water that is adsorbed during adsorption, and significantly reduce the input energy. The novel concept is based on delivering the released heat of adsorption from the high humidity stream to the desorption part of the system, where the drier air stream is being processed. This heat delivery results in an ideal isothermal condition during the adsorption/desorption process, which results in cooler adsorption and warmer desorption processes. This will significantly improve the sorption kinetics in both adsorption and desorption processes.

As part of this research, a proof-of-concept test set up for the proposed IsoHMX is built, aluminum and acrylic are considered for building the heat/mass exchanger and their performance are compared. IsoHMX design is optimized using a new heat/mass transfer model that is also a part of this PhD program and the performance of the optimized IsoHMX is compared to a commercial desiccant wheel (DW).

A quick overview of the different types of moisture control technologies in the greenhouse, and the novel moisture removal system is explained in the current chapter.

At chapter 2, analytical and numerical models are explained, followed by experimental study of the proposed system in chapter 3 which the model was validated with. Then, the optimized design of the system is found in chapter 4, and its performance is compared to a commercial desiccant wheel at chapter 5.

2 Modeling

In the following chapter, numerical and analytical modeling of the IsoHMX is explained. It should be noted that numerical model which is easier to develop was developed before the analytical model. Having a valid numerical code before developing an analytical model, helps to have a better understanding of the phenomenon and importance of each parameter and terms in the equations.

There are only a few studies in the literature that introduced an analytical solution for desiccant-based dehumidification systems. Lee and Kim [81] employed an integral model and simplified the governing equations of a desiccant wheel to a set of ordinary differential equations. Kang et al. [82], [83] assumed linear humidity and temperature profiles along the channel solved the heat and mass transfer equations analytically and reported root mean square errors of less than 10%.

Bahrehmand et al. [84], [85] proposed a novel analytical model to study the performance of coated sorption beds for a sorption closed-cycle, i.e., a sorption system in the absence of non-condensable gases (NCG), e.g., air. Although, the sorption closed-cycle dehumidification system study is not directly applicable to the open-cycle, their analytical approach is quite relevant and noteworthy. Employing an orthogonal expansion technique, they solved the 2D transient heat and mass transfer equations and validated the results with measurements. Bahrehmand and Bahrami [86] also introduced an analytical design tool for sorber bed heat exchangers, and reported that the sorption composite composition, sorber bed geometry, heat transfer characteristics, and cycle time can have conflicting counter effects on the performance and should be optimized simultaneously.

Due to the complicated nature of desiccant-based dehumidification systems, i.e., highly-coupled transient heat and mass transfer phenomena, numerical simulation of these systems is time-consuming. As a result, using a numerical simulation for optimizations and real time control is not practical. Therefore, one of the objectives of this study is to develop a closed-form analytical solution to evaluate the performance of the IsoHMX.

2.1 Analytical model development

A simplified 2D geometry of the experimental test section is considered and is shown schematically in Figure 6. This geometry consisted of two air streams, two desiccant layers, and a substrate. Based on the physics of adsorption/desorption cycles, the cyclic steady state is assumed

for the presented model. Also, in the IsoHMX after one half cycle channel, it behaves like channel two and vice versa, therefore, only a half cycle needs to be modeled. The following additional assumptions are made to simplify the model development:

- Thermophysical properties for the air, substrate, and desiccant layer are assumed constant. As the temperature doesn't vary more than ±25°C and the pressure is almost constant, i.e., system works under atmospheric pressure, this is a valid assumption;
- The regeneration temperature is low (less than 90°C [87]); thus, a constant enthalpy of adsorption (h_{ad}) is assumed following Ref. [88]; This assumption is backed up with experimental measurements of the TPS. The calculated enthalpy of adsorption is 2440 (KJ/Kg);
- The air stream is assumed to be fully-developed over the heat/mass exchanger; therefore, the heat and mass transfer coefficients are considered constant over time. due to low velocity of the air and low ratio of channel height over channel length this is a valid assumption;
- The axial heat conduction in the air stream and desiccant layer are considered negligible; Due to low heat diffusivity of the air and strong advection heat transfer;
- The Lewis number, i.e., the ratio of thermal diffusivity and mass diffusivity, equal to unity is assumed. Lewis number is strong function of the material, and is almost equal to one for air. Thus, this is a valid assumption;
- The effects of unsteady terms in the air stream ($\frac{\partial T_a}{\partial t} \approx \frac{\partial \omega_a}{\partial t} \approx 0$) are assumed negligible, following Ref. [82]. Numerical analysis and comparison of the mentioned terms showed that they are two orders of magnitude lower than the other terms in the air energy and mass transfer equation;
- Water uptake in desiccant layer is equal to its equilibrium uptake [82]. This assumption was also validated by a comparison in numerical simulation, see section 2.2;

- As the desiccant layer is thin (less than 0.3mm [89]), the Biot number is smaller than 0.1 (0.03 in this case), the lumped model assumption is valid. So, averaged properties in the y-direction are used, namely, $T_d(x,t), \omega_d(x,t)$ [90].
- As the substrate is thin and its thermal diffusivity and conductivity are high, constant temperature for substrate in the y-direction is assumed. This assumption was validated with a numerical solution;
- Based on well-stablished internal flow studies [91], the air temperature and humidity profiles are assumed to be exponential in the x-direction [92] ; and
- There is no condensation happening in the system. This assumption depends on the working condition of the system. In the current study based on the experimental results and calculations, this is a valid assumption. (In case of condensation, i.e., substrate's temperature is lower than dew point temperature of the air stream, this model is not valid anymore.)

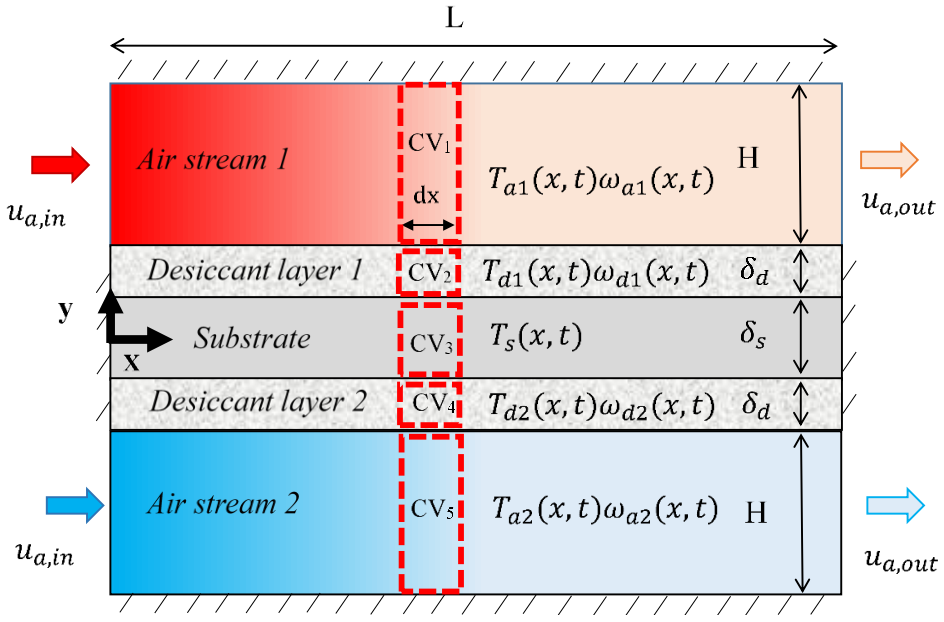

Figure 6. A sectional schematic view of the IsoHMX calculation domain and selected control volumes for the present model

2.1.1 Governing equations

As shown in Figure 6, five control volumes, i.e., CV_1 to CV_5, and the energy and mass exchanges between them are considered. Based on the above-mentioned assumptions, the energy and mass balances for each control volume are expressed as:

Energy and mass balance in CV_1

$$u_{avg}\frac{\partial T_{a1}(x,t)}{\partial x}=\frac{1}{\rho_a c_{P,a}\mathrm{H}}h\big(T_{d1}(x,t)-T_{a1}(x,t)\big) \tag{5}$$

$$u_{avg}\frac{\partial \omega_{a1}(x,t)}{\partial x}=\frac{1}{H}h_m\big(\omega_{d1}(x,t)-\omega_{a1}(x,t)\big) \tag{6}$$

where, H is the channel height, h and h_m are convective heat and mass transfer coefficient, respectively, u_{avg}, $T_a(x,t)$ and $\omega_a(x,t)$ are air bulk values, i.e., average values in the y-direction for air velocity, temperature and humidity ratio, respectively. $T_d(x,t)$ and $\omega_d(x,t)$ are desiccant average value the y-direction for temperature and humidity ratio, respectively. The bulk temperature and humidity ratio of the air as listed in the assumptions, is calculated based on the exponential profile assumption:

$$\begin{aligned} T_{a1(or2)}(t,x)&=a_{T1(or2)}(t)\,exp\left(-\frac{S_1 x}{L}\right)+\left(T_{a1(or2),in}-a_{T1(or2)}(t)\right)\\ \omega_{a1(or2)}(t,x)&=a_{\omega 1(or2)}(t)\,exp\left(-\frac{S_1 x}{L}\right)+\left(\omega_{a1(or2),in}-a_{\omega 1(or2)}(t)\right)\end{aligned} \tag{7}$$

where, $\boldsymbol{a_{T1(or2)}(t)}$ and $\boldsymbol{a_{\omega 1(or2)}(t)}$ are unknown functions of time, which should be calculated and $\boldsymbol{S_1}$ is listed in Table 2:

Table 2.

The same set of equations is defined for **CV_5**:

$$u_{avg}\frac{\partial T_{a2}(x,t)}{\partial x}=\frac{1}{\rho_a c_{P,a}\mathrm{H}}h\big(T_{d2}(x,t)-T_{a2}(x,t)\big) \tag{8}$$

$$u_{avg}\frac{\partial \omega_{a2}(x,t)}{\partial x} = \frac{1}{H}h_m\big(\omega_{d2}(x,t) - \omega_{a2}(x,t)\big) \tag{9}$$

Energy and mass balance in CV$_2$

$$\begin{aligned}\rho_d c_{P,d}\delta_d \frac{\partial T_{d1}(x,t)}{\partial t} \\ = h_{ad}\rho_a h_m\big(\omega_{a1}(x,t) - \omega_{d1}(x,t)\big) + h\big(T_{a1}(x,t) - T_{d1}(x,t)\big) \\ + 2k_d/\delta_d\big(T_s(x,t) - T_{d1}(x,t)\big)\end{aligned} \tag{10}$$

$$\frac{\partial W_{d1}(x,t)}{\partial T_{d1}(x,t)}\frac{\partial T_{d1}(x,t)}{\partial t} + \frac{\partial W_{d1}(x,t)}{\partial \omega_{d1}(x,t)}\frac{\partial \omega_{d1}(x,t)}{\partial t} = \frac{\rho_a}{\rho_d\delta_d}h_m\big(\omega_{a1}(x,t) - \omega_{d1}(x,t)\big) \tag{11}$$

The same set of equations is defined for **CV$_4$**:

$$\begin{aligned}\rho_d c_{P,d}\delta_d \frac{\partial T_{d2}(x,t)}{\partial t} \\ = h_{ad}\rho_a h_m\big(\omega_{a2}(x,t) - \omega_{d2}(x,t)\big) + h\big(T_{a2}(x,t) - T_{d2}(x,t)\big) \\ + 2k_d/\delta_d\big(T_s(x,t) - T_{d2}(x,t)\big)\end{aligned} \tag{12}$$

$$\frac{\partial W_{d2}(x,t)}{\partial T_{d2}(x,t)}\frac{\partial T_{d2}(x,t)}{\partial t} + \frac{\partial W_{d2}(x,t)}{\partial \omega_{d2}(x,t)}\frac{\partial \omega_{d2}(x,t)}{\partial t} = \frac{\rho_a}{\rho_d\delta_d}h_m\big(\omega_{a2}(x,t) - \omega_{d2}(x,t)\big) \tag{13}$$

where, W_d is the desiccant water uptake, and δ_d is the desiccant layer thickness.

Energy balance in CV$_3$

$$\rho_s c_{P,s}\delta_s \frac{\partial T_s(x,t)}{\partial t} = 2k_d/\delta_d\big(T_{d1}(x,t) + T_{d2}(x,t) - 2T_s(x,t)\big) + k_s\delta_s\frac{\partial^2 T_s(x,t)}{\partial x^2} \tag{14}$$

where, T_s is substrate temperature, and δ_s is substrate thickness. The governing equations should be solved simultaneously with the following initial conditions for both air streams and desiccant layers, i.e., 1 and 2. These conditions are derived based on a cyclic steady state assumption and the fact that on the second half of the cycle, stream 1 behaves as stream 2 in the first half and vice versa:

$$\begin{cases} \omega_{d1}(x,0) = \omega_{d2}\left(x, t_{cycle/2}\right) & At\ the\ beginning\ of\ process\ for\ stream\ 1 \\ \omega_{d1}\left(x, t_{cycle/2}\right) = \omega_{d2}(x,0) & At\ the\ beginning\ of\ regeneration\ for\ stream\ 2 \\ T_{d1}(x,0) = T_{d2}\left(x, t_{cycle/2}\right) & At\ the\ beginning\ of\ process\ for\ stream\ 1 \\ T_{d1}\left(x, t_{\frac{cycle}{2}}\right) = T_{d2}(x,0) & At\ the\ beginning\ of regeneration\ for\ stream\ 2 \\ T_s(x,0) = T_s\left(x, t_{cycle/2}\right) & At\ the\ beginning\ and\ end\ of\ a\ half\ cycle \end{cases} \quad (15)$$

where, $t_{cycle/2}$ is half cycle time. The derivation method of the parameters used in the above governing equations are summarized in Table 1.

Table 1. Derivation of used parameters in the governing equations

Parameter	Formula
ω	$0.622\ RH\ P_{sat}/(P_{atm} - RH\ P_{sat})$ [93]
$Nu_{q,lam}$(isoflux)	4.36 [91]
$Nu_{T,lam}$(isothermal)	3.66 [91]
$Nu_{avg,lam}$	$(Nu_{T,lam} + Nu_{q,lam})/2$
h	$Nu_{avg,lam}k_a/H$
h_m	$h/\rho c_p$ [91]

To develop a generalized solution for various conditions and geometries, proper dimensionless parameters should be defined, which are listed in Table 2:

Table 2. Definition of the dimensionless variables and parameters used in the analytical solution with the respective order of magnitude

Variable or Parameter	Formula	Order of magnitude
Dimensionless time	$\tau = \frac{t}{t_{cycle/2}}$	1
Dimensionless temperature	$\theta = \frac{T - T_{a2,in}}{T_{a1,in} - T_{a2,in}} = \frac{T - T_{a2,in}}{\Delta T}$	1
Dimensionless humidity ratio	$\Omega = \frac{\omega - \omega_{a2,in}}{\omega_{a1,in} - \omega_{a2,in}} = \frac{\omega - \omega_{a2,in}}{\Delta \omega}$	1
Rate of change in uptake with dimensionless temperature	$S_\theta = \frac{\partial W_d(\tau)}{\partial \theta_{d,avg}(\tau)}$	-
Rate of change in uptake with dimensionless humidity ratio	$S_\Omega = \frac{\partial W_{d,avg}(\tau)}{\partial \Omega_{d,avg}(\tau)}$	0.1
Convection heat/mass transfer rate in air over heat/mass carried by air mass flow (advection)	$S_1 = \frac{h\ L}{u_{avg}\ \rho_a c_{P,a} H} = \frac{h_m\ L}{u_{avg}\ H}$	1
Adsorption heat generation over heat stored in desiccant layer	$S_2 = \frac{h_{ad} \rho_a h_m\ \Delta\omega\ t_{cycle/2}}{\rho_d c_{P,d} \delta_d\ \Delta T}$	10
Amount of heat transferred from air to desiccant over thermal inertia of desiccant layer	$S_3 = \frac{h\ t_{cycle/2}}{\rho_d c_{P,d} \delta_d}$	10

Amount of heat transferred from substrate to desiccant layer over thermal inertia of desiccant layer	$S_4 = \frac{2k_d\ t_{cycle/2}}{\rho_d c_{P,d} \delta_d^2}$	10^4
Amount of mass transferred from air to desiccant over mass of desiccant layer	$S_5 = \frac{\rho_a h_m \Delta\omega t_{cycle/2}}{\rho_d \delta_d}$	0.01
Amount of heat transferred from substrate to desiccant layer over thermal inertia of substrate	$S_6 = \frac{2k_d\ t_{cycle/2}}{\rho_s c_{P,s} \delta_s \delta_d}$	10^6

By averaging the above equations over the length of the IsoHMX (axial direction) ($\frac{1}{\mathrm{L}} * \int_0^L dx$) and introducing the dimensionless variables listed in Table 2, the following equations are obtained:

- Energy balance in CV_1 & CV_5

$$\left(\theta_{a1,out}(\tau) - \theta_{a1,in}\right) = S_1 \left(\theta_{d1,avg}(\tau) - \theta_{a1,avg}(\tau)\right) \quad (16)$$

$$\left(\theta_{a2,out}(\tau) - \theta_{a2,in}\right) = S_1 \left(\theta_{d2,avg}(\tau) - \theta_{a2,avg}(\tau)\right) \quad (17)$$

- Mass balance in CV_1 & CV_5

$$\left(\Omega_{a1,out}(\tau) - \Omega_{a1,in}\right) = S_1 \left(\Omega_{d1,avg}(\tau) - \Omega_{a1,avg}(\tau)\right) \quad (18)$$

$$\left(\Omega_{a2,out}(\tau) - \Omega_{a2,in}\right) = S_1 \left(\Omega_{d2,avg}(\tau) - \Omega_{a2,avg}(\tau)\right) \quad (19)$$

- Energy balance in CV_2 & CV_4

$$\frac{\partial\theta_{d1,avg}(\tau)}{\partial\tau} = S_2 \left(\Omega_{a1,avg}(\tau) - \Omega_{d1,avg}(\tau)\right) + S_3 \left(\theta_{a1,avg}(\tau) - \theta_{d1,avg}(\tau)\right) + S_4 \left(\theta_{s,avg}(\tau) - \theta_{d1,avg}(\tau)\right) \quad (20)$$

$$\frac{\partial \theta_{d2,avg}(\tau)}{\partial \tau} = S_2\left(\Omega_{a2,avg}(\tau) - \Omega_{d2,avg}(\tau)\right) + S_3\left(\theta_{a2,avg}(\tau) - \theta_{d2,avg}(\tau)\right) + S_4\left(\theta_{s,avg}(\tau) - \theta_{d2,avg}(\tau)\right) \quad (21)$$

- Mass balance in CV_2 & CV_4

$$S_\theta \frac{\partial \theta_{d1,avg}(\tau)}{\partial \tau} + S_\Omega \frac{\partial \Omega_{d1,avg}(\tau)}{\partial \tau} = S_5\left(\Omega_{a1,avg}(\tau) - \Omega_{d1,avg}(\tau)\right) \quad (22)$$

$$S_\theta \frac{\partial \theta_{d2,avg}(\tau)}{\partial \tau} + S_\Omega \frac{\partial \Omega_{d2,avg}(\tau)}{\partial \tau} = S_5\left(\Omega_{a2,avg}(\tau) - \Omega_{d2,avg}(\tau)\right) \quad (23)$$

- Energy balance in CV_3

$$\frac{\partial \theta_{s,avg}(\tau)}{\partial \tau_r} = S_6\left(\theta_{d1,avg}(\tau) + \theta_{d2,avg}(\tau) - 2\theta_{s,avg}(\tau)\right) \quad (24)$$

The above system of equations needs five initial values. As it was mentioned, considering the cyclic nature of the IsoHMX operation in one half cycle, five initial conditions for $\Omega_{d1,avg}$, $\Omega_{d2,avg}$, $\theta_{d1,avg}$, $\theta_{d2,avg}$, and $\theta_{s,avg}$ could be obtained as follows:

$$\begin{cases} \Omega_{d1,avg}(0) = \Omega_{d2,avg}(1) & At\ the\ beginning\ of\ process\ for\ stream\ 1 \\ \Omega_{d1,avg}(1) = \Omega_{d2,avg}(0) & At\ the\ beginning\ of\ regeneration\ for\ stream\ 2 \\ \theta_{d1,avg}(0) = \theta_{d2,avg}(1) & At\ the\ beginning\ of\ process\ for\ stream\ 1 \\ \theta_{d1,avg}(1) = \theta_{d2,avg}(0) & At\ the\ beginning\ of\ regeneration\ for\ stream\ 2 \\ \theta_{s,avg}(0) = \theta_{s,avg}(1) & At\ the\ beginning\ and\ end\ of\ a\ half\ cycle \end{cases} \quad (25)$$

Before solving these sets of equations, it should be noted that in integrating the equations, S_θ and S_Ω are treated as constant values, which results in no error in the solution; This claim is verified in Section 0. The following steps are taken to make the equations into a simpler form:

Performing a scale analysis on Eq.(24) will result in:

$$\left(\theta_{d1,avg}(\tau) + \theta_{d2,avg}(\tau) - 2\theta_{s,avg}(\tau)\right) \propto O\left(\frac{1}{S_6}\right)\frac{\partial \theta_{s,avg}(\tau)}{\partial \tau} \approx O(10^{-6}) \quad (26)$$

So, even with a huge temperature jump in the substrate (which is not the case), it can be concluded that:

$$\theta_{s,avg}(\tau) \approx \left(\theta_{d1,avg}(\tau) + \theta_{d2,avg}(\tau)\right)/2 \quad (27)$$

Eq.(20) shows that the rate of change in desiccant layer temperature is equal to the right-hand side. The physics of the problem shows that neither of the terms on the right-hand side are trivial. So, replacing $\theta_{s,avg}$ with Eq.(27) in Eq.(20) and running a scale analysis on the right-hand side will lead to:

$$\left(\theta_{d2,avg}(\tau) - \theta_{d1,avg}(\tau)\right) \propto O\left(\frac{S_2 \Delta\Omega}{S_4} + \frac{S_3 \Delta\theta}{S_4}\right) \approx O(10^{-3}) \quad (28)$$

This indicates that at any given time, the average temperature of desiccant on both sides, as well as the substrate's average temperature (Eq.(27)), are almost identical. Based on this, $\theta_{d1\&2}(\tau)$ is defined as:

$$\theta_{d1\&2}(\tau) = \theta_{s,avg}(\tau) \approx \theta_{d1,avg}(\tau) \approx \theta_{d2,avg}(\tau) \quad (29)$$

**** Note on Eq.(29)***(34)***:*** Thermal contact resistance (TCR) between metal surface and adsorbent varies between 1.3 to 3.8 (K/W) [94]. Adding the effect of the TCR will result to a negligible temperature difference (less than 0.5 ℃) between substrate and coating layer.

Based on Eq.(29), rewriting Eq.(16)-(23) will lead to:

- The energy balance in CV_1 & CV_5

$$\left(\theta_{a1,out}(\tau) - \theta_{a1,in}\right) = S_1\left(\theta_{d1\&2}(\tau) - \theta_{a1,avg}(\tau)\right) \quad (30)$$

$$\left(\theta_{a2,out}(\tau) - \theta_{a2,in}\right) = S_1\left(\theta_{d1\&2}(\tau) - \theta_{a2,avg}(\tau)\right) \quad (31)$$

- Mass balance in CV_1 & CV_5

$$\left(\Omega_{a1,out}(\tau) - \Omega_{a1,in}\right) = S_1\left(\Omega_{d1,avg}(\tau) - \Omega_{a1,avg}(\tau)\right) \quad (32)$$

$$\left(\Omega_{a2,out}(\tau) - \Omega_{a2,in}\right) = S_1 \left(\Omega_{d2,avg}(\tau) - \Omega_{a2,avg}(\tau)\right) \tag{33}$$

- Adding up the energy balance in CV_2 & CV_4 ***(see the note below)**

$$\begin{aligned} 2\frac{\partial\theta_{d1\&2}(\tau)}{\partial\tau} = {} & S_2\left(\Omega_{a1,avg}(\tau) + \Omega_{a2,avg}(\tau) - \Omega_{d1,avg}(\tau) - \Omega_{d2,avg}(\tau)\right) \\ & + S_3\left(\theta_{a1,avg}(\tau) + \theta_{a2,avg}(\tau) - 2\theta_{d1\&2}(\tau)\right) \end{aligned} \tag{34}$$

- Mass balance in CV_2 & CV_4

$$S_\theta \frac{\partial\theta_{d1\&2}(\tau)}{\partial\tau} + S_\Omega \frac{\partial\Omega_{d1,avg}(\tau)}{\partial\tau} = S_5 \left(\Omega_{a1,avg}(\tau) - \Omega_{d1,avg}(\tau)\right) \tag{35}$$

$$S_\theta \frac{\partial\theta_{d1\&2}(\tau)}{\partial\tau} + S_\Omega \frac{\partial\Omega_{d2,avg}(\tau)}{\partial\tau} = S_5 \left(\Omega_{a2,avg}(\tau) - \Omega_{d2,avg}(\tau)\right) \tag{36}$$

Based on Eq.(29), the initial conditions, i.e., Eq.(25), are rewritten as follows:

$$\begin{cases} \Omega_{d1,avg}(0) = \Omega_{d2,avg}(1) & At\ the\ beginning\ of\ process\ for\ stream\ 1 \\ \Omega_{d1,avg}(1) = \Omega_{d2,avg}(0) & At\ the\ beginning\ of\ regeneration\ for\ stream\ 2 \\ \theta_{d1\&2}(0) = \theta_{d1\&2}(1) & At\ the\ beginning\ of\ process\ for\ stream\ 1 \end{cases} \tag{37}$$

**** Note on Eq.(34)**:* By subtracting Eq.(20) from (21), the transient term would have been disappeared and so would have $\theta_{s,avg}(\tau)$. But, on the right-hand side, $S_4\left(\theta_{d2,avg}(\tau) - \theta_{d1,avg}(\tau)\right)$ would have shown up. Based on Eq.(29), at first glance, this term appears to be negligible; But, based on Table 2:

Table 2, S_4 has an order of magnitude of 10e4, and based on Eq.(28), $\left(\theta_{d2,avg}(\tau) - \theta_{d1,avg}(\tau)\right)$ has an order of magnitude 10e-3, so the whole term has order of magnitude 10, which is on par with other terms and can't be neglected. But, if instead of subtracting, we add up Eq.(20) and (21), the term $S_4\left(\theta_{d1,avg}(\tau) + \theta_{d2,avg}(\tau) - 2\theta_{s,avg}(\tau)\right)$ appears. Running the same procedure based on Eq.(26) and Table 2, it could easily be shown that this term has an order of magnitude of 10e-2 and could be neglected.

Using the exponential temperature/humidity ratio profile, see Eq.(7) and calculate the average and outlet values will lead to:

$$\theta_{a1(or2),out}(\tau) = \frac{a_{T1(or2)}(\tau)}{\Delta T}\ (exp(-S_1) - 1) + \ \theta_{a1(or2),in} \tag{38}$$

$$\theta_{a1(or2),avg}(\tau) = \frac{a_{T1(or2)}(\tau)}{\Delta T}\ (\frac{1}{S_1} - \frac{exp(-S_1)}{S_1} - 1) + \ \theta_{a1(or2),in} \tag{39}$$

$$\Omega_{a1(or2),out}(\tau) = \frac{a_{\omega 1(or2)}(\tau)}{\Delta T}\ (exp(-S_1) - 1) + \ \Omega_{a1(or2),in} \tag{40}$$

$$\Omega_{a1(or2),avg}(\tau) = \frac{a_{\omega 1(or2)}(\tau)}{\Delta T}\ (\frac{1}{S_1} - \frac{exp(-S_1)}{S_1} - 1) + \ \Omega_{a1(or2),in} \tag{41}$$

Replacing these values in Eq.(30)-(33), will result in the following:

$$a_{T1(or2)} = \big(\theta_{a1(or2),in} - \theta_{d1\&2}(\tau)\big)\Delta T \tag{42}$$

$$a_{\omega 1(or2)} = \big(\Omega_{a1(or2),in} - \Omega_{d1(or2),avg}(\tau)\big)\Delta T \tag{43}$$

Replacing these equations in Eq.(7), we have:

$$\theta_{a1(or2),out}(\tau) = A\ \theta_{d1\&2}(\tau) + (1 - A)\ \theta_{a1(or2),in} \tag{44}$$

$$\theta_{a1(or2),avg}(\tau) = (1 - \frac{A}{S_1})\theta_{d1\&2}(\tau) + \frac{A}{S_1}\ \theta_{a1(or2),in} \tag{45}$$

$$\Omega_{a1(or2),out}(\tau) = A\ \Omega_{d1\&2}(\tau) + (1 - A)\ \Omega_{a1(or2),in} \tag{46}$$

$$\Omega_{a1(or2),avg}(\tau) = (1 - \frac{A}{S_1})\ \Omega_{d1\&2}(\tau) + \frac{A}{S_1}\ \Omega_{a1(or2),in} \tag{47}$$

Replacing these values in Eqs.(34)-(36):

$$\begin{aligned} 2\frac{\partial \theta_{d1\&2}(\tau)}{\partial \tau} = {} & \frac{S_2 A}{S_1}\Big(\Omega_{a1,in} + \Omega_{a2,in} - \Omega_{d1,avg}(\tau) - \Omega_{d2,avg}(\tau)\Big) \\ & + \frac{S_3 A}{S_1}\Big(\theta_{a1,in} + \theta_{a2,in} - 2\theta_{d1\&2}(\tau)\Big) \end{aligned} \tag{48}$$

$$S_\theta \frac{\partial \theta_{d1\&2}(\tau)}{\partial \tau} + S_\Omega \frac{\partial \Omega_{d1,avg}(\tau)}{\partial \tau} = \frac{S_5 A}{S_1} \left(\Omega_{a1,in} - \Omega_{d1,avg}(\tau)\right) \tag{49}$$

$$S_\theta \frac{\partial \theta_{d1\&2}(\tau)}{\partial \tau} + S_\Omega \frac{\partial \Omega_{d2,avg}(\tau)}{\partial \tau} = \frac{S_5 A}{S_1} \left(\Omega_{a2,in} - \Omega_{d2,avg}(\tau)\right) \tag{50}$$

Adding Eq.(49) to (50), we have:

$$2S_\theta \frac{\partial \theta_{d1\&2}(\tau)}{\partial \tau} + 2S_\Omega \frac{\partial \left(\Omega_{d1,avg}(\tau) + \Omega_{d2,avg}(\tau)\right)}{\partial \tau} = \frac{S_5 A}{S_1} \left(\Omega_{a1,in} + \Omega_{a2,in} - \left(\Omega_{d2,avg}(\tau) + \Omega_{d1,avg}(\tau)\right)\right) \tag{51}$$

From Eq.(48), $\left(\Omega_{d1,avg}(\tau) + \Omega_{d2,avg}(\tau)\right)$ could be calculated as:

$$\Omega_{d1,avg}(\tau) + \Omega_{d2,avg}(\tau) = -2\frac{S_3}{S_2}\frac{\partial \theta_{d1\&2}(\tau)}{\partial \tau} - 2\frac{S_3}{S_2}\theta_{d1\&2}(\tau) + \left(\Omega_{a1,in} + \Omega_{a2,in}\right) + \frac{S_3}{S_2}\left(\theta_{a1,in} + \theta_{a2,in}\right) \tag{52}$$

Replacing $\Omega_{d1,avg}(\tau) + \Omega_{d2,avg}(\tau)$ with Eq.(52) in Eq.(51) will lead to the following differential equation:

$$\frac{\partial^2 \theta_{d1\&2}(\tau)}{\partial \tau^2} + X_1 \frac{\partial \theta_{d1\&2}(\tau)}{\partial \tau} + \mathrm{X}_2 \theta_{d1\&2}(\tau) = \mathrm{X}_3 \tag{53}$$

In which:

$$\mathrm{X}_1 = \frac{A}{S_1 S_w}(S_3 S_w + S_5 - S_\theta S_2) \tag{54}$$

$$\mathrm{X}_2 = \frac{A}{S_1 S_w}\left(\frac{A S_3 S_5}{S_1}\right) \tag{55}$$

$$\mathrm{X}_3 = X_2\left(\frac{\theta_{a1,in} + \theta_{a2,in}}{2}\right) \tag{56}$$

Solving Eq.(53), we have:

$$\theta_{d1\&2}(\tau) = \mathrm{B}_1 \exp(-\lambda_1 \tau) + \mathrm{B}_2 \exp(-\lambda_2 \tau) + \left(\frac{\theta_{a1,in} + \theta_{a2,in}}{2}\right) \tag{57}$$

Where, $B_1$and B_2 are unknown constants and:

$$\lambda_{1,2} = \left(X_{1,j} \pm \sqrt{X_{1,j}^2 - 4X_{2,j}}\right)/2 \tag{58}$$

Replacing $\theta_{d1\&2}$ with Eq.(57) in (52), we have:

$$\begin{aligned} &\Omega_{d1,avg}(\tau) + \Omega_{d2,avg}(\tau) = \\ &\frac{\mathrm{B}_1}{S_2}\left(-S_3 + \frac{\lambda_1 S_1}{A}\right)\exp(-\lambda_1 \tau) - \frac{B_2}{S_2}\left(-S_3 + \frac{\lambda_2 S_1}{A}\right)\exp(-\lambda_2 \tau) + \left(\Omega_{a1,in} + \Omega_{a2,in}\right) \end{aligned} \tag{59}$$

Based on initial conditions, see Eq.(37), for $\left(\Omega_{d1,avg}(\tau) + \Omega_{d2,avg}(\tau)\right)$, we have:

$$\Omega_{d1,avg}(1) + \Omega_{d2,avg}(1) = \Omega_{d2,avg}(0) + \Omega_{d1,avg}(0) = \Omega_{d1,avg}(0) + \Omega_{d2,avg}(0) \tag{60}$$

Using the finding in Eq.(60) and the third term of initial conditions, Eq.(37), in Eq.(57) and Eq.(59), we have the following set of two linear equations and two unknows, i.e., $B_1$and B_2:

$$\begin{cases} \mathrm{B}_1(1 - \exp(-\lambda_1)) + \mathrm{B}_2(1 - \exp(-\lambda_2)) = 0 \\ \mathrm{B}_1\left(-\frac{S_3}{S_2} + \frac{\lambda_1 S_1}{A S_2}\right)(1 - \exp(-\lambda_1)) - B_2\left(-\frac{S_3}{S_2} + \frac{\lambda_2 S_1}{A S_2}\right)(1 - \exp(-\lambda_2)) = 0 \end{cases} \tag{61}$$

Eq.(61) is a homogeneous linear system of equations, and the coefficient determinant is a none zero value, so the only possible solution is:

$$B_1 = B_2 = 0 \tag{62}$$

Applying Eq.(62) into Eq.(57), we have:

$$\theta_{d1\&2}(\tau) = \left(\frac{\theta_{a1,in} + \theta_{a2,in}}{2}\right) = 0.5 \tag{63}$$

Which indicates that the average temperature of the desiccant layers and the substrate are always constant and equal to the average inlet temperatures (or are equal to 0.5 in non-dimensional form). Replacing $\theta_{d1\&2}$ with Eq.(63) in Eq.(49) and (50):

$$\frac{\partial \Omega_{d1,avg}(\tau)}{\partial \tau} + N\,\Omega_{d1,avg}(\tau) - N\,\Omega_{a1,in} = 0 \tag{64}$$

$$\frac{\partial \Omega_{d2,avg}(\tau)}{\partial \tau} + N\,\Omega_{d2,avg}(\tau) - N\,\Omega_{a2,in} = 0 \tag{65}$$

In which:

$$N = \frac{S_5 A}{S_1 S_\Omega} \tag{66}$$

The solution to the differential Eqs.(64) and (65) is:

$$\Omega_{d1,avg}(\tau) = C_1 \exp(-N\tau) + \Omega_{a1,in} \tag{67}$$

$$\Omega_{d2,avg}(\tau) = C_2 \exp(-N\tau) + \Omega_{a2,in} \tag{68}$$

where, $C_1$and C_2 are unknown constants. Applying the initial conditions, Eq.(37), will lead to the following set of two linear equations and two unknows, i.e., $C_1$and C_2:

$$\begin{cases} C_1 \exp(-N) + \Omega_{a1,in} = C_2 + \Omega_{a2,in} \\ C_1 + \Omega_{a1,in} = C_2 \exp(-N) + \Omega_{a2,in} \end{cases} \tag{69}$$

Solving this set of equations, we have:

$$\begin{cases} C_1 = \dfrac{\Omega_{a2,in} - \Omega_{a1,in}}{1 + \exp(-N)} \\ C_2 = \dfrac{\Omega_{a1,in} - \Omega_{a2,in}}{1 + \exp(-N)} \end{cases} \tag{70}$$

Thus, the temperature and humidity ratio of the desiccant layer is found. Based on the findings and by replacing them in Eq.(44) and Eq.(46), the temperature and humidity ratio for the outlet air could be calculated. A general form of the final solution for the dimensionless desiccant temperature, outlet air temperature, desiccant humidity ratio, and outlet air humidity ratio are shown in Eq.(71)-Eq.(74), respectively, and the constants are listed in

Table 3.

$$\theta_{d1(or2),avg}(\tau) = \frac{\left(\theta_{a1,in} + \theta_{a2,in}\right)}{2} = 0.5 \tag{71}$$

$$\theta_{a1(or2),out}(\tau) = \frac{A}{2}\theta_{a2(or1),in} + \left(1 - \frac{A}{2}\right)\theta_{a1(or2),in} \tag{72}$$

$$\Omega_{d1(or2),avg}(\tau) = \frac{\left(\Omega_{a2(or1),in} - \Omega_{a1(or2),in}\right)}{1 + exp\ (-N)}\, exp(-N\tau) + \Omega_{a1(or2),in} \tag{73}$$

$$\Omega_{a1(or2),out}(\tau) = A\ \frac{\left(\Omega_{a2(or1),in} - \Omega_{a1(or2),in}\right)}{1 + exp\ (-N)}\, exp(-N\tau) + \Omega_{a1(or2),in} \tag{74}$$

Table 3. List of constants in the final solution of outlet air temperature

Formula	Order of magnitude
$A = (1 - \exp(-S_1))$	1
$N = \frac{A\ S_5}{S_\Omega\ S_1}$	0.1
$S_\Omega = C_{slope}\ 8 \times 10^{-12} \Delta\omega\ P_{tot} \exp\left(\frac{5356.5}{273.15 + \Delta T\ \theta_{d1\&2} + T_{a2,in}}\right)$	0.1

2.1.2 Performance metrics closed-form solution

A closed-form solution for the MRC^* and $the\ DCOP_{IsoHMX}$ can be described based on the non-dimensional solution as:

$$MRC^* = \frac{3600}{t_{cycle}} \int_0^{t_{cycle/2}} \dot{m}_{\mathrm{a}} \left(\omega_{a,out} - \omega_{a,in}\right) dt$$

$$= 1.8 \times 10^3 \rho_a u \Delta\omega \int_0^1 \left(\Omega_{a1,in} - \Omega_{a1,out}\right) d\tau \tag{75}$$

$$= 1.8 \times 10^3 \frac{A}{N} \rho_a u \Delta\omega \frac{\left(1 - exp(-N)\right)}{(1 + \exp(-N))}$$

$$DCOP_{IsoHMX} = \frac{\dot{Q}_{lat}}{\dot{Q}_{reg}} = \frac{\frac{1}{t_{cycle}} \int_0^{t_{cycle/2}} h_{ad} \dot{m}_{ads} dt}{\frac{1}{t_{cycle}} \int_0^{t_{cycle/2}} \dot{m}_{air} c_{p,a} (T_{a1,in} - T_{a2,out}) dt}$$

$$= \frac{h_{ad} \frac{MRC}{3.6 \times 10^3}}{\int_0^1 \dot{m}_{air} c_{p,a} \Delta T \left(\theta_{a1,in} - \theta_{a1,out}\right) d\tau} \tag{76}$$

$$= \frac{2S_2}{NS_3} \frac{\left(1 - exp(-N)\right)}{(1 + exp(-N))}$$

2.1.3 Uptake derivatives with time

As mentioned, it's claimed that treating S_θ and S_Ω as constants, will result in no errors. As it could be seen from the solution, $\theta_d$is constant so its time derivative is equal to zero. Thus, S_θ is omitted from the calculations and taking it as a constant has no effect on the results. In the following, it's shown that a constant desiccant temperature will result in constant S_Ω and this will validate the claim.

The equilibrium humidity ratio as it was shown in Section 3.1.2.1 is governed by the following isotherm relationship:

$$W_d = W_{eq} = 1.39 \exp\left(-0.069\left((T-273)ln\left(\frac{p_{sat}}{p}\right)\right)^{0.52}\right) \tag{77}$$

In which, W_{eq} is the equilibrium uptake, p is the equilibrium vapor pressure over the desiccant and p_{sat} is the vapor saturation pressure in the desiccant temperature. Figure 7 illustrates Eq.(77) and its linear correlation. Using this correlation will result in error if the working range of the system is located at the second half of the curve. So, a piecewise linear correlation is needed for the different working ranges; Generally, each part of the fitted linear piecewise function could be described as:

$$W_d \approx C_{slope}\, RH + C_{intercept} = C_s\, \frac{p}{p_{sat}} + C_i \tag{78}$$

In which, C_{slope} and $C_{intercept}$ are the slope and intercept of the fitted line which could be calculated based on the working range of the system.

Using the experimental data of TGA test, the following linear piecewise function was fitted to the data:

$$W_d = \begin{cases} C_s = 0.92 \;\; C_i = 0.06 & @\ \dfrac{p}{p_{sat}} < 0.4 \\ C_s = 0.64 \;\; C_i = -0.13 & @\ 0.4 < \dfrac{p}{p_{sat}} < 0.65 \\ C_s = 1.51 \;\; C_i = -0.43 & @\ \dfrac{p}{p_{sat}} > 0.65 \end{cases} \tag{79}$$

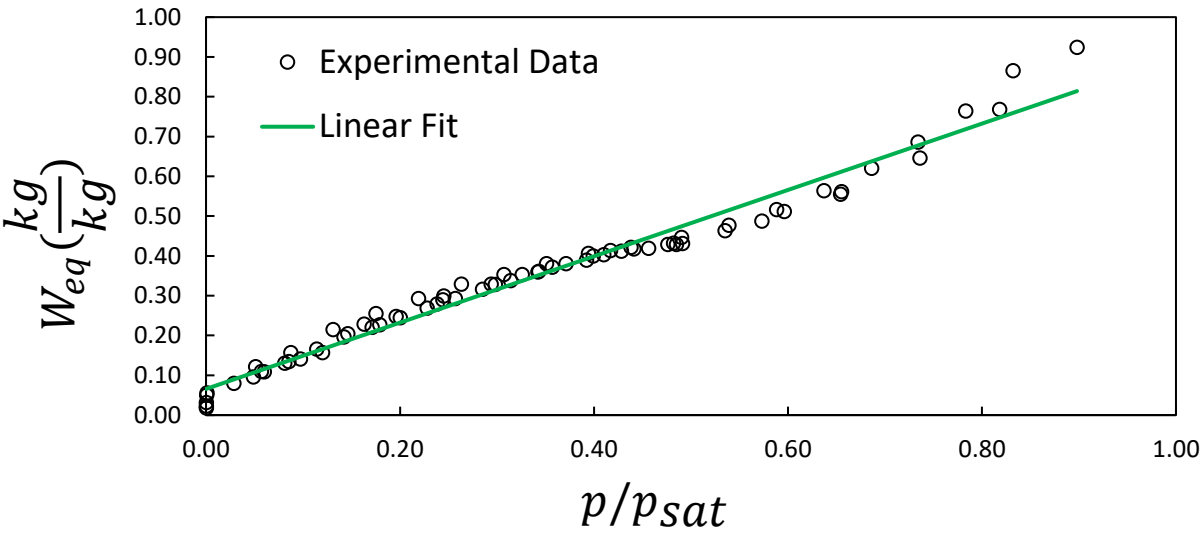

Figure 7. Equilibrium Water uptake (W_{eq}) vs the equilibrium relative humidity of the desiccant

The equilibrium vapor pressure over the total pressure (p_{tot}) could be calculated from the following [93]:

$$\frac{p}{p_{tot}} = \frac{\omega_d}{0.621 + \omega_d} \approx 1.6\,\omega_d \tag{80}$$

Vapor saturation pressure could be expressed as [93]:

$$p_{sat} = 10^{\left(8.07131 - \frac{1730.63}{233.426 + T_d}\right)} \times 133.3$$
$$\Rightarrow \frac{1}{p_{sat}} \approx 5 \times 10^{-12} \exp\left(\frac{5356.5}{273.15 + T_d}\right) \tag{81}$$

Replacing p/p_{tot} and $1/p_{sat}$ with Eq.(80) and Eq.(81) in Eq.(78) will result in the following:

$$W_d \approx C_{slope}\, 8 \times 10^{-12} \omega_d p_{tot} \exp\left(\frac{5356.5}{273.15 + T_d}\right) + C_{intercept}$$
$$= C_{slope}\, 8 \times 10^{-12} (\Omega_d \Delta\omega + \omega_{a1,in})\, p_{tot} \exp\left(\frac{5356.5}{273.15 + T_d}\right) + C_{intercept} \tag{82}$$

Based on Eq.(82), S_Ω is calculated:

$$S_\Omega = \frac{\partial W_{d1(or2),avg}(\tau)}{\partial \Omega_{d1(or2),avg}(\tau)} \approx C_{slope}\, 8 \times 10^{-12} \Delta\omega\, p_{tot} \exp\left(\frac{5356.5}{273.15 + \Delta T\, \theta_{d1\&2} + T_{a2,in}}\right) \tag{83}$$

With respect to that, $\theta_{d1\&2}$ is constant. Eq.(83) shows that S_Ω is also constant.

2.1.4 Analytical model validation with experimental data

The analytical model DCOP and MRC* was verified with experimental data over different conditions, explained in section 3.3. The maximum difference between the data and analytical model for the MRC* and DCOP are 10%, see Figure 8.

Measured data and model are compared in a graph brought in Figure 8. As it can be seen for the DCOP, the model falls between +10% and – 5% of experimental data and for the MRC* in ±10%.

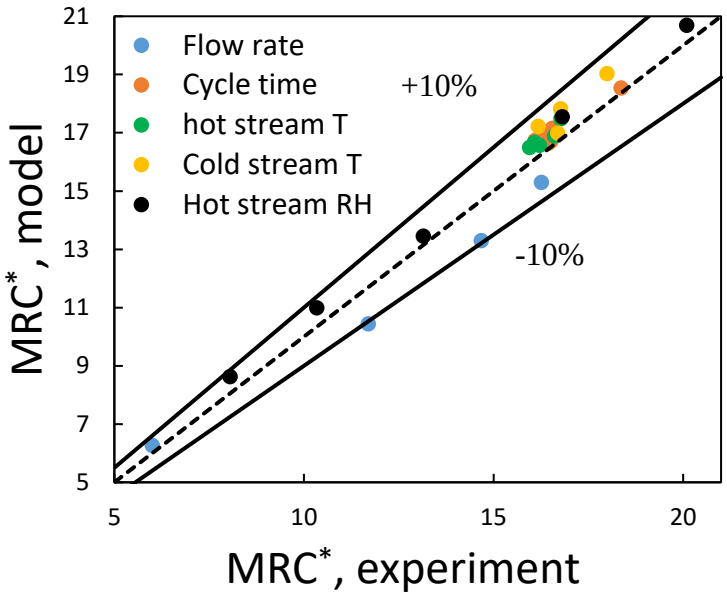

a)

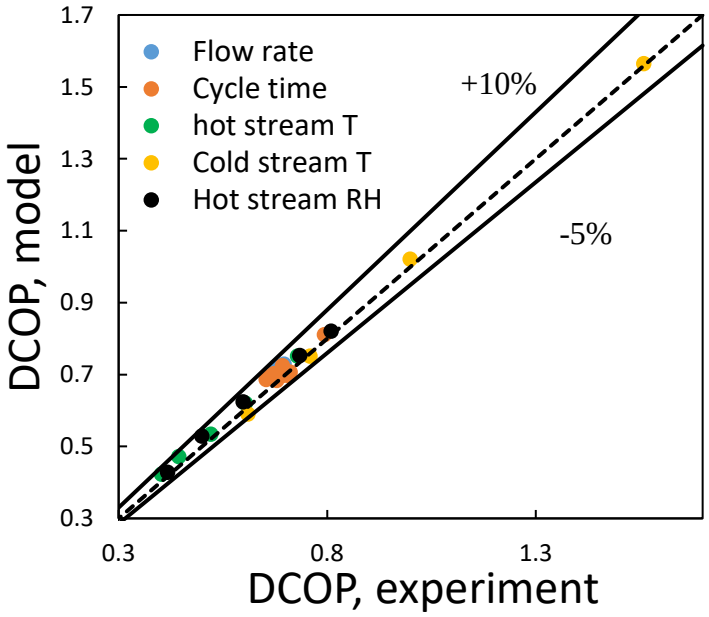

b)

Figure 8. a) MRC* and b) DCOP analytical solution validation with experimental data

2.2 Numerical simulation

The numerical work of this study is based on an already existing MATLAB[95] code for desiccant wheel dehumidification, which was developed and validated by measurements in our lab by former students [96]. The mentioned code was enhanced and changed to be able to simulate the IsoHMX. Enhancements that are included: make the code faster, validate for a wider range of conditions, and make it more robust mostly by changing discretization method explained at the following.

The same geometry and control volume for the analytical model (except for substrate) is used for the numerical simulation, see Figure 9. The control volume for the substrate has a width of dx and height of dy.

It should be noted that the analytical model needed more assumptions to simplify the problem so it would be solved.

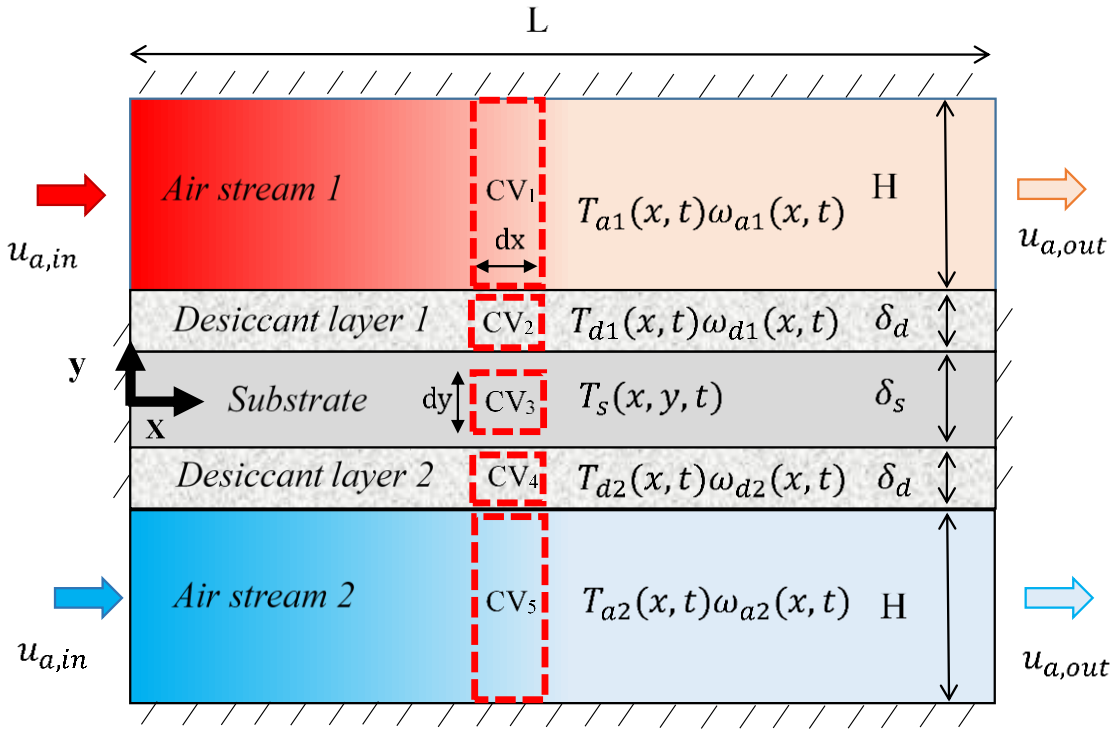

Figure 9. A sectional schematic view of the IsoHMX calculation domain and selected control volumes for the numerical simulation

The following assumptions are made for the simulation:

- The thermophysical properties for the air, substrate, and desiccant layer are assumed constant;
- The air stream is assumed to be fully-developed over the heat/mass exchanger. Therefore, the heat and mass transfer coefficients are considered constant over time;
- The axial heat conduction in the air stream and desiccant layer are considered negligible;
- As the desiccant layer is thin (less than 0.3mm [89]), the averaged properties in the y-direction are used, namely, $T_d(x,t), \omega_d(x,t)$ [90];
- There is no condensation happening in the system; and
- Both equilibrium and liner driving force (LDF) were considered for adsorption kinetics and results were compared.

2.2.1 Governing equations

Based on the above assumptions, the heat and mass transfer equations with equilibrium assumption could be described as follows:

Energy and mass balance in CV_1

$$\frac{\partial T_{a1}(x,t)}{\partial t} + u_{avg}\frac{\partial T_{a1}(x,t)}{\partial x} = \frac{1}{\rho_a c_{P,a}\mathrm{H}} h\big(T_{d1}(x,t) - T_{a1}(x,t)\big) \tag{84}$$

$$\frac{\partial \omega_{a1}(x,t)}{\partial t} + u_{avg}\frac{\partial \omega_{a1}(x,t)}{\partial x} = \frac{1}{H} h_m\big(\omega_{d1}(x,t) - \omega_{a1}(x,t)\big) \tag{85}$$

The same set of equations is defined for **CV_5**.

$$\frac{\partial T_{a2}(x,t)}{\partial t} + u_{avg}\frac{\partial T_{a2}(x,t)}{\partial x} = \frac{1}{\rho_a c_{P,a}\mathrm{H}} h\big(T_{d2}(x,t) - T_{a2}(x,t)\big) \tag{86}$$

$$\frac{\partial \omega_{a2}(x,t)}{\partial t} + u_{avg}\frac{\partial \omega_{a2}(x,t)}{\partial x} = \frac{1}{H} h_m\big(\omega_{d2}(x,t) - \omega_{a2}(x,t)\big) \tag{87}$$

With the following boundary conditions for both control volumes:

$$\begin{cases} @x = 0 \ : T_a = T_{a,in}\,, \omega_a = \omega_{a,in} \\ @\ x = L: \dfrac{\partial T_a}{\partial x} = \dfrac{\partial \omega_a}{\partial x} = 0 \end{cases} \tag{88}$$

Energy and mass balance in CV_2

$$\begin{aligned} \rho_d c_{P,d} \delta_d \frac{\partial T_{d1}(x,t)}{\partial t} \\ = h_{ad} \rho_a h_m \big(\omega_{a1}(x,t) - \omega_{d1}(x,t)\big) + h\big(T_{a1}(x,t) - T_{d1}(x,t)\big) \\ + 2k_d/\delta_d \big(T_s(x, \delta_s/2, t) - T_{d1}(x,t)\big) \end{aligned} \tag{89}$$

$$\frac{\partial W_{d1}(x,t)}{\partial T_{d1}(x,t)} \frac{\partial T_{d1}(x,t)}{\partial t} + \frac{\partial W_{d1}(x,t)}{\partial \omega_{d1}(x,t)} \frac{\partial \omega_{d1}(x,t)}{\partial t} = \frac{\rho_a}{\rho_d \delta_d} h_m \big(\omega_{a1}(x,t) - \omega_{d1}(x,t)\big) \tag{90}$$

The same set of equations is defined for **CV_4**:

$$\begin{aligned} \rho_d c_{P,d} \delta_d \frac{\partial T_{d2}(x,t)}{\partial t} \\ = h_{ad} \rho_a h_m \big(\omega_{a2}(x,t) - \omega_{d2}(x,t)\big) + h\big(T_{a2}(x,t) - T_{d2}(x,t)\big) \\ + 2k_d/\delta_d \big(T_s(x, -\delta_s/2, t) - T_{d2}(x,t)\big) \end{aligned} \tag{91}$$

$$\frac{\partial W_{d2}(x,t)}{\partial T_{d2}(x,t)} \frac{\partial T_{d2}(x,t)}{\partial t} + \frac{\partial W_{d2}(x,t)}{\partial \omega_{d2}(x,t)} \frac{\partial \omega_{d2}(x,t)}{\partial t} = \frac{\rho_a}{\rho_d \delta_d} h_m \big(\omega_{a2}(x,t) - \omega_{d2}(x,t)\big) \tag{92}$$

Energy balance in CV_3

$$\frac{\partial T_s(x,t)}{\partial t} = \alpha_s \left(\frac{\partial^2 T_s(x,y,t)}{\partial x^2} + \frac{\partial^2 T_s(x,y,t)}{\partial y^2}\right) \tag{93}$$

With the following boundary conditions:

$$\begin{cases} @\ y = \delta_s \ : -k_s \dfrac{\partial T_s(x,y,t)}{\partial y} = \dfrac{2k_d}{\delta_d T_{d1}(x,t)} \\ @\ y = -\delta_s : -k_s \dfrac{\partial T_s(x,y,t)}{\partial y} = 2k_d/\delta_d T_{d2}(x,t) \\ @\ x = 0\,, L: \dfrac{\partial T_s}{\partial x} = 0 \end{cases} \tag{94}$$

The aforementioned governing equations for the air and desiccant, i.e., CVs 1, 2, 4, and 5, are discretized into finite difference equations by an explicit, forward difference method in time and the backward difference method in space. Even the central method for space discretization is a better approximation than the backward method. It should be noted that this is a transient simulation and physically speaking, in the air stream, most of the data is coming from the upstream and there is no derivative of space for the desiccant, so, backward discretization for space for the air stream resulted in a more robust code. The 2D heat conduction equation in CV_3, is discretized into finite difference equation by the explicit, forward difference method in time and a second-order central difference method in space.

All of the simulations are performed with a grid of 10 for space in *x*, and 4 in the *y* direction. The grid independence has been proven to be valid within a tolerable limit. A cyclic steady state is obtained within 100 cycles.

In 2D heat conduction simulation, see Eq.(88), there is a limitation for the Fourier number i.e., diffusivity multiplied by the ratio of time step over the grid size in both *x* and *y* direction[91]:

$$Fo = \frac{\alpha_s \, dt}{dx^2 (or \; dy^2)} < \frac{1}{2} \tag{95}$$

The default value for the time step in the code is 5ms. This value is iteratively updated at the beginning of the code to meet the requirement in Eq.(95).

The code is included in Appendix A: MATLAB code.

2.2.2 Numerical model validation with experimental data

The numerical code was validated against the experimental data and other existing desiccant wheel data from references[97]. The measured data and numerical model are compared in a graph brought in Figure 10. As it can be seen for the DCOP, the model falls between ±7% of experimental data and for the MRC*, in +6% and -5%.

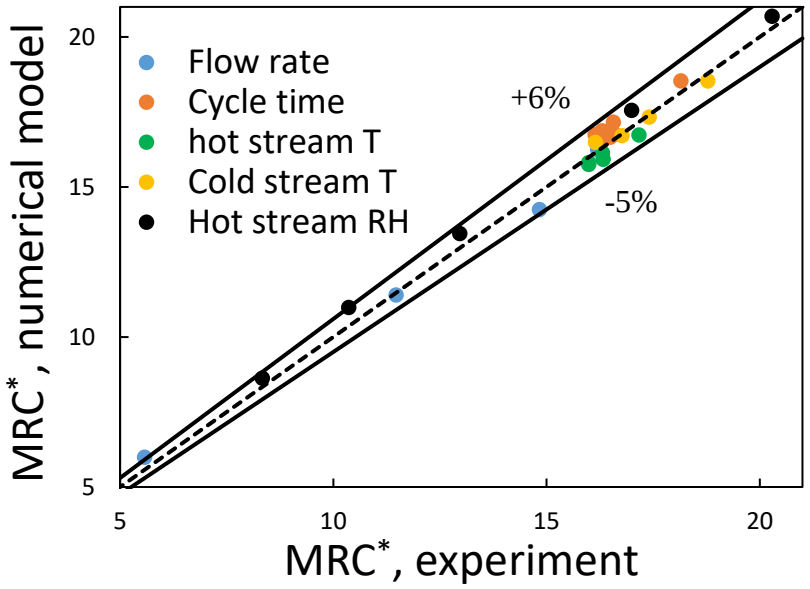

a)

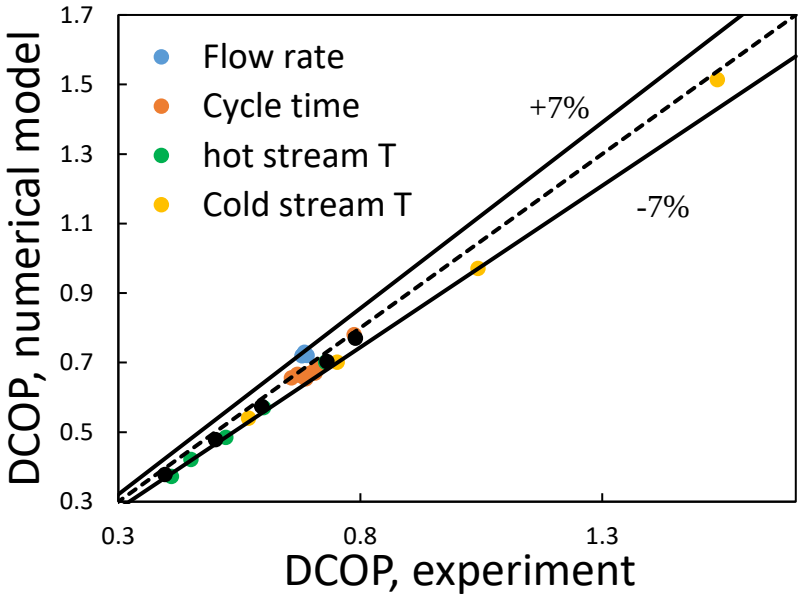

b)

Figure 10. a) MRC* and b) DCOP analytical solution validation with experimental data

2.3 Conclusion

A closed-form analytical model and a numerical model to predict the performance of IsoHMX is developed and has shown good agreement with the experimental data. The calculated DCOP for analytical model falls between +10% and – 5% of experimental data and for the MRC^* in ±10%. For the numerical model, the DCOP falls between ±7% of the experimental data and for the MRC^*, in +6% and -5%.

The numerical code is more accurate but takes time to converge and for optimization and real time control using such a model is not applicable. On the other hand, the analytical model is a closed-form, which can be easily used for optimization and real time control applications.

3 Experimental work

The aim of the experimental study of the IsoHMX is a proof-of-concept for a range of conditions. Thus, the analytical model and numerical simulation could be validated based on the measurements and any further change in the inlet conditions, or the geometry could be predicted by the model.

Parallel flow IsoHMX was chosen for the test bed design, see Figure 5. So, a test bed was needed to be able to hold a sample with coting on the both sides between two air channels and measures the inlet and outlet's relative humidity and temperature. As the adsorption is cyclic phenomenon and works with two different air streams, test bed had to be able to provide these two air streams and change them between the channels with a known interval. Also, the relative humidity, temperature, and velocity of the air streams should've been controllable to be able to measure their effect on the performance of the system. More particularly, a cold dry air stream that represents the outside cold condition, and warm humid air stream which represents the inside of the greenhouse.

The experimental study consists of two major parts, the double side coated sample preparation and the test bed design and build.

3.1 Sample preparation

Two samples are needed for the proof-of-concept and achieving the isothermal adsorption/desorption; one with high and the other one with low thickness, thermal conductivity and diffusivity. The conductive substrate represents the IsoHMX and the insulation one represents the conventional desiccant wheel. Another important feature that should be considered is the thickness of the coating. A thin coating (less than 0.3mm [89]) will result in a uniform temperature distribution in a radial direction in the coating layer, which is a necessity for achieving isothermal adsorption and desorption. The substrate properties and coating procedure is detailed in the following.

3.1.1 Substrate

Two different substrates are chosen to investigate the effect of the substrate properties on the performance of the IsoHMX; a thin (0.66mm) aluminum substrate which has high thermal conductivity and diffusivity (to have a better heat transfer from one side to the other one), and a thick (3mm) acrylic substrate which has low thermal conductivity and diffusivity(to prevent heat transfer from one side to the other one), see Figure 11.

Aluminum and acrylic were chosen based on the fact that: one has low and one high thermal conductivity and diffusivity, coating has good adhesion to both, they don't melt or deform at 180℃ temperatures. Any other material that has the mentioned properties, could be used instead.

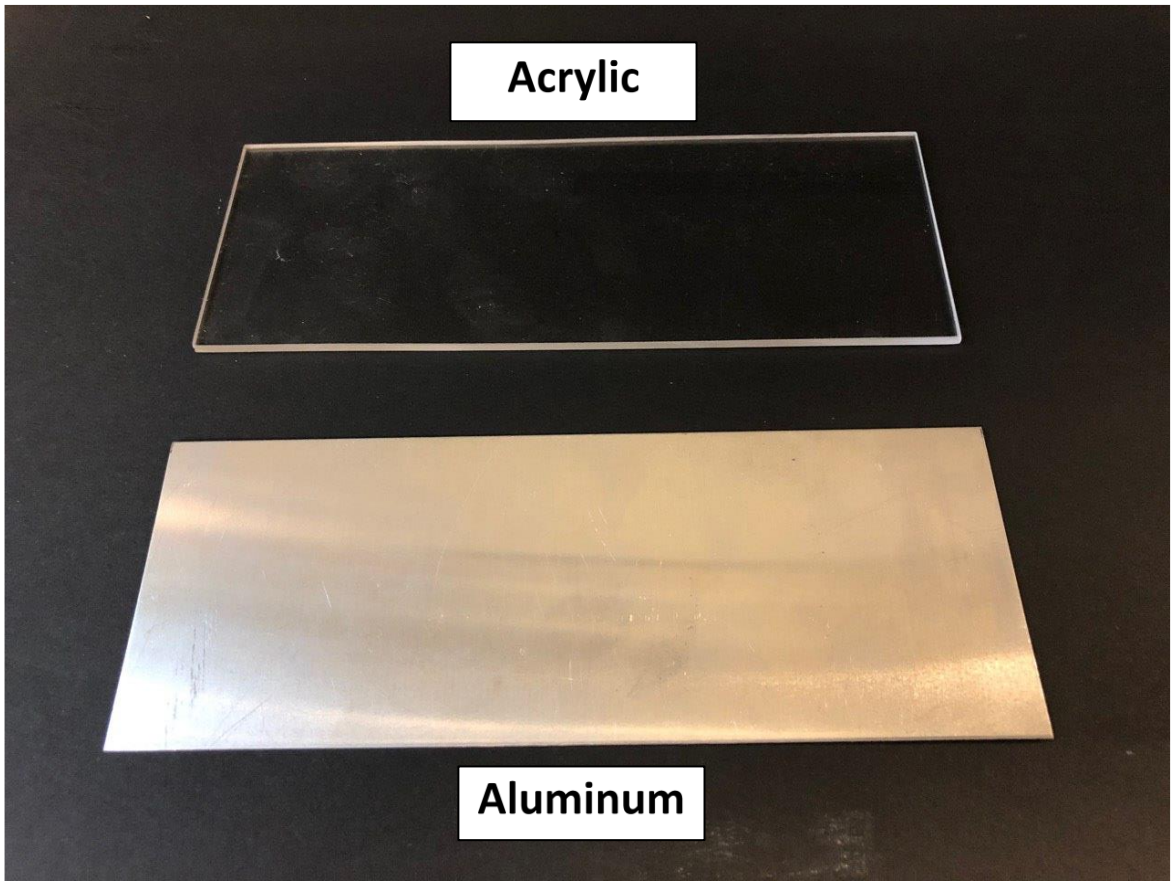

Figure 11. Substrate sheets for the experimental test. Aluminum with high conductivity and acrylic with low conductivity

3.1.1.1 Thermal Conductivity and diffusivity measurement

As this experiment aimed to find the effect of the substrates' thermal diffusivity and conductivity on the performance of the IsoHMX, there was a need to measure the named properties. Thermal conductivity and diffusivity of the substrate were measured using a transient plane source (TPS) method [98], as per ISO 22007-2 [99] (TPS 2500S, ThermTest Inc., Fredericton, Canada), available in our lab. (Figure 12) The results of the TPS measurements are shown in Table 4. Details of TPS testing can be found in other references [98] [99].

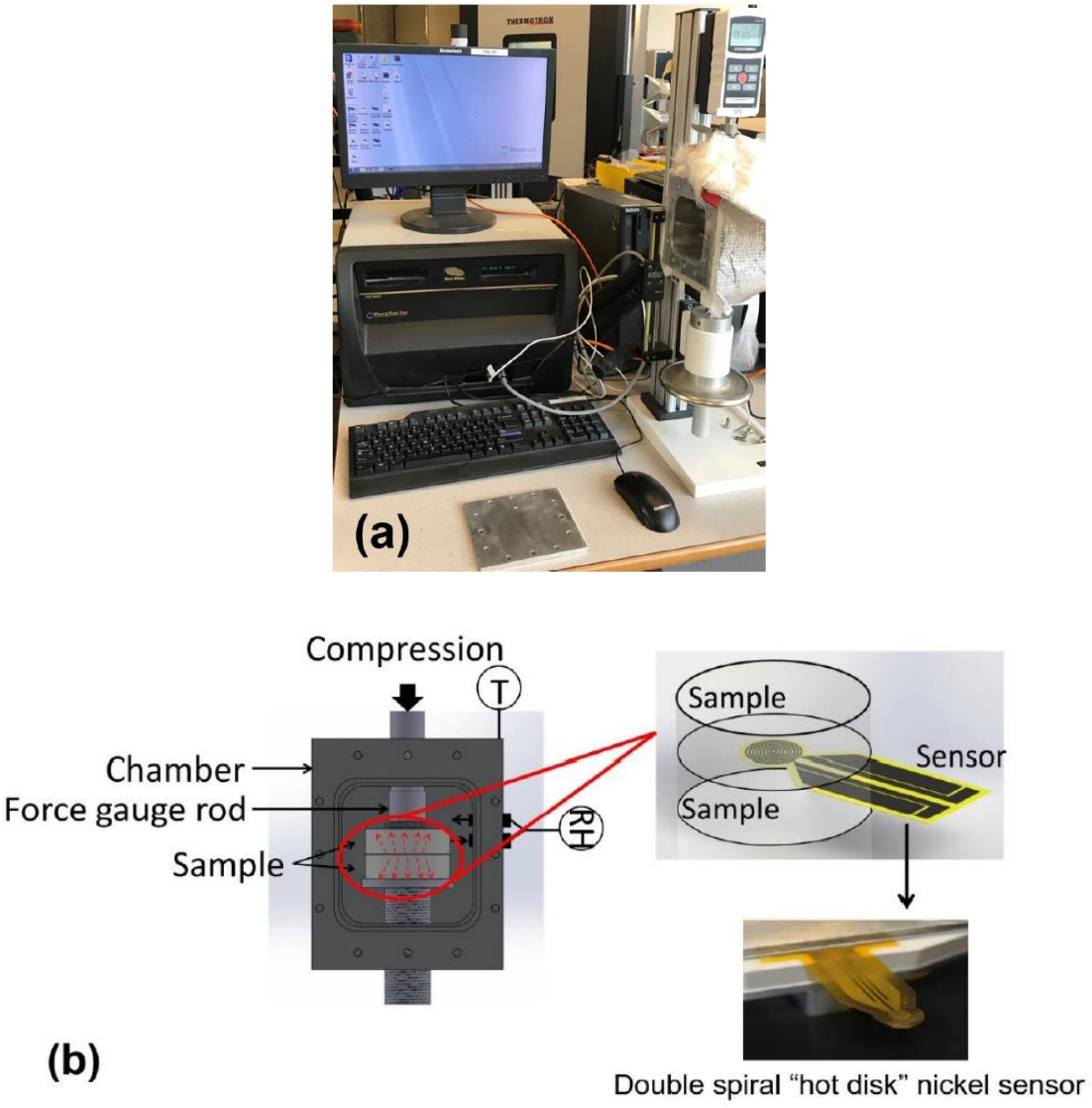

Figure 12. a) Setup; and b) a schematic of transient plane source (TPS) [99]

Table 4. Transient plane source (TPS) measurements for the substrate

Material	Thickness (mm)	Thermal conductivity (W/mK)	Thermal diffusivity (mm^2/s)
Aluminum	0.66	212.59	85.72
Acrylic	3	0.21	0.13

3.1.1.2 Surface roughness measurement

Surface roughness impacts the thermal contact resistance between substate and the coating, the smoother the surface, the lower the contact resistance is. Surface roughness was measured using the Mitutoyo SJ-400 surface roughness tester shown in Figure 13. [100]

Figure 13. A Mitutoyo SJ-400 surface roughness tester

Roughness parameters based on EN ISO 4287 are defined as follows: [100]

- Arithmetical mean roughness value (Ra): The arithmetical mean of the absolute values of the profile deviations from the mean line of the roughness profile (Figure 14-a).
- Greatest height of the roughness profile (Rz_i): Sum of the height of the highest profile peak and the depth of the deepest profile valley, relative to the mean line, within a sampling length lr_i. (Figure 14-b)
- Maximum roughness depth (Rz1max): Largest of the five Rz_i values from the five sampling lengths lr_i within the evaluation length ln. (Figure 14-b)
- Mean roughness depth (Rz): Mean value of the five Rz_i values from the five sampling lengths lr_i within the evaluation length ln. (Figure 14-b)

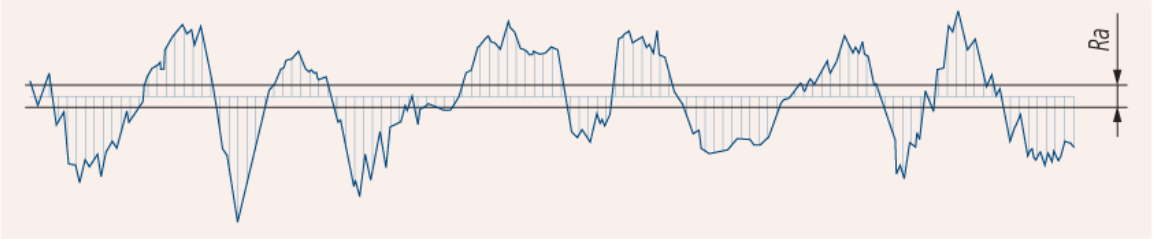

a)

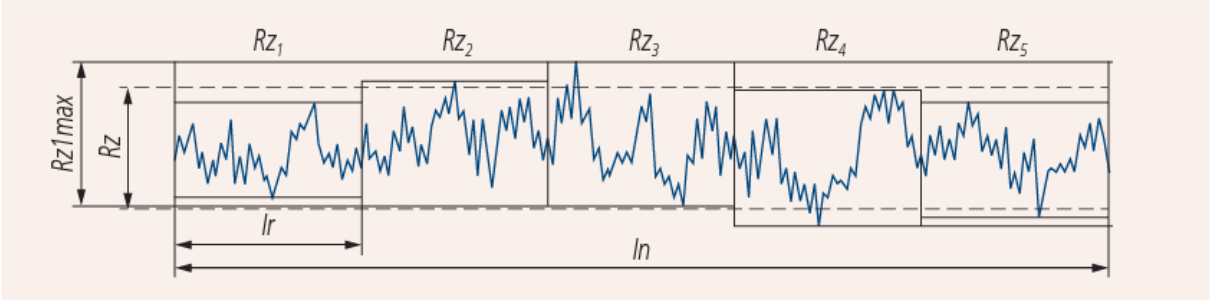

b)

Figure 14. A schematic of the roughness parameters: a) arithmetical mean roughness value (Ra); and b) the greatest height of the roughness profile (Rz_i), maximum roughness depth (Rz1max), and mean roughness depth (Rz) [100]

Mean values of roughness parameters, i.e., Ra and Rz, are measured and reported. (Figure 15). The results of surface roughness measurements with the uncertainty of 0.001 µm are brought in Table 5.

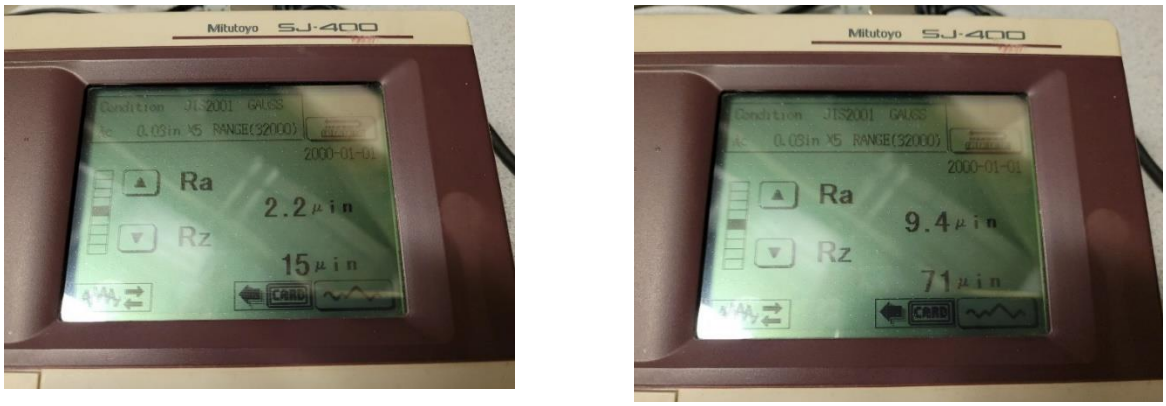

a) b)

Figure 15. a) Acrylic; and b) aluminum surface roughness measurement results for the arithmetical mean roughness value (Ra) and the mean roughness depth (Rz)

Table 5. Acrylic and aluminum surface roughness measurement results for the arithmetical mean roughness value (Ra) and mean roughness depth (Rz)

	Ra	Rz
Acrylic (µm)	0.056	0.381
Aluminum (µm)	0.239	1.803

3.1.2 Coating

Composites of salt inside a porous matrix (CSPM) is a porous host matrix (silica, alumina, etc.) with an inorganic salt ($CaCl_2$, LiBr, $MgCl_2$, $MgSO_4$, $Ca(NO_3)_2$, etc.) impregnated inside the pores. Several studies investigated the sorption properties of CSPMs in adsorption cooling systems and reported a higher COP compared to the parent host matrix gel + water systems [101]–[105]. Among the different CSPMs, the "$CaCl_2$ confined to mesoporous silica gel (average pore size 15

nm)" shows a very high water sorption capacity (up to 0.8 g of water per 1 g of dry adsorbent). Most of the adsorbed water was removed at temperatures of 80–100°C, and the curing temperature was 150°C. The salt content of the CSPM was 33.7 wt.%.[104]. Based on this high water uptake capacity, $CaCl_2$ that was confined to silica gel was chosen as the CSPM in this study.

Polyvinyl alcohol (PVA) was chosen as the binder because of the good results with silica gel powder composites in terms of surface area and pore volume [106], and suitable adhesion to aluminum and acrylic surfaces. The coating material ingredients are listed in Table 6.

Table 6. The composition of the coasting materials

Material	Description
Silica gel	SiliaFlash® Irregular Silica Gels, F60, 40-63 µm (230-400 mesh), 60 Å (R10030B) [107]
$CaCl_2$	Anhydrous, 4-8 mesh purified
Polyvinyl alcohol (PVA)	Poly (vinyl alcohol) average M_w 130,000, 99+% hydrolyzed [108]

Based on the literature mentioned and previous studies, without including the binder, the mass percentage of $CaCl_2$ and silica gel are chosen as 30% and 70%, respectively. To meet the desired adhesion, binder was added to the mentioned mixture with different total mass percentages, i.e., 5, 10 and 15 wt.%. The different sample ingredients are shown in Table 7. The sample with a 5 wt.% gave the best results and was chosen over the others.

Table 7. The mass percentage of different sample ingredients

Sample	Silica gel (wt.%)	$CaCl_2$ (wt.%)	PVA (wt.%)
1	70% of the 95%	30% of the 95%	5%
2	70% of the 90%	30% of the 90%	10%
3	70% of the 85%	30% of the 85%	15%

The procedure for mixing, drying, and curing of the coating was found after trial and error with the different samples. The procedure which led to the most desirable sample is listed as follows:

1- Tape the substrate with two rows of tape (height= 0.2 mm), see Figure 16.
2- Mix the ingredients with the mentioned percentage (first row of Table 7) in a beaker.
3- Add distilled water (10 mL is enough for 5g of the mixture).
4- Place the beaker on the hot plate and stir it continuously for 20 minutes (do not let it boil), then raise the heat so that the solution is close to the boiling point, and let it be in this state (again, do not let it boil) until most of the water is evaporated. The coating shouldn't be too thick or contain too much water as both will cause a problem in the coating phase.
5- Coat the sample in a way that the coating would have the same height as the tape around it. Extra height could be shaved by pushing the blade against the tapes and moving it slowly forward, see Figure 17.
6- Dry the coated sample in the oven for 1hr at 80°C.
7- Dry the coated sample in the oven for 1hr at 180°C.
8- Take the sample out of the oven and let it cool down.

An image of the final samples with different substrates is shown in Figure 18. The measured coating thickness was from 0.2 to 0.25 mm.

Figure 16. Taping of the substrate to maintain 0.2 mm thickness for coating

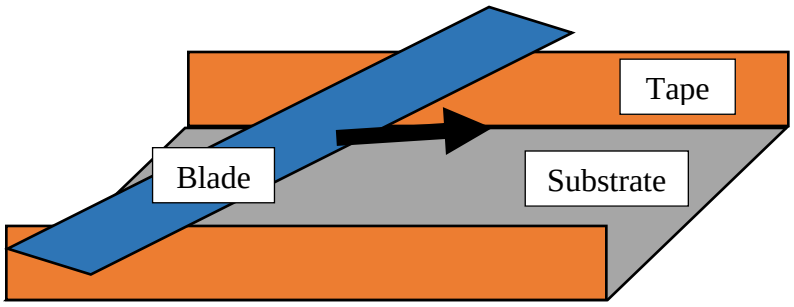

Figure 17. A schematic of shaving the coating. The blade is pushed against the tape and moved slowly forward, so the thickness of the coating would be equal to that of the tape (0.2 mm)

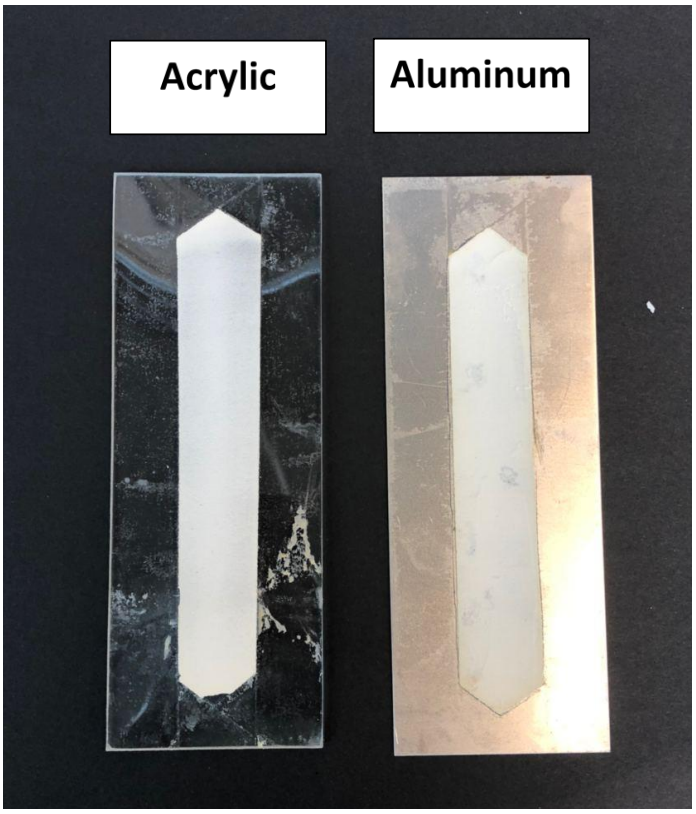

Figure 18. Double-coated samples with different substrates: acrylic (left); and aluminum (right) to show the effect of the substrate conductivity on the heat and mass transfer. The measured coating thickness was from 0.2 to 0.25 mm.

3.1.2.1 Isotherm of the material

The water sorption isotherm curve of the coating sorbent material was obtained using an IGA-002 thermogravimetric sorption analyzer (TGA) (Hiden Isochema Ltd.), the schematic and picture of the TGA is shown in Figure 19 [106]. The TGA contains a very accurate microbalance to measure the mass of the sorbent material placed in the sample cell under controlled temperature and water vapor pressure. Table 8 shows the temperature and pressure range in which the mass of the sample was measured. To obtain more reliable data, these measurements were conducted under the working temperature range of the substrate in the experimental setup, i.e., 10-40 °C. The uptake in each measured data point was calculated from Equation (96):

$$W_{eq} = \frac{m_{wet} - m_{dry}}{m_{dry}} \tag{96}$$

where, W_{eq} is the equilibrium uptake at the given temperature and pressure (kg/kg), m_{wet} is the measured mass of the sample after introducing it to the water vapor (kg), and m_{dry} is the dry sample's mass (kg). More details regarding the TGA measurements can be found elsewhere[109].

Table 8. The temperature and pressure range of the TGA for which the equilibrium uptake was measured.

Measurement	Temperature (°C)	Pressure range (kPa)	Pressure step (kPa)
1	10	0-1.1	0.1
2	15	0-1.1	0.1
3	20	0-1.1	0.1
4	30	0-3.4	0.2
5	40	0-3.4	0.2

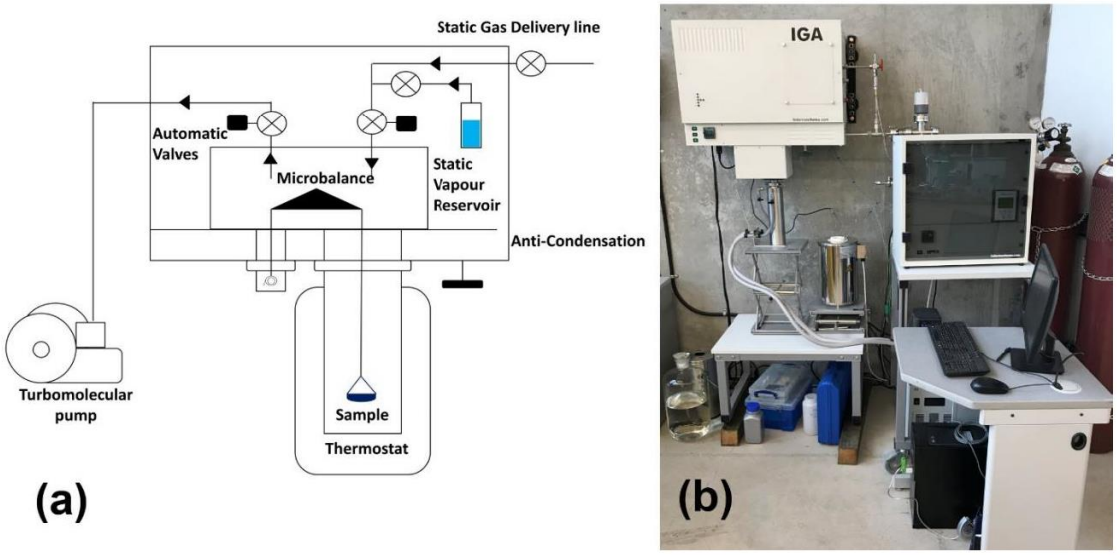

Figure 19. a) Schematic ; and b) picture of IGA-002 thermogravimetric sorption analyzer (TGA) (Hiden Isochema Ltd.) [109]

Figure 20 shows the water sorption isotherms of the composite sorbents obtained from the TGA. Figure 21 shows the water sorption isotherms curves fitted to the data, the arrows show the direction of the process (adsorption is left to right and desorption is right to left). The difference between the adsorption and desorption curves is due to the capillary condensation in the pores [110]. A modified (using T-273 instead of T) Dubinin–Astakhov (D–A) adsorption equilibrium model [111] [112] was fitted to the adsorption equilibrium uptake data using MATLAB. The following correlation was obtained with an R^2 of 0.98:

$$W_{eq} = W_0 \exp\left(-D\left(Tln\left(\frac{p_{sat}}{p}\right)\right)^n\right) = 1.39\exp\left(-0.069\left((T-273)ln\left(\frac{p_{sat}}{p}\right)\right)^{0.52}\right) \quad (97)$$

where, T is the sorbent material temperature (K), p is the water partial pressure on the sorbent material (kPa), and p_{sat} is the water saturation pressure at the sorbent material temperature (kPa).

The experimental data of the TGA test is included in Appendix C: Experimental data of TGA test.

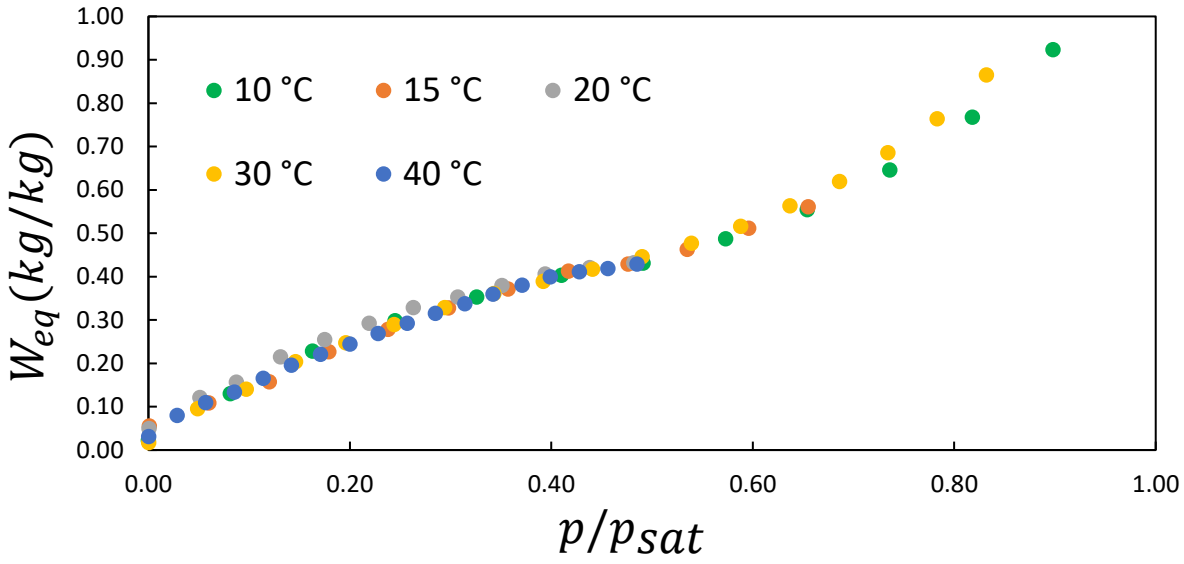

Figure 20. Isotherms of the adsorption composite sorbents with a 5 wt. % PVA content in Table 7. Data was obtained at the temperature and pressure range shown in Table 8

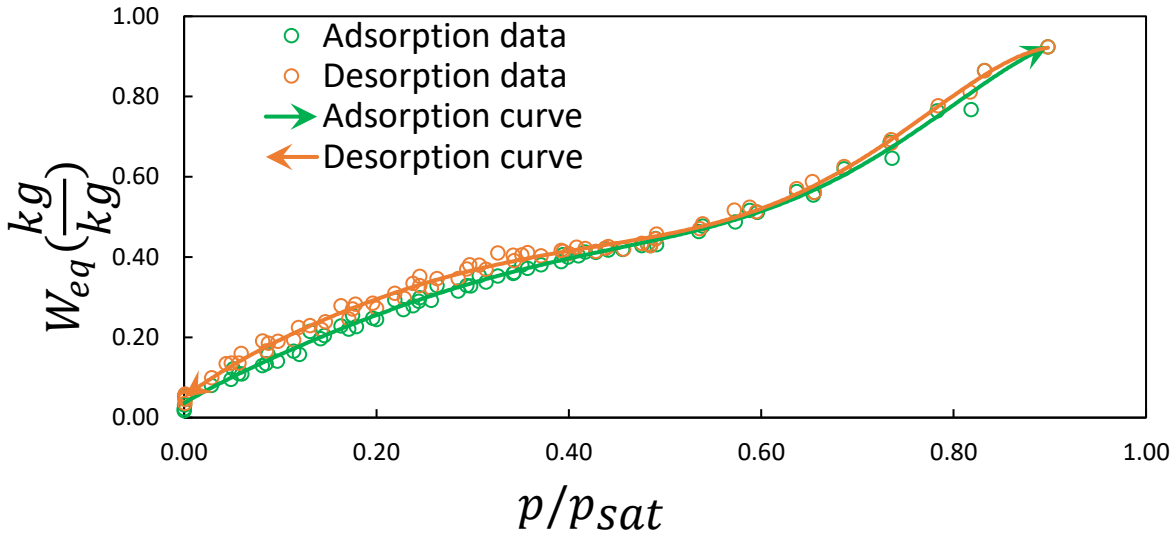

Figure 21. Isotherm curves for adsorption and desorption of the composite sorbents with a 5 wt. % PVA content in Table 7, data was obtained at the temperature and pressure range shown in Table 8. The arrows show the direction of the process (adsorption left to right and desorption right to left).

3.1.2.2 Pull-off Adhesion Test

Adhesion of the coating to the substrate and cohesion in the coating layer should be measured to ensure the coting won't fail during the test/running of the system. The adhesion was measured by the Pull-off adhesion test. The test procedure is as follows:

1- Glue the dollies to the coating layer for both samples with the aluminum and acrylic substrate (Figure 22)
2- Pull the dolly with the adhesion tester (PosiTest AT-M [113] in the current experiment) until there is a failure in coating. (Figure 23) There are three types of failure in coating: (see Figure 24)
    - Cohesive: Failure within the coating layer;
    - Adhesive: Failure between coating layer and the substrate (or different coating layers if there more than one layer which is not the case in this study); and
    - Glue: Failure between coating layer and glue.

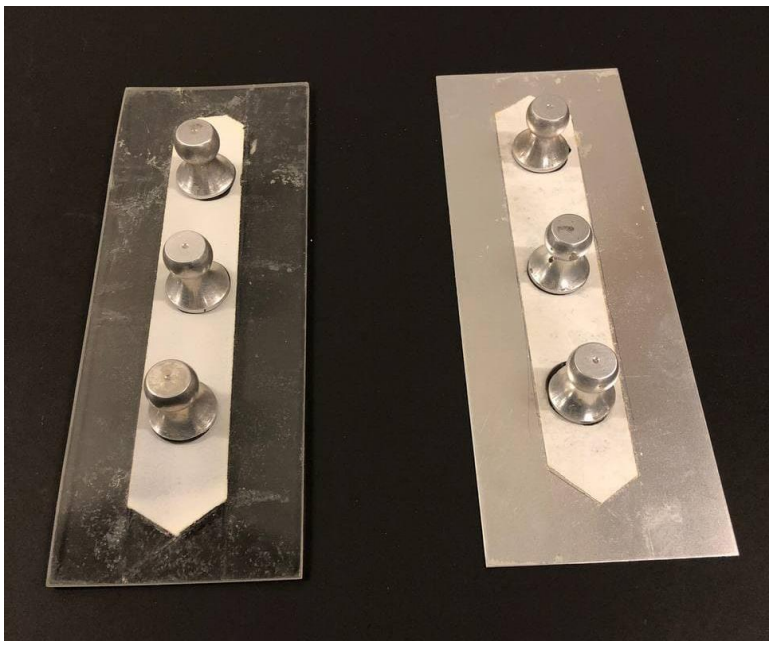

Figure 22. Samples with aluminum (right) and acrylic (left) substrate with the dollies glued to the coating prepare to measure the adhesion of the coating to the substrate

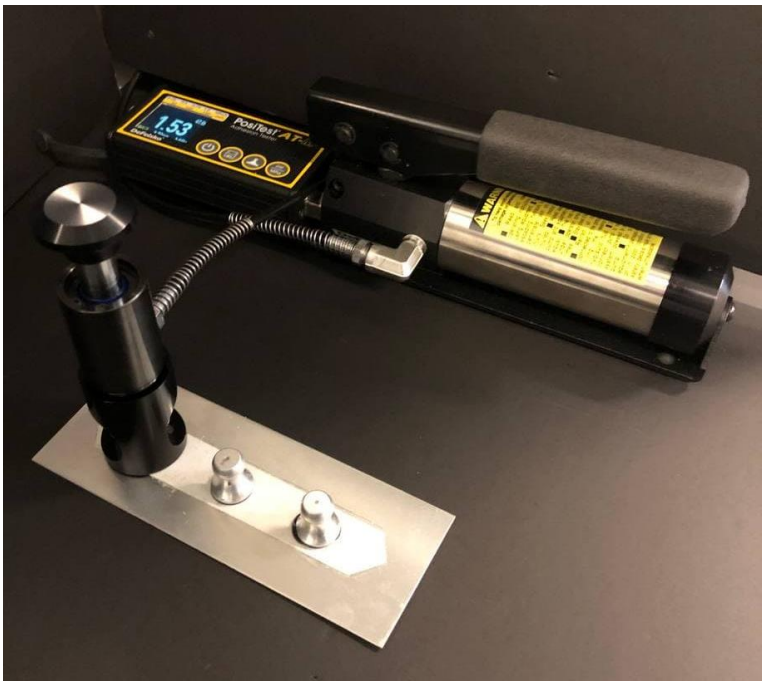

Figure 23. Pulling off the dollies with the PosiTest AT-M Adhesion tester. The failure pressure is reported by the adhesion tester

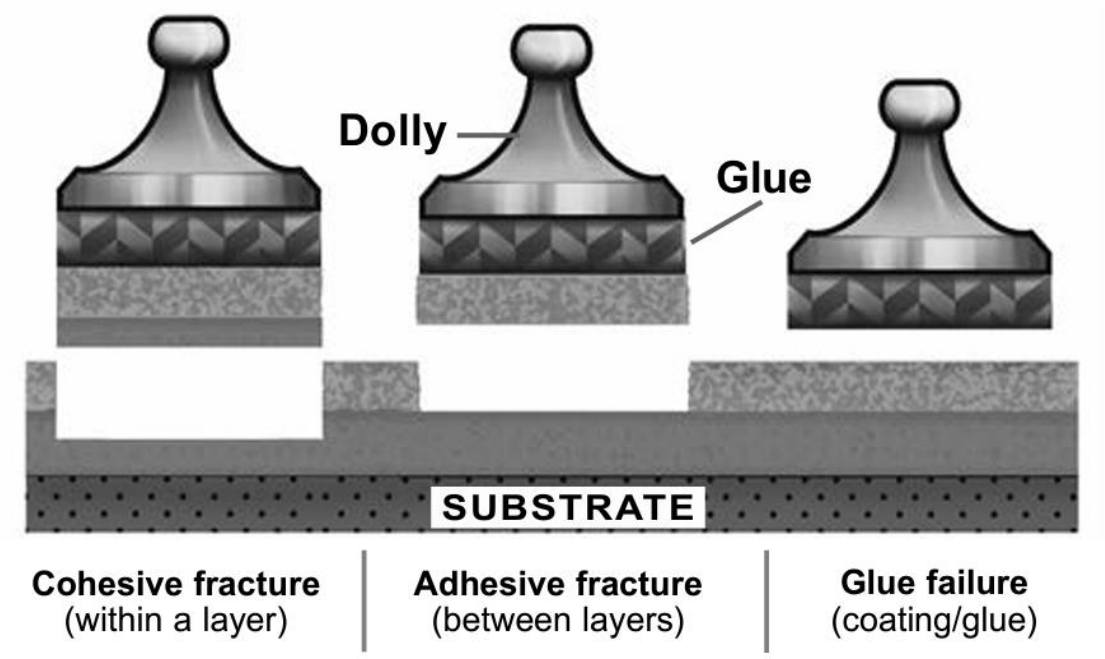

Figure 24. Types of failure in coating: cohesive, adhesive and glue failure [113]

Failure in samples with aluminum and acrylic substrate are both adhesive (see Figure 25 and Figure 26) and the average measured failure pressure is 48psi and 63psi, respectively as shown in Table 9 . The uncertainty of the measurements of the PosiTest AT-M is ±0.6 psi [113].

Table 9. average measured failure pressure for samples with aluminum and acrylic substrate

Substrate	Failure pressure (psi)
Aluminum	48
Acrylic	63

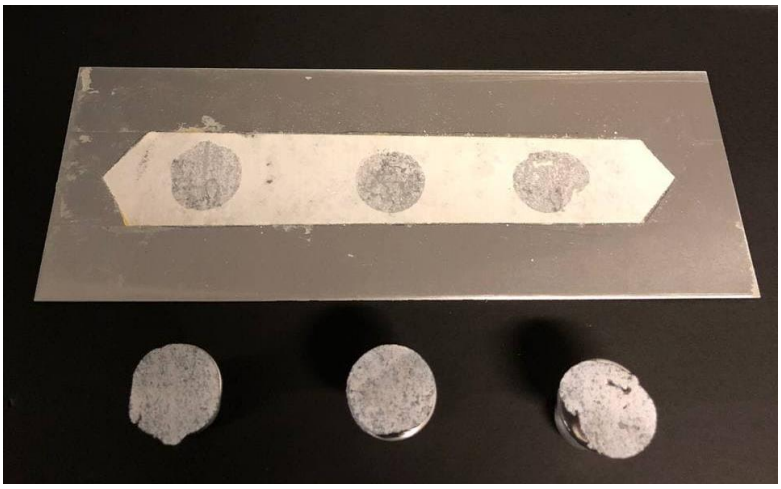

Figure 25. Adhesive failure in a sample with aluminum substrate

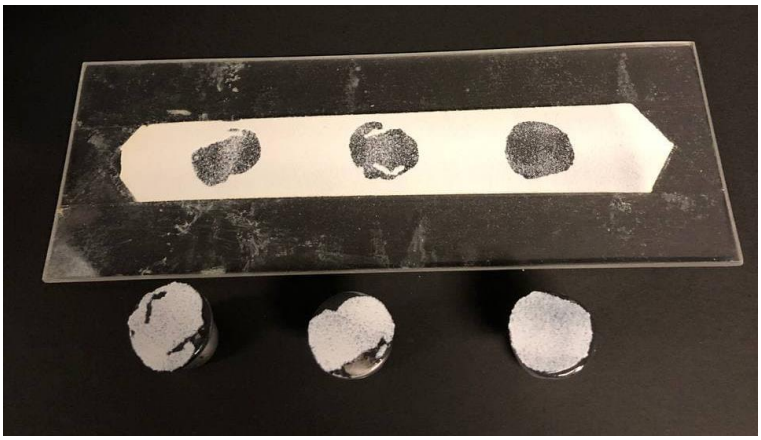

Figure 26. Adhesive failure in a sample with acrylic substrate

3.2 Test bed design and build

The test bed could be divided into the following two sections:

1- Test section: Where the sample is placed and all of the measurements are taken; and
2- Air stream provider: The rest of the test bed which delivers the two air streams and switches them between the channels.

3.2.1 Test section

The test section consists of four identical 3D printed parts (Figure 27a) which are connected two-by-two and make up the top and bottom half of the test section (Figure 27b and c). 3D printing was chosen due to accuracy and simplicity of the manufacturing, and low conductivity of the used material, i.e., Polylactic acid (PLA) with conductivity of 0.1 W/m℃, so there would be no heat transfer through the test section wall. The sample is sandwiched between these two top and bottom halves. The dimensions of the test section are shown in Figure 28. To be able to get good results that are close to real working condition of the system, the dimension was chosen based on the model study which is explained on chapter 2 Modeling. The holes at the beginning and end of the channels are dedicated to the Kimo 210 [114] humidity and temperature sensor in the top channel and the differential pressure transducer in the bottom one. Also, the are three temperature sensors along the top channel, see Figure 30.

The inside and outside the surface of the 3D printed part, needed to be coated to make sure that it's airtight and there is no water stored in it since it's porous. The part was coated and checked for water tightness and was inspected under the microscope to make sure there weren't any pores open, see Figure 29.

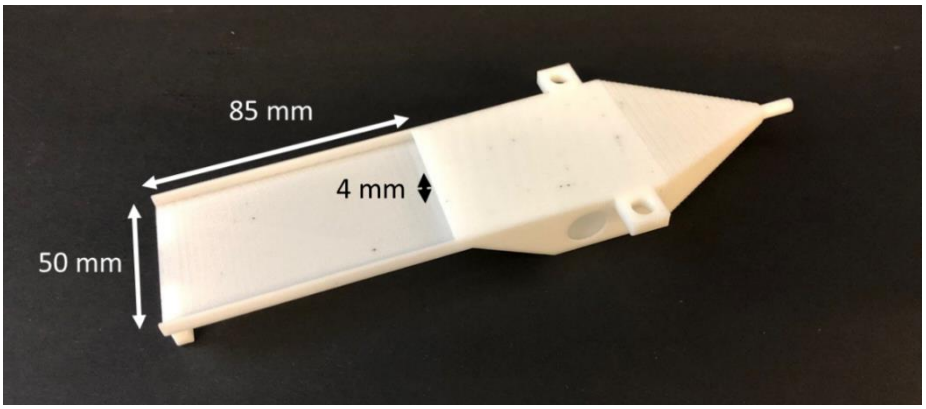

a)

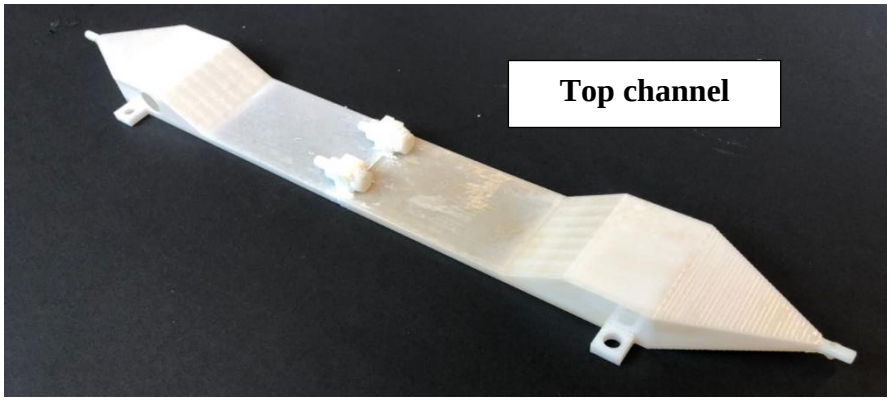

b)

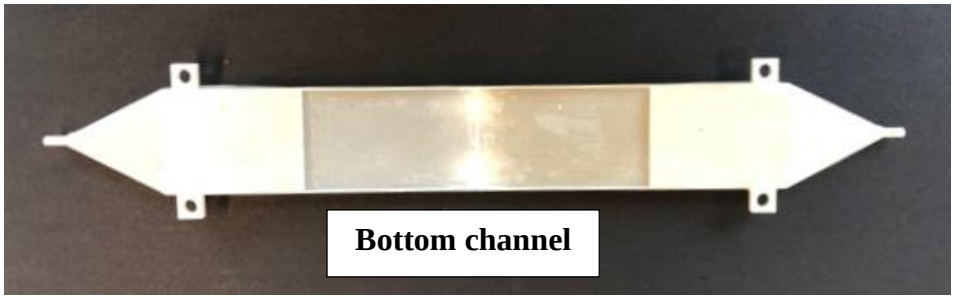

c)

Figure 27. View of the 3D printed test section: a) a quarter of the test section with dimensions shown; b) the top half of the test section; and c) the bottom half of the test section

The double side coated sample with different substrate material (Figure 18) is sandwiched between the channels. See Figure 28 for the schematic view of the top and bottom channels.

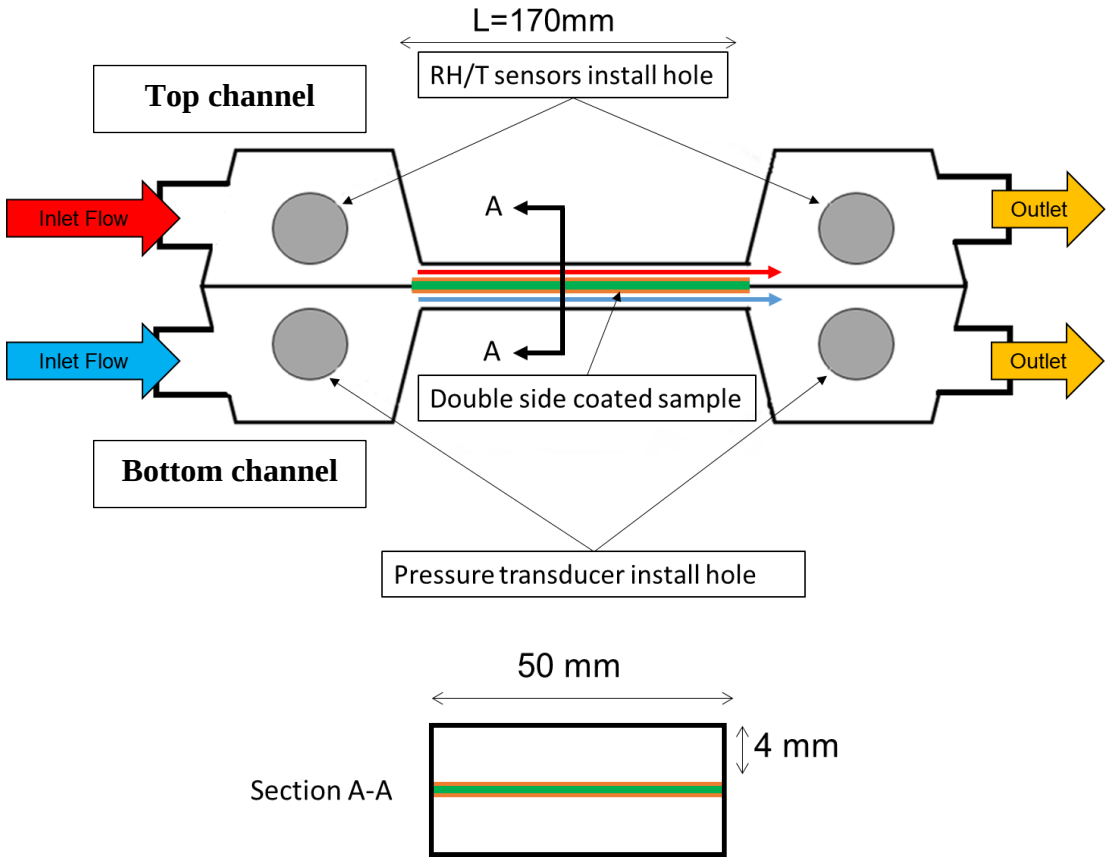

Figure 28. A schematic of the test section with the dimensions and RH/T and differential pressure transducer's placement shown in it. The top and bottom channel are 3D printed (Figure 27) and the double side coated sample with different substrate material (Figure 18) sandwiched between them.

Figure 29. A microscopic view of the 3D printed test section coated with epoxy (XTC-3D™ [115])

3.2.2 Air stream provider

Figure 30 shows a schematic and Figure 31 shows an actual picture of the test bed; the driving force of the air streams is provided by a compressor. Using a compressor has the advantage of dry outlet air which gives humidity control freedom in the humid stream and prevents condensation in the pipes in the cold stream. Dry air is divided into two streams: 1) goes to the humidifier which is able to heat up the air and adds humidity to it; and 2) the other stream goes to the heat exchanger and will be cooled down by a cold water glycol mixture that the chiller provides. Then, both streams go to the 4-way valve which switches them between two channels. At the beginning and end of the top channel, the temperature of the air is measured. The pressure drop is measured in the bottom channel. The temperature of the substrate is measured in three locations along the channel. A schematic of the control circuit of the 4-way valves is shown in Figure 32.

It should be noted that since the air flow rate is not that high and the channel height and pipe diameter are small (~1mm), that heat loss is a major issue in such a system. So, many layers of insulation are needed to make sure there is minimum heat loss.

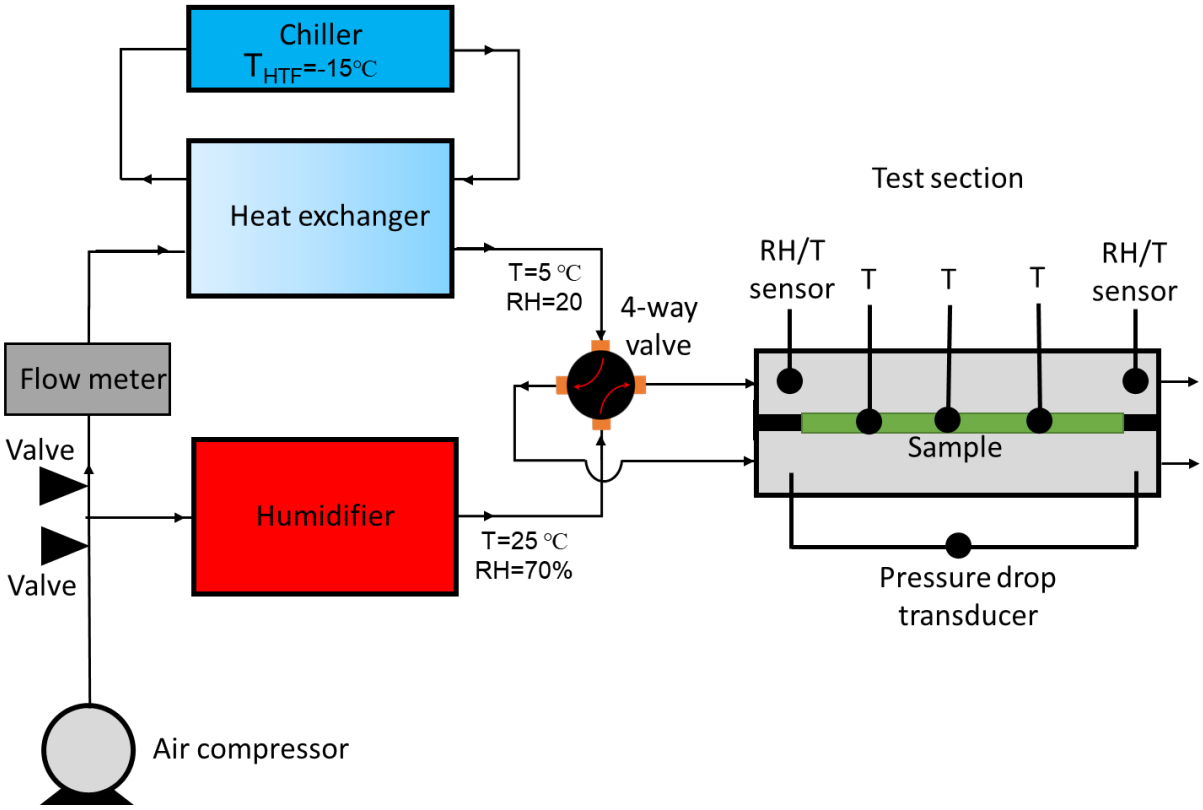

Figure 30. A schematic of the test bed: air compressor provides system with dry air, valves control flow rate in channels, humidifier provides system with warm air with known relative humidity, chiller and heat exchanger provides system with dry cold air, 4-way valve changes stream between the channels, and the test section consists of two channels and the sample sandwiched between them (Figure 28)

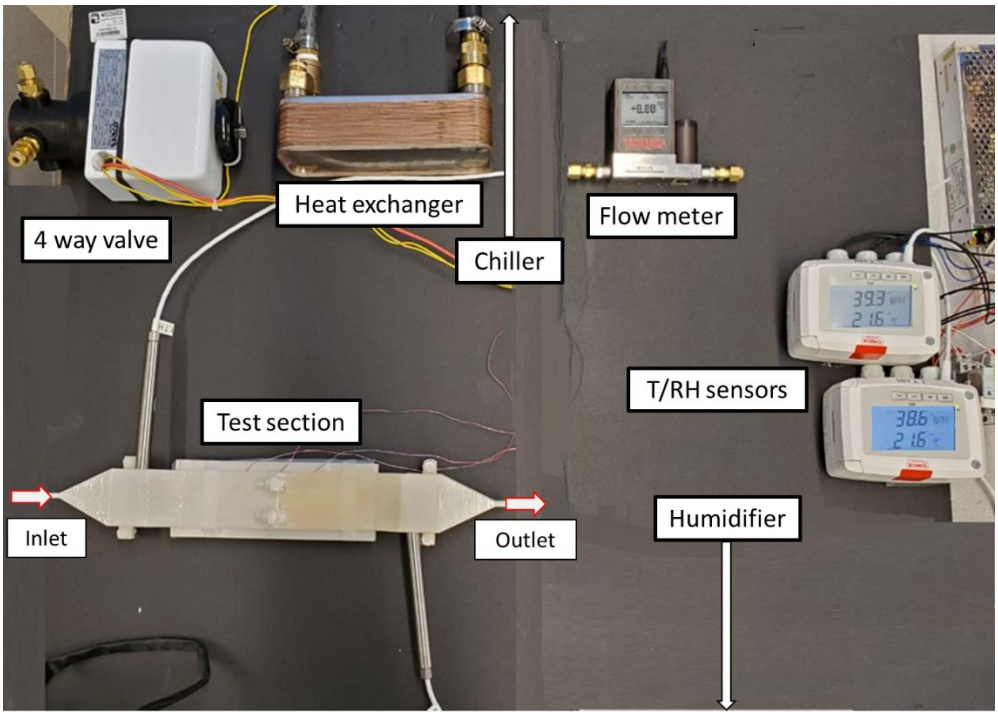

Figure 31. The view of the test bed

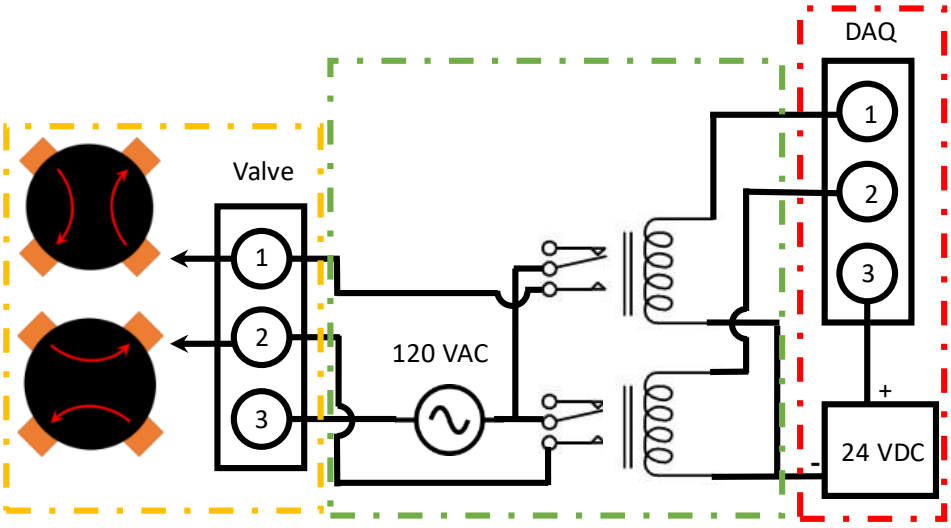

Figure 32. A schematic of the control circuit of the 4-way valves

3.2.3 Sensors' accuracy and uncertainty analysis

Measurement devices with their working range and accuracy are listed in Table 10.

Table 10. Working range and accuracy of the measurement devices

Device	Measured property	Working range	Accuracy
Kimo 210	Temperature	-250…+400°C	$\Delta T = \pm 0.4\%$ reading OR $\pm$ 0.5°C
Kimo 210	Relative humidity	5…95 %	if $15 < T < 25$°C $\Delta RH = \pm 1.5$ %reading if $T < 15$°C or $T > 25$°C $\Delta RH = \pm 0.04(T - 20)$ %reading
Cellkraft Humidifier p10	Flow rate	0…10 lpm	$\pm$ 0.5 % reading OR $\pm$ 0.01 lpm
Setra Model 267	Differential Pressure Transducer	0...5 ″W.C. (0…1244.2 Pa)	$\pm$ 0.0125 ″W.C. (3 Pa)

The method proposed by Kline and McClintock [116] is used to calculate the uncertainty of the experimental study. Based on this method, calculated uncertainties of the measured MRC^* and $DCOP_{IsoHMX}$ are around 5% and 6%, respectively. These values may change based on the actual measurements. For more detail, see Appendix B: Uncertainty Analysis.

3.3 Results and discussion

In order to have a better understanding of the performance of the IsoHMX, the MRC^* and DCOP were measured under different conditions brought in Table 11. All of the measurements were conducted for both samples with aluminum and acrylic as the substrate.

Table 11. Experimental measured properties with their respective working rage

Measured property	Cold stream range	Hot stream range
Temperature (°C)	0-15	20-40
Relative humidity (%)	20	40-85
Flow rate of each stream (lpm)	2-10	
Cycle time (min)	1-10	

The effect of each parameter on the MRC^* and DCOP was measured while keeping all of the other parameters constant. These values are compared with results of the modeling which is explained in chapter 2 Modeling. These constant values (benchmark condition) were chosen based on the greenhouse condition in Vancouver, BC's cold season (Figure 33) with the only difference of the cold stream relative humidity due to experimental limitations, which is brought in Table 12.

It should be noted that for the sample with acrylic substrate DCOP can't be defined as there is no input heat in the system. So, DCOP graphs only shows that of sample with aluminum substrate.

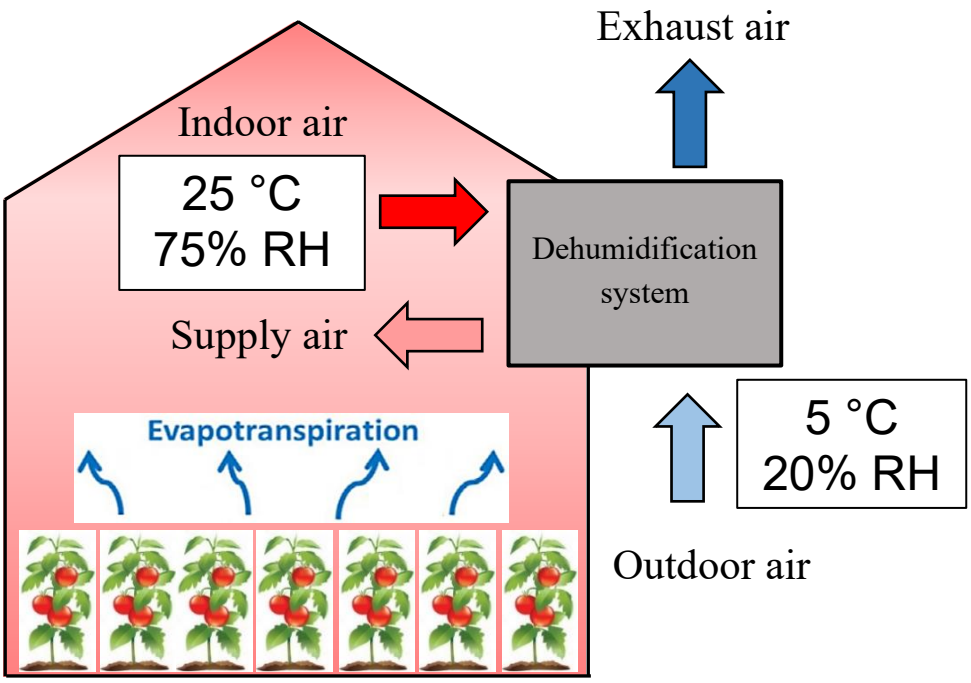

Figure 33. The greenhouse condition of Vancouver, BC's average cold season

Table 12. The benchmark measured properties chosen based on the greenhouse condition of Vancouver, BC's cold season

Measured property	Cold stream	Hot stream
Temperature (°C)	5	25
Humidity ratio (g/kg)	1.1	14.9
Relative humidity (%)	20	75
Flow rate (lpm)	10	
Cycle time (min)	3	

Results for the experimental study on the effect of each parameter are brought in the following. Results for the MRC* and DCOP were compared to the developed analytical model which is described in Section 2.1.

As the effect of fan power (pressure drop effect) on the DCOP is less than 1%, so, it's not included in the calculations and is brought in Figure 34.

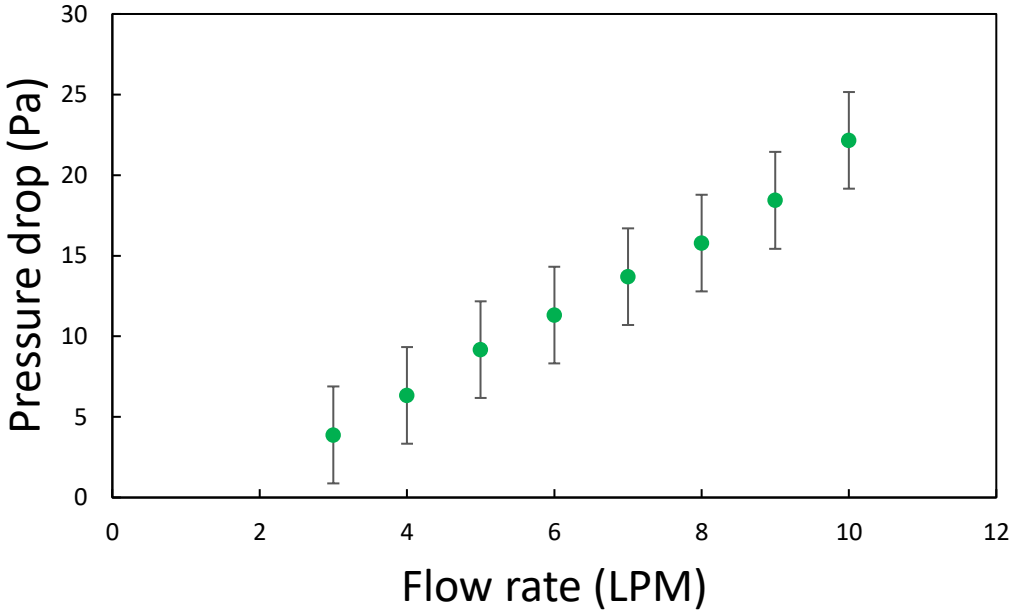

Figure 34. Measured pressure drop for different inlet flow rates

3.3.1 Effect of cold stream temperature

The effect of cold stream (desorption) temperature on the MRC^* and DCOP was studied with inlet temperatures of 0, 5, 10 and 15 ℃. The humidity ratio (water content) of the inlet stream was kept constant at 1.1 g/kg.

Figure 35 shows the experimental results of the inlet and outlet temperatures for the two samples with acrylic and aluminum substrate over time. These results are for the inlet temperatures of 0 and 15 ℃.

As can be seen in Figure 35-a and Figure 35-b, the temperature difference of the inlet and outlet temperatures for aluminum and acrylic substrate have a different trend when the cold stream temperature increases. For the sample with aluminum substrate, as the cold stream temperature increases, the difference between the two streams and substrate will become lower. The lower temperature difference between the substrate and streams means that there is less heat transfer and a lower outlet and inlet temperature difference.

For the acrylic substrate, as the temperature of the cold stream (desorption) becomes higher, there would be more desorption. This will result in more heat of adsorption generation/consumption so the outlet of adsorption would be hotter and desorption would be cooler. Figure 36 shows the experimental results of the inlet and outlet humidity ratio for the two samples with acrylic and aluminum substrate. As was mentioned for the sample with aluminum substrate, a rise in cold stream temperature will result with a rise in substrate temperature. Hotter substrate is better for desorption but worse for adsorption. The sum of these two opposite effects will result in slightly less removed water. For the acrylic substrate, as the desorption area is hotter, there is improvement in desorption and as the adsorption temperature remains constant, there is more removed water. Therefore, the difference between the outlet and inlet humidity ratio becomes larger.

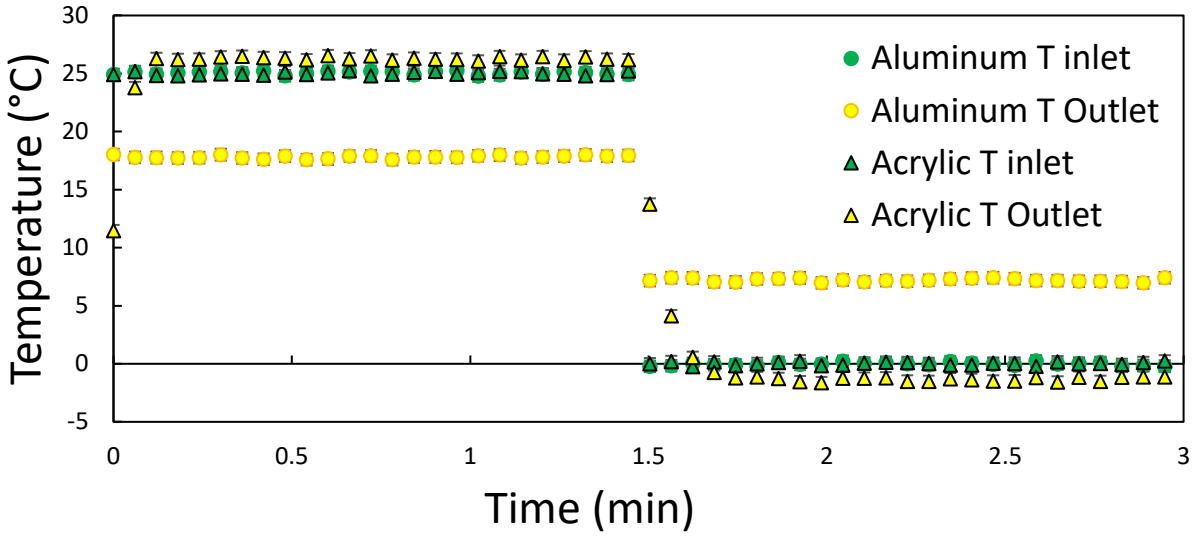

a)

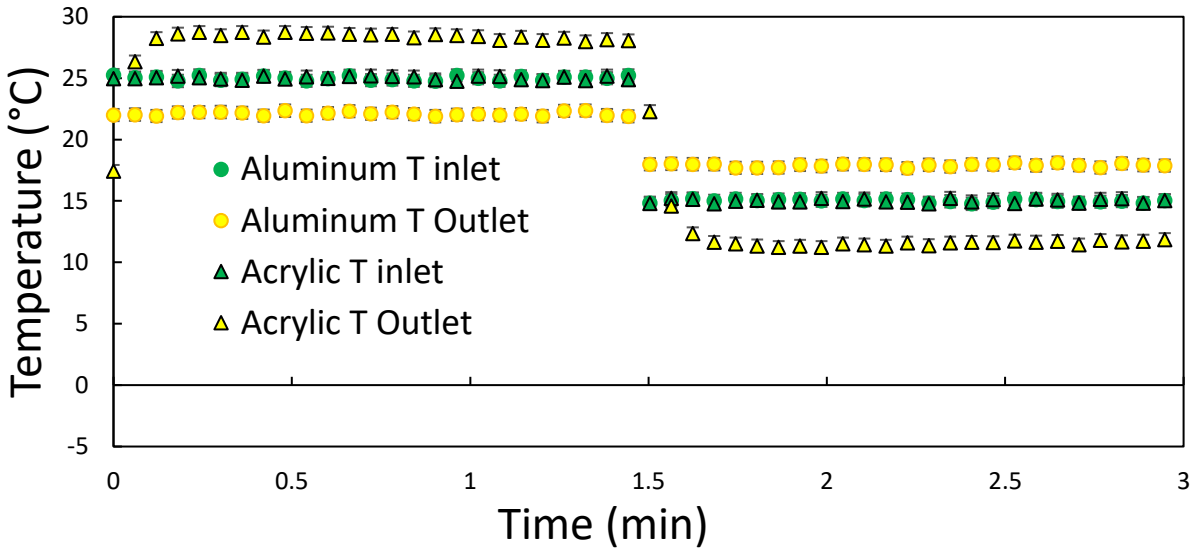

b)

Figure 35. The inlet and outlet temperature measured at cold stream inlet temperatures: a) 0°C; and b) 15°C for samples with aluminum and acrylic substrate (other working conditions were chosen based on the benchmark condition, see Table 12)

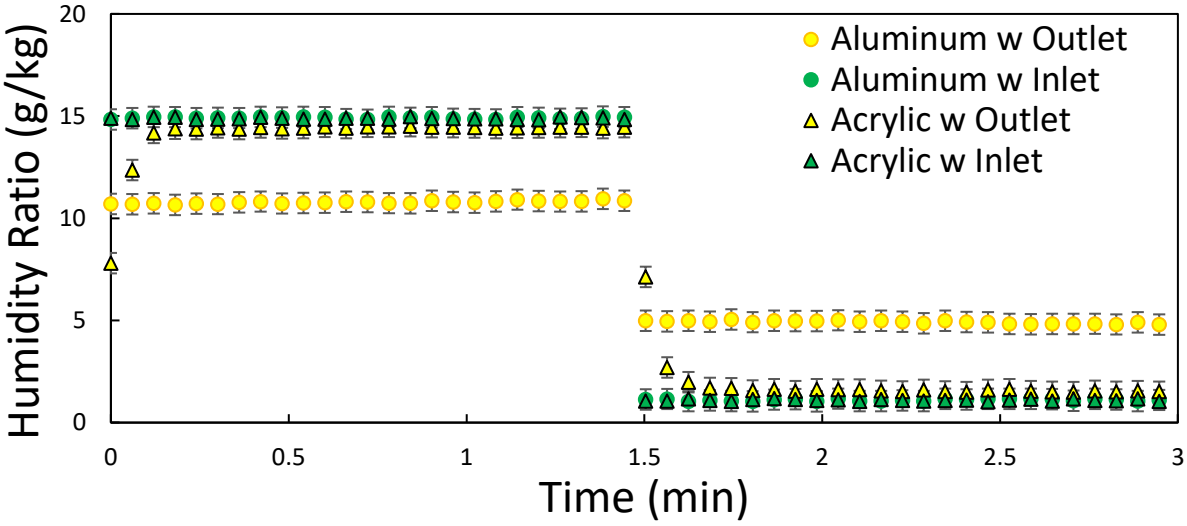

a)

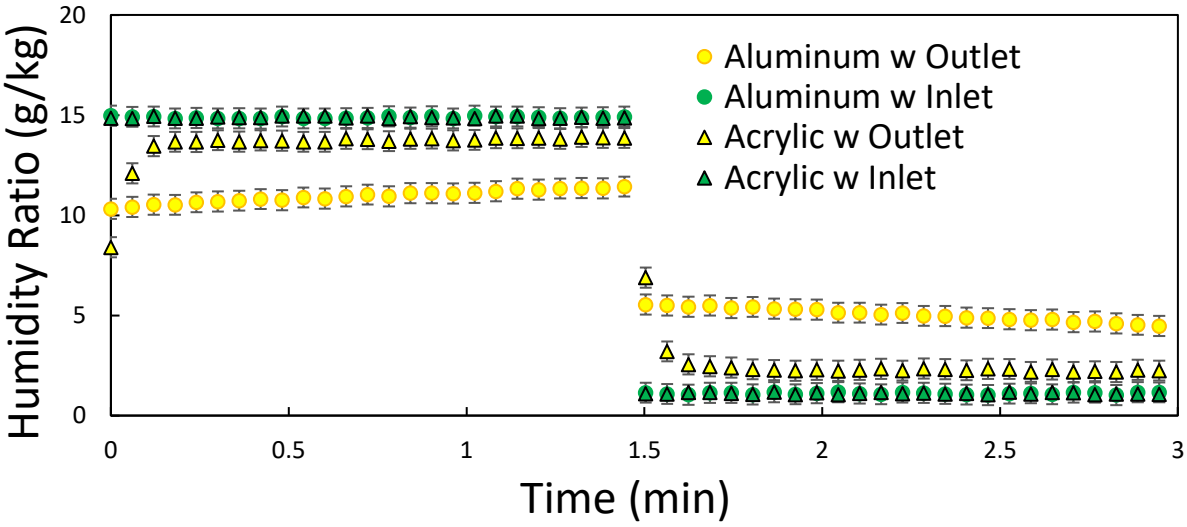

b)

Figure 36. The inlet and outlet humidity ratio measured at cold stream inlet temperatures: a) 0°C; and b) 15°C for samples with aluminum and acrylic substrate (other working conditions were chosen based on the bench mark condition, see Table 12)

Figure 37-a shows the results for the MRC^* for different cold stream inlet temperatures per square meter of the front surface area. The sample with aluminum substrate shows better performance compared to the sample with acrylic substrate. As was mentioned before, the amount of adsorbed water of the sample with aluminum substrate doesn't change that much with a change in cold stream temperature so the MRC^* would remain almost constant. Also, the amount of adsorbed water for the sample with acrylic substrate increases as does the MRC^*.

Figure 37-b shows the results for the DCOP of the sample with aluminum substrate for different cold stream inlet temperatures. As the MRC^* doesn't change that much and the outlet air of the hot stream is hotter, the DCOP would increase with increase in cold stream temperature. As it was mentioned earlier for the sample with acrylic substrate DCOP can't be defined as there is no input heat in the system.

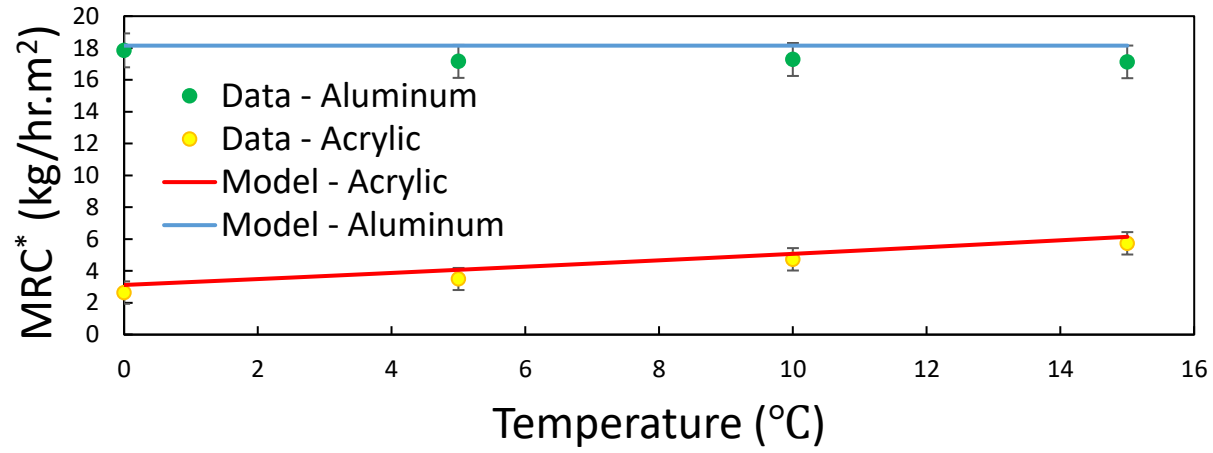

a)

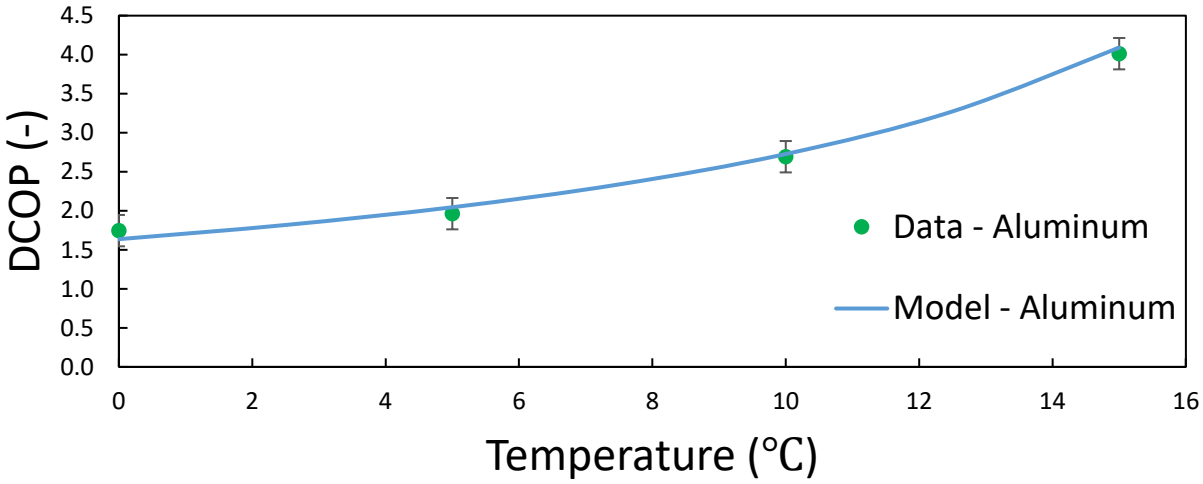

b)

Figure 37. a) The MRC*; and b) the DCOP measured against different cold stream inlet temperatures for samples with aluminum and acrylic substrate compared to analytical model results (other working conditions were chosen based on the benchmark condition, see Table 12)

3.3.2 Effect of hot stream temperature

The effect of hot stream (adsorption) temperature on the MRC^* and DCOP was studied with an inlet temperature of 20, 25, 30 and 35℃.

Two sets of experiments were conducted: one with a constant inlet relative humidity of 75% for all temperatures (Figure 38, Figure 39 and Figure 40) and one with a constant inlet humidity ratio of 14.9 g/kg (Figure 41, Figure 42, and Figure 43). For the second set of experiments, the 20℃ tests could not be performed since 20℃ and 14.9 g/kg HR means a RH that is higher than 100%.

Figure 38 shows the experimental results of the inlet and outlet temperature for the two samples with acrylic and aluminum substrate over time. These results are for an inlet hot stream temperature of 20℃ and 35℃. For the aluminum substrate, as the hot stream temperature goes higher, the difference between the two streams and substrate will become higher. The higher temperature difference between the substrate and streams means that more heat transfer and a higher outlet and inlet temperature difference.

Relative humidity was kept constant during these tests. As the relative humidity is a function of the temperature and humidity ratio of the air, keeping it constant and changing temperature will result in a change in the inlet humidity ratio as well, see Figure 39.

For the acrylic substrate, outlet temperature (Figure 38) and humidity ratio (Figure 39) are functions of temperature and humidity ratio of the air. For the aluminum substrate, the humidity ratio (Figure 39) is also functions of temperature and humidity ratio of the air. So, the shown MRC^* and DCOP (Figure 40) are not showing results for the effect of temperature, instead, they show results for the effect of simultaneous change in temperature and humidity ratio. To address this issue and to be able to study effect of inlet temperature, second sets of the experiment were conducted in which the humidity ratio was kept constant and the temperature was the only variable (Figure 41, Figure 42, and Figure 43).

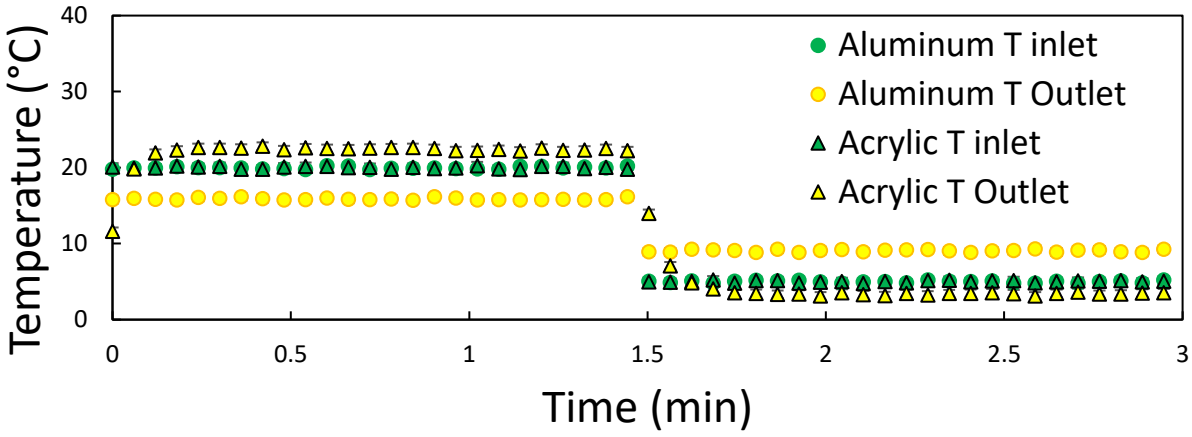

a)

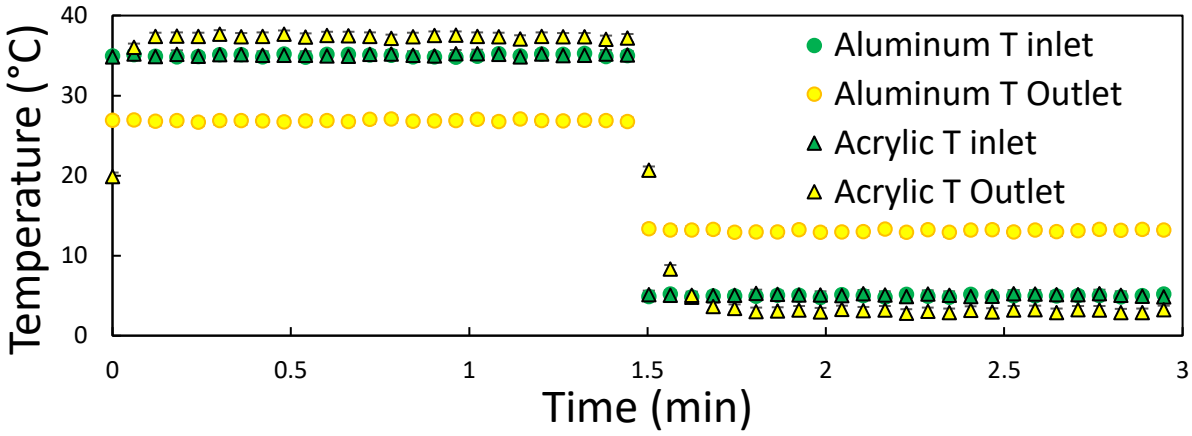

b)

Figure 38. The inlet and outlet temperature measured at hot stream inlet temperatures: a) 20°C; and b) 35°C for samples with aluminum and acrylic substrate (other working conditions were chosen based on the benchmark condition, see Table 12)

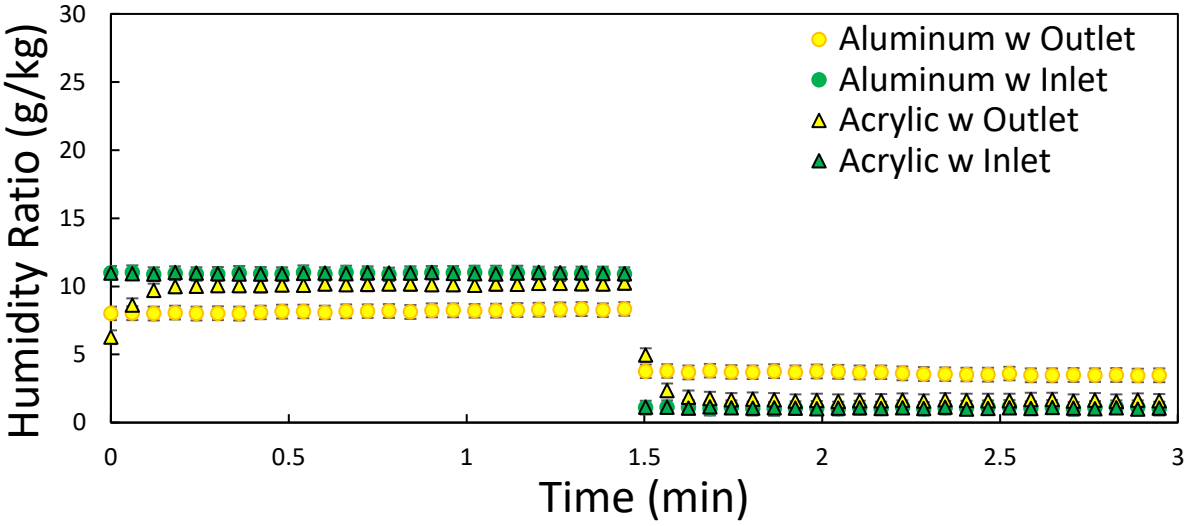

a)

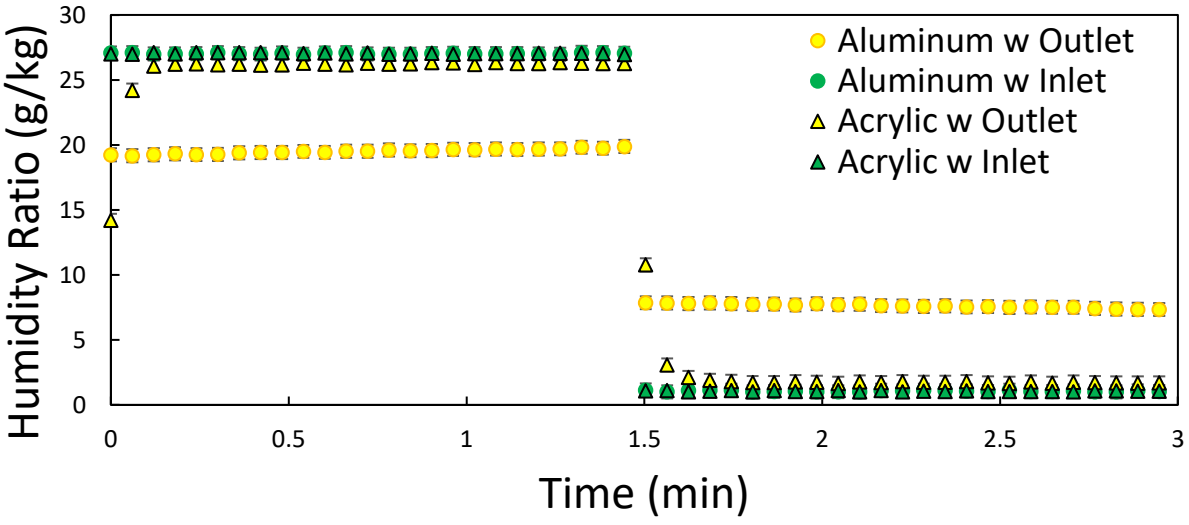

b)

Figure 39. The inlet and outlet humidity ratio measured at hot stream inlet temperatures: a) 20℃; and b) 35℃ for samples with aluminum and acrylic substrate (other working conditions were chosen based on the benchmark condition, see Table 12)

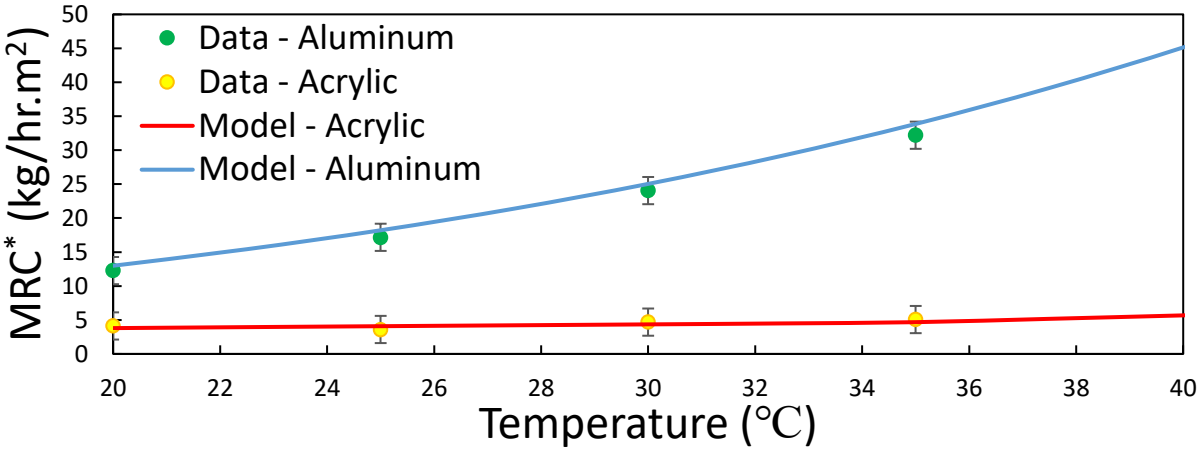

a)

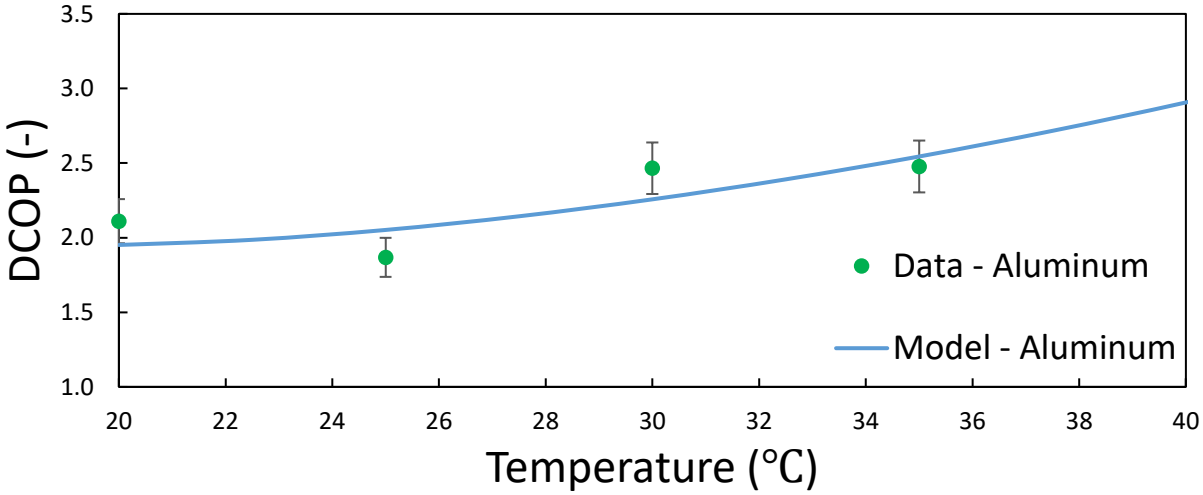

b)

Figure 40. a) The MRC*; and b) the DCOP measured against different hot stream inlet temperatures for samples with aluminum and acrylic substrate (other working conditions were chosen based on the benchmark condition, see Table 12)

Figure 41 shows the experimental results of the inlet and outlet temperatures for the two samples with acrylic and aluminum substrate over time. These results are for inlet temperatures of 25℃ and 35 ℃. As it can be seen in Figure 41-a and Figure 41-b, the temperature difference of the inlet and outlet for aluminum and acrylic substrate have different trends when the hot stream temperature increases. For the aluminum substrate, as the hot stream temperature increases, the difference between two streams and substrate temperatures also will increase. The higher temperature difference between the substrate and streams means that more heat transfer and higher outlet and inlet temperature difference. For the acrylic substrate, as the temperature of the hot stream (adsorption) goes higher, there would be less adsorption. This will result in less heat of adsorption generation so the temperature difference between adsorption and desorption is decreased.

Figure 42 shows the experimental results of the inlet and outlet humidity ratio for the two samples with acrylic and aluminum substrate. As was mentioned earlier for the sample with aluminum substrate, the rise in hot stream temperature will result in the rise in substrate temperature. Hotter substrate is better for desorption but worse for adsorption. The sum of these two opposite effects will result in slightly less removed water.

For the acrylic substrate, as the adsorption area is hotter, water adsorption is decreased. So, the difference between the outlet and inlet humidity ratio becomes smaller.

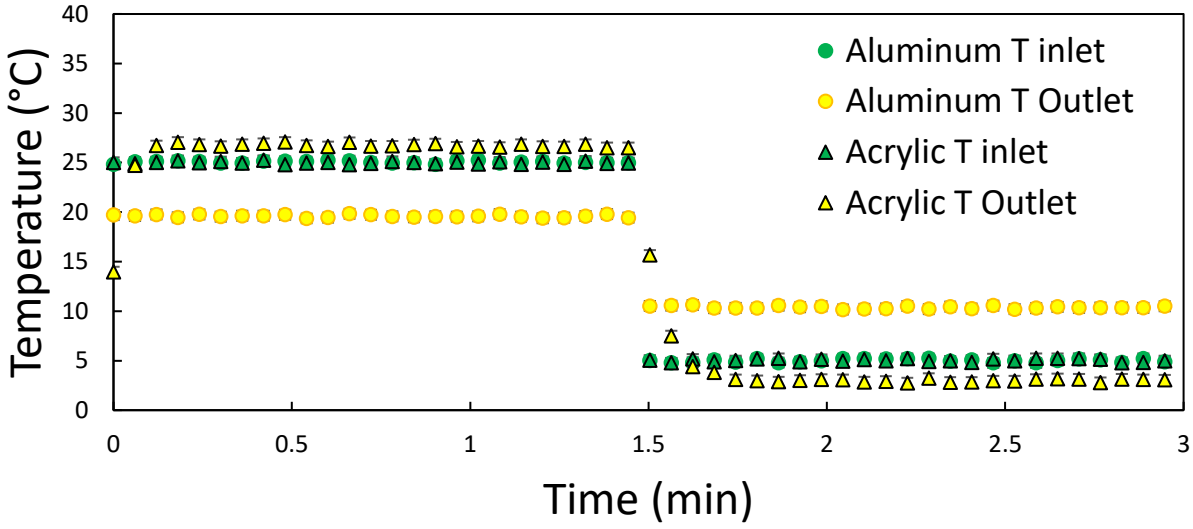

a)

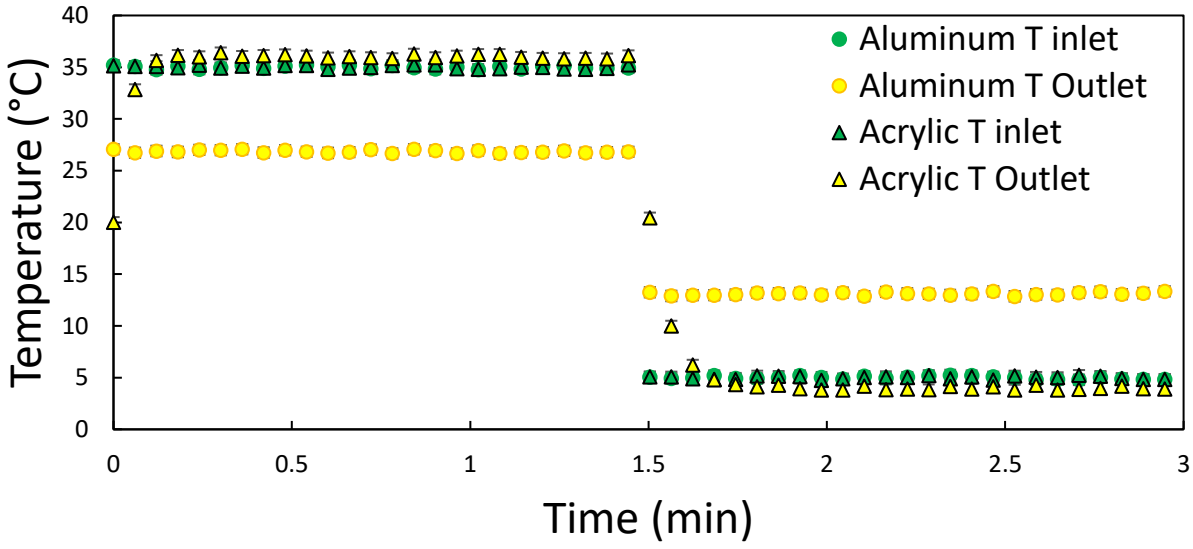

b)

Figure 41. The inlet and outlet temperature measured at hot stream inlet temperatures: a) 25°C; and b) 35°C for samples with aluminum and acrylic substrate (other working conditions were chosen based on the benchmark condition, see Table 12)

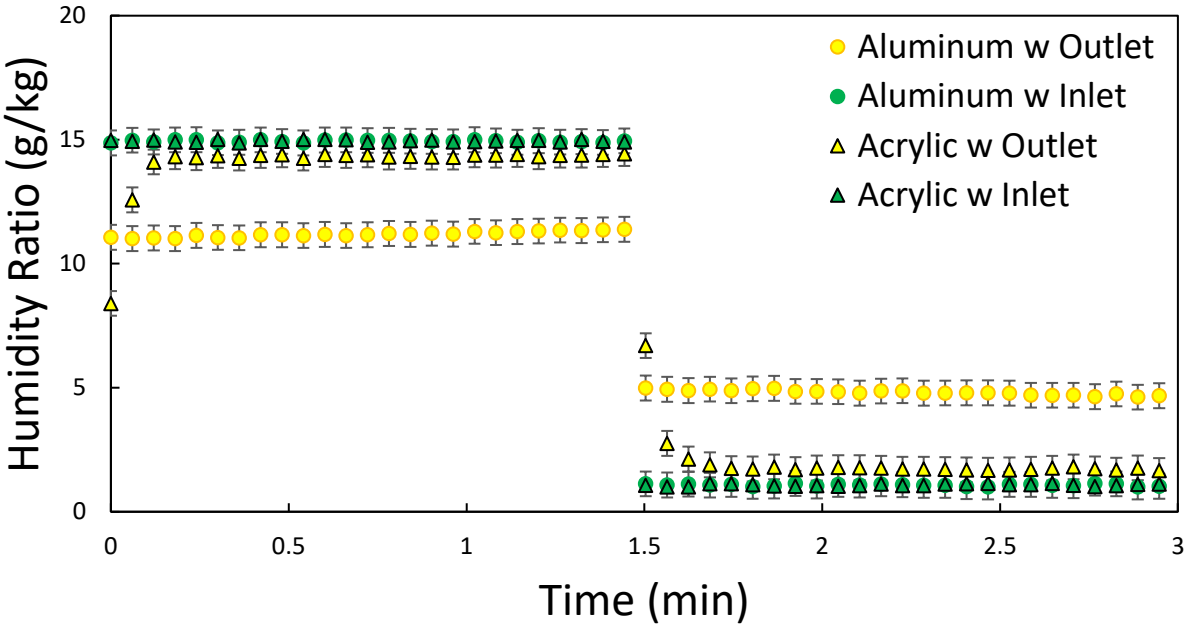

a)

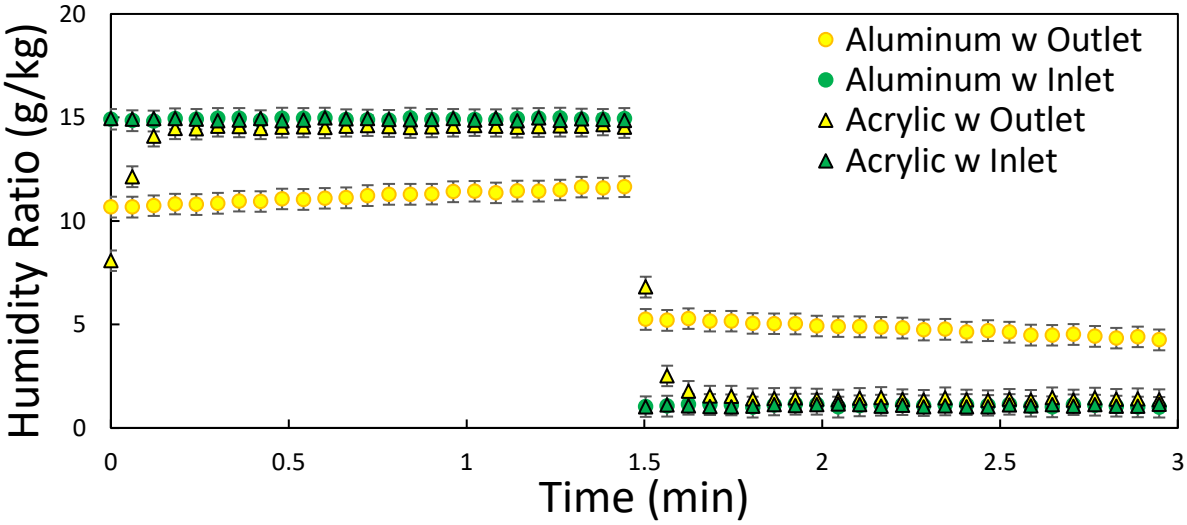

b)

Figure 42. The inlet and outlet humidity ratio measured at hot stream inlet temperatures: a) 25°C; and b) 35°C for samples with aluminum and acrylic substrate (other working conditions were chosen based on the benchmark condition, see Table 12)

Figure 43-a shows the results for the MRC^* for different hot stream inlet temperatures with constant humidity ratio per square meter of the front surface area. The sample with aluminum substrate shows better performance compared to the sample with acrylic substrate. This difference slightly increases as the inlet temperature approaches higher values.

Figure 43-b shows the results for the DCOP of the sample with aluminum substrate for different cold stream inlet temperatures. As the MRC^* doesn't change that much and the temperature difference of the outlet and inlet air of hot stream increases, the DCOP decreases.

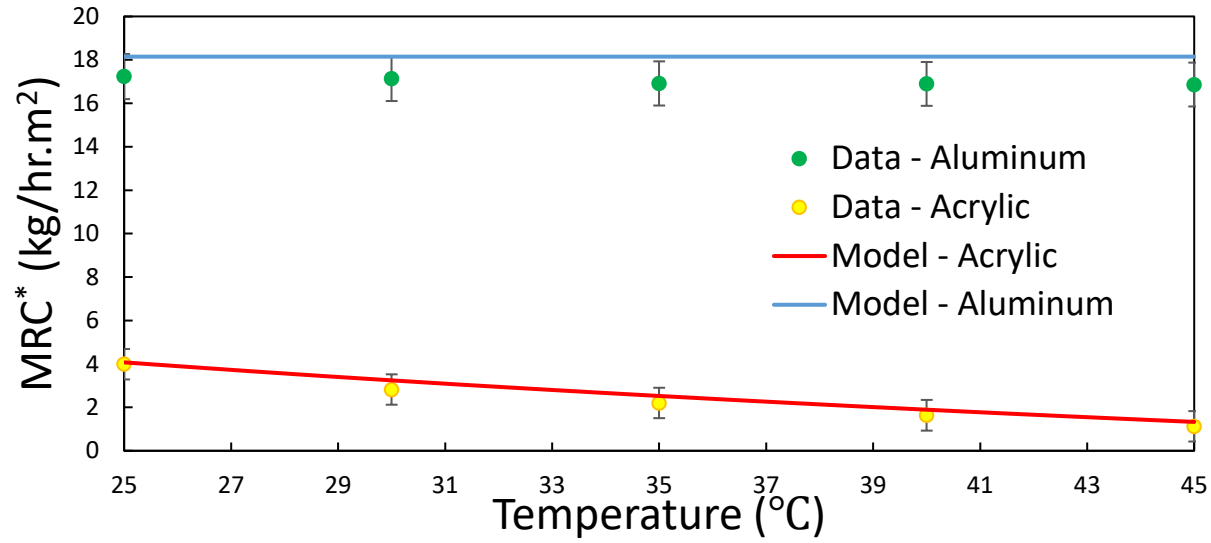

a)

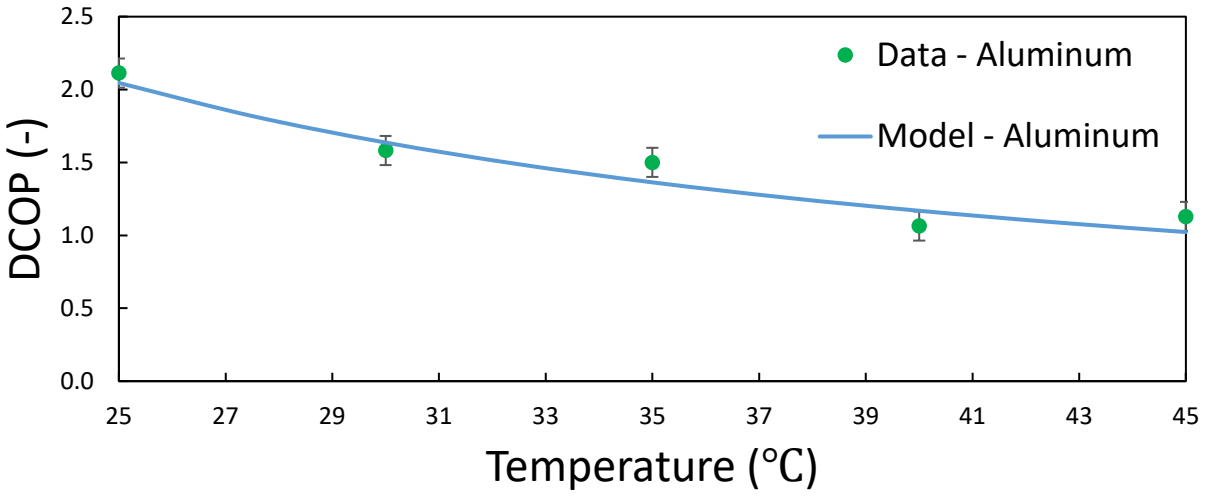

b)

Figure 43. a) the MRC*; and b) the DCOP measured against different hot stream inlet temperatures for samples with aluminum and acrylic substrate compared to analytical model results (other working conditions were chosen based on the benchmark condition, see Table 12)

3.3.3 Effect of hot stream relative humidity

The effect of hot stream (adsorption) relative humidity on the MRC* and DCOP was studied with an inlet relative humidity of 40, 50, 60, 75 and 85%.

Figure 44 shows the experimental results of the inlet and outlet temperature for the two samples with acrylic and aluminum substrate over time. These results are for the relative humidity of 40 and 85%.

As it can be seen in Figure 44-a and Figure 44-b, the temperature difference of the inlet and outlet for aluminum and acrylic substrate have a different trend when the hot stream relative humidity increases. For aluminum substrate, the temperature is independent of the inlet relative humidity. On the other hand, the outlet temperature of the sample with acrylic substrate is highly dependent on the inlet air humidity ratio; the higher the adsorption/desorption, the higher the temperature difference between inlet and outlet. In this case, as the adsorption increases, the temperature difference of the inlet and outlet will increase.

Figure 45 shows the experimental results of the inlet and outlet humidity ratio for the two samples with acrylic and aluminum substrate. For the both samples, as the water content of the inlet air is increasing, they adsorb more water and the difference in water content from inlet to outlet is also increasing. It should be noted for acrylic substrate, the change in adsorption is not significant since the substrate is hotter in higher relative humidity.

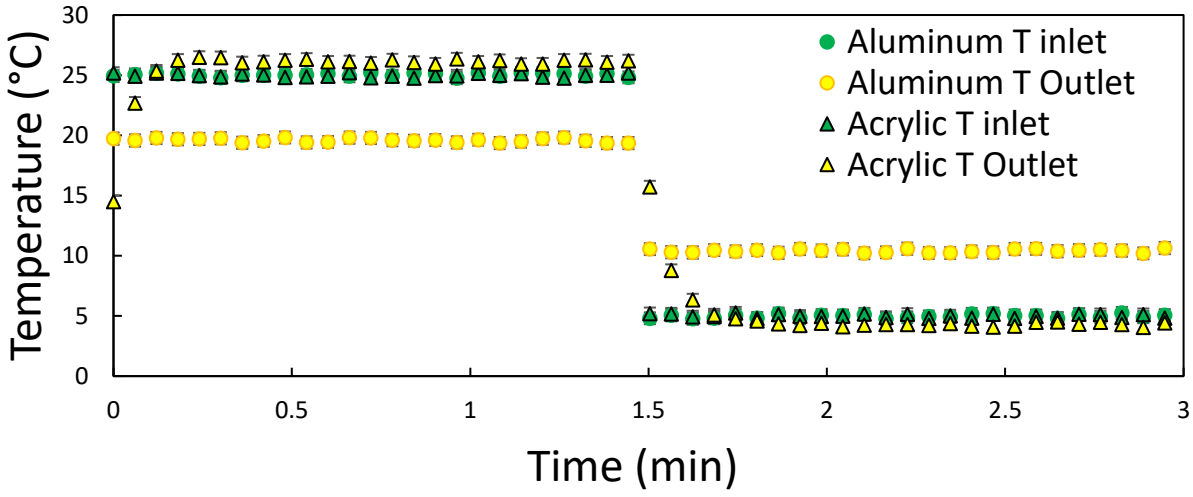

a)

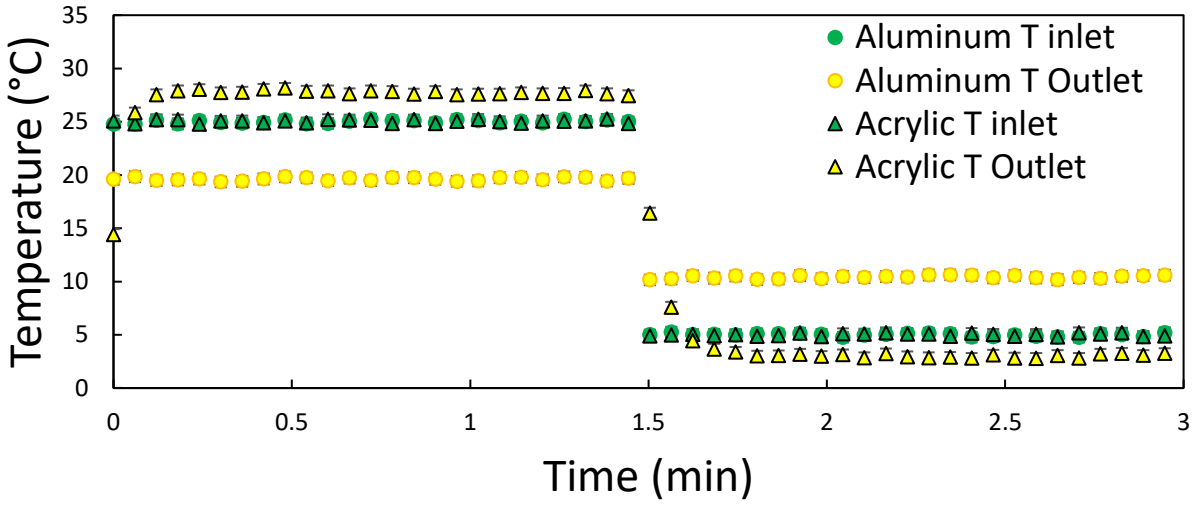

b)

Figure 44. The inlet and outlet temperature measured at the hot stream inlet relative humidity: a) 40%; and b) 85% for samples with aluminum and acrylic substrate (other working conditions were chosen based on the benchmark condition, see Table 12)

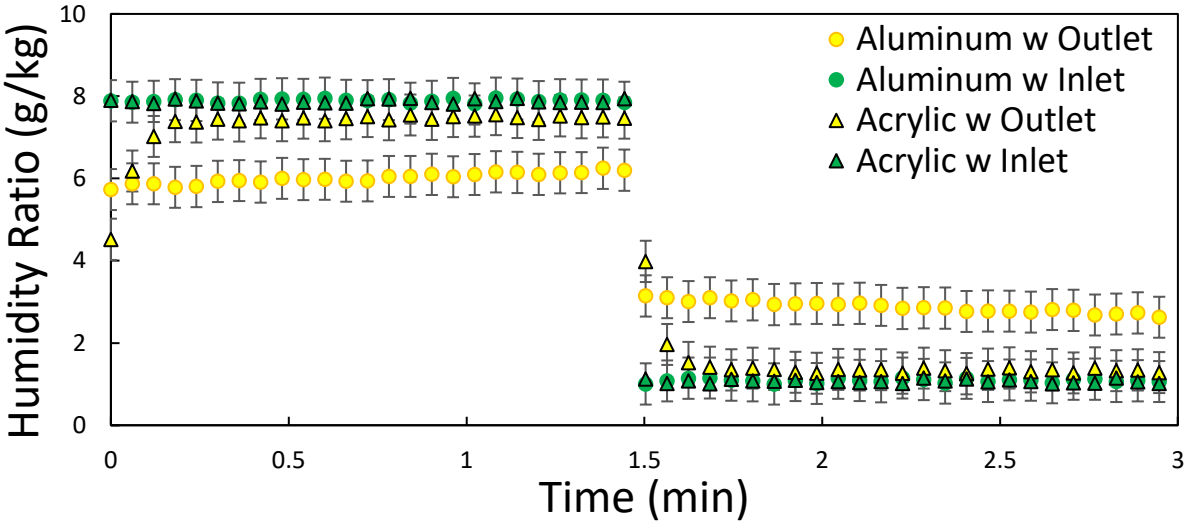

a)

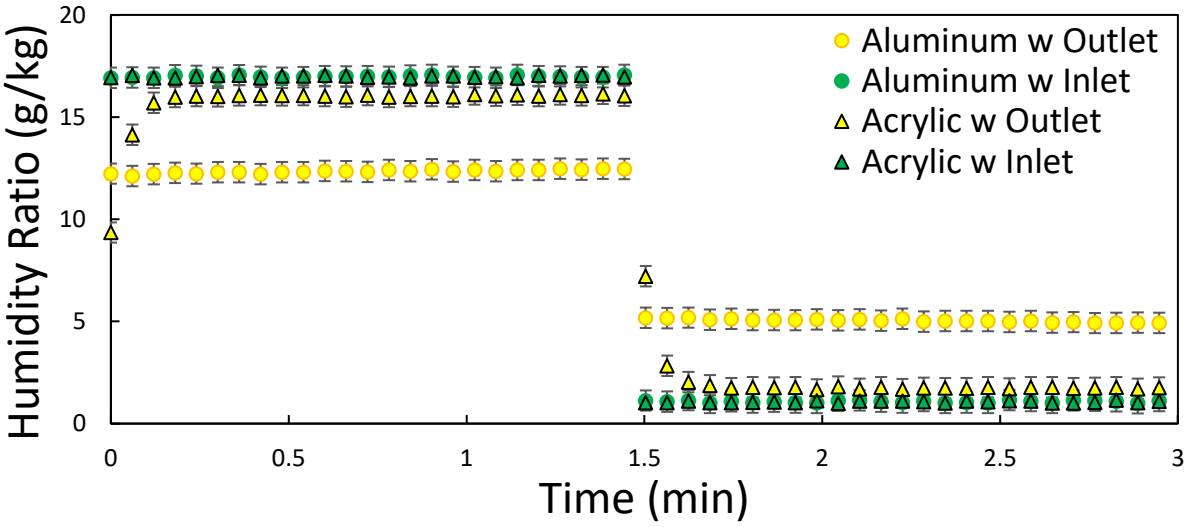

b)

Figure 45. The outlet humidity ratio measured at the hot stream inlet relative humidity:

a) 40%; b) 85% for samples with aluminum and acrylic substrate (other working conditions were chosen based on the benchmark condition, see Table 12)

Figure 46-a shows the results for the MRC^* for different hot stream inlet relative humidity of 40, 50, 60, 75 and 85% per square meter of the front surface area. The sample with aluminum substrate shows better performance compared to the sample with acrylic substrate. This difference increases as the inlet temperature approaches higher values. The reason is as the inlet air water content increases so will the adsorption but the sample with acrylic substrate will have a higher temperature in adsorption which hinders the adsorption process.

Figure 46-b shows the results for the DCOP of the sample with aluminum substrate for different hot stream inlet relative humidity of 40, 50, 60, 75 and 85%. As the MRC^* is increasing with the increase of relative humidity and the outlet temperature doesn't change, the DCOP will also increase.

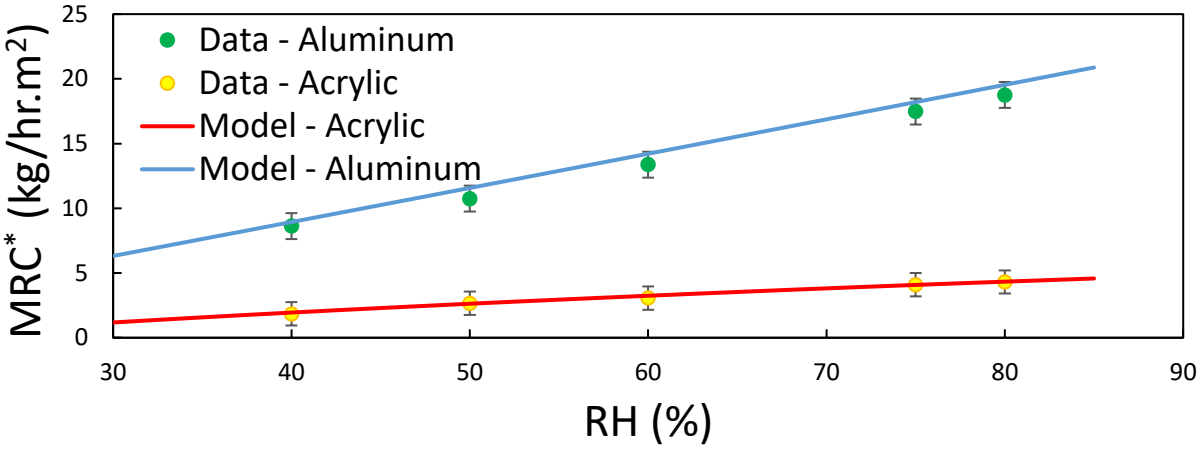

a)

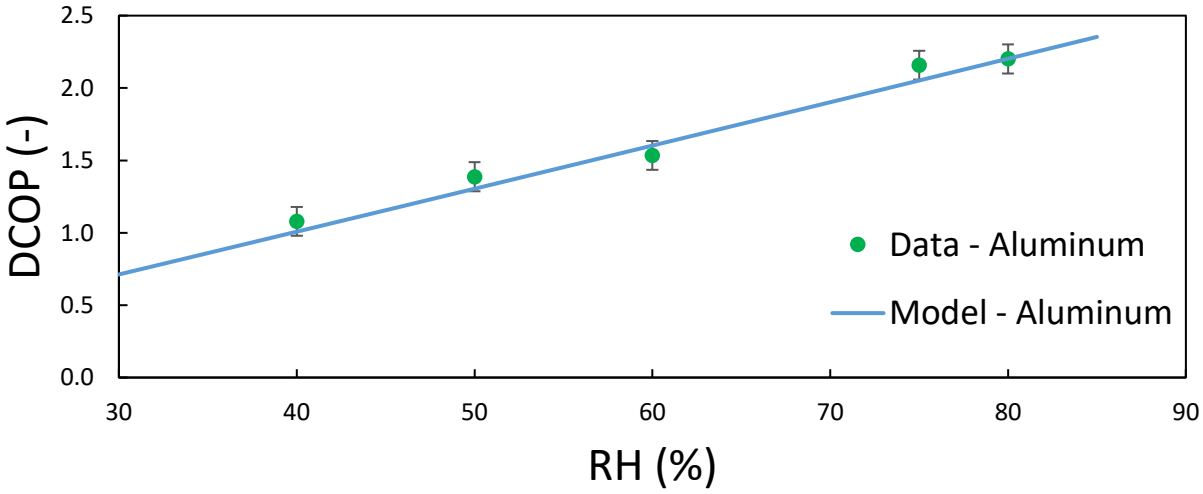

b)

Figure 46. a) The MRC*; and b) the DCOP measured against different hot stream inlet relative humidity for samples with aluminum and acrylic substrate compared to the analytical model results (other working conditions were chosen based on the benchmark condition, see Table 12)

3.3.4 Effect of flow rate

The effect of flow rate on the MRC* and DCOP was studied with a flow rate of 2, 5, 8 and 10 LPM.

Figure 47 shows the experimental results of the inlet and outlet temperatures for both samples with acrylic and aluminum substrate for a flow rate of 2 and 10 LPM. As it can be seen in Figure 47-a and Figure 47-b, the temperature difference of inlet and outlet for aluminum and acrylic substrate have the same trend when the flow rate is increasing. The reason for this is that as the air is moving slower, it has more time to exchange heat with substrate, so the difference between inlet and outlet air temperature increases when the flow rate is lower.

Figure 48 shows the experimental results of the inlet and outlet humidity ratio for both samples with acrylic and aluminum substrate for different flow rates. It can be seen that as the flow rate is decreased, heat transfer air has more time to exchange water with the adsorbent; therefore, the difference of the inlet and outlet humidity ratio for both samples decreases when approaching higher flow rates.

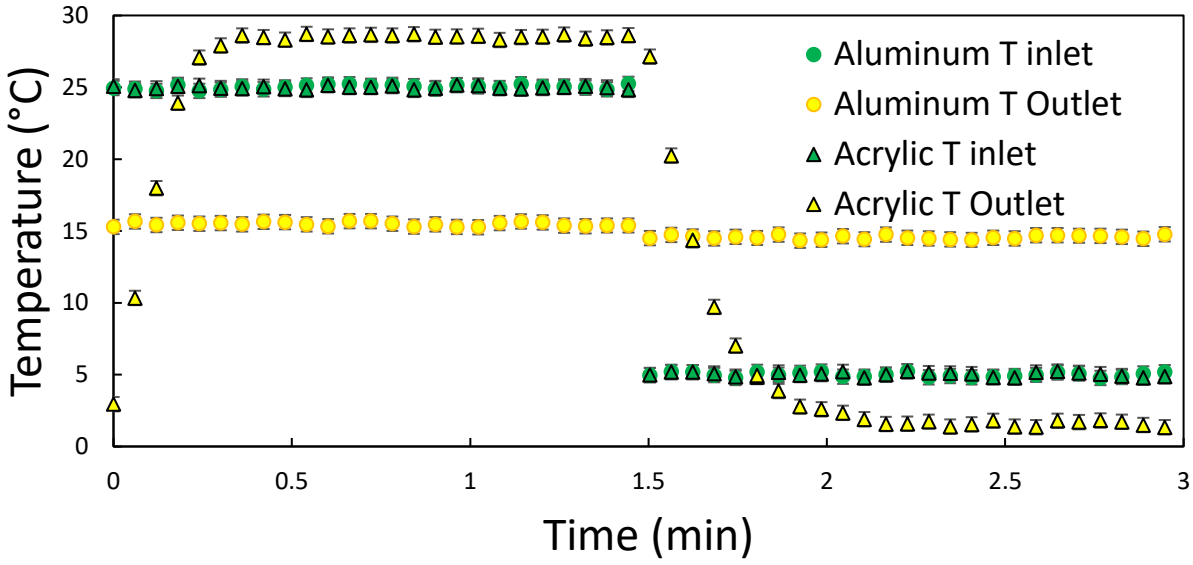

a)

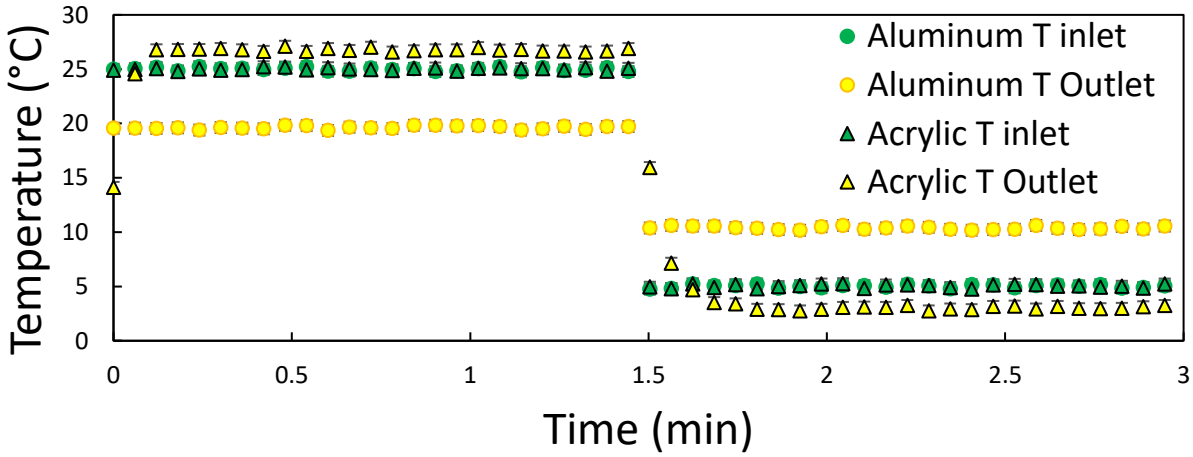

b)

Figure 47. The inlet and outlet temperature measured at inlet flow rates of: a) 2 LPM; and b) 10 LPM for both streams for samples with aluminum and acrylic substrate (other working conditions were chosen based on the benchmark condition, see Table 12)

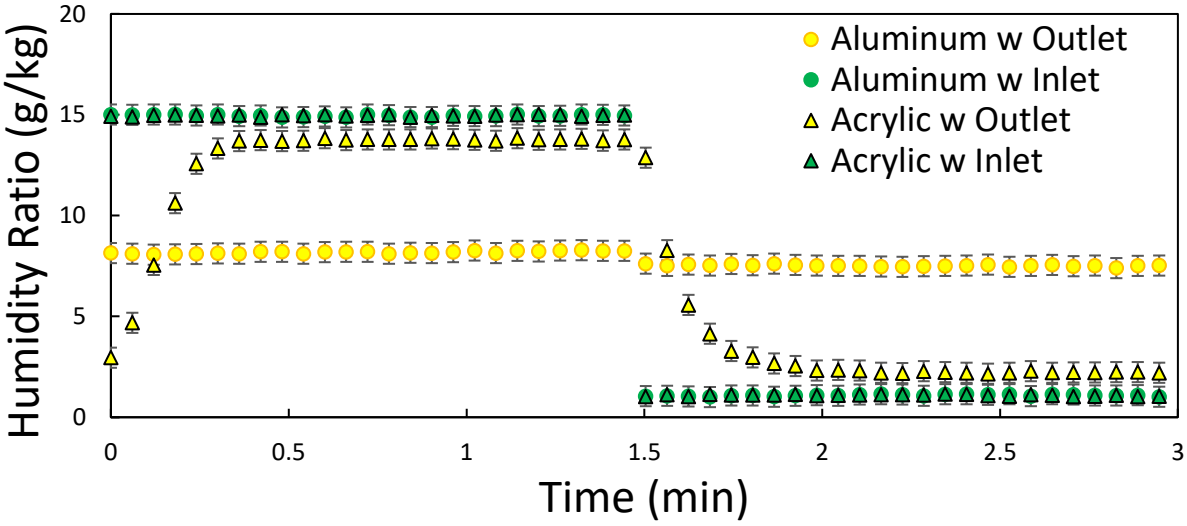

a)

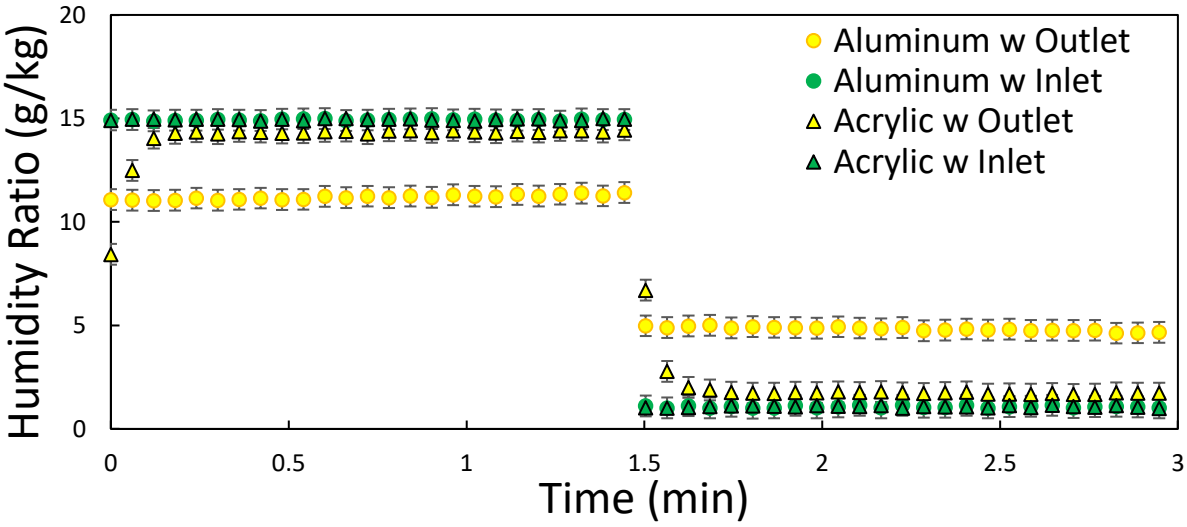

b)

Figure 48. The inlet and outlet humidity ratio measured at inlet flow rates of: a) 2 LPM; and b) 10 LPM for both streams for samples with aluminum and acrylic substrate (other working conditions were chosen based on the benchmark condition, see Table 12)

Figure 49-a shows the results for the MRC^* for different flow rates per square meter of the front surface area. Increasing the flow rate makes the air stream outlet condition (and so, the condition along the channel) close to the inlet condition. It means that in the adsorption (desorption) period, the desiccant along the channel is introduced to an air stream with higher (lower) water content so this will expedite the adsorption (desorption) process. So, there is an increase in the MRC^*.

Figure 49-b shows the results for the DCOP of the sample with aluminum substrate for different flow rates. As the flow rate increases, for the same reason that the MRC^* was increasing, the input heat will be increased. So, the denominator and nominator are both increasing which will result in an almost constant DCOP.

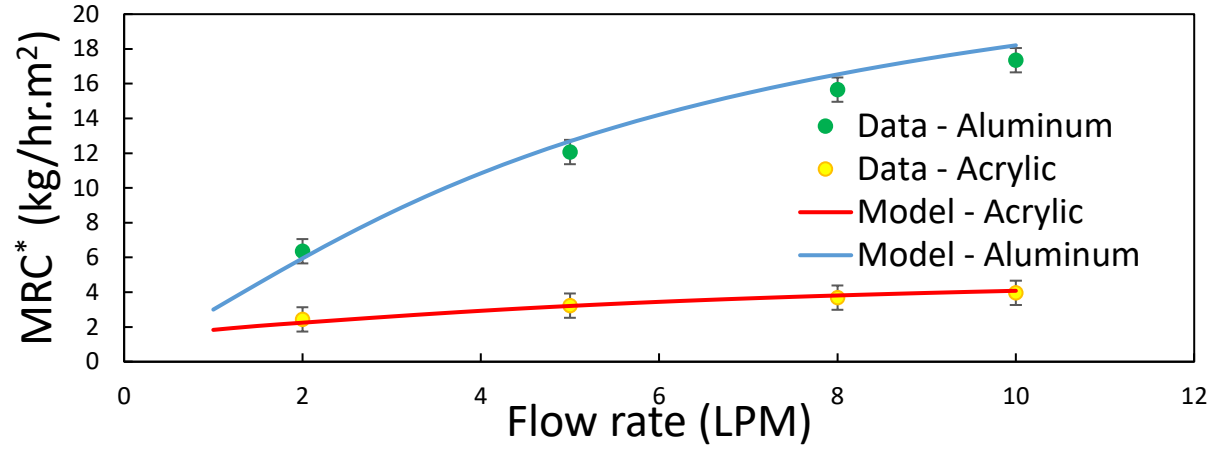

a)

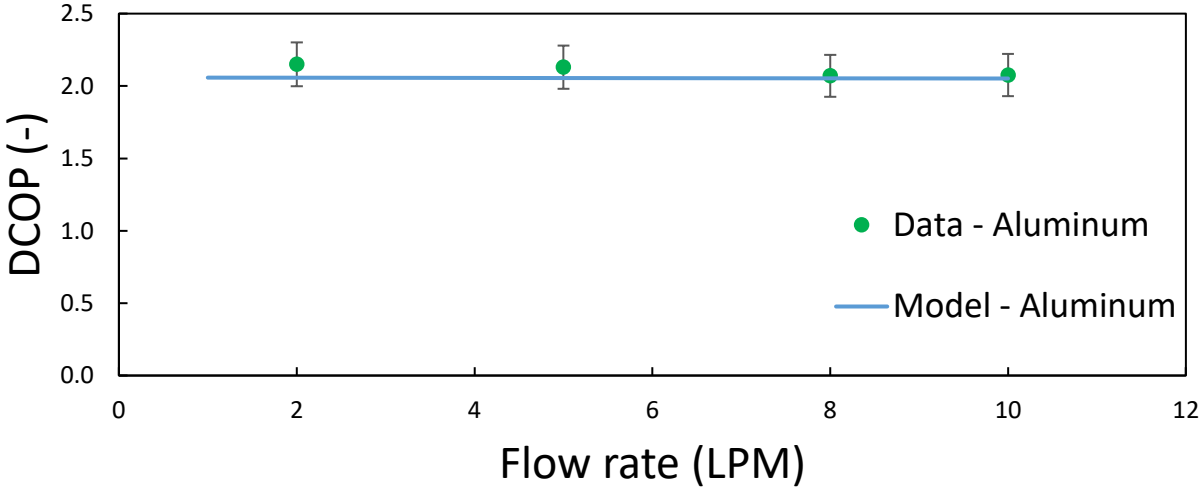

b)

Figure 49. a) The MRC; and b) the DCOP measured against different inlet flow rates of each stream for samples with aluminum and acrylic substrate compared to the analytical model results (other working conditions were chosen based on the benchmark condition, see Table 12)

3.3.5 Effect of cycle time

The effect of cycle time on the MRC* and DCOP was studied with the cycle times of: 0.5, 1, 1.5, 2, 4, 6, 8 and 10 minutes.

Figure 50 shows the experimental results of the inlet and outlet temperatures for the two samples with acrylic and aluminum substrate over time. For both samples with aluminum and acrylic substrate (except for first few seconds), the outlet temperature is almost constant with respect to changes in cycle time.

Figure 51 shows the experimental results of the inlet and outlet humidity ratio for the two samples with acrylic and aluminum substrate. Again, here for the acrylic substrate, the results show that the outlet humidity ratio is constant except for the first few seconds. The difference between the inlet and outlet humidity slightly increases for both samples when the cycle time is shorter. This is due the fact that the longer the cycle time, the closer the desiccant gets to the saturation.

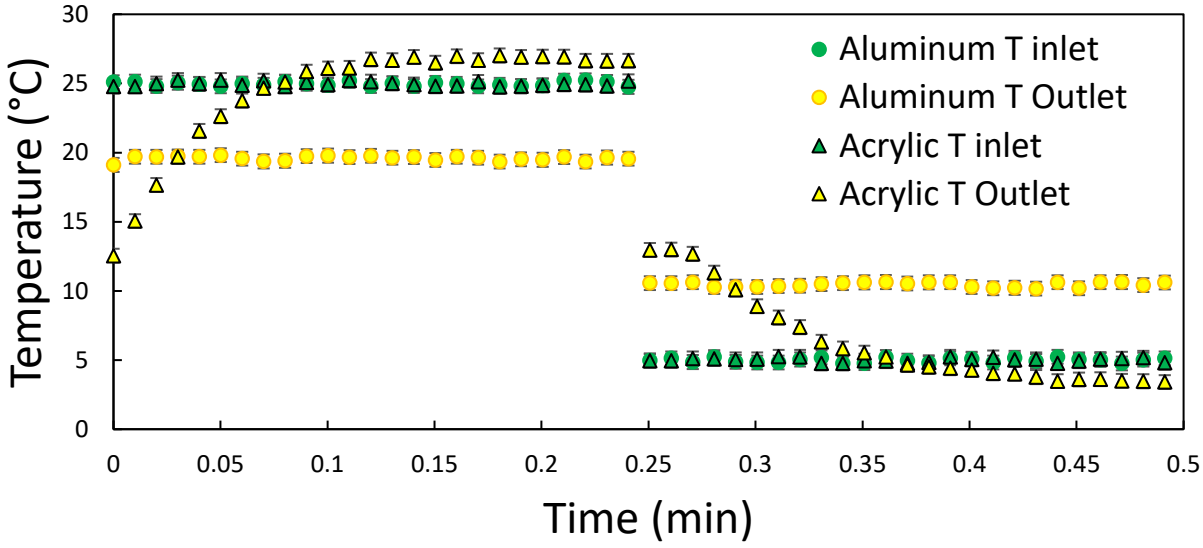

a)

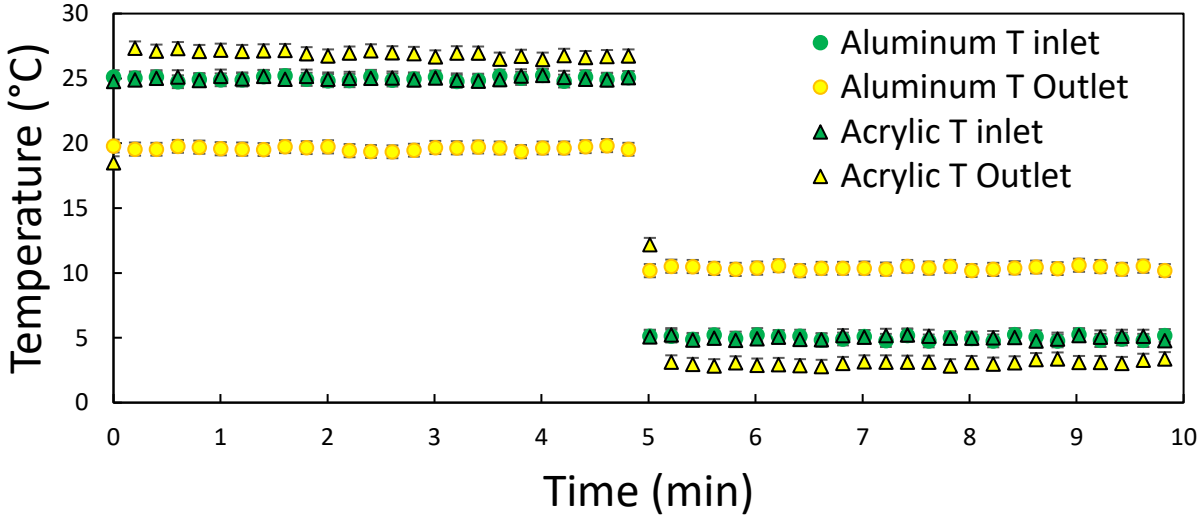

b)

Figure 50. The inlet and outlet temperature measured at cycle times of: a) 0.5 min; and b) 10 min for samples with aluminum and acrylic substrate (other working conditions were chosen based on the benchmark condition, see Table 12)

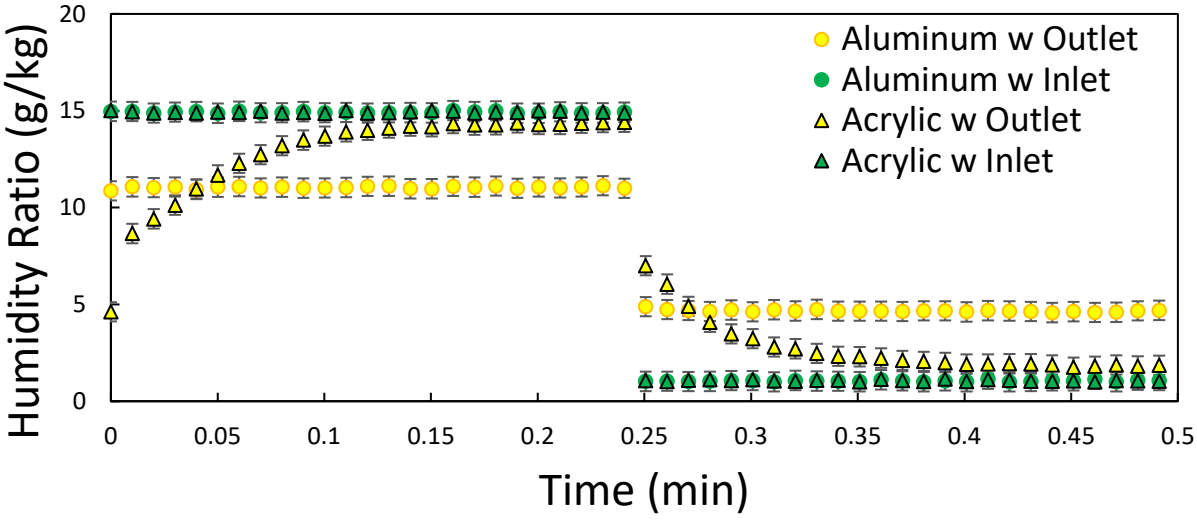

a)

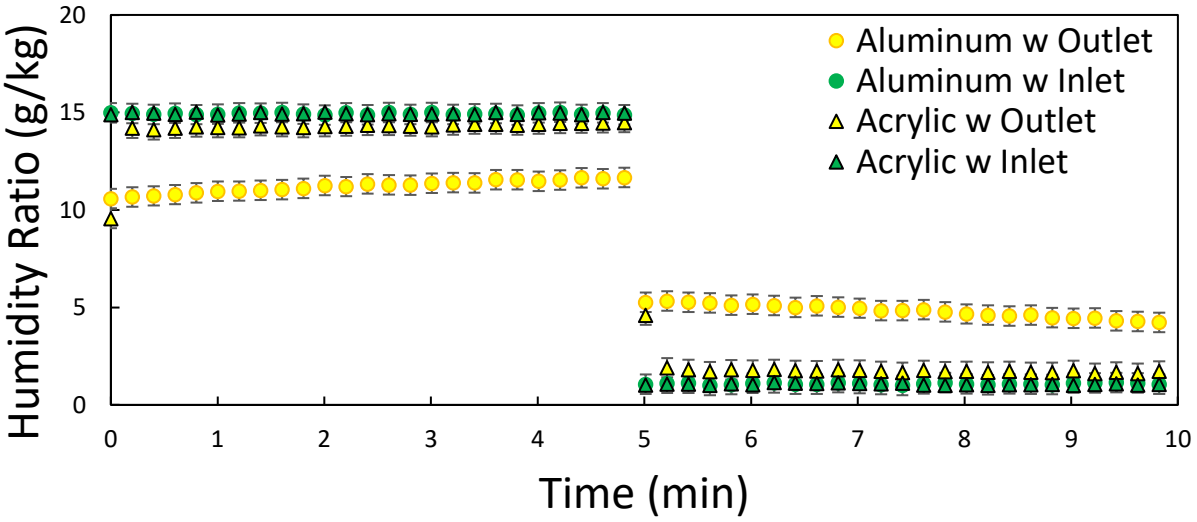

b)

Figure 51. The inlet and outlet humidity ratio measured at cycle times of: a) 0.5 min; and b) 10 min for samples with aluminum and acrylic substrate (other working conditions were chosen based on the benchmark condition, see Table 12)

Figure 52-a shows the results for the MRC^* of both samples for different cycle times per square meter of the front surface area. Following the outlet humidity ratio results, the low cycle time results in a slightly higher the MRC^*.

Figure 52-b shows the results for the DCOP of the sample with aluminum substrate for different cycle times. As the outlet temperature doesn't change that much, the DCOP follows the footsteps of the MRC^*.

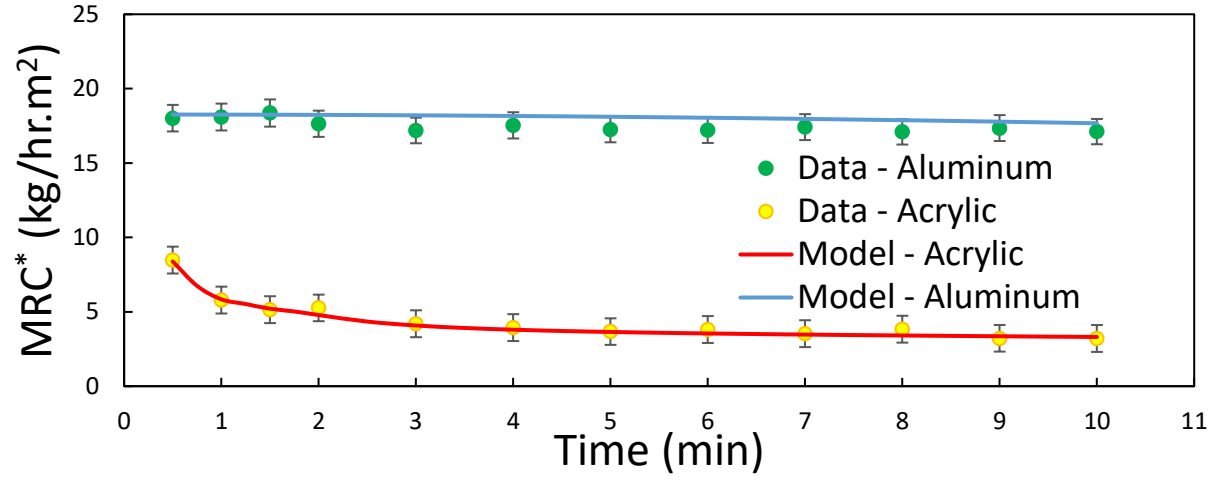

a)

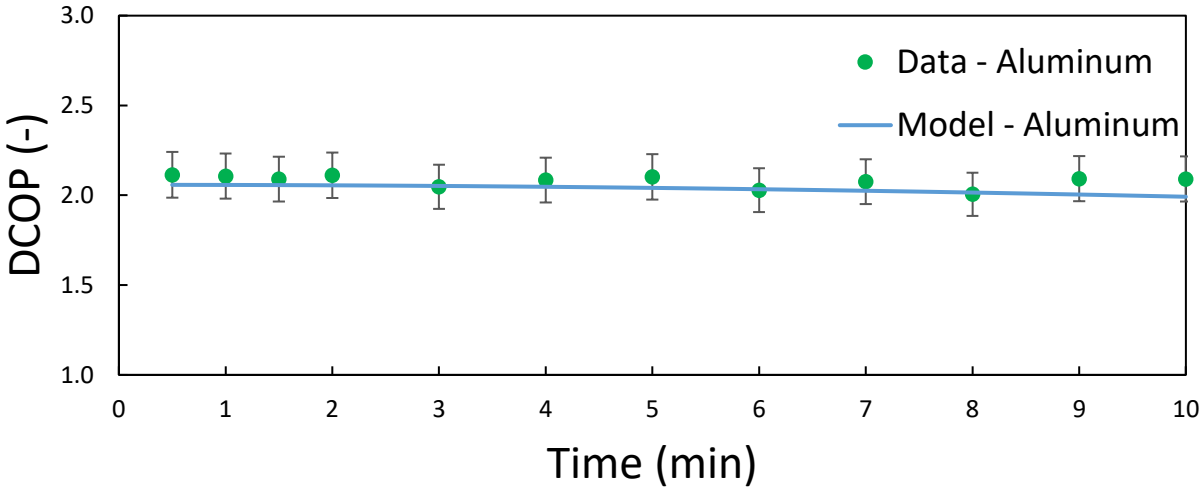

b)

Figure 52. a) The MRC*; and b) The DCOP measured against different cycle times for samples with aluminum and acrylic substrate compared to the analytical model results (other working conditions were chosen based on the benchmark condition, see Table 12)

3.4 Conclusion

The test bed for measuring the performance of a novel isothermal heat and mass exchanger was developed. Samples were prepared and TGA and TPS tests were conducted to find the properties of the coating and substrate.

The effect of different parameters, i.e., inlet temperature, humidity ratio, flow rate and cycle time, on the MRC^* and DCOP was investigated. The results showed that:

- Increasing cold stream temperature from 0℃ to 15℃ results in 150% increase in DCOP of the aluminum sample, negligible change in MRC^* of the aluminum sample (less than 1%), and 100% increase in MRC^* of the acrylic sample.
- Increasing hot stream temperature from 25℃ to 45℃ results in 50% decrees in DCOP of the aluminum sample, negligible change in MRC^* of the aluminum sample (less than 1%), and 70% decrease in MRC^* of the acrylic sample.
- Increasing hot stream relative humidity from 30% to 85% results in 200% Increase in DCOP of the aluminum sample, 200% raise in MRC^* of the aluminum sample, and 300% Increase in MRC^* of the acrylic sample.
- Increasing flow rate from 1 LPM to 10 LPM will result in results in negligible change in DCOP of the aluminum sample (less than 1%), 500% Increase in MRC^* of the aluminum sample, and 300% Increase in MRC^* of the acrylic sample.
- As the cycle time changes from 1 to 10 minutes, MRC^* and DCOP decrees 5%.

The tests also showed that samples with aluminum substrate outperforms the sample with acrylic substrate with 5 times higher average MRC^*.

4 Optimization study

In this chapter, a multi-objective optimization study is performed on the IsoHMX and the optimum MRC^* and DCOP along with optimum design parameters are found.

4.1 Problem setup

An optimization problem always starts with defining the objective function/functions which is the function that needs to be minimized. Objective functions are defined as $1/MRC$ and $1/DCOP_{isoHMX}$, as the target of the current study is to maximize the MRC and $DCOP_{isoHMX}$.

The next step is to define the optimization variables, which are the parameters that could be changed and changing them would affect the value of objective functions. In the current study, the optimization variables are:

- Geometry parameters: channel height and length, coating and substrate thickness;
- Material properties: conductivity, density, specific heat capacity, uptake rate;
- Convective heat and mass coefficient; and
- Cycle time and inlet velocity.

Running an optimization problem with so many optimization variables requires a lot of time and might not converge to the global minimum. Thus, based on the closed-form analytical solution of MRC and $DCOP_{isoHMX}$these variables were included in the four new optimization variables: $u, S_1, S_5/S_\Omega$ andS_2/S_3.(In the current case $S_2/S_3 = h_{ad}\Delta\omega/c_p\Delta T$ and is constant). It should be noted that these variables are not independent and this will be shown as constraint, and constraints could become complicated. To address this issue, based on the named variables, channel velocity (u_{avg}), channel length (L), channel height (H), and cycle time over coating thickness (t_{cycle}/δ_d) are introduced as new variables with simple constraints.

Also, in this optimization. inlet air parameters are considered as the input for optimization. All of the named optimization parameters are listed in Table 13.

Table 13. Optimization parameters

Input parameters	Objective parameters	Optimization variables
$\omega_{a1,in}, \omega_{a2,in}, T_{a1,in}, T_{a2,in}$	$1/MRC, 1/DCOP_{isoHMX}$	$u_{avg}, L, H, t_{cycle}/\delta_d$

For most optimization problems, there are some constraints, and in this study, there are both physical and manufacturing limitations. An example of a physical limitation is the conductivity of the material that can't be a negative number and for manufacturing limitation, the minimum coating thickness is a good example.

A list of assumed constraints for independent design parameters are brought in Table 14, this constraint could be different from case to case, e.g., using an advanced coating technology and reaching lower coating thickness. It should be noted that the material properties and Nusselt number are considered as constant in this study.

Table 14. Design parameters constraints

parameter	constraint
Channel length, $\boldsymbol{L}$(cm)	1< <40
Channel height, $\boldsymbol{H}$(mm)	1 < <10
Coating thickness $\boldsymbol{\delta_d}$(mm)	0.1< <0.3
Cycle time, $\boldsymbol{t_{cycle}}$(s)	30 <
Channel velocity, $\boldsymbol{u_{avg}}$(m/s)	0.1< <3

Based on the constraint for each design variable, see Table 14, and the definition of each variable, see Table 2. The optimization variables are listed in Table 15.

Table 15. Optimization variables constraints

parameter	constraint
Channel velocity, $\boldsymbol{u_{avg}}$(m/s)	0.1< <3
Channel length, $\boldsymbol{L}$ (m)	0.01< <0.4
Channel height, $\boldsymbol{H}$ (m)	0.001< <0.01
cycle time over coating thickness, $\boldsymbol{t_{cycle}/\delta_d}$ (s/m)	10^5 <

To solve this multi-objective optimization problem, a genetic algorithm (GA) [117] will be used in order to find the global pareto frontier (a set of optimal points, see Figure 53); GA algorithm was chosen to find the global optimum although it doesn't guarantee it. The optimization code is brought in Appendix D: Optimization MATLAB code.

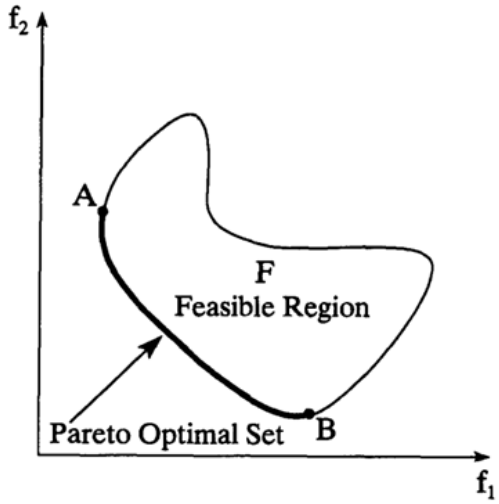

Figure 53. The feasible region and pareto frontier in objective space. Each represents one optimization objective parameter which should be minimized, i.e., f1 and f2. The highlighted part of the curve is the pareto frontier which covers all the optimum points. [117]

4.2 Results

4.2.1 Results for the benchmark condition

The pareto frontier of the optimum designs at the benchmark condition**,** i.e., inlet temperatures of 25℃ and 5℃ and humidity ratio of 14.9 kg/kg and 1.1 kg/kg (see Table 12), are brought in Figure 54. The design point with an MRC^* of 42 kg/hr and a DCOP of 2.05 is selected as the optimum design. Usually, the closest point to the origin is selected as the optimum point, but due to the fact that the DCOP doesn't change that much, the point with the highest MRC^* was selected as the optimum point. (See Figure 54)

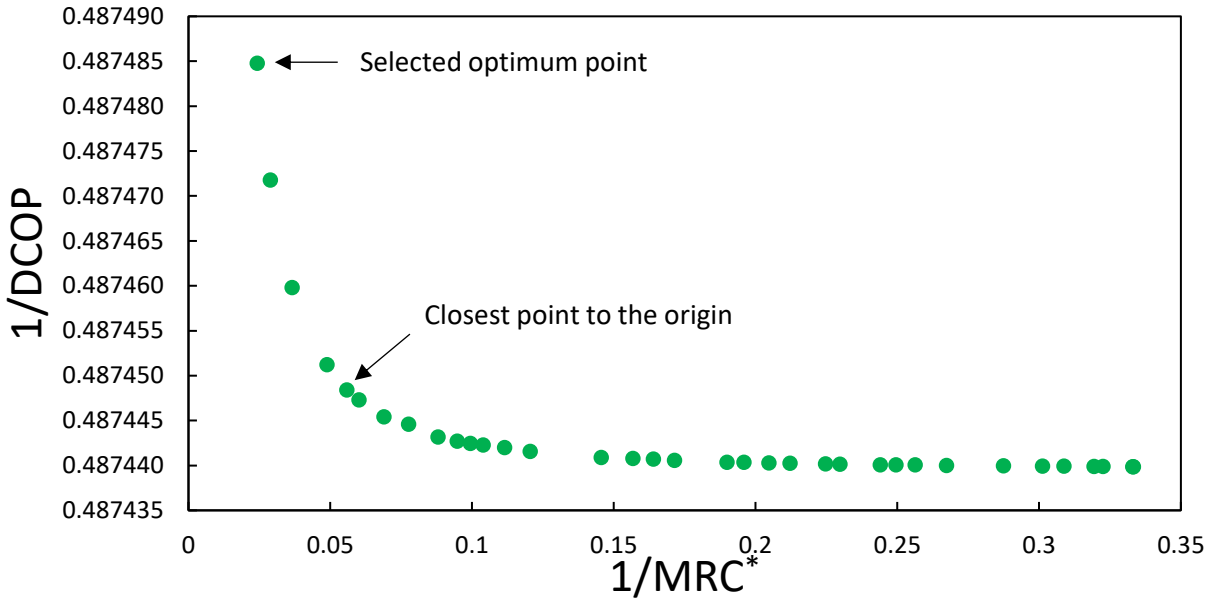

Figure 54. The pareto frontier of the $1/MRC^*$-1/DCOP graph for the IsoHMX for the benchmark working condition, i.e., inlet temperatures of 25℃ and 5℃ and a humidity ratio of 14.9 kg/kg and 1.1 kg/kg (see Table 12)

The optimization parameter values for the optimum point are shown in Table 16.

Table 16. Optimization variables optimum values

parameter	Optimum point value
$\boldsymbol{u_{avg}}$(m/s)	3
$\boldsymbol{L}$ (m)	0.4
$\boldsymbol{H}$ (m)	0.001
$\boldsymbol{t_{cycle}/\delta_d}$ (s/m)	10^5

Optimum values for the parameters were chosen as design values. Higher coating thickness means more adsorbent material and more capacity for water uptake. So, coating thickness and cycle time values were picked based on the maximum permitted thickness, i.e., 3 (mm). The chosen design parameters are shown in Table 17:

Table 17. Design parameters chosen optimum value

parameter	Optimum point value
$\boldsymbol{L}$(cm)	40
$\boldsymbol{H}$(mm)	1
$\boldsymbol{\delta_d}$(mm)	0.3
$\boldsymbol{t_{cycle}}$(s)	30
$\boldsymbol{u_{avg}}$(m/s)	3

4.2.2 Results for different conditions

To have a better understanding of the effect of the inlet condition, one of the four input parameters, i.e., $T_{a1,in}, T_{a2,in}, \omega_{a1,in}$ and $\omega_{a2,in}$, was changed and the same pareto frontier was calculated. To have a better understanding of the actual results, instead of plotting the 1/ MRC^* and 1/DCOP, the MRC^* and DCOP was plotted. The results are shown in the Figure 55 to Figure 58.

Based on this optimization study, the optimum point for each condition (the right point on each set/row of data) in all the graphs, has the same optimization parameter value which was shown in Table 16. It can be concluded that the optimum design point is independent of the inlet condition. So, the chosen design parameters in Table 17 are the global optimum point.

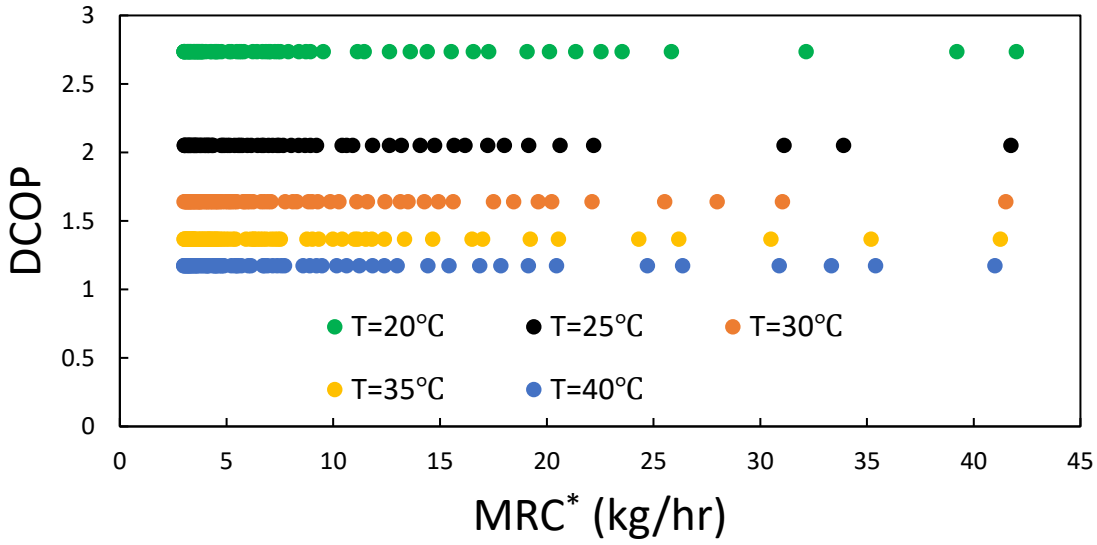

Figure 55. The pareto frontier of the MRC*-DCOP graph for the IsoHMX for different hot inlet temperatures and a cold inlet temperature of 5°C, a hot inlet humidity ratio of 14.9 kg/kg and a cold inlet humidity ratio 1.1 kg/kg.

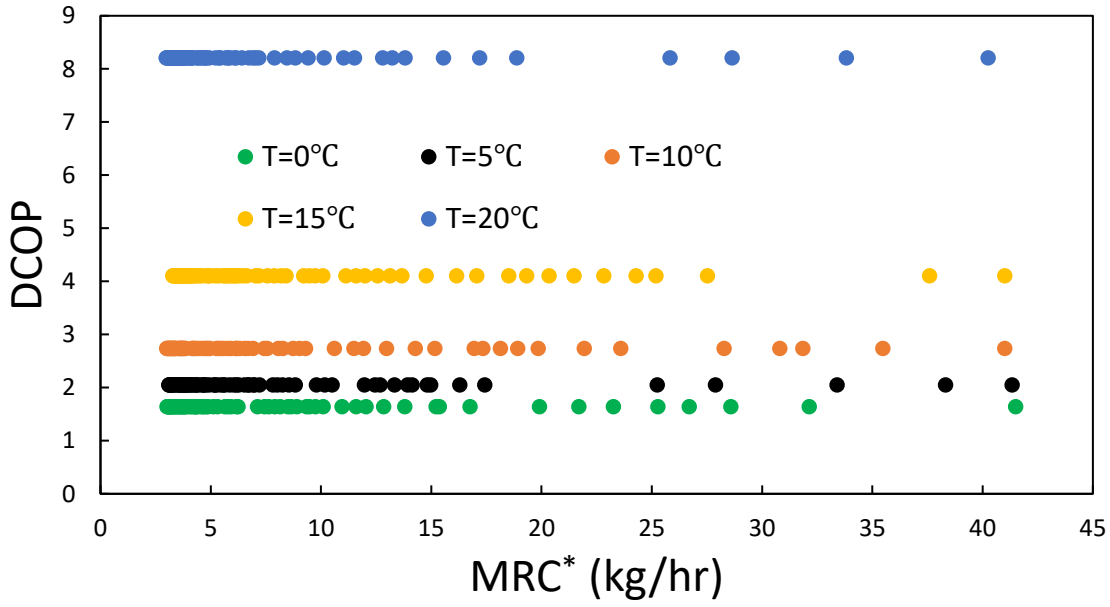

Figure 56. The pareto frontier of the MRC*-DCOP graph for the IsoHMX for different cold inlet temperatures and a hot inlet temperature of 25°C, a hot inlet humidity ratio of 14.9 kg/kg and a cold inlet humidity ratio of 1.1 kg/kg.

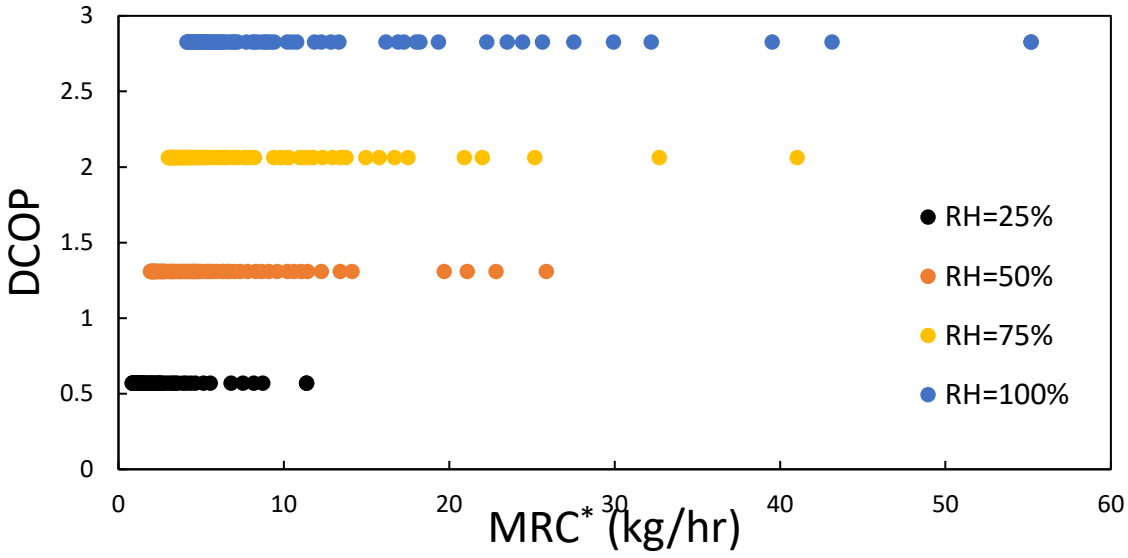

Figure 57. The pareto frontier of MRC*-DCOP graph for the IsoHMX for the different hot inlet relative humidity (or humidity ratio) and a hot inlet temperature of 25°C, a cold inlet temperature of 5°C and a cold inlet humidity ratio 1.1 kg/kg.

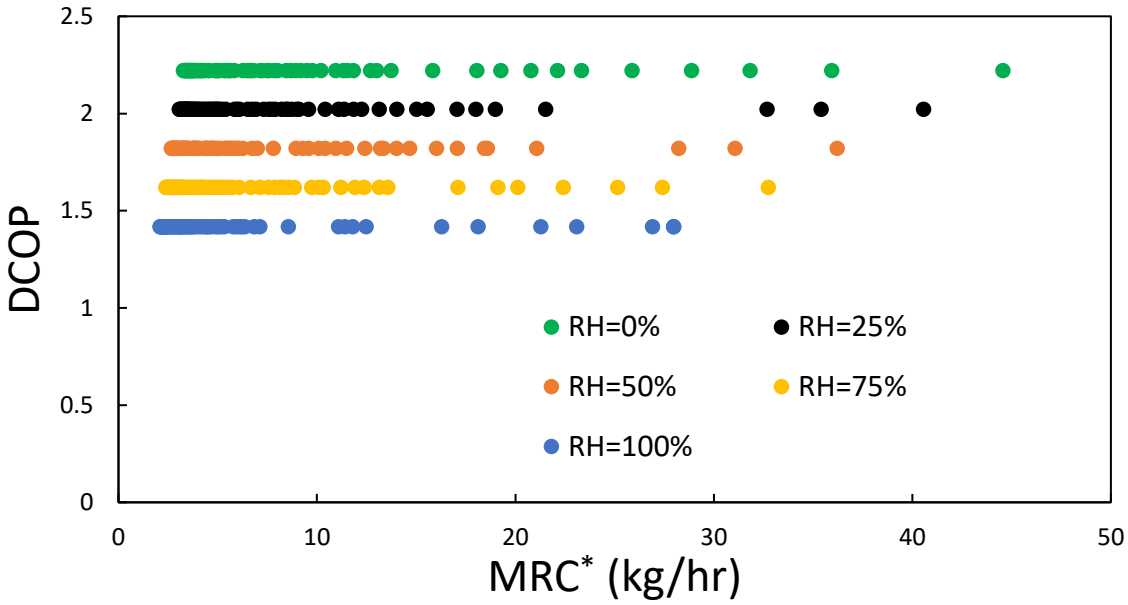

Figure 58. The pareto frontier of the MRC*-DCOP graph for the IsoHMX for a different cold inlet relative humidity (or humidity ratio) and a hot inlet temperature of 25°C, a cold inlet temperature of 5°C and a hot inlet humidity ratio of 14.9 kg/kg.

4.3 Conclusion

A genetic algorithm was used to perform a multi-objective optimization study on the geometry and working condition of the ISOHMX to find the optimal value for the MRC^* and DCOP. It was found that the optimum value of DCOP doesn't change that much along the pareto frontier. Under the benchmark working condition, the design with an MRC^* of 42 kg/hr and a DCOP of 2.05 was selected. The design parameters of the mentioned design are listed in Table 17. Later, with running optimization for different inlet conditions, it was found that the named design parameters are the global optimum design.

The following could be mentioned as the final conclusion: (These are valid as long as the desiccant doesn't reach saturation.)

- Maximum inlet velocity results in maximum MRC^* and has less than 1% effect on the DCOP.
- Minimum channel height results in maximum MRC^* has less than 1% effect on the DCOP.
- Maximum coating height results in maximum MRC^* and has less than 1% effect on the DCOP. This is valid as long as the coating thickness is less than 0.3 mm and on the coating, has a constant temperature in the radial direction.
- Maximum channel length results in maximum MRC^* and has less than 1% effect on the DCOP.
- Minimum cycle time results in maximum MRC^* and has less than 1% effect the on DCOP.

5 Performance Evaluation

In this chapter, the performance of the optimized IsoHMX is compared to a commercial desiccant wheel. To do so, following the footsteps of Goodarzia et al. [94], the comparison is made to the desiccant wheel model no. WSG 965*200 (diameter: 965 mm and depth: 200) from NovelAire Technologies using their Desiccant Wheel Simulation software, shown in Figure 59. [119]. This comparison is made over different temperatures and relative humidity.

In this study, overall dimensional limitations for both systems are considered the same, i.e., the front surface area of 1m^2 and the channel length of 20cm, and the same channel velocity of 3m/s.

The regeneration temperature was chosen as 90 degrees for the WSG 965*200 desiccant wheel.

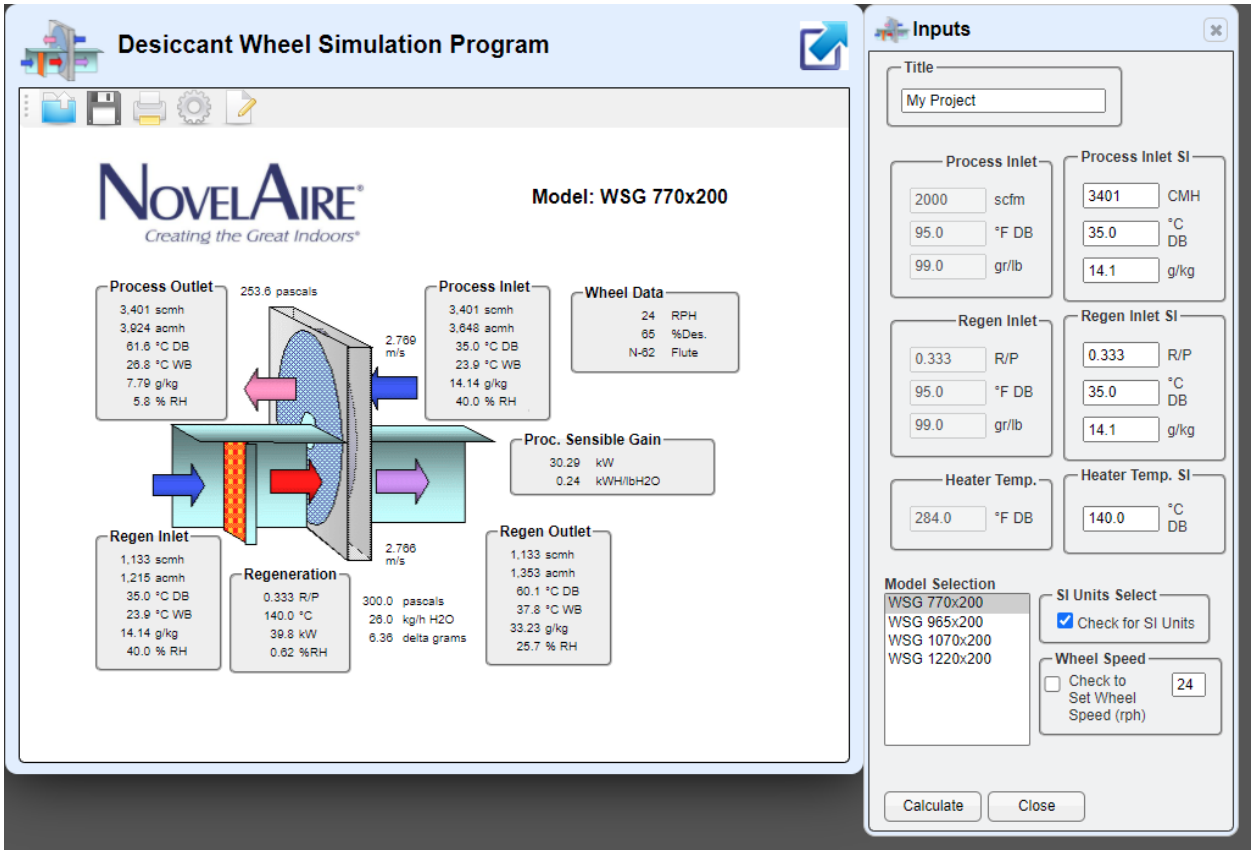

Figure 59. NovelAire Desiccant Wheel Simulation software [119]

Figure 60-a shows that cold stream temperature has a negligible effect (less than 1%) on MRC^* for both systems. The reason for this is that for the WSG 965*200 desiccant wheel, this air is preheated to 90°C so it won't affect the regeneration temperature or the MRC^*. For the IsoHMX, as the adoption temperature is constant and the rate of adsorption is dependent on the uptake rate of change with the humidity ratio, i.e., $\partial W / \partial \omega$ see Section 0, the MRC^* will remain constant.

On other hand, an increase in cold stream temperature will result in an increase of the DCOP for the IsoHMX and has a small effect on the DCOP of the WSG 965*200 desiccant wheel, see Figure 60-b. The reason for this is that for the WSG 965*200 desiccant wheel, the regeneration heat doesn't change that much and the MRC^* is constant, therefore the DCOP will remain almost constant. For the IsoHMX, as the MRC^* is constant and the cold stream temperature is increasing, the heat loss is reduced so the DCOP is increased.

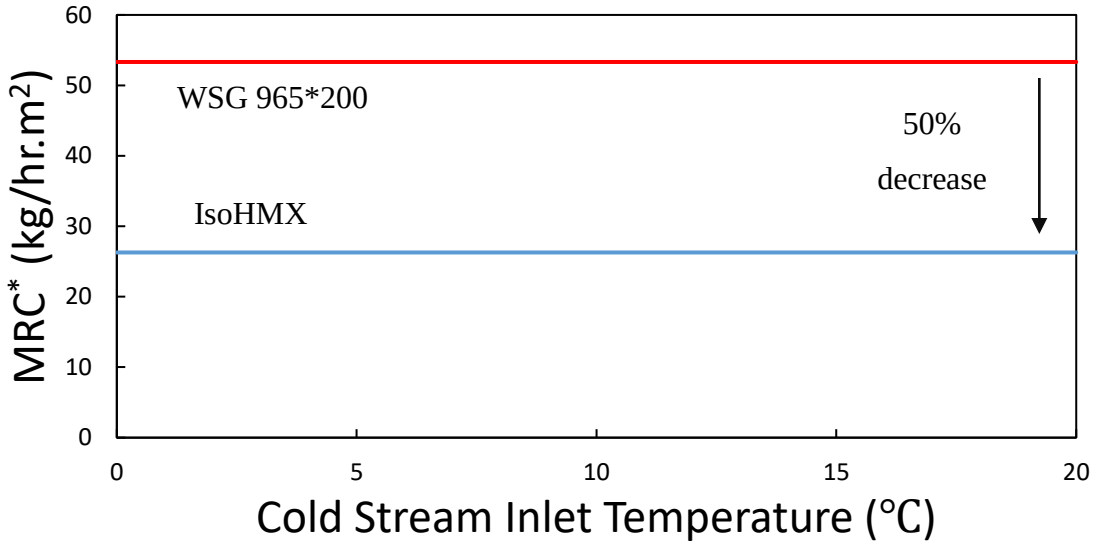

a)

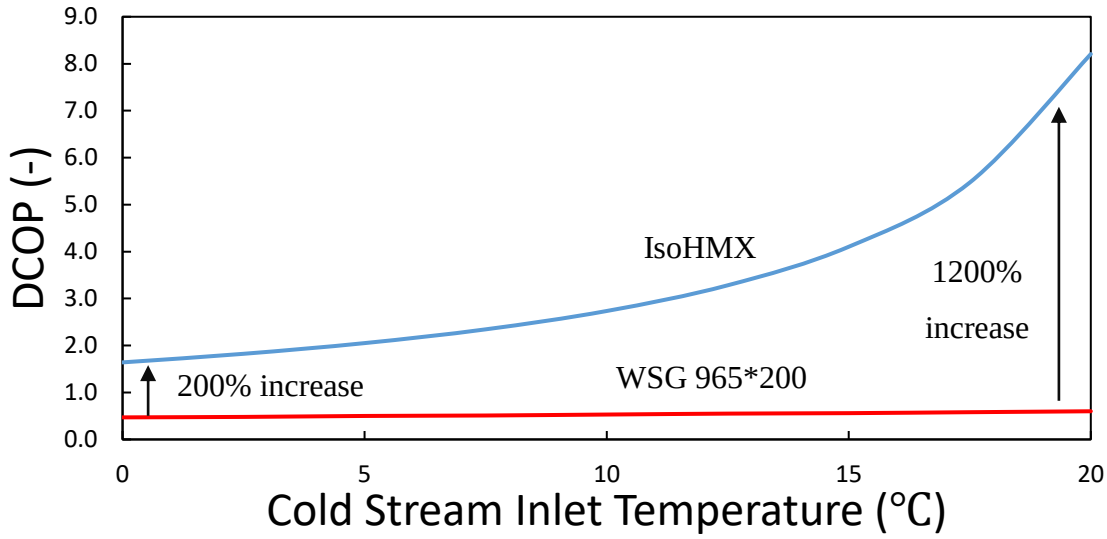

b)

Figure 60. a) the MRC* and b) the DCOP against different cold stream inlet temperatures for the IsoHMX and the WSG 965*200 desiccant wheel. Other conditions are chosen based on a greenhouse in an average Vancouver cold season working condition, i.e., hot inlet temperatures of 25°C, a hot humidity ratio of 14.9 g/kg, and a cold humidity ratio of 4.3 g/kg.

Figure 61-a shows that an increasing hot stream temperature has a negligible effect on the MRC^* of an IsoHMX (less than 1%) but results in a decrease for the WSG 965*200 MRC^* desiccant wheel. The reason for this is that for WSG 965*200 desiccant wheel, an increase in temperature of the adsorption area will result in a hotter adsorption part and a lower uptake. The effect of the hot stream temperature for the IsoHMX is the same as the cold stream temperature.

Figure 61-b shows that an increasing hot stream temperature has same effect on both systems but results in much more of a decrease in the DCOP of the IsoHMX. For the WSG 965*200 desiccant wheel, the regeneration heat is constant and the MRC^* is decreasing, therefore the DCOP will also decrease. For the IsoHMX, the heat loss is increasing as the temperature difference of the hot and cold air is increasing, and the MRC^* is constant, therefore the DCOP will decrease.

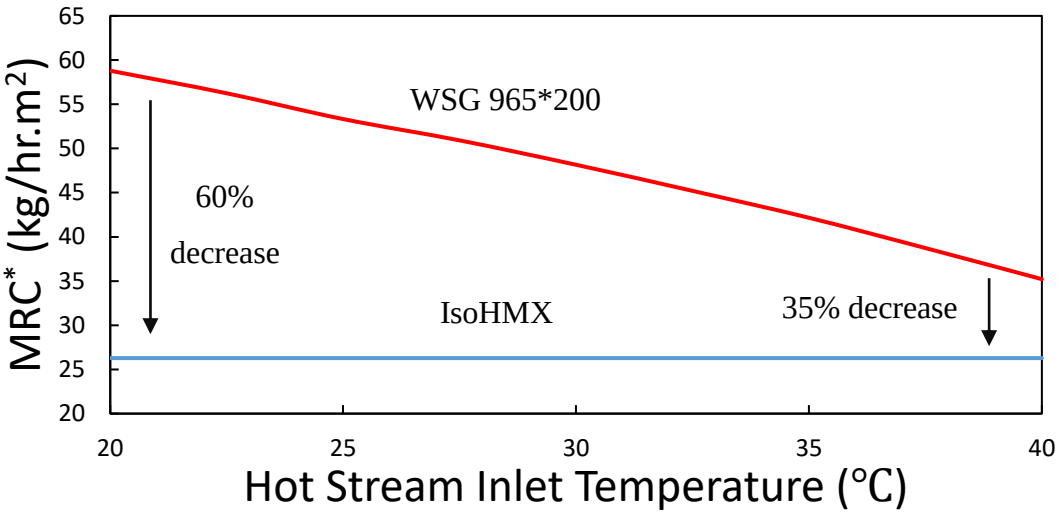

a)

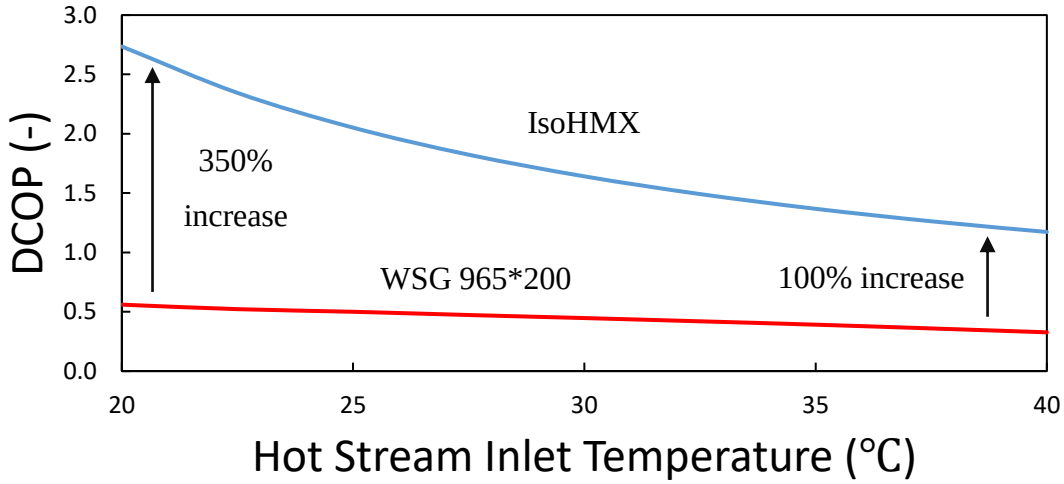

b)

Figure 61. a) The MRC* and b) the DCOP against different hot stream inlet temperatures for the IsoHMX and the WSG 965*200 desiccant wheel. Other conditions are chosen based on a greenhouse in an average Vancouver cold season working condition, i.e., cold inlet temperature of 5°C, hot humidity ratio of 14.9 g/kg and a cold humidity ratio of 4.3 g/kg.

Figure 62-a shows that an increasing cold stream relative humidity will result in a decrease of MRC^* for both systems but the IsoHMX MRC^* drops more rapidly. The drier the desorption air is, the better the MRC^*, but for the IsoHMX, as there is no preheating, the humidity of the desorption air has more effect on the system's performance.

Figure 62-b shows that an increasing cold stream relative humidity won't affect the DCOP of WSG 965*200 desiccant wheel that much as the regeneration heat and the MRC^* are constant. Increasing the cold stream relative humidity results in a decrease of the IsoHMX DCOP as the MRC^* drops and the heat loss remains the same.

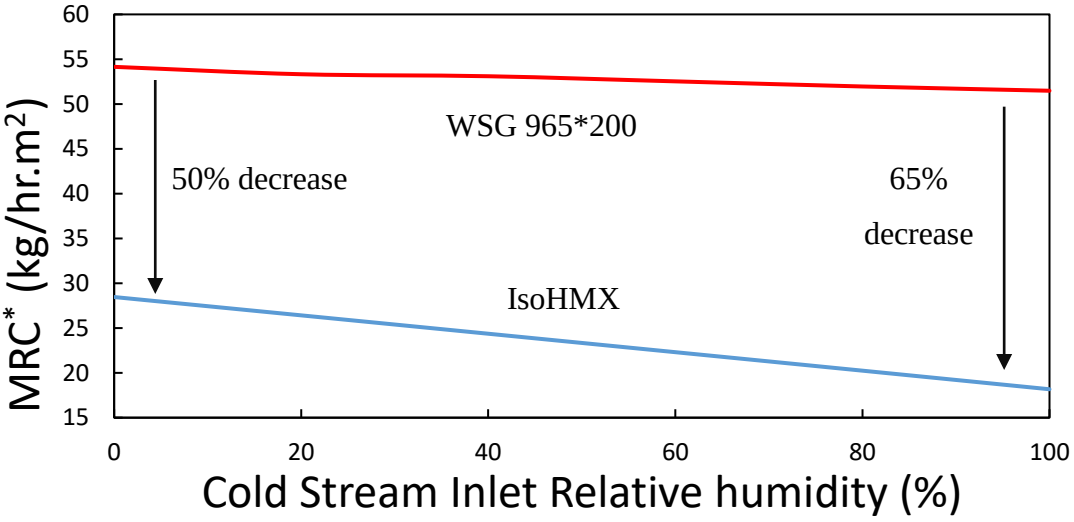

a)

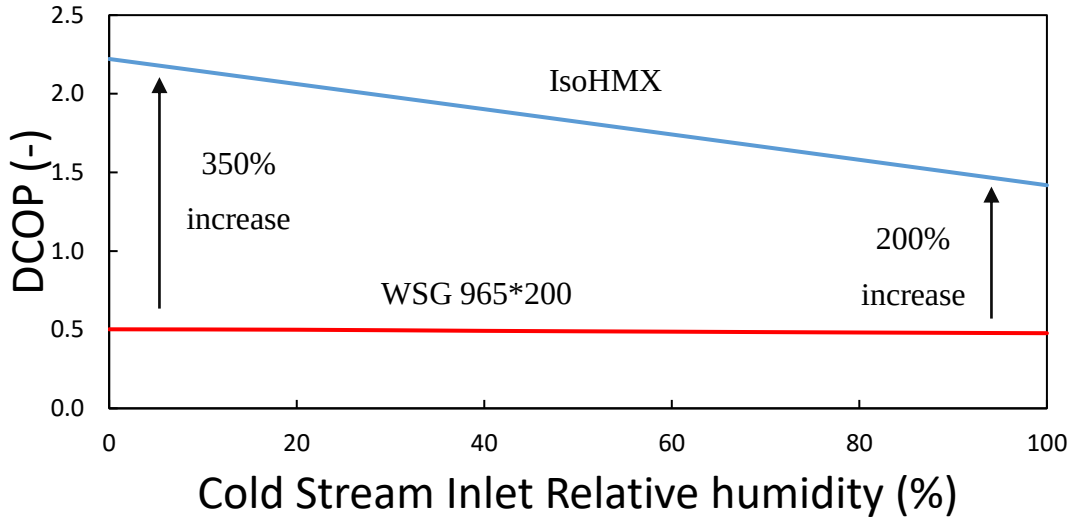

b)

Figure 62. a) The MRC*; and b) the DCOP plotted against different cold stream inlet relative humidity (humidity ratio) values for the IsoHMX and the WSG 965*200 desiccant wheel. Other conditions are chosen based on a greenhouse in an average Vancouver cold season working condition, i.e., hot inlet temperatures of 25°C, a cold inlet temperature of 5°C, and a hot humidity ratio of 14.9 g/kg. (See Table 12)

Figure 63-a shows that increasing hot stream relative humidity results in an increase of the MRC^* for both systems at almost the same rate of change. The reason for this is that when adsorption air contains more water, there would be more adsorption.

Figure 63-b shows that increasing hot stream relative humidity results in an increase of the DCOP for both systems. The reason for this is that for both systems the denominator of the DCOP, i.e., regeneration heat for the WSG 965*200 desiccant wheel and heat loss for the IsoHMX, is constant and the change of the DCOP has the same ratio as the change in the MRC^*. As the MRC^* of the WSG 965*200 desiccant wheel goes from 20 kg/hr to 55 kg/hr (~2.5 times higher) and for the IsoHMX, it goes from 5 kg/hr to 30 kg/hr (~6 times higher), the change in the MRC^* of the IsoHMX is more rapid.

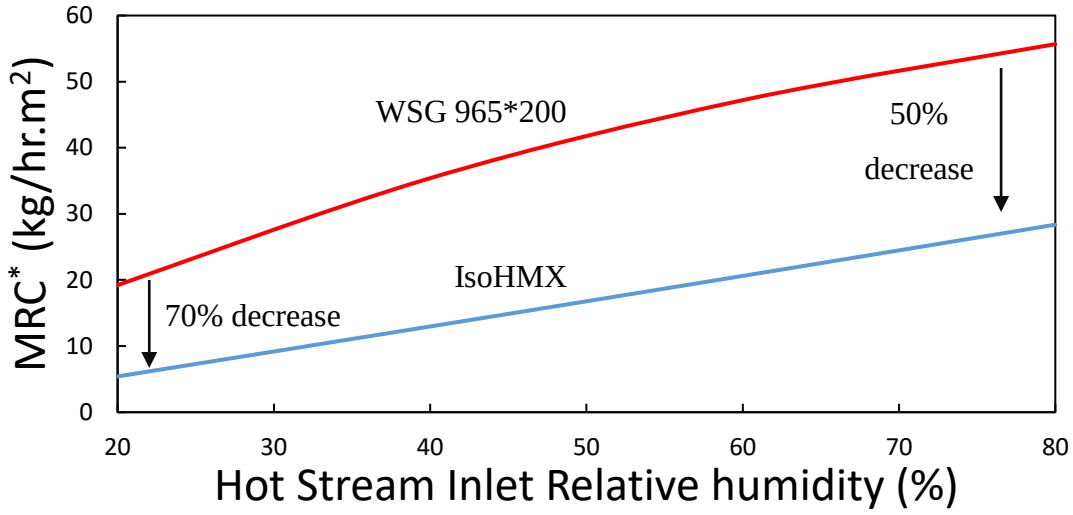

a)

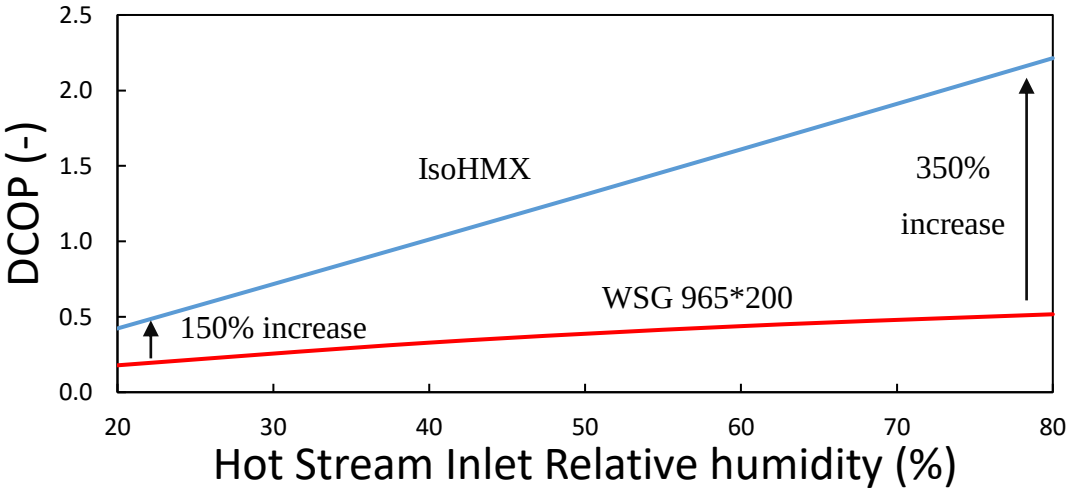

b)

Figure 63. a) The MRC* and b) the DCOP against different hot stream inlet relative humidity (humidity ratio) values for the IsoHMX and the WSG 965*200 desiccant wheel. Other conditions are chosen based on a greenhouse in an average Vancouver cold season working condition, i.e., a hot inlet temperature of 25℃, a cold inlet temperatures of 5℃, and a cold humidity ratio of 4.3 g/kg.

5.1 Conclusion

The performance of the optimized IsoHMX is compared to a commercial desiccant wheel, i.e., the desiccant wheel model no. WSG 965*200 from NovelAire Tevchnologies.

The results show that, in general, the WSGG 965*200 wheel has better MRC^* (almost double) in most cases. On the other hand, the IsoHMX's DCOP is almost four times higher.

This means to remove certain amount of moisture from air, the needed IsoHMX's size would be two times higher compared to WSGG 965*200 but consumes around 75% less energy. So, the IsoHMX would have a higher capital cost and a lower running cost.

6 Summary and Future work

6.1 Summary

The objective or goal of this PhD project was to develop a novel desiccant-based sorption system for dehumidification in cold areas. The focus of this study was on dehumidification of the greenhouse; however, the system could be used for other applications, such as dehumification of residential and commercial buildings.

In Chapter 1.Introduction:, different dehumidification systems of the greenhouse were reviewed. Based on the concept of the closed greenhouse and energy efficiency, desiccant-based dehumidification systems were championed for this study. To increase the performance of the desiccant-based dehumification systems in a greenhouse in the cold climate, a novel isothermal heat and mass exchanger (IsoHMX) was introduced to deliver the heat of adsorption to the desorption area through a conductive substrate.

7 In Chapter 2.Modeling

In the following chapter, numerical and analytical modeling of the IsoHMX is explained. It should be noted that numerical model which is easier to develop was developed before the analytical model. Having a valid numerical code before developing an analytical model, helps to have a better understanding of the phenomenon and importance of each parameter and terms in the equations.

There are only a few studies in the literature that introduced an analytical solution for desiccant-based dehumidification systems. Lee and Kim [81] employed an integral model and simplified the governing equations of a desiccant wheel to a set of ordinary differential equations. Kang et al. [82], [83] assumed linear humidity and temperature profiles along the channel solved the heat and mass transfer equations analytically and reported root mean square errors of less than 10%.

Bahrehmand et al. [84], [85] proposed a novel analytical model to study the performance of coated sorption beds for a sorption closed-cycle, i.e., a sorption system in the absence of non-condensable gases (NCG), e.g., air. Although, the sorption closed-cycle dehumidification system study is not directly applicable to the open-cycle, their analytical approach is quite relevant and noteworthy. Employing an orthogonal expansion technique, they solved the 2D transient heat and mass transfer

equations and validated the results with measurements. Bahrehmand and Bahrami [86] also introduced an analytical design tool for sorber bed heat exchangers, and reported that the sorption composite composition, sorber bed geometry, heat transfer characteristics, and cycle time can have conflicting counter effects on the performance and should be optimized simultaneously.

Due to the complicated nature of desiccant-based dehumidification systems, i.e., highly-coupled transient heat and mass transfer phenomena, numerical simulation of these systems is time-consuming. As a result, using a numerical simulation for optimizations and real time control is not practical. Therefore, one of the objectives of this study is to develop a closed-form analytical solution to evaluate the performance of the IsoHMX.

7.1 Analytical model development

A simplified 2D geometry of the experimental test section is considered and is shown schematically in Figure 6. This geometry consisted of two air streams, two desiccant layers, and a substrate. Based on the physics of adsorption/desorption cycles, the cyclic steady state is assumed for the presented model. Also, in the IsoHMX after one half cycle channel, it behaves like channel two and vice versa, therefore, only a half cycle needs to be modeled. The following additional assumptions are made to simplify the model development:

- Thermophysical properties for the air, substrate, and desiccant layer are assumed constant. As the temperature doesn't vary more than ±25℃ and the pressure is almost constant, i.e., system works under atmospheric pressure, this is a valid assumption;
- The regeneration temperature is low (less than 90°C [87]); thus, a constant enthalpy of adsorption (h_{ad}) is assumed following Ref. [88]; This assumption is backed up with experimental measurements of the TPS. The calculated enthalpy of adsorption is 2440 (KJ/Kg);
- The air stream is assumed to be fully-developed over the heat/mass exchanger; therefore, the heat and mass transfer coefficients are considered constant over time. due to low velocity of the air and low ratio of channel height over channel length this is a valid assumption;

- The axial heat conduction in the air stream and desiccant layer are considered negligible; Due to low heat diffusivity of the air and strong advection heat transfer;
- The Lewis number, i.e., the ratio of thermal diffusivity and mass diffusivity, equal to unity is assumed. Lewis number is strong function of the material, and is almost equal to one for air. Thus, this is a valid assumption;
- The effects of unsteady terms in the air stream ($\frac{\partial T_a}{\partial t} \approx \frac{\partial \omega_a}{\partial t} \approx 0$) are assumed negligible, following Ref. [82]. Numerical analysis and comparison of the mentioned terms showed that they are two orders of magnitude lower than the other terms in the air energy and mass transfer equation;
- Water uptake in desiccant layer is equal to its equilibrium uptake [82]. This assumption was also validated by a comparison in numerical simulation, see section 2.2;
- As the desiccant layer is thin (less than 0.3mm [89]), the Biot number is smaller than 0.1 (0.03 in this case), the lumped model assumption is valid. So, averaged properties in the y-direction are used, namely, $T_d(x,t), \omega_d(x,t)$ [90].
- As the substrate is thin and its thermal diffusivity and conductivity are high, constant temperature for substrate in the y-direction is assumed. This assumption was validated with a numerical solution;
- Based on well-stablished internal flow studies [91], the air temperature and humidity profiles are assumed to be exponential in the x-direction [92] ; and
- There is no condensation happening in the system. This assumption depends on the working condition of the system. In the current study based on the experimental results and calculations, this is a valid assumption. (In case of condensation, i.e., substrate's

temperature is lower than dew point temperature of the air stream, this model is not valid anymore.)

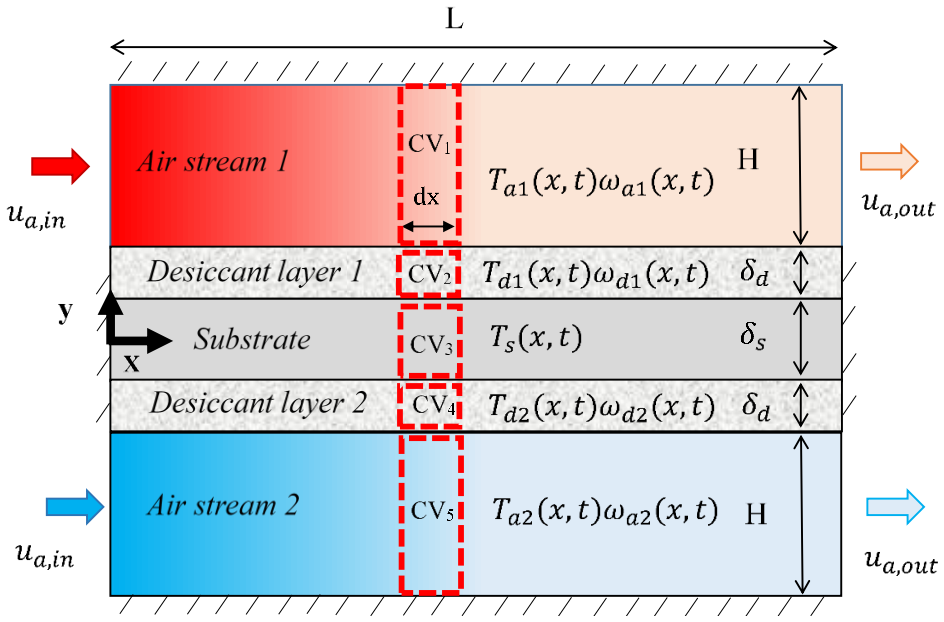

Figure 6. A sectional schematic view of the IsoHMX calculation domain and selected control volumes for the present model

7.1.1 Governing equations

As shown in Figure 6, five control volumes, i.e., CV_1 to CV_5, and the energy and mass exchanges between them are considered. Based on the above-mentioned assumptions, the energy and mass balances for each control volume are expressed as:

Energy and mass balance in CV_1

$$u_{avg}\frac{\partial T_{a1}(x,t)}{\partial x}=\frac{1}{\rho_a c_{P,a}\mathrm{H}}h\left(T_{d1}(x,t)-T_{a1}(x,t)\right) \tag{5}$$

$$u_{avg}\frac{\partial \omega_{a1}(x,t)}{\partial x}=\frac{1}{H}h_m\left(\omega_{d1}(x,t)-\omega_{a1}(x,t)\right) \tag{6}$$

where, H is the channel height, h and h_m are convective heat and mass transfer coefficient, respectively, u_{avg}, $T_a(x,t)$ and $\omega_a(x,t)$ are air bulk values, i.e., average values in the y-direction for air velocity, temperature and humidity ratio, respectively. $T_d(x,t)$ and $\omega_d(x,t)$ are desiccant

average value the y-direction for temperature and humidity ratio, respectively. The bulk temperature and humidity ratio of the air as listed in the assumptions, is calculated based on the exponential profile assumption:

$$T_{a1(or2)}(t,x) = a_{T1(or2)}(t)\ exp\left(-\frac{S_1 x}{L}\right) + \left(T_{a1(or2),in} - a_{T1(or2)}(t)\right)$$
$$\omega_{a1(or2)}(t,x) = a_{\omega 1(or2)}(t)\ exp\left(-\frac{S_1 x}{L}\right) + \left(\omega_{a1(or2),in} - a_{\omega 1(or2)}(t)\right) \quad (7)$$

where, $\boldsymbol{a_{T1(or2)}(t)}$ and $\boldsymbol{a_{\omega 1(or2)}(t)}$ are unknown functions of time, which should be calculated and $\boldsymbol{S_1}$ is listed in Table 2:

Table 2.

The same set of equations is defined for **CV5**:

$$u_{avg}\frac{\partial T_{a2}(x,t)}{\partial x} = \frac{1}{\rho_a c_{P,a}\mathrm{H}} h\left(T_{d2}(x,t) - T_{a2}(x,t)\right) \quad (8)$$

$$u_{avg}\frac{\partial \omega_{a2}(x,t)}{\partial x} = \frac{1}{H} h_m\left(\omega_{d2}(x,t) - \omega_{a2}(x,t)\right) \quad (9)$$

Energy and mass balance in CV2

$$\rho_d c_{P,d}\delta_d \frac{\partial T_{d1}(x,t)}{\partial t} = h_{ad}\rho_a h_m\left(\omega_{a1}(x,t) - \omega_{d1}(x,t)\right) + h\left(T_{a1}(x,t) - T_{d1}(x,t)\right) + 2k_d/\delta_d\left(T_s(x,t) - T_{d1}(x,t)\right) \quad (10)$$

$$\frac{\partial W_{d1}(x,t)}{\partial T_{d1}(x,t)}\frac{\partial T_{d1}(x,t)}{\partial t} + \frac{\partial W_{d1}(x,t)}{\partial \omega_{d1}(x,t)}\frac{\partial \omega_{d1}(x,t)}{\partial t} = \frac{\rho_a}{\rho_d \delta_d} h_m\left(\omega_{a1}(x,t) - \omega_{d1}(x,t)\right) \quad (11)$$

The same set of equations is defined for **CV4**:

$$\rho_d c_{P,d} \delta_d \frac{\partial T_{d2}(x,t)}{\partial t} = h_{ad}\rho_a h_m\left(\omega_{a2}(x,t) - \omega_{d2}(x,t)\right) + h\left(T_{a2}(x,t) - T_{d2}(x,t)\right) + 2k_d/\delta_d\left(T_s(x,t) - T_{d2}(x,t)\right) \quad (12)$$

$$\frac{\partial W_{d2}(x,t)}{\partial T_{d2}(x,t)}\frac{\partial T_{d2}(x,t)}{\partial t} + \frac{\partial W_{d2}(x,t)}{\partial \omega_{d2}(x,t)}\frac{\partial \omega_{d2}(x,t)}{\partial t} = \frac{\rho_a}{\rho_d \delta_d} h_m\left(\omega_{a2}(x,t) - \omega_{d2}(x,t)\right) \quad (13)$$

where, W_d is the desiccant water uptake, and δ_d is the desiccant layer thickness.

Energy balance in CV3

$$\rho_s c_{P,s} \delta_s \frac{\partial T_s(x,t)}{\partial t} = 2k_d/\delta_d\left(T_{d1}(x,t) + T_{d2}(x,t) - 2T_s(x,t)\right) + k_s \delta_s \frac{\partial^2 T_s(x,t)}{\partial x^2} \quad (14)$$

where, T_s is substrate temperature, and δ_s is substrate thickness. The governing equations should be solved simultaneously with the following initial conditions for both air streams and desiccant layers, i.e., 1 and 2. These conditions are derived based on a cyclic steady state assumption and the fact that on the second half of the cycle, stream 1 behaves as stream 2 in the first half and vice versa:

$$\begin{cases} \omega_{d1}(x,0) = \omega_{d2}\left(x, t_{cycle/2}\right) & At\ the\ beginning\ of\ process\ for\ stream\ 1 \\ \omega_{d1}\left(x, t_{cycle/2}\right) = \omega_{d2}(x,0) & At\ the\ beginning\ of\ regeneration\ for\ stream\ 2 \\ T_{d1}(x,0) = T_{d2}\left(x, t_{cycle/2}\right) & At\ the\ beginning\ of\ process\ for\ stream\ 1 \\ T_{d1}\left(x, t_{\frac{cycle}{2}}\right) = T_{d2}(x,0) & At\ the\ beginning\ of regeneration\ for\ stream\ 2 \\ T_s(x,0) = T_s\left(x, t_{cycle/2}\right) & At\ the\ beginning\ and\ end\ of\ a\ half\ cycle \end{cases} \quad (15)$$

where, $t_{cycle/2}$ is half cycle time. The derivation method of the parameters used in the above governing equations are summarized in Table 1.

Table 1. Derivation of used parameters in the governing equations

Parameter	Formula
ω	$0.622\ RH\ P_{sat}/(P_{atm} - RH\ P_{sat})$ [93]
$Nu_{q,lam}$(isoflux)	4.36 [91]
$Nu_{T,lam}$(isothermal)	3.66 [91]
$Nu_{avg,lam}$	$(Nu_{T,lam} + Nu_{q,lam})/2$
h	$Nu_{avg,lam}k_a/H$
h_m	$h/\rho c_p$ [91]

To develop a generalized solution for various conditions and geometries, proper dimensionless parameters should be defined, which are listed in Table 2:

Table 2. Definition of the dimensionless variables and parameters used in the analytical solution with the respective order of magnitude

Variable or Parameter	Formula	Order of magnitude
Dimensionless time	$\tau = \frac{t}{t_{cycle/2}}$	1
Dimensionless temperature	$\theta = \frac{T - T_{a2,in}}{T_{a1,in} - T_{a2,in}} = \frac{T - T_{a2,in}}{\Delta T}$	1
Dimensionless humidity ratio	$\Omega = \frac{\omega - \omega_{a2,in}}{\omega_{a1,in} - \omega_{a2,in}} = \frac{\omega - \omega_{a2,in}}{\Delta\omega}$	1

Rate of change in uptake with dimensionless temperature	$S_\theta = \frac{\partial W_d(\tau)}{\partial \theta_{d,avg}(\tau)}$	-
Rate of change in uptake with dimensionless humidity ratio	$S_\Omega = \frac{\partial W_{d,avg}(\tau)}{\partial \Omega_{d,avg}(\tau)}$	0.1
Convection heat/mass transfer rate in air over heat/mass carried by air mass flow (advection)	$S_1 = \frac{h\,L}{u_{avg}\,\rho_a c_{P,a} H} = \frac{h_m\,L}{u_{avg}\,H}$	1
Adsorption heat generation over heat stored in desiccant layer	$S_2 = \frac{h_{ad}\rho_a h_m\,\Delta\omega\,t_{cycle/2}}{\rho_d c_{P,d}\delta_d\,\Delta T}$	10
Amount of heat transferred from air to desiccant over thermal inertia of desiccant layer	$S_3 = \frac{h\,t_{cycle/2}}{\rho_d c_{P,d}\delta_d}$	10
Amount of heat transferred from substrate to desiccant layer over thermal inertia of desiccant layer	$S_4 = \frac{2k_d\,t_{cycle/2}}{\rho_d c_{P,d}\delta_d^2}$	10^4
Amount of mass transferred from air to desiccant over mass of desiccant layer	$S_5 = \frac{\rho_a h_m \Delta\omega t_{cycle/2}}{\rho_d \delta_d}$	0.01
Amount of heat transferred from substrate to desiccant layer over thermal inertia of substrate	$S_6 = \frac{2k_d\,t_{cycle/2}}{\rho_s c_{P,s}\delta_s\delta_d}$	10^6

By averaging the above equations over the length of the IsoHMX (axial direction) ($\frac{1}{\mathrm{L}} * \int_0^L dx$) and introducing the dimensionless variables listed in Table 2, the following equations are obtained:

- Energy balance in CV_1 & CV_5

$$\left(\theta_{a1,out}(\tau) - \theta_{a1,in}\right) = S_1\left(\theta_{d1,avg}(\tau) - \theta_{a1,avg}(\tau)\right) \quad (16)$$

$$\left(\theta_{a2,out}(\tau) - \theta_{a2,in}\right) = S_1 \left(\theta_{d2,avg}(\tau) - \theta_{a2,avg}(\tau)\right) \tag{17}$$

- Mass balance in CV_1 & CV_5

$$\left(\Omega_{a1,out}(\tau) - \Omega_{a1,in}\right) = S_1 \left(\Omega_{d1,avg}(\tau) - \Omega_{a1,avg}(\tau)\right) \tag{18}$$

$$\left(\Omega_{a2,out}(\tau) - \Omega_{a2,in}\right) = S_1 \left(\Omega_{d2,avg}(\tau) - \Omega_{a2,avg}(\tau)\right) \tag{19}$$

- Energy balance in CV_2 & CV_4

$$\frac{\partial \theta_{d1,avg}(\tau)}{\partial \tau} = S_2 \left(\Omega_{a1,avg}(\tau) - \Omega_{d1,avg}(\tau)\right) + S_3 \left(\theta_{a1,avg}(\tau) - \theta_{d1,avg}(\tau)\right) + S_4 \left(\theta_{s,avg}(\tau) - \theta_{d1,avg}(\tau)\right) \tag{20}$$

$$\frac{\partial \theta_{d2,avg}(\tau)}{\partial \tau} = S_2 \left(\Omega_{a2,avg}(\tau) - \Omega_{d2,avg}(\tau)\right) + S_3 \left(\theta_{a2,avg}(\tau) - \theta_{d2,avg}(\tau)\right) + S_4 \left(\theta_{s,avg}(\tau) - \theta_{d2,avg}(\tau)\right) \tag{21}$$

- Mass balance in CV_2 & CV_4

$$S_\theta \frac{\partial \theta_{d1,avg}(\tau)}{\partial \tau} + S_\Omega \frac{\partial \Omega_{d1,avg}(\tau)}{\partial \tau} = S_5 \left(\Omega_{a1,avg}(\tau) - \Omega_{d1,avg}(\tau)\right) \tag{22}$$

$$S_\theta \frac{\partial \theta_{d2,avg}(\tau)}{\partial \tau} + S_\Omega \frac{\partial \Omega_{d2,avg}(\tau)}{\partial \tau} = S_5 \left(\Omega_{a2,avg}(\tau) - \Omega_{d2,avg}(\tau)\right) \tag{23}$$

- Energy balance in CV_3

$$\frac{\partial \theta_{s,avg}(\tau)}{\partial \tau_r} = S_6 \left(\theta_{d1,avg}(\tau) + \theta_{d2,avg}(\tau) - 2\theta_{s,avg}(\tau)\right) \tag{24}$$

The above system of equations needs five initial values. As it was mentioned, considering the cyclic nature of the IsoHMX operation in one half cycle, five initial conditions for $\Omega_{d1,avg}$, $\Omega_{d2,avg}$, $\theta_{d1,avg}$, $\theta_{d2,avg}$, and $\theta_{s,avg}$ could be obtained as follows:

$$\begin{cases} \Omega_{d1,avg}(0) = \Omega_{d2,avg}(1) & At\ the\ beginning\ of\ process\ for\ stream\ 1 \\ \Omega_{d1,avg}(1) = \Omega_{d2,avg}(0) & At\ the\ beginning\ of\ regeneration\ for\ stream\ 2 \\ \theta_{d1,avg}(0) = \theta_{d2,avg}(1) & At\ the\ beginning\ of\ process\ for\ stream\ 1 \\ \theta_{d1,avg}(1) = \theta_{d2,avg}(0) & At\ the\ beginning\ of\ regeneration\ for\ stream\ 2 \\ \theta_{s,avg}(0) = \theta_{s,avg}(1) & At\ the\ beginning\ and\ end\ of\ a\ half\ cycle \end{cases} \quad (25)$$

Before solving these sets of equations, it should be noted that in integrating the equations, S_θ and S_Ω are treated as constant values, which results in no error in the solution; This claim is verified in Section 0. The following steps are taken to make the equations into a simpler form:

Performing a scale analysis on Eq.(24) will result in:

$$\left(\theta_{d1,avg}(\tau) + \theta_{d2,avg}(\tau) - 2\theta_{s,avg}(\tau)\right) \propto O\left(\frac{1}{S_6}\right)\frac{\partial\theta_{s,avg}(\tau)}{\partial\tau} \approx O(10^{-6}) \quad (26)$$

So, even with a huge temperature jump in the substrate (which is not the case), it can be concluded that:

$$\theta_{s,avg}(\tau) \approx \left(\theta_{d1,avg}(\tau) + \theta_{d2,avg}(\tau)\right)/2 \quad (27)$$

Eq.(20) shows that the rate of change in desiccant layer temperature is equal to the right-hand side. The physics of the problem shows that neither of the terms on the right-hand side are trivial. So, replacing $\theta_{s,avg}$ with Eq.(27) in Eq.(20) and running a scale analysis on the right-hand side will lead to:

$$\left(\theta_{d2,avg}(\tau) - \theta_{d1,avg}(\tau)\right) \propto O\left(\frac{S_2\Delta\Omega}{S_4} + \frac{S_3\Delta\theta}{S_4}\right) \approx O(10^{-3}) \quad (28)$$

This indicates that at any given time, the average temperature of desiccant on both sides, as well as the substrate's average temperature (Eq.(27)), are almost identical. Based on this, $\theta_{d1\&2}(\tau)$ is defined as:

$$\theta_{d1\&2}(\tau) = \theta_{s,avg}(\tau) \approx \theta_{d1,avg}(\tau) \approx \theta_{d2,avg}(\tau) \quad (29)$$

**** Note on Eq.(29)***(34)***:*** Thermal contact resistance (TCR) between metal surface and adsorbent varies between 1.3 to 3.8 (K/W) [94]. Adding the effect of the TCR will result to a negligible temperature difference (less than 0.5 °C) between substrate and coating layer.

Based on Eq.(29), rewriting Eq.(16)-(23) will lead to:

- The energy balance in CV_1 & CV_5

$$\left(\theta_{a1,out}(\tau) - \theta_{a1,in}\right) = S_1 \left(\theta_{d1\&2}(\tau) - \theta_{a1,avg}(\tau)\right) \tag{30}$$

$$\left(\theta_{a2,out}(\tau) - \theta_{a2,in}\right) = S_1 \left(\theta_{d1\&2}(\tau) - \theta_{a2,avg}(\tau)\right) \tag{31}$$

- Mass balance in CV_1 & CV_5

$$\left(\Omega_{a1,out}(\tau) - \Omega_{a1,in}\right) = S_1 \left(\Omega_{d1,avg}(\tau) - \Omega_{a1,avg}(\tau)\right) \tag{32}$$

$$\left(\Omega_{a2,out}(\tau) - \Omega_{a2,in}\right) = S_1 \left(\Omega_{d2,avg}(\tau) - \Omega_{a2,avg}(\tau)\right) \tag{33}$$

- Adding up the energy balance in CV_2 & CV_4 *******(see the note below)*

$$\begin{aligned} 2\frac{\partial \theta_{d1\&2}(\tau)}{\partial \tau} = {} & S_2 \left(\Omega_{a1,avg}(\tau) + \Omega_{a2,avg}(\tau) - \Omega_{d1,avg}(\tau) - \Omega_{d2,avg}(\tau)\right) \\ & + S_3 \left(\theta_{a1,avg}(\tau) + \theta_{a2,avg}(\tau) - 2\theta_{d1\&2}(\tau)\right) \end{aligned} \tag{34}$$

- Mass balance in CV_2 & CV_4

$$S_\theta \frac{\partial \theta_{d1\&2}(\tau)}{\partial \tau} + S_\Omega \frac{\partial \Omega_{d1,avg}(\tau)}{\partial \tau} = S_5 \left(\Omega_{a1,avg}(\tau) - \Omega_{d1,avg}(\tau)\right) \tag{35}$$

$$S_\theta \frac{\partial \theta_{d1\&2}(\tau)}{\partial \tau} + S_\Omega \frac{\partial \Omega_{d2,avg}(\tau)}{\partial \tau} = S_5 \left(\Omega_{a2,avg}(\tau) - \Omega_{d2,avg}(\tau)\right) \tag{36}$$

Based on Eq.(29), the initial conditions, i.e., Eq.(25), are rewritten as follows:

$$\begin{cases} \Omega_{d1,avg}(0) = \Omega_{d2,avg}(1) & At\ the\ beginning\ of\ process\ for\ stream\ 1 \\ \Omega_{d1,avg}(1) = \Omega_{d2,avg}(0) & At\ the\ beginning\ of\ regeneration\ for\ stream\ 2 \\ \theta_{d1\&2}(0) = \theta_{d1\&2}(1) & At\ the\ beginning\ of\ process\ for\ stream\ 1 \end{cases} \tag{37}$$

**** Note on Eq.(34):*** By subtracting Eq.(20) from (21), the transient term would have been disappeared and so would have $\theta_{s,avg}(\tau)$. But, on the right-hand side, $S_4\left(\theta_{d2,avg}(\tau)-\theta_{d1,avg}(\tau)\right)$ would have shown up. Based on Eq.(29), at first glance, this term appears to be negligible; But, based on Table 2:

Table 2, S_4 has an order of magnitude of 10e4, and based on Eq.(28), $\left(\theta_{d2,avg}(\tau)-\theta_{d1,avg}(\tau)\right)$ has an order of magnitude 10e-3, so the whole term has order of magnitude 10, which is on par with other terms and can't be neglected. But, if instead of subtracting, we add up Eq.(20) and (21), the term $S_4\left(\theta_{d1,avg}(\tau)+\theta_{d2,avg}(\tau)-2\theta_{s,avg}(\tau)\right)$ appears. Running the same procedure based on Eq.(26) and Table 2, it could easily be shown that this term has an order of magnitude of 10e-2 and could be neglected.

Using the exponential temperature/humidity ratio profile, see Eq.(7) and calculate the average and outlet values will lead to:

$$\theta_{a1(or2),out}(\tau)=\frac{a_{T1(or2)}(\tau)}{\Delta T}\ (exp(-S_1)-1)+\ \theta_{a1(or2),in} \tag{38}$$

$$\theta_{a1(or2),avg}(\tau)=\frac{a_{T1(or2)}(\tau)}{\Delta T}\ (\frac{1}{S_1}-\frac{exp(-S_1)}{S_1}-1)+\ \theta_{a1(or2),in} \tag{39}$$

$$\Omega_{a1(or2),out}(\tau)=\frac{a_{\omega 1(or2)}(\tau)}{\Delta T}\ (exp(-S_1)-1)+\ \Omega_{a1(or2),in} \tag{40}$$

$$\Omega_{a1(or2),avg}(\tau)=\frac{a_{\omega 1(or2)}(\tau)}{\Delta T}\ (\frac{1}{S_1}-\frac{exp(-S_1)}{S_1}-1)+\ \Omega_{a1(or2),in} \tag{41}$$

Replacing these values in Eq.(30)-(33), will result in the following:

$$a_{T1(or2)}=\left(\theta_{a1(or2),in}-\theta_{d1\&2}(\tau)\right)\Delta T \tag{42}$$

$$a_{\omega 1(or2)}=\left(\Omega_{a1(or2),in}-\Omega_{d1(or2),avg}(\tau)\right)\Delta T \tag{43}$$

Replacing these equations in Eq.(7), we have:

$$\theta_{a1(or2),out}(\tau)=A\ \theta_{d1\&2}(\tau)+(1-A)\ \theta_{a1(or2),in} \tag{44}$$

$$\theta_{a1(or2),avg}(\tau) = (1 - \frac{A}{S_1})\theta_{d1\&2}(\tau) + \frac{A}{S_1}\ \theta_{a1(or2),in} \tag{45}$$

$$\Omega_{a1(or2),out}(\tau) = A\ \Omega_{d1\&2}(\tau) + (1 - A)\ \Omega_{a1(or2),in} \tag{46}$$

$$\Omega_{a1(or2),avg}(\tau) = (1 - \frac{A}{S_1})\ \Omega_{d1\&2}(\tau) + \frac{A}{S_1}\ \Omega_{a1(or2),in} \tag{47}$$

Replacing these values in Eqs.(34)-(36):

$$\begin{aligned} 2\frac{\partial\theta_{d1\&2}(\tau)}{\partial\tau} &= \frac{S_2 A}{S_1}\Big(\Omega_{a1,in} + \Omega_{a2,in} - \Omega_{d1,avg}(\tau) - \Omega_{d2,avg}(\tau)\Big) \\ &\quad + \frac{S_3 A}{S_1}\Big(\theta_{a1,in} + \theta_{a2,in} - 2\theta_{d1\&2}(\tau)\Big) \end{aligned} \tag{48}$$

$$S_\theta \frac{\partial\theta_{d1\&2}(\tau)}{\partial\tau} + S_\Omega \frac{\partial\Omega_{d1,avg}(\tau)}{\partial\tau} = \frac{S_5 A}{S_1}\Big(\Omega_{a1,in} - \Omega_{d1,avg}(\tau)\Big) \tag{49}$$

$$S_\theta \frac{\partial\theta_{d1\&2}(\tau)}{\partial\tau} + S_\Omega \frac{\partial\Omega_{d2,avg}(\tau)}{\partial\tau} = \frac{S_5 A}{S_1}\Big(\Omega_{a2,in} - \Omega_{d2,avg}(\tau)\Big) \tag{50}$$

Adding Eq.(49) to (50), we have:

$$\begin{aligned} 2S_\theta \frac{\partial\theta_{d1\&2}(\tau)}{\partial\tau} &+ 2S_\Omega \frac{\partial\Big(\Omega_{d1,avg}(\tau) + \Omega_{d2,avg}(\tau)\Big)}{\partial\tau} \\ &= \frac{S_5 A}{S_1}\Big(\Omega_{a1,in} + \Omega_{a2,in} - \Big(\Omega_{d2,avg}(\tau) + \Omega_{d1,avg}(\tau)\Big)\Big) \end{aligned} \tag{51}$$

From Eq.(48), $\Big(\Omega_{d1,avg}(\tau) + \Omega_{d2,avg}(\tau)\Big)$ could be calculated as:

$$\begin{aligned} &\Omega_{d1,avg}(\tau) + \Omega_{d2,avg}(\tau) = \\ &-2\frac{S_3}{S_2}\frac{\partial\theta_{d1\&2}(\tau)}{\partial\tau} - 2\frac{S_3}{S_2}\theta_{d1\&2}(\tau) + \big(\Omega_{a1,in} + \Omega_{a2,in}\big) + \frac{S_3}{S_2}\big(\theta_{a1,in} + \theta_{a2,in}\big) \end{aligned} \tag{52}$$

Replacing $\Omega_{d1,avg}(\tau) + \Omega_{d2,avg}(\tau)$ with Eq.(52) in Eq.(51) will lead to the following differential equation:

$$\frac{\partial^2\theta_{d1\&2}(\tau)}{\partial\tau^2} + X_1\frac{\partial\theta_{d1\&2}(\tau)}{\partial\tau} + \mathrm{X}_2\theta_{d1\&2}(\tau) = \mathrm{X}_3 \tag{53}$$

In which:

$$\mathrm{X}_1 = \frac{A}{S_1 S_w}(S_3 S_w + S_5 - S_\theta S_2) \tag{54}$$

$$\mathrm{X}_2 = \frac{A}{S_1 S_w}\left(\frac{AS_3 S_5}{S_1}\right) \tag{55}$$

$$\mathrm{X}_3 = X_2\left(\frac{\theta_{a1,in} + \theta_{a2,in}}{2}\right) \tag{56}$$

Solving Eq.(53), we have:

$$\theta_{d1\&2}(\tau) = \mathrm{B}_1\exp(-\lambda_1\tau) + \mathrm{B}_2\exp(-\lambda_2\tau) + \left(\frac{\theta_{a1,in} + \theta_{a2,in}}{2}\right) \tag{57}$$

Where, $B_1$and B_2 are unknown constants and:

$$\lambda_{1,2} = \left(X_{1,j} \pm \sqrt{X_{1,j}^2 - 4X_{2,j}}\right)/2 \tag{58}$$

Replacing $\theta_{d1\&2}$ with Eq.(57) in (52), we have:

$$\begin{aligned}&\Omega_{d1,avg}(\tau) + \Omega_{d2,avg}(\tau) = \\ &\frac{\mathrm{B}_1}{S_2}\left(-S_3 + \frac{\lambda_1 S_1}{A}\right)\exp(-\lambda_1\tau) - \frac{B_2}{S_2}\left(-S_3 + \frac{\lambda_2 S_1}{A}\right)\exp(-\lambda_2\tau) + \left(\Omega_{a1,in} + \Omega_{a2,in}\right)\end{aligned} \tag{59}$$

Based on initial conditions, see Eq.(37), for $\left(\Omega_{d1,avg}(\tau) + \Omega_{d2,avg}(\tau)\right)$, we have:

$$\Omega_{d1,avg}(1) + \Omega_{d2,avg}(1) = \Omega_{d2,avg}(0) + \Omega_{d1,avg}(0) = \Omega_{d1,avg}(0) + \Omega_{d2,avg}(0) \tag{60}$$

Using the finding in Eq.(60) and the third term of initial conditions, Eq.(37), in Eq.(57) and Eq.(59), we have the following set of two linear equations and two unknows, i.e., $B_1$and B_2:

$$\begin{cases} \mathrm{B}_1(1-\exp(-\lambda_1)) + \mathrm{B}_2(1-\exp(-\lambda_2)) = 0 \\ \mathrm{B}_1\left(-\frac{S_3}{S_2}+\frac{\lambda_1 S_1}{AS_2}\right)(1-\exp(-\lambda_1)) - B_2\left(-\frac{S_3}{S_2}+\frac{\lambda_2 S_1}{AS_2}\right)(1-\exp(-\lambda_2)) = 0 \end{cases} \quad (61)$$

Eq.(61) is a homogeneous linear system of equations, and the coefficient determinant is a none zero value, so the only possible solution is:

$$B_1 = B_2 = 0 \quad (62)$$

Applying Eq.(62) into Eq.(57), we have:

$$\theta_{d1\&2}(\tau) = \left(\frac{\theta_{a1,in}+\theta_{a2,in}}{2}\right) = 0.5 \quad (63)$$

Which indicates that the average temperature of the desiccant layers and the substrate are always constant and equal to the average inlet temperatures (or are equal to 0.5 in non-dimensional form). Replacing $\theta_{d1\&2}$ with Eq.(63) in Eq.(49) and (50):

$$\frac{\partial \Omega_{d1,avg}(\tau)}{\partial \tau} + N\,\Omega_{d1,avg}(\tau) - N\,\Omega_{a1,in} = 0 \quad (64)$$

$$\frac{\partial \Omega_{d2,avg}(\tau)}{\partial \tau} + N\,\Omega_{d2,avg}(\tau) - N\,\Omega_{a2,in} = 0 \quad (65)$$

In which:

$$N = \frac{S_5 A}{S_1 S_\Omega} \tag{66}$$

The solution to the differential Eqs.(64) and (65) is:

$$\Omega_{d1,avg}(\tau) = C_1 \exp(-N\tau) + \Omega_{a1,in} \tag{67}$$

$$\Omega_{d2,avg}(\tau) = C_2 \exp(-N\tau) + \Omega_{a2,in} \tag{68}$$

where, $C_1$and C_2 are unknown constants. Applying the initial conditions, Eq.(37), will lead to the following set of two linear equations and two unknows, i.e., $C_1$and C_2:

$$\begin{cases} C_1 \exp(-N) + \Omega_{a1,in} = C_2 + \Omega_{a2,in} \\ C_1 + \Omega_{a1,in} = C_2 \exp(-N) + \Omega_{a2,in} \end{cases} \tag{69}$$

Solving this set of equations, we have:

$$\begin{cases} C_1 = \dfrac{\Omega_{a2,in} - \Omega_{a1,in}}{1 + \exp(-N)} \\ C_2 = \dfrac{\Omega_{a1,in} - \Omega_{a2,in}}{1 + \exp(-N)} \end{cases} \tag{70}$$

Thus, the temperature and humidity ratio of the desiccant layer is found. Based on the findings and by replacing them in Eq.(44) and Eq.(46), the temperature and humidity ratio for the outlet air could be calculated. A general form of the final solution for the dimensionless desiccant temperature, outlet air temperature, desiccant humidity ratio, and outlet air humidity ratio are shown in Eq.(71)-Eq.(74), respectively, and the constants are listed in

Table 3.

$$\theta_{d1(or2),avg}(\tau) = \frac{\left(\theta_{a1,in} + \theta_{a2,in}\right)}{2} = 0.5 \tag{71}$$

$$\theta_{a1(or2),out}(\tau) = \frac{A}{2}\theta_{a2(or1),in} + \left(1 - \frac{A}{2}\right)\theta_{a1(or2),in} \tag{72}$$

$$\Omega_{d1(or2),avg}(\tau) = \frac{\left(\Omega_{a2(or1),in} - \Omega_{a1(or2),in}\right)}{1 + exp\ (-N)} exp(-N\tau) + \Omega_{a1(or2),in} \tag{73}$$

$$\Omega_{a1(or2),out}(\tau) = A\ \frac{\left(\Omega_{a2(or1),in} - \Omega_{a1(or2),in}\right)}{1 + exp\ (-N)} exp(-N\tau) + \Omega_{a1(or2),in} \tag{74}$$

Table 3. List of constants in the final solution of outlet air temperature

Formula	Order of magnitude
$A = (1 - \exp(-S_1))$	1

$N = \frac{A\ S_5}{S_\Omega\ S_1}$	0.1
$S_\Omega = C_{slope}\ 8 \times 10^{-12} \Delta\omega\ P_{tot} \exp\left(\frac{5356.5}{273.15 + \Delta T\ \theta_{d1\&2} + T_{a2,in}}\right)$	0.1

7.1.2 Performance metrics closed-form solution

A closed-form solution for the MRC^* and $the\ DCOP_{IsoHMX}$ can be described based on the non-dimensional solution as:

$$MRC^* = \frac{3600}{t_{cycle}} \int_0^{t_{cycle/2}} \dot{m}_{\mathrm{a}} \left(\omega_{a,out} - \omega_{a,in}\right) dt$$

$$= 1.8 \times 10^3 \rho_a u \Delta\omega \int_0^1 \left(\Omega_{a1,in} - \Omega_{a1,out}\right) d\tau \tag{75}$$

$$= 1.8 \times 10^3 \frac{A}{N} \rho_a u \Delta\omega \frac{\left(1 - exp(-N)\right)}{(1 + \exp(-N))}$$

$$DCOP_{IsoHMX} = \frac{\dot{Q}_{lat}}{\dot{Q}_{reg}} = \frac{\frac{1}{t_{cycle}} \int_0^{t_{cycle/2}} h_{ad} \dot{m}_{ads} dt}{\frac{1}{t_{cycle}} \int_0^{t_{cycle/2}} \dot{m}_{air} c_{p,a} (T_{a1,in} - T_{a2,out}) dt}$$

$$= \frac{h_{ad} \frac{MRC}{3.6 \times 10^3}}{\int_0^1 \dot{m}_{air} c_{p,a} \Delta T \left(\theta_{a1,in} - \theta_{a1,out}\right) d\tau} \tag{76}$$

$$= \frac{2S_2}{NS_3} \frac{\left(1 - exp(-N)\right)}{(1 + exp(-N))}$$

7.1.3 Uptake derivatives with time

As mentioned, it's claimed that treating S_θ and S_Ω as constants, will result in no errors. As it could be seen from the solution, $\theta_d$is constant so its time derivative is equal to zero. Thus, S_θ is omitted from the calculations and taking it as a constant has no effect on the results. In the following, it's shown that a constant desiccant temperature will result in constant S_Ω and this will validate the claim.

The equilibrium humidity ratio as it was shown in Section 3.1.2.1 is governed by the following isotherm relationship:

$$W_d = W_{eq} = 1.39 \exp\left(-0.069\left((T-273)ln\left(\frac{p_{sat}}{p}\right)\right)^{0.52}\right) \tag{77}$$

In which, W_{eq} is the equilibrium uptake, p is the equilibrium vapor pressure over the desiccant and p_{sat} is the vapor saturation pressure in the desiccant temperature. Figure 7 illustrates Eq.(77) and its linear correlation. Using this correlation will result in error if the working range of the system is located at the second half of the curve. So, a piecewise linear correlation is needed for the different working ranges; Generally, each part of the fitted linear piecewise function could be described as:

$$W_d \approx C_{slope}\, RH + C_{intercept} = C_s\, \frac{p}{p_{sat}} + C_i \tag{78}$$

In which, C_{slope} and $C_{intercept}$ are the slope and intercept of the fitted line which could be calculated based on the working range of the system.

Using the experimental data of TGA test, the following linear piecewise function was fitted to the data:

$$W_d = \begin{cases} C_s = 0.92 \;\; C_i = 0.06 & @\ \dfrac{p}{p_{sat}} < 0.4 \\ C_s = 0.64 \;\; C_i = -0.13 & @\ 0.4 < \dfrac{p}{p_{sat}} < 0.65 \\ C_s = 1.51 \;\; C_i = -0.43 & @\ \dfrac{p}{p_{sat}} > 0.65 \end{cases} \tag{79}$$

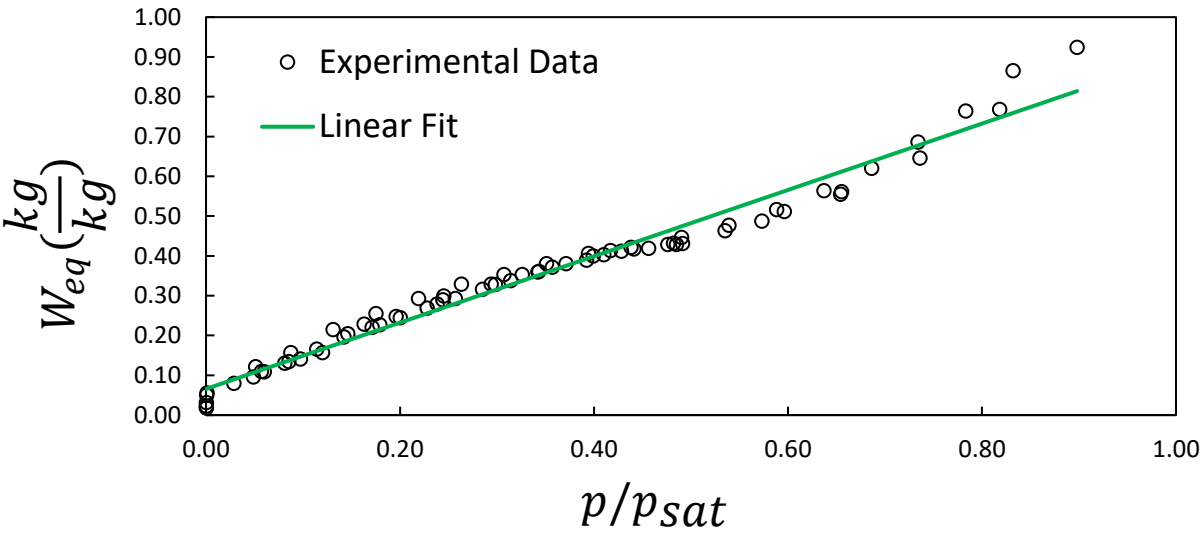

Figure 7. Equilibrium Water uptake (W_{eq}) vs the equilibrium relative humidity of the desiccant

The equilibrium vapor pressure over the total pressure (p_{tot}) could be calculated from the following [93]:

$$\frac{p}{p_{tot}} = \frac{\omega_d}{0.621 + \omega_d} \approx 1.6\,\omega_d \tag{80}$$

Vapor saturation pressure could be expressed as [93]:

$$\begin{aligned} p_{sat} &= 10^{\left(8.07131 - \frac{1730.63}{233.426 + T_d}\right)} \times 133.3 \\ \Rightarrow \quad \frac{1}{p_{sat}} &\approx 5 \times 10^{-12} \exp\left(\frac{5356.5}{273.15 + T_d}\right) \end{aligned} \tag{81}$$

Replacing p/p_{tot} and $1/p_{sat}$ with Eq.(80) and Eq.(81) in Eq.(78) will result in the following:

$$\begin{aligned} W_d &\approx C_{slope}\, 8 \times 10^{-12} \omega_d p_{tot} \exp\left(\frac{5356.5}{273.15 + T_d}\right) + C_{intercept} \\ &= C_{slope}\, 8 \times 10^{-12} (\Omega_d \Delta\omega + \omega_{a1,in})\, p_{tot} \exp\left(\frac{5356.5}{273.15 + T_d}\right) + C_{intercept} \end{aligned} \tag{82}$$

Based on Eq.(82), S_Ω is calculated:

$$S_\Omega = \frac{\partial W_{d1(or2),avg}(\tau)}{\partial \Omega_{d1(or2),avg}(\tau)} \approx C_{slope}\, 8 \times 10^{-12} \Delta\omega\, p_{tot} \exp\left(\frac{5356.5}{273.15 + \Delta T\, \theta_{d1\&2} + T_{a2,in}}\right) \tag{83}$$

With respect to that, $\theta_{d1\&2}$ is constant. Eq.(83) shows that S_Ω is also constant.

7.1.4 Analytical model validation with experimental data

The analytical model DCOP and MRC* was verified with experimental data over different conditions, explained in section 3.3. The maximum difference between the data and analytical model for the MRC* and DCOP are 10%, see Figure 8.

Measured data and model are compared in a graph brought in Figure 8. As it can be seen for the DCOP, the model falls between +10% and – 5% of experimental data and for the MRC* in ±10%.

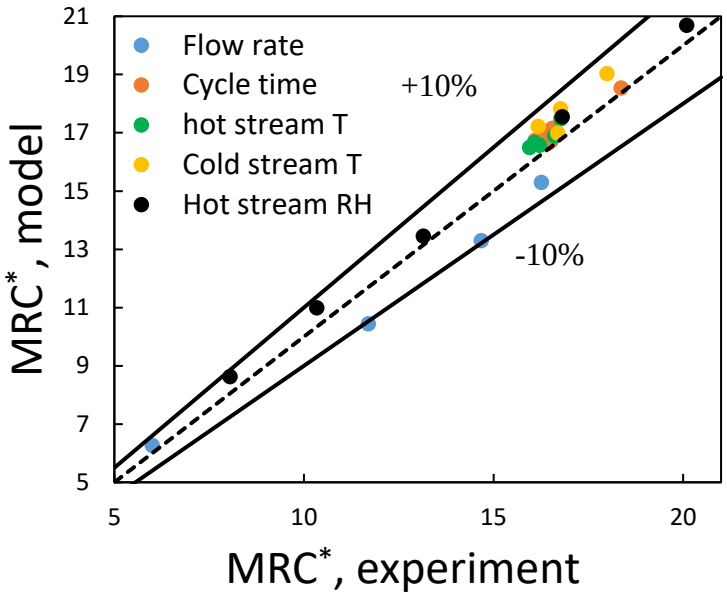

a)

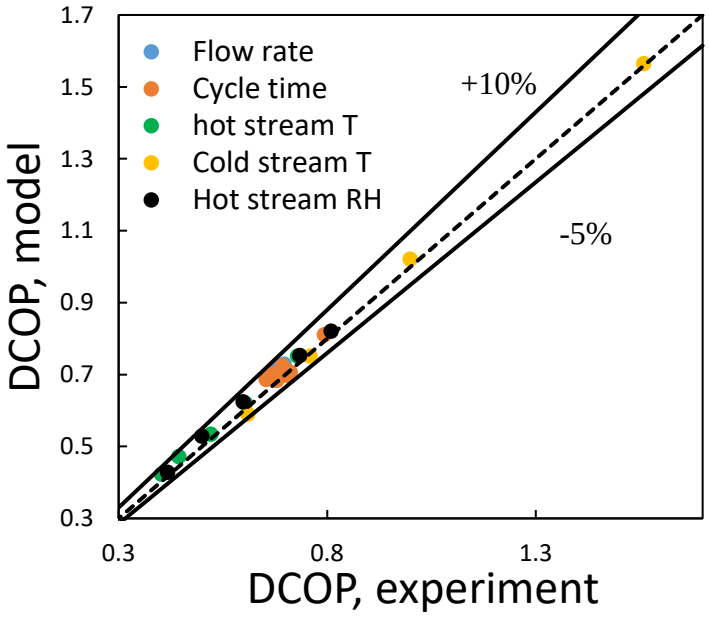

b)

Figure 8. a) MRC* and b) DCOP analytical solution validation with experimental data

7.2 Numerical simulation

The numerical work of this study is based on an already existing MATLAB[95] code for desiccant wheel dehumidification, which was developed and validated by measurements in our lab by former students [96]. The mentioned code was enhanced and changed to be able to simulate the IsoHMX. Enhancements that are included: make the code faster, validate for a wider range of conditions, and make it more robust mostly by changing discretization method explained at the following.

The same geometry and control volume for the analytical model (except for substrate) is used for the numerical simulation, see Figure 9. The control volume for the substrate has a width of dx and height of dy.

It should be noted that the analytical model needed more assumptions to simplify the problem so it would be solved.

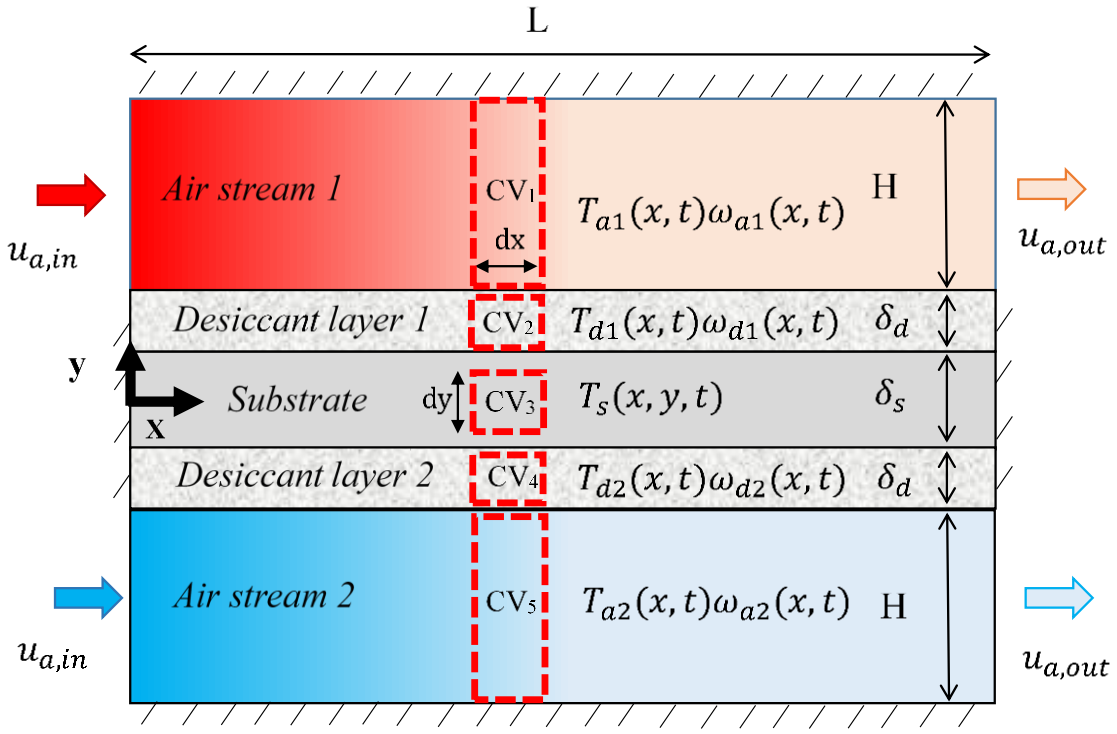

Figure 9. A sectional schematic view of the IsoHMX calculation domain and selected control volumes for the numerical simulation

The following assumptions are made for the simulation:

- The thermophysical properties for the air, substrate, and desiccant layer are assumed constant;
- The air stream is assumed to be fully-developed over the heat/mass exchanger. Therefore, the heat and mass transfer coefficients are considered constant over time;
- The axial heat conduction in the air stream and desiccant layer are considered negligible;
- As the desiccant layer is thin (less than 0.3mm [89]), the averaged properties in the y-direction are used, namely, $T_d(x,t), \omega_d(x,t)$ [90];
- There is no condensation happening in the system; and
- Both equilibrium and liner driving force (LDF) were considered for adsorption kinetics and results were compared.

7.2.1 Governing equations

Based on the above assumptions, the heat and mass transfer equations with equilibrium assumption could be described as follows:

Energy and mass balance in CV_1

$$\frac{\partial T_{a1}(x,t)}{\partial t} + u_{avg}\frac{\partial T_{a1}(x,t)}{\partial x} = \frac{1}{\rho_a c_{P,a}\mathrm{H}} h\big(T_{d1}(x,t) - T_{a1}(x,t)\big) \tag{84}$$

$$\frac{\partial \omega_{a1}(x,t)}{\partial t} + u_{avg}\frac{\partial \omega_{a1}(x,t)}{\partial x} = \frac{1}{H} h_m\big(\omega_{d1}(x,t) - \omega_{a1}(x,t)\big) \tag{85}$$

The same set of equations is defined for **CV_5**.

$$\frac{\partial T_{a2}(x,t)}{\partial t} + u_{avg}\frac{\partial T_{a2}(x,t)}{\partial x} = \frac{1}{\rho_a c_{P,a}\mathrm{H}} h\big(T_{d2}(x,t) - T_{a2}(x,t)\big) \tag{86}$$

$$\frac{\partial \omega_{a2}(x,t)}{\partial t} + u_{avg}\frac{\partial \omega_{a2}(x,t)}{\partial x} = \frac{1}{H} h_m\big(\omega_{d2}(x,t) - \omega_{a2}(x,t)\big) \tag{87}$$

With the following boundary conditions for both control volumes:

$$\begin{cases} @x = 0 \ : T_a = T_{a,in}\,, \omega_a = \omega_{a,in} \\ @\ x = L: \dfrac{\partial T_a}{\partial x} = \dfrac{\partial \omega_a}{\partial x} = 0 \end{cases} \tag{88}$$

Energy and mass balance in CV_2

$$\begin{aligned} \rho_d c_{P,d} \delta_d \frac{\partial T_{d1}(x,t)}{\partial t} \\ = h_{ad} \rho_a h_m \big(\omega_{a1}(x,t) - \omega_{d1}(x,t)\big) + h\big(T_{a1}(x,t) - T_{d1}(x,t)\big) \\ + 2k_d/\delta_d \big(T_s(x, \delta_s/2, t) - T_{d1}(x,t)\big) \end{aligned} \tag{89}$$

$$\frac{\partial W_{d1}(x,t)}{\partial T_{d1}(x,t)} \frac{\partial T_{d1}(x,t)}{\partial t} + \frac{\partial W_{d1}(x,t)}{\partial \omega_{d1}(x,t)} \frac{\partial \omega_{d1}(x,t)}{\partial t} = \frac{\rho_a}{\rho_d \delta_d} h_m \big(\omega_{a1}(x,t) - \omega_{d1}(x,t)\big) \tag{90}$$

The same set of equations is defined for **CV_4**:

$$\begin{aligned} \rho_d c_{P,d} \delta_d \frac{\partial T_{d2}(x,t)}{\partial t} \\ = h_{ad} \rho_a h_m \big(\omega_{a2}(x,t) - \omega_{d2}(x,t)\big) + h\big(T_{a2}(x,t) - T_{d2}(x,t)\big) \\ + 2k_d/\delta_d \big(T_s(x, -\delta_s/2, t) - T_{d2}(x,t)\big) \end{aligned} \tag{91}$$

$$\frac{\partial W_{d2}(x,t)}{\partial T_{d2}(x,t)} \frac{\partial T_{d2}(x,t)}{\partial t} + \frac{\partial W_{d2}(x,t)}{\partial \omega_{d2}(x,t)} \frac{\partial \omega_{d2}(x,t)}{\partial t} = \frac{\rho_a}{\rho_d \delta_d} h_m \big(\omega_{a2}(x,t) - \omega_{d2}(x,t)\big) \tag{92}$$

Energy balance in CV_3

$$\frac{\partial T_s(x,t)}{\partial t} = \alpha_s \left(\frac{\partial^2 T_s(x,y,t)}{\partial x^2} + \frac{\partial^2 T_s(x,y,t)}{\partial y^2}\right) \tag{93}$$

With the following boundary conditions:

$$\begin{cases} @\ y = \delta_s \ : -k_s \dfrac{\partial T_s(x,y,t)}{\partial y} = \dfrac{2k_d}{\delta_d T_{d1}(x,t)} \\ @\ y = -\delta_s : -k_s \dfrac{\partial T_s(x,y,t)}{\partial y} = 2k_d/\delta_d T_{d2}(x,t) \\ @\ x = 0\,, L: \dfrac{\partial T_s}{\partial x} = 0 \end{cases} \tag{94}$$

The aforementioned governing equations for the air and desiccant, i.e., CVs 1, 2, 4, and 5, are discretized into finite difference equations by an explicit, forward difference method in time and the backward difference method in space. Even the central method for space discretization is a better approximation than the backward method. It should be noted that this is a transient simulation and physically speaking, in the air stream, most of the data is coming from the upstream and there is no derivative of space for the desiccant, so, backward discretization for space for the air stream resulted in a more robust code. The 2D heat conduction equation in CV_3, is discretized into finite difference equation by the explicit, forward difference method in time and a second-order central difference method in space.

All of the simulations are performed with a grid of 10 for space in *x*, and 4 in the *y* direction. The grid independence has been proven to be valid within a tolerable limit. A cyclic steady state is obtained within 100 cycles.

In 2D heat conduction simulation, see Eq.(88), there is a limitation for the Fourier number i.e., diffusivity multiplied by the ratio of time step over the grid size in both *x* and *y* direction[91]:

$$Fo = \frac{\alpha_s \, dt}{dx^2 (or \; dy^2)} < \frac{1}{2} \tag{95}$$

The default value for the time step in the code is 5ms. This value is iteratively updated at the beginning of the code to meet the requirement in Eq.(95).

The code is included in Appendix A: MATLAB code.

7.2.2 Numerical model validation with experimental data

The numerical code was validated against the experimental data and other existing desiccant wheel data from references[97]. The measured data and numerical model are compared in a graph brought in Figure 10. As it can be seen for the DCOP, the model falls between ±7% of experimental data and for the MRC*, in +6% and -5%.

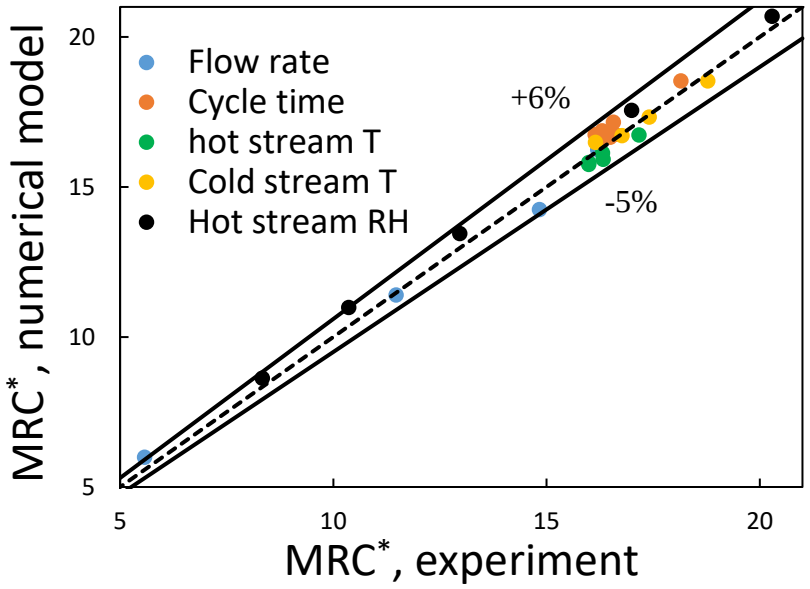

a)

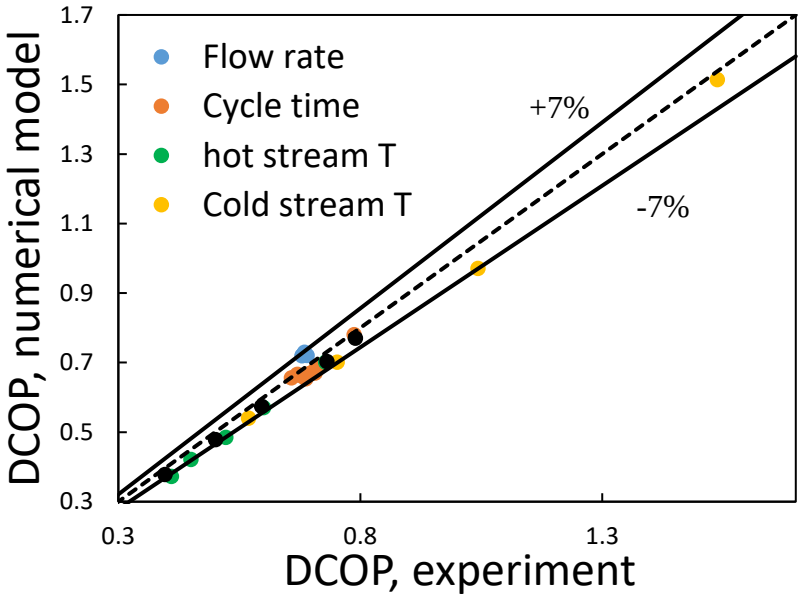

b)

Figure 10. a) MRC* and b) DCOP analytical solution validation with experimental data

7.3 Conclusion

A closed-form analytical model and a numerical model to predict the performance of IsoHMX is developed and has shown good agreement with the experimental data. The calculated DCOP for analytical model falls between +10% and – 5% of experimental data and for the MRC^* in ±10%. For the numerical model, the DCOP falls between ±7% of the experimental data and for the MRC^*, in +6% and -5%.

The numerical code is more accurate but takes time to converge and for optimization and real time control using such a model is not applicable. On the other hand, the analytical model is a closed-form, which can be easily used for optimization and real time control applications.

Experimental work , an experimental test bed was built to test the performance of the IsoHMX with other desiccant-based dehumidification systems. In order to achieve this, two samples were made, one with aluminum substrate and one with acrylic substrate. The sample with aluminum substrate delivers heat from the adsorption to desorption part and represents the IsoHMX and the sample with acrylic substrate represents a typical desiccant-based system. The two systems were compared under different inlet temperatures, relative humidity and flow rate and different cycle times.

The experimental results showed that using aluminum will increase both the water removal capacity (MRC^*) and the dehumidification coefficient of performance (DCOP).

In Chapter 2.Modeling, analytical and numerical modeling of the IsoHMX was studied. Both models showed a very good agreement with the experimental results, but as every other numerical modeling, the code takes time to converge and it is not a suitable tool for optimization and real time control. So, a closed-form analytical solution was developed to predict the performance of the IsoHMX.

In Chapter 4.Optimization study, with the help of the closed-form analytical solution, an optimized design of the IsoHMX was found using a multi-objective genetic algorithm. The study showed that this design is independent of the inlet temperature and relative humidity.

In Chapter 5.Performance Evaluation, performance of the optimized IsoHMX is compared to a commercial desiccant wheel, i.e., desiccant wheel model no. WSG 965*200 from NovelAire Technologies. This comparison is done over different inlet temperature and relative humidity.

The results showed that the IsoHMX is more energy efficient, i.e., it has an order of magnitude higher DCOP, and the WSG 965*200 desiccant wheel has more capacity to remove the water, i.e., its MRC^* is almost double of IsoHMX.

7.4 Future work

The following future work is suggested to further improve the work carried out in this thesis:

- Building a prototype: A prototype of the counter-cross/cross flow IsoHMX should be built and tested in the lab under different temperatures and relative humidity. This protype should then be tested in a real greenhouse;

- Enhancement of the system, including: Optimizing the channel geometry and enhance convective mass transfer, looking for other lightweight highly conductive material like graphite as the substrate, optimizing the coating material and enhance the performance

- Real time control system: A control system based on the closed-form analytical solution should be developed. This system should get feedback from the temperature and relative humidity sensors and adjust the flow rate using a variable speed fan;

- Experimental study on the effect of condensation: In extreme conditions, i.e., high humidity inside the greenhouse and cold outside temperature, there is a chance of condensation. Studying these phenomena need modifications in the test bed and should be further studied;

- Include condensation in modeling: The prediction of condensation and its effects on the performance of the system should be included in both numerical and analytical modeling; and

- Use this idea for other applications: The basic idea of the IsoHMX, which is using a conductive substrate, could be applied and used in other applications such as in air water generating systems.

References

[1] "Residential Sector Canada Table 2: Secondary Energy Use and GHG Emissions by End-Use | Natural Resources Canada." https://oee.nrcan.gc.ca/corporate/statistics/neud/dpa/showTable.cfm?type=CP&sector=res&juris=ca&rn=2&page=4 (accessed Dec. 09, 2020).

[2] M. Orme, "Estimates of the energy impact of ventilation and associated financial expenditures," *Energy Build*, vol. 33, no. 3, pp. 199–205, Feb. 2001, doi: 10.1016/S0378-7788(00)00082-7.

[3] P. Nejat, F. Jomehzadeh, M. M. Taheri, M. Gohari, and M. Z. Muhd, "A global review of energy consumption, CO2 emissions and policy in the residential sector (with an overview of the top ten CO2 emitting countries)," *Renewable and Sustainable Energy Reviews*, vol. 43. Elsevier Ltd, pp. 843–862, Mar. 01, 2015. doi: 10.1016/j.rser.2014.11.066.

[4] M. Justo Alonso, P. Liu, H. M. Mathisen, G. Ge, and C. Simonson, "Review of heat/energy recovery exchangers for use in ZEBs in cold climate countries," *Building and Environment*, vol. 84. Elsevier Ltd, pp. 228–237, Jan. 01, 2015. doi: 10.1016/j.buildenv.2014.11.014.

[5] T. Kovesi *et al.*, "Indoor air quality and the risk of lower respiratory tract infections in young Canadian Inuit children," *CMAJ*, vol. 177, no. 2, pp. 155–160, Jul. 2007, doi: 10.1503/cmaj.061574.

[6] ASHRAE, "ASHRAE 62.1-2015 Ventilation for Acceptable Indoor Air Quality."

[7] B. Grace and R. Zentner, "Energy Consumption in the Canadian Agricultural and Food Sector," 1998.

[8] "No Title." https://www.statcan.gc.ca/

[9] B. Wong, L. McClung, D. McClenahan, A. Snijders, and J. Thornton, "The application of aquifer thermal energy storage in the Canadian greenhouse industry," *Acta Hortic*, vol. 893, pp. 437–444, Apr. 2011, doi: 10.17660/ActaHortic.2011.893.42.

[10] J. B. Campen, F. L. K. Kempkes, and G. P. A. Bot, "Mechanically controlled moisture removal from greenhouses," *Biosyst Eng*, vol. 102, no. 4, pp. 424–432, Apr. 2009, doi: 10.1016/j.biosystemseng.2009.01.001.

[11] M. Farooq, A. Wahid, N. Kobayashi, D. Fujita, and S. M. A. Basra, “Plant drought stress: Effects, mechanisms and management,” *Agronomy for Sustainable Development*, vol. 29, no. 1. Springer, pp. 185–212, Jan. 2009. doi: 10.1051/agro:2008021.

[12] E. Chantoiseau, C. Migeon, G. Chasseriaux, and P. E. Bournet, “Heat-pump dehumidifier as an efficient device to prevent condensation in horticultural greenhouses,” *Biosyst Eng*, vol. 142, pp. 27–41, 2016, doi: 10.1016/j.biosystemseng.2015.11.011.

[13] J. B. Campen, G. P. A. Bot, and H. F. De Zwart, “Dehumidification of Greenhouses at Northern Latitudes,” *Biosyst Eng*, vol. 86, no. 4, pp. 487–493, 2003, doi: 10.1016/j.biosystemseng.2003.08.008.

[14] A. Vadiee and V. Martin, “Energy management in horticultural applications through the closed greenhouse concept, state of the art,” *Renewable and Sustainable Energy Reviews*, vol. 16, no. 7. Pergamon, pp. 5087–5100, Sep. 01, 2012. doi: 10.1016/j.rser.2012.04.022.

[15] D. W. Hand, “EFFECTS OF ATMOSPHERIC HUMIDITY ON GREENHOUSE CROPS,” *Acta Hortic*, no. 229, pp. 143–158, Dec. 1988, doi: 10.17660/actahortic.1988.229.12.

[16] R. R. Shamshiri, J. W. Jones, K. R. Thorp, D. Ahmad, H. C. Man, and S. Taheri, “Review of optimum temperature, humidity, and vapour pressure deficit for microclimate evaluation and control in greenhouse cultivation of tomato: a review,” *Int. Agrophys*, vol. 32, pp. 287–302, 2018, doi: 10.1515/intag-2017-0005.

[17] E. Cuce, D. Harjunowibowo, and P. M. Cuce, “Renewable and sustainable energy saving strategies for greenhouse systems: A comprehensive review,” *Renewable and Sustainable Energy Reviews*, vol. 64. Elsevier Ltd, pp. 34–59, Oct. 01, 2016. doi: 10.1016/j.rser.2016.05.077.

[18] G. Li, L. Tang, X. Zhang, J. Dong, and M. Xiao, “Factors affecting greenhouse microclimate and its regulating techniques: A review,” in *IOP Conference Series: Earth and Environmental Science*, Jul. 2018, vol. 167, no. 1, p. 012019. doi: 10.1088/1755-1315/167/1/012019.

[19] M. Chand Singh *et al.*, “A Review of Three Commonly Used Techniques of Controlling Greenhouse Microclimate,” *Int J Curr Microbiol Appl Sci*, vol. 7, no. 1, pp. 3491–3505, Jan. 2018, doi: 10.20546/ijcmas.2018.701.411.

[20] Guillermo De la Torre-Gea, “Computational fluid dynamics in greenhouses: A review,” *Afr J Biotechnol*, vol. 10, no. 77, Dec. 2011, doi: 10.5897/AJB10.2488.

[21] B. Mohammadi, F. Ranjbar, and Y. Ajabshirchi, “Exergoeconomic analysis and multi-objective optimization of a semi-solar greenhouse with experimental validation,” *Appl Therm Eng*, vol. 164, p. 114563, Jan. 2020, doi: 10.1016/j.applthermaleng.2019.114563.

[22] E. Romantchik, E. Ríos, E. Sánchez, I. López, and J. R. Sánchez, “Determination of energy to be supplied by photovoltaic systems for fan-pad systems in cooling process of greenhouses,” *Appl Therm Eng*, vol. 114, pp. 1161–1168, Mar. 2017, doi: 10.1016/j.applthermaleng.2016.10.011.

[23] M. Amani, S. Foroushani, M. Sultan, and M. Bahrami, “Comprehensive review on dehumidification strategies for agricultural greenhouse applications,” *Appl Therm Eng*, vol. 181, p. 115979, Nov. 2020, doi: 10.1016/j.applthermaleng.2020.115979.

[24] F. J. Baptista, B. J. Bailey, J. M. Randall, and J. F. Meneses, “Greenhouse ventilation rate: Theory and measurement with tracer gas techniques,” *Journal of Agricultural and Engineering Research*, vol. 72, no. 4, pp. 363–374, Apr. 1999, doi: 10.1006/jaer.1998.0381.

[25] A. Mistriotis, G. P. A. Bot, P. Picuno, and G. Scarascia-Mugnozza, “Analysis of the efficiency of greenhouse ventilation using computational fluid dynamics,” *Agric For Meteorol*, vol. 85, no. 3–4, pp. 217–228, Jul. 1997, doi: 10.1016/S0168-1923(96)02400-8.

[26] C. Kittas, M. Karamanis, and N. Katsoulas, “Air temperature regime in a forced ventilated greenhouse with rose crop,” *Energy Build*, vol. 37, no. 8, pp. 807–812, Aug. 2005, doi: 10.1016/j.enbuild.2004.10.009.

[27] K. Maslak and S. Nimmermark, “Thermal energy use for dehumidification of a tomato greenhouse by natural ventilation and a system with an air-to-air heat exchanger,” *Agricultural and Food Science*, vol. 26, no. 1, pp. 56–66, Apr. 2017, doi: 10.23986/afsci.58936.

[28] J. B. Campen and G. P. A. Bot, “Determination of greenhouse-specific aspects of ventilation using three-dimensional computational fluid dynamics,” *Biosyst Eng*, vol. 84, no. 1, pp. 69–77, Jan. 2003, doi: 10.1016/S1537-5110(02)00221-0.

[29] B. Zühlsdorf, “High-performance heat pump systems,” Technical University of Denmark, 2019.

[30] A. Saye, W. K. P. Van Loon, G. P. A. Bot, and H. F. De Zwart, “The solar greenhouse: A survey of energy saving methods,” in *Acta Horticulturae*, 2000, vol. 534, pp. 131–138. doi: 10.17660/ActaHortic.2000.534.14.

[31] I. Yildiz and D. P. Stombaugh, “Heat pump cooling and greenhouse microclimates in open and confined greenhouse systems,” in *Acta Horticulturae*, 2006, vol. 719, pp. 255–262. doi: 10.17660/ActaHortic.2006.719.28.

[32] C. Gilli *et al.*, “Potential of different energy saving strategies in heated greenhouse,” in *Acta Horticulturae*, Jun. 2017, vol. 1164, pp. 467–474. doi: 10.17660/ActaHortic.2017.1164.61.

[33] J. Han, Z. Gao, H. Guo, R. Brad, and D. Waterer, “Comparison of greenhouse dehumidification strategies in cold regions,” *Appl Eng Agric*, vol. 31, no. 1, pp. 133–142, 2015, doi: 10.13031/aea.31.10723.

[34] J. Han, H. Guo, R. Brad, and D. Waterer, “Mechanical Refrigeration Dehumidifier Performance Evaluation in a Tomato Greenhouse in Cold Regions,” *Trans ASABE*, vol. 59, no. 4, pp. 933–941, Aug. 2016, doi: 10.13031/trans.59.11662.

[35] J. Fernández-Seara, R. Diz, F. J. Uhía, A. Dopazo, and J. M. Ferro, “Experimental analysis of an air-to-air heat recovery unit for balanced ventilation systems in residential buildings,” in *Energy Conversion and Management*, Jan. 2011, vol. 52, no. 1, pp. 635–640. doi: 10.1016/j.enconman.2010.07.040.

[36] M. I. Nizovtsev, V. Y. Borodulin, V. N. Letushko, and A. A. Zakharov, “Analysis of the efficiency of air-to-air heat exchanger with a periodic change in the flow direction,” *Appl Therm Eng*, vol. 93, pp. 113–121, Jan. 2016, doi: 10.1016/j.applthermaleng.2015.09.029.

[37] D. De Halleux and L. Gauthier, “Energy consumption due to dehumidification of greenhouses under northern latitudes,” *Journal of Agricultural and Engineering Research*, vol. 69, no. 1, pp. 35–42, 1998, doi: 10.1006/jaer.1997.0221.

[38] J. Han, H. Guo, R. Brad, Z. Gao, and D. Waterer, “Dehumidification Requirement for aGreenhouse Located in a Cold Region,” *Appl Eng Agric*, vol. 31, no. 2, pp. 291–300, Mar. 2015, doi: 10.13031/aea.31.10844.

[39] ASHRAE, *HVAC systems and equipment handbook*. Atlanta, 2008. doi: 10.2172/1129366.

[40] M. Rafati Nasr, M. Fauchoux, R. W. Besant, and C. J. Simonson, “A review of frosting in air-to-air energy exchangers,” *Renewable and Sustainable Energy Reviews*, vol. 30. Elsevier Ltd, pp. 538–554, Feb. 01, 2014. doi: 10.1016/j.rser.2013.10.038.

[41] Y. Abbassi, E. Baniasadi, and H. Ahmadikia, “Comparative performance analysis of different solar desiccant dehumidification systems,” *Energy Build*, vol. 150, pp. 37–51, Sep. 2017, doi: 10.1016/j.enbuild.2017.05.075.

[42] C. X. Jia, Y. J. Dai, J. Y. Wu, and R. Z. Wang, “Experimental comparison of two honeycombed desiccant wheels fabricated with silica gel and composite desiccant material,” *Energy Convers Manag*, vol. 47, no. 15–16, pp. 2523–2534, Sep. 2006, doi: 10.1016/j.enconman.2005.10.034.

[43] T. S. Ge, F. Ziegler, and R. Z. Wang, “A mathematical model for predicting the performance of a compound desiccant wheel (A model of compound desiccant wheel),” *Appl Therm Eng*, vol. 30, no. 8–9, pp. 1005–1015, Jun. 2010, doi: 10.1016/j.applthermaleng.2010.01.012.

[44] R. R. Smith, C. C. Hwang, and R. S. Dougall, “Modeling of a solar-assisted desiccant air conditioner for a residential building,” *Energy*, vol. 19, no. 6, pp. 679–691, Jun. 1994, doi: 10.1016/0360-5442(94)90007-8.

[45] A. Ali, K. Ishaque, A. Lashin, and N. Al Arifi, “Modeling of a liquid desiccant dehumidification system for close type greenhouse cultivation,” *Energy*, vol. 118, pp. 578–589, Jan. 2017, doi: 10.1016/j.energy.2016.10.069.

[46] X. Hao, J. Zheng, L. Celeste, X. Guo, and S. Kholsa, “Liquid desiccant dehumidification system for improving microclimate and plant growth in greenhouse cucumber production,” in *Acta Horticulturae*, Jul. 2017, vol. 1170, pp. 861–866. doi: 10.17660/ActaHortic.2017.1170.110.

[47] G. Lychnos and P. A. Davies, “Modelling and experimental verification of a solar-powered liquid desiccant cooling system for greenhouse food production in hot climates,” *Energy*, vol. 40, no. 1, pp. 116–130, Apr. 2012, doi: 10.1016/j.energy.2012.02.021.

[48] I. H. Lycoskoufis and G. Mavrogianopoulos, “A hybrid dehumidification system for greenhouses,” in *Acta Horticulturae*, 2008, vol. 797, pp. 55–60. doi: 10.17660/ActaHortic.2008.797.5.

[49] G. A. Longo and A. Gasparella, “Comparative experimental analysis and modelling of a flower greenhouse equipped with a desiccant system,” *Appl Therm Eng*, vol. 47, pp. 54–62, Dec. 2012, doi: 10.1016/j.applthermaleng.2012.03.008.

[50] X. Zheng, T. S. Ge, and R. Z. Wang, “Recent progress on desiccant materials for solid desiccant cooling systems,” *Energy*, vol. 74, no. 1. Elsevier Ltd, pp. 280–294, Sep. 01, 2014. doi: 10.1016/j.energy.2014.07.027.

[51] M. Sultan, T. Miyazaki, B. B. Saha, and S. Koyama, “Steady-state investigation of water vapor adsorption for thermally driven adsorption based greenhouse air-conditioning system,” *Renew Energy*, vol. 86, pp. 785–795, Feb. 2016, doi: 10.1016/j.renene.2015.09.015.

[52] K. Ghali, “Energy savings potential of a hybrid desiccant dehumidification air conditioning system in Beirut,” *Energy Convers Manag*, vol. 49, no. 11, pp. 3387–3390, Nov. 2008, doi: 10.1016/j.enconman.2008.04.014.

[53] C. Aprea, A. Greco, and A. Maiorino, “The application of a desiccant wheel to increase the energetic performances of a transcritical cycle,” *Energy Convers Manag*, vol. 89, pp. 222–230, Jan. 2015, doi: 10.1016/j.enconman.2014.09.066.

[54] E. Cerrah, “Sorbent based Enthalpy Recovery Ventilator (SERV) in Northern Building Applications,” Simon Fraser University, 2019.

[55] G. Angrisani, F. Minichiello, C. Roselli, and M. Sasso, “Experimental analysis on the dehumidification and thermal performance of a desiccant wheel,” *Appl Energy*, vol. 92, pp. 563–572, Apr. 2012, doi: 10.1016/J.APENERGY.2011.11.071.

[56] R. Tu, J. Li, and Y. Hwang, “Performance analysis of desiccant wheels assisted fresh air humidifiers in winter using natural gas boilers: Applied in cold and dry climate regions,” *International Journal of Refrigeration*, vol. 119, pp. 24–36, Nov. 2020, doi: 10.1016/J.IJREFRIG.2020.08.003.

[57] M. Kashif Shahzad, M. Ali, N. Ahmed Sheikh, G. Qadar Chaudhary, M. Shahid Khalil, and T. U. Rashid, “Experimental evaluation of a solid desiccant system integrated with cross flow Maisotsenko cycle evaporative cooler,” *Appl Therm Eng*, vol. 128, pp. 1476–1487, Jan. 2018, doi: 10.1016/J.APPLTHERMALENG.2017.09.105.

[58] C. Aprea, A. Greco, and A. Maiorino, “The application of a desiccant wheel to increase the energetic performances of a transcritical cycle,” *Energy Convers Manag*, vol. 89, pp. 222–230, Jan. 2015, doi: 10.1016/J.ENCONMAN.2014.09.066.

[59] H. Kang and D. Y. Lee, “Experimental investigation and introduction of a similarity parameter for characterizing the heat and mass transfer in polymer desiccant wheels,” *Energy*, vol. 120, pp. 705–717, Feb. 2017, doi: 10.1016/J.ENERGY.2016.11.122.

[60] H. Caliskan, D. Y. Lee, and H. Hong, “Enhanced thermodynamic assessments of the novel desiccant air cooling system for sustainable energy future,” *J Clean Prod*, vol. 211, pp. 213–221, Feb. 2019, doi: 10.1016/J.JCLEPRO.2018.11.174.

[61] L. Chen, W. Deng, and Y. Chu, “Experimental study on desiccant evaporative combined chilled air/chilled water air conditioning systems,” *Appl Therm Eng*, vol. 199, p. 117534, Nov. 2021, doi: 10.1016/J.APPLTHERMALENG.2021.117534.

[62] H. Ren, Z. Ma, W. Lin, W. Fan, and W. Li, “Integrating photovoltaic thermal collectors and thermal energy storage systems using phase change materials with rotary desiccant cooling systems,” *Sustain Cities Soc*, vol. 36, pp. 131–143, Jan. 2018, doi: 10.1016/J.SCS.2017.10.021.

[63] Y. Liu *et al.*, “Performance evaluation of a hybrid solar powered rotary desiccant wheel air conditioning system for low latitude isolated islands,” *Energy Build*, vol. 224, p. 110208, Oct. 2020, doi: 10.1016/J.ENBUILD.2020.110208.

[64] X. Zhou, “Thermal and energy performance of a solar-driven desiccant cooling system using an internally cooled desiccant wheel in various climate conditions,” *Appl Therm Eng*, vol. 185, p. 116077, Feb. 2021, doi: 10.1016/J.APPLTHERMALENG.2020.116077.

[65] M. Ukai, H. Tanaka, H. Tanaka, and M. Okumiya, “Performance analysis and evaluation of desiccant air-handling unit under various operation condition through measurement and simulation in hot and humid climate,” *Energy Build*, vol. 172, pp. 478–492, Aug. 2018, doi: 10.1016/J.ENBUILD.2018.04.040.

[66] K. F. Fong and C. K. Lee, “New perspectives in solid desiccant cooling for hot and humid regions,” *Energy Build*, vol. 158, pp. 1152–1160, Jan. 2018, doi: 10.1016/J.ENBUILD.2017.11.016.

[67] A. E. Kabeel and M. Abdelgaied, “Solar energy assisted desiccant air conditioning system with PCM as a thermal storage medium,” *Renew Energy*, vol. 122, pp. 632–642, Jul. 2018, doi: 10.1016/J.RENENE.2018.02.020.

[68] M. Kashif Shahzad, M. Ali, N. Ahmed Sheikh, G. Qadar Chaudhary, M. Shahid Khalil, and T. U. Rashid, “Experimental evaluation of a solid desiccant system integrated with cross flow Maisotsenko cycle evaporative cooler,” *Appl Therm Eng*, vol. 128, pp. 1476–1487, Jan. 2018, doi: 10.1016/J.APPLTHERMALENG.2017.09.105.

[69] S. Tian, X. Su, H. Li, and Y. Huang, “Using a coupled heat pump desiccant wheel system to improve indoor humidity environment of nZEB in Shanghai: Analysis and optimization,” *Build Environ*, vol. 206, p. 108391, Dec. 2021, doi: 10.1016/J.BUILDENV.2021.108391.

[70] M. F. Habib, M. Ali, N. A. Sheikh, A. W. Badar, and S. Mehmood, “Building thermal load management through integration of solar assisted absorption and desiccant air conditioning systems: A model-based simulation-optimization approach,” *Journal of Building Engineering*, vol. 30, p. 101279, Jul. 2020, doi: 10.1016/J.JOBE.2020.101279.

[71] A. Asadi and B. Roshanzadeh, “Improving performance of two-stage desiccant cooling system by analyzing different regeneration configurations,” *Journal of Building Engineering*, vol. 25, p. 100807, Sep. 2019, doi: 10.1016/J.JOBE.2019.100807.

[72] A. S. Binghooth and Z. A. Zainal, “Performance of desiccant dehumidification with hydronic radiant cooling system in hot humid climates,” *Energy Build*, vol. 51, pp. 1–5, Aug. 2012, doi: 10.1016/J.ENBUILD.2012.01.031.

[73] M. Sultan, T. Miyazaki, B. B. Saha, S. Koyama, and V. S. Maisotsenko, “Steady-state Analysis on Thermally Driven Adsorption Air-conditioning System for Agricultural Greenhouses,” in *Procedia Engineering*, Jan. 2015, vol. 118, pp. 185–192. doi: 10.1016/j.proeng.2015.08.417.

[74] M. H. Mahmood, M. Sultan, and T. Miyazaki, “Solid desiccant dehumidification-based air-conditioning system for agricultural storage application: Theory and experiments,” *Proceedings of the Institution of Mechanical Engineers, Part A: Journal of Power and Energy*, vol. 234, no. 4, pp. 534–547, Jun. 2020, doi: 10.1177/0957650919869503.

[75] A. Rjibi, S. Kooli, and A. Guizani, “The effects of regeneration temperature of the desiccant wheel on the performance of desiccant cooling cycles for greenhouse thermally insulated,”

Heat and Mass Transfer/Waerme- und Stoffuebertragung, vol. 54, no. 11, pp. 3427–3443, Nov. 2018, doi: 10.1007/s00231-018-2369-4.

[76] A. Saeed and A. Al-Alili, "A review on desiccant coated heat exchangers," *Sci Technol Built Environ*, vol. 23, no. 1, pp. 136–150, Jan. 2017, doi: 10.1080/23744731.2016.1226076.

[77] P. Vivekh, M. Kumja, D. T. T. Bui, and K. J. J. Chua, "Recent developments in solid desiccant coated heat exchangers – A review," *Appl Energy*, vol. 229, no. August, pp. 778–803, Nov. 2018, doi: 10.1016/j.apenergy.2018.08.041.

[78] M. Amani and M. Bahrami, "Greenhouse dehumidification by zeolite-based desiccant coated heat exchanger," *Appl Therm Eng*, vol. 183, p. 116178, Jan. 2021, doi: 10.1016/j.applthermaleng.2020.116178.

[79] E. Cerrah, C. McCague, and M. Bahrami, "Sorbent based enthalpy recovery ventilator," *Energy Build*, vol. 211, p. 109755, 2020, doi: 10.1016/j.enbuild.2020.109755.

[80] L. Liu *et al.*, "Numerical modelling and parametric study of an air-cooled desiccant coated cross-flow heat exchanger," *Appl Therm Eng*, vol. 169, no. January, p. 114901, 2020, doi: 10.1016/j.applthermaleng.2020.114901.

[81] D.-Y. Lee and D.-S. Kim, "Analytical modeling of a desiccant wheel," *International Journal of Refrigeration*, vol. 42, no. 3, pp. 97–111, Jun. 2014, doi: 10.1016/j.ijrefrig.2014.02.003.

[82] H. Kang, G. Lee, and D. Y. Lee, *Explicit analytic solution for heat and mass transfer in a desiccant wheel using a simplified model*, vol. 93. Elsevier Ltd, p. 2559−2567. doi: 10.1016/j.energy.2015.10.091.

[83] H. Kang, S. Choi, and D.-Y. Lee, "Analytic solution to predict the outlet air states of a desiccant wheel with an arbitrary split ratio," *Energy*, vol. 153, pp. 301–310, Jun. 2018, doi: 10.1016/j.energy.2018.03.177.

[84] H. Bahrehmand, M. Ahmadi, and M. Bahrami, "Oscillatory heat transfer in coated sorber beds: An analytical solution," *International Journal of Refrigeration*, vol. 105, pp. 169–177, Sep. 2019, doi: 10.1016/j.ijrefrig.2018.05.006.

[85] H. Bahrehmand, M. Ahmadi, and M. Bahrami, “Analytical modeling of oscillatory heat transfer in coated sorption beds,” *Int J Heat Mass Transf*, vol. 121, pp. 1–9, 2018, doi: 10.1016/j.ijheatmasstransfer.2017.12.147.

[86] H. Bahrehmand and M. Bahrami, “An analytical design tool for sorber bed heat exchangers of sorption cooling systems,” *International Journal of Refrigeration*, vol. 100, pp. 368–379, 2019, doi: 10.1016/j.ijrefrig.2019.02.003.

[87] A. A. Pesaran and A. F. Mills, “Moisture transport in silica gel packed beds-I.Theoretical study,” *Int J Heat Mass Transf*, vol. 30, no. 6, pp. 1037–1049, Jun. 1987, doi: 10.1016/0017-9310(87)90034-2.

[88] P. D. Dipinlal, S. Shankara Narayanan, S. Ramanathan, and S. Prabhu, “Experimental Investigation of Composite Desiccant Wheel Dehumidifier,” *Applied Mechanics and Materials*, vol. 813–814, pp. 1080–1084, 2015, doi: 10.4028/www.scientific.net/amm.813-814.1080.

[89] C. R. Ruivo, J. J. Costa, and A. R. Figueiredo, “On the validity of lumped capacitance approaches for the numerical prediction of heat and mass transfer in desiccant airflow systems,” *International Journal of Thermal Sciences*, vol. 47, no. 3, pp. 282–292, Mar. 2008, doi: 10.1016/j.ijthermalsci.2007.01.032.

[90] W. Zheng and W. M. Worek, “Numerical simulation of combined heat and mass transfer processes in a rotary dehumidifier,” *Numeri Heat Transf A Appl*, vol. 23, no. 2, pp. 211–232, 1993, doi: 10.1080/10407789308913669.

[91] D. P. D. Theodore L. Bergman, Adrienne S. Lavine, Frank P. Incropera, *Fundamentals of Heat and Mass Transfer, 8th Edition | Wiley*. 2017.

[92] A. Rahnama, M. Amani, and M. Bahrami, “Analytical Solution for Heat and Mass Transfer in Desiccant Coated Heat Exchangers,” *Appl Therm Eng*, 2021.

[93] Vaisala, “Humidity conversion formulas.” https://www.hatchability.com/Vaisala.pdf (accessed Dec. 15, 2020).

[94] A. Sharafian, K. Fayazmanesh, C. McCague, and M. Bahrami, “Thermal conductivity and contact resistance of mesoporous silica gel adsorbents bound with polyvinylpyrrolidone in contact with a metallic substrate for adsorption cooling system applications,” *Int J Heat*

Mass Transf, vol. 79, pp. 64–71, Dec. 2014, doi: 10.1016/J.IJHEATMASSTRANSFER.2014.07.086.

[95] "MATLAB - MathWorks - MATLAB & Simulink." https://www.mathworks.com/products/matlab.html (accessed Feb. 22, 2021).

[96] E. Cerrah, "Sorbent based Enthalpy Recovery Ventilator (SERV) in Northern Building Applications," Simon Fraser University, 2019.

[97] R. Narayanan, W. Y. Saman, S. D. White, and M. Goldsworthy, "Comparative study of different desiccant wheel designs," *Appl Therm Eng*, vol. 31, no. 10, pp. 1613–1620, 2011, doi: 10.1016/j.applthermaleng.2011.01.043.

[98] S. E. Gustafsson, "Transient plane source techniques for thermal conductivity and thermal diffusivity measurements of solid materials," *Review of Scientific Instruments*, vol. 62, no. 3, pp. 797–804, Mar. 1991, doi: 10.1063/1.1142087.

[99] ISO 22007-2, "Plastics — Determination of thermal conductivity and thermal diffusivity — Part 2: Transient plane heat source (hot disc) method," 2015. Accessed: Jan. 27, 2022. [Online]. Available: https://www.iso.org/standard/61190.html

[100] "Mitutoyo America Corporation | Precision Metrology Solutions." https://www.mitutoyo.com/ (accessed Jan. 27, 2022).

[101] A. Entezari, T. S. Ge, and R. Z. Wang, "Water adsorption on the coated aluminum sheets by composite materials (LiCl + LiBr)/silica gel," *Energy*, vol. 160, pp. 64–71, Oct. 2018, doi: 10.1016/j.energy.2018.06.210.

[102] C. Bongs, A. Morgenstern, Y. Lukito, and H. M. Henning, "Advanced performance of an open desiccant cycle with internal evaporative cooling," *Solar Energy*, vol. 104, pp. 103–114, Jun. 2014, doi: 10.1016/j.solener.2013.07.022.

[103] T. S. Ge, Y. J. Dai, and R. Z. Wang, "Performance study of silica gel coated fin-tube heat exchanger cooling system based on a developed mathematical model," *Energy Convers Manag*, vol. 52, no. 6, pp. 2329–2338, Jun. 2011, doi: 10.1016/j.enconman.2010.12.047.

[104] B. B. Saha, A. Chakraborty, S. Koyama, and Y. I. Aristov, "A new generation cooling device employing CaCl2-in-silica gel-water system," *Int J Heat Mass Transf*, vol. 52, no. 1–2, pp. 516–524, Jan. 2009, doi: 10.1016/j.ijheatmasstransfer.2008.06.018.

[105] Y. I. Aristov, G. Restuccia, G. Cacciola, and V. N. Parmon, “A family of new working materials for solid sorption air conditioning systems,” *Appl Therm Eng*, vol. 22, no. 2, pp. 191–204, Feb. 2002, doi: 10.1016/S1359-4311(01)00072-2.

[106] M. M. Younes *et al.*, “Synthesis and characterization of silica gel composite with polymer binders for adsorption cooling applications,” *International Journal of Refrigeration*, vol. 98, pp. 161–170, Feb. 2019, doi: 10.1016/j.ijrefrig.2018.09.003.

[107] “SiliaFlash Irregular Silica Gels, F60, 40 - 63 µm, 60 Å (R10030B).” https://www.silicycle.com/ca/products/siliaflash-irregular-silica-gels/portfolio/r10030b (accessed Mar. 01, 2021).

[108] “Poly(vinyl alcohol) average Mw 130,000, 99+% hydrolyzed | 9002-89-5 | Sigma-Aldrich.” https://www.sigmaaldrich.com/catalog/product/aldrich/563900?lang=en&region=CA (accessed Mar. 01, 2021).

[109] K. Fayazmanesh, C. McCague, and M. Bahrami, “Consolidated adsorbent containing graphite flakes for heat-driven water sorption cooling systems,” *Appl Therm Eng*, vol. 123, pp. 753–760, Aug. 2017, doi: 10.1016/J.APPLTHERMALENG.2017.05.114.

[110] T. Horikawa, D. D. Do, and D. Nicholson, “Capillary condensation of adsorbates in porous materials,” *Advances in Colloid and Interface Science*, vol. 169, no. 1. Elsevier B.V., pp. 40–58, Nov. 14, 2011. doi: 10.1016/j.cis.2011.08.003.

[111] Y. Zhao, E. Hu, and A. Blazewicz, “Dynamic modelling of an activated carbon-methanol adsorption refrigeration tube with considerations of interfacial convection and transient pressure process,” *Appl. Energy*, vol. 95, pp. 276–284, 2012, doi: 10.1016/J.APENERGY.2012.02.050.

[112] R. E. Critoph, “Simulation of a continuous multiple-bed regenerative adsorption cycle,” *International Journal of Refrigeration*, vol. 24, no. 5, pp. 428–437, Aug. 2001, doi: 10.1016/S0140-7007(00)00026-8.

[113] “Adhesion Testers - PosiTest AT Series | DeFelsko.” https://www.defelsko.com/positest-at?gclid=Cj0KCQjw3f6HBhDHARIsAD_i3D_3LrSXslMgn8JQxvN0-cwksumCtmq5EbcIhpRvCcos76rQmaG34DAaApepEALw_wcB (accessed Jan. 31, 2022).

[114] “TECHNICAL FEATURES IN TEMPERATURE Measuring range Ambient model : from 0 to +50 °C Remote model with polycarbonate probe : from-20 to +80 °C Remote model with stainless steel probe : from-40 to +180 °C.”

[115] “XTC-3D™, High Performance 3D Print Coating | Smooth-On, Inc.” https://www.smooth-on.com/product-line/xtc-3d/ (accessed Feb. 28, 2021).

[116] S. Kline and F. McClintock, “Describing uncertainties in single sample experiments.,” *Mechanical Engineering*, vol. 78, pp. 3–8, 1953.

[117] F. Y. Cheng and D. Li, “Multiobjective Optimization Design with Pareto Genetic Algorithm,” *Journal of Structural Engineering*, vol. 123, no. 9, pp. 1252–1261, Sep. 1997, doi: 10.1061/(ASCE)0733-9445(1997)123:9(1252).

[118] G. Goodarzia, N. Thirukonda, S. Heidari, A. Akbarzadeh, and A. Date, “Performance Evaluation of Solid Desiccant Wheel Regenerated by Waste Heat or Renewable Energy,” in *Energy Procedia*, 2017, vol. 110, pp. 434–439. doi: 10.1016/j.egypro.2017.03.165.

[119] “Commercial and Residential Air Solutions.” https://www.novelaire.com/ (accessed Jan. 19, 2022).

Appendix A: MATLAB code

```
clc
clear
close all
for Mode=1:1
%% %%%%%%%%%%%%%%%%%%%%%%%%%%%%%%%%%%%%
%%%%%%%%%%%%%%%%    Mode          %%%%%%%
%%%%%%%%%%%%%%%%%%%%%%%%%%%%%%%%%%%%%%%%
% 1  IsoHMX : substrate high conductivity , DCOP_IsoHMX
% 2 Desiccant wheel with no heater: substrate low conductivity, no DCOP is
defined
% 3 Desiccant wheel with a heater: substrate low conductivity, T_heater is
defined, DCOP normal definition (Qreg=Qheater)
%Mode=3;
if Mode==1
    display('IsoHMX')
elseif Mode==2
    display('Desiccant wheel with no heater')
else
    display('Desiccant wheel with a heater')
end


%% %%%%%%%%%%%%%%%%%%%%%%%%%%%%%%%%%%%%
%%%%%%%%%%%%%%%% Cycle parameter %%%%%%%
%%%%%%%%%%%%%%%%%%%%%%%%%%%%%%%%%%%%%%%%


Nx=10;
Ny=4;
cycle_time=180;
NN=100;
t_end=NN*cycle time;
dt=0.005;
counter=0;
Sr=0.5; %supply regeneration area ratio
t_pro =(1-Sr)*cycle_time; % s
```

```
t_rg = Sr*cycle_time; %s


%% %%%%%%%%%%%%%%%%%%%%%%%%%%%%%%%%%%%%
%%%%%%%%%%%%%%%%  geometry %%%%%%%%%%%%%
%%%%%%%%%%%%%%%%%%%%%%%%%%%%%%%%%%%%%%%%


Channel_length = 0.01 * 20;
H_a = 0.00175;     % channel height m
H_d = 0.15*0.001;  %coating thickness , m
H_s=0.03 ; % substrate thickness , m
dx = Channel_length / (Nx);
dy= H_s/Ny;


%Front_area=pi*(0.30)^2/4; %front area of a dessicant wheel to calculate the
MRC
Front_area=1* H_a;    %front area of the exchanger with 1 layer and depth of
1 to calculate the MRC
%% %%%%%%%%%%%%%%%%%%%%%%%%%%%%%%%%%%%%
%%%%%%%%%%%%%%%% Inlet Parameters %%%%%
%%%%%%%%%%%%%%%%%%%%%%%%%%%%%%%%%%%%%%%%


P_total = 101325;                 % [Pa]
u0= 2;                    % [m/s]


%ads
u_ad = u0;
T_ad = 25;
RH_ad=0.75;
PsaT_ad =  22064000*exp(647.096/(T_ad+273.15)*(-7.85951783*(1-
((T_ad+273.15)/647.096))+1.84408259*(1-((T_ad+273.15)/647.096))^1.5-
11.7866497*(1-((T_ad+273.15)/647.096))^3+22.6807411*(1-
((T_ad+273.15)/647.096))^3.5-15.9618719* (1-
((T_ad+273.15)/647.096))^4+1.80122502*(1-((T_ad+273.15)/647.096))^7.5));
w_ad = 0.622 * RH_ad * PsaT_ad / ( P_total -  RH_ad * PsaT_ad ) ;


%reg
u_rg = u0;
```

```
T_rg = 5;                % [degree C]
RH_rg=0.8;
Psat_rg =  22064000*exp(647.096/(T_rg+273.15)*(-7.85951783*(1-
((T_rg+273.15)/647.096))+1.84408259*(1-((T_rg+273.15)/647.096))^1.5-
11.7866497*(1-((T_rg+273.15)/647.096))^3+22.6807411*(1-
((T_rg+273.15)/647.096))^3.5-15.9618719* (1-
((T_rg+273.15)/647.096))^4+1.80122502*(1-((T_rg+273.15)/647.096))^7.5));
w_rg = 0.622 * RH_rg * Psat_rg / ( P_total -  RH_rg * Psat_rg ) ;


if Mode==3
    T_heater=120;
    DelT_heater=T_heater-T_rg;
    T_rg=T_heater;
    Psat_rg =  22064000*exp(647.096/(T_rg+273.15)*(-7.85951783*(1-
((T_rg+273.15)/647.096))+1.84408259*(1-((T_rg+273.15)/647.096))^1.5-
11.7866497*(1-((T_rg+273.15)/647.096))^3+22.6807411*(1-
((T_rg+273.15)/647.096))^3.5-15.9618719* (1-
((T_rg+273.15)/647.096))^4+1.80122502*(1-((T_rg+273.15)/647.096))^7.5));
    RH_rg=w_rg*P_total./(0.622*Psat_rg+w_rg.*Psat_rg);
end


%% %%%%%%%%%%%%%%%%%%%%%%%%%%%%%%%%%%%%%%%%%%%%%%%%%%%%%%%%%%%%
%%%%%%%%%%%%%%%% Material Properties %%%%%%%%%%%%%%%%
%%%%%%%%%%%%%%%%%%%%%%%%%%%%%%%%%%%%%%%%%%%%%%%%%%%%%%%%%%%%


cp_a = 1009;     % air J/kgK
cp_d=921;        % desiccant J/kgK
cp_v=1872;       % vapor J/kgK
cp_w=4181.3;     % water J/kgK
cp_s=4181.3;     % substrate J/kgK
rho_a = 1.204;   % kg / m^3        % can be defined as a function of
temperature
rho_d = 720;     % kg / m^3        %REF NARAYANAN et al.
rho_s = 720;     % kg / m^3
k_a = 0.0263;    % W/mK
k_d = 1;         % W/mK
if Mode==1
    k_s = 200;       % W/mK
```

```
else
    k_s = 1e-100;     % W/mK
end
Nu_T = 4.3;
Nu_H = 3.5;
Nu = (Nu_T+Nu_H)/2;
d_h=4*H_a;
h = Nu * k_a / d_h;  % convective heat transfer coefficient
hm = h / (cp_a*rho_a); % convective mass transfer coefficient  ro_a should
not be there   does not change if it is ca


h_ad=3000000; % enthalpy of adsorption kJ/kg



%% %%%%%
% For numerical conduction problem Fo should be less than 0.5 or the cod will
diverge
% Fo=k_s*dt/ (rho_s*cp_s*dy^2 or (dx^2)) < 0.5
while k_s*dt/ (rho_s*cp_s*(dy^2)) > 0.5
dt=dt/2
end


while  k_s*dt/ (rho_s*cp_s*(dx^2)) > 0.5
dt=dt/2
end


%% %%%%%%%%%%%%%%%%%%%%%%%%%%%%%%%%%%%%%%%%%%%%%%%%%%%%%%%%%%%%%%%%
%%%%%%%%%%%%%%%%%%%% Variables Initialize %%%%%%%%%%
%%%%%%%%%%%%%%%%%%%%%%%%%%%%%%%%%%%%%%%%%%%%%%%%%%%%%%%%%%%%%%%%%%%%
d_wa_1(1:Nx+2,1)=0;
d_Ta_1(1:Nx+2,1)=0;
Q_ad_1(1:Nx+2,1)=0;
correct_1(1:Nx+2,1)=1;
wa_1 (1:Nx+2,1)=w_ad;
wd_1(1:Nx+2,1)=w_ad;
```

```
Wd_1(1:Nx+2,1)=0.0268;
Ta_1 (1:Nx+2,1)=T_ad;
Td_1(1:Nx+2,1)=T_ad;
% wat_1(1:Nx+2,(NN*cycle_time-1)/dt)= 0 ;
% wdt_1(1:Nx+2,(NN*cycle_time-1)/dt)= 0 ;
% Wdt_1(1:Nx+2,(NN*cycle_time-1)/dt)= 0;
% Tat_1(1:Nx+2,(NN*cycle_time-1)/dt)= 0 ;
% Tdt_1(1:Nx+2,(NN*cycle_time-1)/dt)= 0 ;

%light version
wat_1(1:Nx+2,(cycle_time+2)/dt)= 0 ;
wdt_1(1:Nx+2,(cycle_time+2)/dt)= 0 ;
Wdt_1(1:Nx+2,(cycle_time+2)/dt)= 0;
Tat_1(1:Nx+2,(cycle_time+2)/dt)= 0 ;
Tdt_1(1:Nx+2,(cycle_time+2)/dt)= 0 ;



d_wa_2(1:Nx+2,1)=0;
d_Ta_2(1:Nx+2,1)=0;
Q_ad_2(1:Nx+2,1)=0;
correct_2(1:Nx+2,1)=1;
wa_2 (1:Nx+2,1)=w_ad;
wd_2(1:Nx+2,1)=w_ad;
Wd_2(1:Nx+2,1)=0.0268;
Ta_2 (1:Nx+2,1)=(T_ad+T_rg)/2;
Td_2(1:Nx+2,1)=(T_ad+T_rg)/2;
wat_2(1:Nx+2,(NN*cycle_time-1)/dt)= 0 ;
wdt_2(1:Nx+2,(NN*cycle_time-1)/dt)= 0 ;
Wdt_2(1:Nx+2,(NN*cycle_time-1)/dt)= 0;
Tat_2(1:Nx+2,(NN*cycle_time-1)/dt)= 0 ;
Tdt_2(1:Nx+2,(NN*cycle_time-1)/dt)= 0 ;
Tst(1:Nx+2,(NN*cycle_time-1)/dt)= 0 ;

ca_1(1:Nx+2,1)=0;
cb_1(1:Nx+2,1)=0;
```

```
ca_2(1:Nx+2,1)=0;
cb_2(1:Nx+2,1)=0;

Ts(1:Nx+2,1:Ny)=(T_ad+T_rg)/2;
d_Ts_x(1:Nx+2,1:Ny)=0;
d_Ts_y(1:Nx+2,1:Ny)=0;

%% %%%%%%%%%%%%%%%%%%%%%%%%%%%%%%%%%%%%%%%%%%%%%%%%%%%%%%%%%%%%%%%%%%%%%%%
%%%%%%%%%%%%%%%%%%%% Solution %%%%%%%%%%%%%%%%%%%%%%%%%%%%%%%%%%%%%%%%%%%%
%%%%%%%%%%%%%%%%%%%%%%%%%%%%%%%%%%%%%%%%%%%%%%%%%%%%%%%%%%%%%%%%%%%%%%%%%%

for t=1:dt:t_end

%light version


 remain = rem (t,(cycle_time));

     if (0<=remain && remain<= t_pro)
         u_in_1 = u_ad;
         Ta_1(1)=2*T_ad-Ta_1(2);
         Ta_1(Nx+2)=Ta_1(Nx+1);
         wa_1(1)=2*w_ad-wa_1(2);
         wa_1(Nx+2)=wa_1(Nx+1);
         for i = 2 : Nx+1
             d_Ta_1(i)=(Ta_1(i)-Ta_1(i-1))/(dx);
             d_wa_1(i)=(wa_1(i)-wa_1(i-1))/(dx);
         end

         u_in_2= u_rg;
         Ta_2(1)=2*T_rg-Ta_2(2);
         Ta_2(Nx+2)=Ta_2(Nx+1);
         wa_2(1)=2*w_rg-wa_2(2);
         wa_2(Nx+2)=wa_2(Nx+1);
```

```
        for i = 2 : Nx+1
            d_Ta_2(i)=(Ta_2(i)-Ta_2(i-1))/(dx);
            d_wa_2(i)=(wa_2(i)-wa_2(i-1))/(dx);
        end

    else
        % counter flow
%       u_in_1=-u_rg;
%       T_1(N+2)=2*T_rg-T_1(N+1);
%       T_1(1)=T_1(2);
%       w_1(N+2)=2*w_rg-w_1(N+1);
%       w_1(1)=w_1(2);
%       for i = 2 : N+1
%       d_TA_1(i)=( -T_1 (i) + T_1 (i+1) ) / (  dx );
%       d_WA_1(i)=( -w_1 (i) + w_1 (i+1) ) / (  dx );
%       end

        % parallel flow
        u_in_1 = u_rg;
        Ta_1(1)=2*T_rg-Ta_1(2);
        Ta_1(Nx+2)=Ta_1(Nx+1);
        wa_1(1)=2*w_rg-wa_1(2);
        wa_1(Nx+2)=wa_1(Nx+1);
        for i = 2 : Nx+1
            d_Ta_1(i)=(Ta_1(i)-Ta_1(i-1))/(dx);
            d_wa_1(i)=(wa_1(i)-wa_1(i-1))/(dx);
        end

        u_in_2 = u_ad;
        Ta_2(1)=2*T_ad-Ta_2(2);
        Ta_2(Nx+2)=Ta_2(Nx+1);
        wa_2(1)=2*w_ad-wa_2(2);
        wa_2(Nx+2)=wa_2(Nx+1);
        for i = 2 : Nx+1
            d_Ta_2(i)=(Ta_2(i)-Ta_2(i-1))/(dx);
```

```
            d_wa_2(i)=(wa_2(i)-wa_2(i-1))/(dx);
        end


    end


  if t>(NN-1)*cycle_time-1
      counter = counter+1 ;


      wat_1(1:Nx+2,counter)= wa_1(1:Nx+2) ;
      wdt_1(1:Nx+2,counter)= wd_1(1:Nx+2) ;
      Wdt_1(1:Nx+2,counter)= Wd_1(1:Nx+2);
      Tat_1(1:Nx+2,counter)= Ta_1(1:Nx+2) ;
      Tdt_1(1:Nx+2,counter)= Td_1(1:Nx+2) ;
      Tst(1:Nx+2,counter)= mean(Ts,2);
      Qcond(counter)=mean( -(1./(cb_1 * rho_d*H_d)* 2.*(Td_1 -
Ts(:,1))/(H_d/k_d+dy/k_s)));
      Qads(counter)= mean((Q_ad_1 .*rho_a*hm./(rho_d* H_d.*cb_1)  .* ( wa_1
- wd_1  )));
      Qconv(counter)=mean(- (h ./(cb_1 * rho_d * H_d) .* ( Td_1  - Ta_1
)));
      delw(counter)=((wa_1(1)+wa_1(2))/2 -(wa_1(Nx+2)+wa_1(Nx+1))/2) ;
      delT(counter)=((Ta_1(1)+Ta_1(2))/2 -(Ta_1(Nx+2)+Ta_1(Nx+1))/2) ;
      h_adt_1(counter)=mean(Q_ad_1(1:Nx+2));
  end


       for j=1:Ny
            Ts(Nx+2,j)=Ts(Nx+1,j);
            Ts(1,j)=Ts(2,j);
            for i = 2 : Nx+1
               d_Ts_x (i,j) = (k_s/(cp_s * rho_s))*( Ts (i+1,j) - 2*Ts(i,j)+
Ts(i-1,j) ) / (dx^2 );
            end
       end
```

```
        for i = 2:Nx+1
            for j = 2 : Ny-1
                d_Ts_y (i,j) =  (k_s/(cp_s * rho_s))*( Ts (i,j-1)+Ts (i,j+1)-
2*Ts (i,j) ) / (dy^2 );
            end


            d_Ts_y (i,1) = (1/(cp_s * rho_s*dy))*2*(Td_1(i) -
Ts(i,1))/(H_d/k_d+dy/k_s)-(k_s/(cp_s * rho_s))*(Ts (i,1)-Ts (i,2)) / (dy^2 );
            d_Ts_y (i,Ny) = (1/(cp_s * rho_s*dy))*2*(Td_2(i) -
Ts(i,Ny))/(H_d/k_d+dy/k_s)-(k_s/(cp_s * rho_s))*(Ts (i,Ny)-Ts (i,Ny-1)) /
(dy^2 );
        end




        [wd_1,correct_1] = isotherm (Nx, P_total, Wd_1, Td_1,wd_1,wa_1);
        [wd_2,correct_2] = isotherm (Nx, P_total, Wd_2, Td_2,wd_2,wa_2);

        for i = 1 : Nx+2
             if (Wd_1 (i) <= 0.05)
               Q_ad_1(i) = 1000*(-12400 * Wd_1(i) + 3500);  %J/kg
            else
               Q_ad_1(i) = 1000*(-1400 * Wd_1(i) + 2900);
             end

             if (Wd_2 (i) <= 0.05)
               Q_ad_2(i) = 1000*(-12400 * Wd_2 (i) + 3500);  %J/kg
            else
               Q_ad_2(i) = 1000*(-1400 * Wd_2 (i) + 2900);
             end

        end
```

```
%              ca_1 = (cp_v * wa_1  + cp_a * (1.0 - wa_1 )); %J/kg
%              cb_1 = (cp_w * Wd_1  + cp_d);                 % J/kg
%
%              ca_2 = (cp_v * wa_2  + cp_a * (1.0 - wa_2 )); %J/kg
%              cb_2 = (cp_w * Wd_2  + cp_d);                 % J/kg

            ca_1 = cp_a;    %J/kg
            cb_1 = cp_d;    % J/kg

            ca_2 = cp_a ;   %J/kg
            cb_2=cp_d;      %J/kg

            %%%%%%%%%%%%%%%%%%%%%%%%%%%%%%%%%%%%%%%%%%%%%%%%%%%%%%%%%%%%%%%%

            Psat_1 =  22064000*exp(647.096./(Ta_1+273.15).*(-7.85951783*(1-
((Ta_1+273.15)/647.096))+1.84408259*(1-((Ta_1+273.15)/647.096)).^1.5-
11.7866497.*(1-((Ta_1+273.15)/647.096)).^3+22.6807411*(1-
((Ta_1+273.15)/647.096)).^3.5-15.9618719.* (1-
((Ta_1+273.15)/647.096)).^4+1.80122502*(1-((Ta_1+273.15)/647.096)).^7.5));
            RHa_1=wa_1*P_total./(0.622*Psat_1+wa_1.*Psat_1);
            Psat_2 =  22064000*exp(647.096./(Ta_2+273.15).*(-7.85951783*(1-
((Ta_2+273.15)/647.096))+1.84408259*(1-((Ta_2+273.15)/647.096)).^1.5-
11.7866497.*(1-((Ta_2+273.15)/647.096)).^3+22.6807411*(1-
((Ta_2+273.15)/647.096)).^3.5-15.9618719.* (1-
((Ta_2+273.15)/647.096)).^4+1.80122502*(1-((Ta_2+273.15)/647.096)).^7.5));
            RHa_2=wa_2*P_total./(0.622*Psat_2+wa_2.*Psat_2);


            for i=1:Nx+2
               if RHa_1(i)>1 && wd_1(i)>wa_1(i)
                   correct_1(i)=0;
               end

               if RHa_2(i)>1 && wd_2(i)>wa_2(i)
                   correct_2(i)=0;
```

```
            end
        end


        % Moisture Transport in gas phase (w)
        wa_1 = wa_1+dt*(-(u_in_1 * d_wa_1 ) - (hm  /(H_a) * ( wa_1  -
wd_1  ).*correct_1))  ;
        wa_2 = wa_2+dt*(-(u_in_2 * d_wa_2 ) - (hm  /(H_a) * ( wa_2  -
wd_2  ).*correct_2))  ;


        % Moisture Transport in solid phase (Wd)
        Wd_1 =Wd_1+dt*(rho_a*hm/(rho_d* H_d))  * ( wa_1  - wd_1
).*correct_1;
        Wd_2 =Wd_2+dt*(rho_a*hm/(rho_d* H_d))  * ( wa_2  - wd_2
).*correct_2;




        % Heat Transfer in gas phase (T)
        Ta_1 = Ta_1+dt*(-(u_in_1 * d_Ta_1)  - (h./(H_a*rho_a*ca_1).* (
Ta_1  - Td_1  )));  %cp_v*hm * ( w  - wd  )
        Ta_2 = Ta_2+dt*(-(u_in_2 * d_Ta_2)  - (h./(H_a*rho_a*ca_2).* (
Ta_2  - Td_2  )));  %cp_v*hm * ( w  - wd  )




        % Heat Transfer in solid phase (Td)
        Td_1 =Td_1  +dt*( (h_ad .*rho_a*hm./(rho_d* H_d.*cb_1)  .* ( wa_1
- wd_1  ).*correct_1) - (h ./(cb_1 * rho_d * H_d) .* ( Td_1  - Ta_1  ))-
(1./(cb_1 * rho_d*H_d)* 2.*(Td_1 - Ts(:,1))/(H_d/k_d+dy/k_s)));
        Td_2 =Td_2 +dt*( (h_ad .*rho_a*hm./(rho_d* H_d.*cb_2)   .* ( wa_2
- wd_2  ).*correct_2) - (h ./(cb_2 * rho_d * H_d) .* ( Td_2  - Ta_2  ))-
(1./(cb_2 * rho_d*H_d)* 2.*(Td_2 - Ts(:,Ny))/(H_d/k_d+dy/k_s)));



        % Heat Transfer in substrate (Ts)
         Ts =Ts +dt*(  d_Ts_y+ d_Ts_x  )  ; %
```

```
end


%% MRC DCOP


MRC1=abs(0.5*(
mean(Wdt_1(1:Nx+2,cycle_time/dt))+mean(Wdt_1(2:Nx+1,cycle_time/dt)))-0.5*(
mean(Wdt_1(1:Nx+2,0.5*cycle_time/dt))+mean(Wdt_1(2:Nx+1,0.5*cycle_time/dt))))
*(rho_d* Front_area/H_a * H_d*Channel_length)*3600000/(cycle_time/2);  %MRC=
(Max W-Min W)M_tot_desiccant (kg/hr)

%Or

%MRC2=sum(delw(1:counter/2))*u0*Front_area*rho_a*dt*3600000/(cycle_time/2);
%MRC= sum(m-dot*(w_out - w_in)*dt)  (kg/hr)

%MRC=0.5*(MRC1+MRC2)

MRC=MRC1


PressureDrop=(H_a*u0*1)/(16*H_a^3)*3*1.9*Channel_length*10^-5;

Wfan=PressureDrop*(H_a*u0*1)


if Mode==1


DCOP_IsoHMX1=(MRC/3600000*mean(h_adt_1(1:counter/2)))/(sum(delT(1:counter/2))
*u0*Front_area*rho_a*cp_a*dt/(cycle_time/2));

    %Or

    %
DCOP_IsoHMX2=(sum(delw(1:counter/2).*h_adt_1(1:counter/2))*u0*Front_area*rho_
a*dt/(cycle_time/2))/(sum(delT(1:counter/2))*u0*Front_area*rho_a*cp_a*dt/(cyc
le_time/2))

    DCOP_IsoHMX=DCOP_IsoHMX1

elseif Mode==2

    DCOP_IsoHMX= (MRC/3600000*mean(h_adt_1(1:counter/2)))/Wfan;

elseif Mode==3


DCOP_IsoHMX=(MRC/3600000*mean(h_adt_1(1:counter/2)))/(DelT_heater*u0*Front_ar
ea*rho_a*cp_a)

end


%% plots
```

```
t=0:dt:cycle_time;


%light version
f11 = figure('Name','w in out');
plot(t(1:cycle_time/dt),(wat_1(1,1:cycle_time/dt)+wat_1(2,1:cycle_time/dt))/2
) ;
grid on
hold on
plot(t(1:cycle_time/dt),(wat_1(Nx+2,1:cycle_time/dt)+wat_1(Nx+1,1:cycle_time/
dt))/2) ;
legend('1','N')


f12 = figure('Name','Tt in out');
plot(t(1:cycle_time/dt),(Tat_1(1,1:cycle_time/dt)+Tat_1(2,1:cycle_time/dt))/2
) ;
grid on
hold on
plot(t(1:cycle_time/dt),(Tat_1(Nx+2,1:cycle_time/dt)+Tat_1(Nx+1,1:cycle_time/
dt))/2) ;
legend('1','N')


f14 = figure('Name','Wd');
plot(t(1:cycle_time/dt),(Wdt_1(1,1:cycle_time/dt)+Wdt_1(2,1:cycle_time/dt))/2
) ;
grid on
hold on
plot(t(1:cycle_time/dt),(Wdt_1(Nx+2,1:cycle_time/dt)+Wdt_1(Nx+1,1:cycle_time/
dt))/2) ;
hold on
plot(t(1:cycle_time/dt),mean(Wdt_1(1:Nx+2,1:cycle_time/dt),1)) ;
legend('1','N','avg')


f15 = figure('Name','Mean-y Ts');
plot(t(1:cycle_time/dt),(Tst(1,1:cycle_time/dt)+Tst(2,1:cycle_time/dt))/2) ;
grid on
hold on
```

```
plot(t(1:cycle_time/dt),(Tst(Nx+2,1:cycle_time/dt)+Tst(Nx+1,1:cycle_time/dt))
/2) ;
legend('1','N')



Stepsize=floor(length(Tat_1)/(180));


counter2=0;
for i= Stepsize:Stepsize:length(Tat_1)-Stepsize
    counter2=counter2+1;
    Comp_TaIn(counter2,1)=(Tat_1(1,i)+Tat_1(2,i))/2;
    Comp_TaOut(counter2,1)=(Tat_1(Nx+2,i)+Tat_1(Nx+1,i))/2;
    Comp_Td(counter2,1)=mean(Tdt_1(1:Nx+2,i),1);
    Comp_waIn(counter2,1)=(wat_1(1,i)+wat_1(2,i))/2;
    Comp_waOut(counter2,1)=(wat_1(Nx+2,i)+wat_1(Nx+1,i))/2;
    Comp_wd(counter2,1)=mean(wdt_1(1:Nx+2,i),1);
end


if Mode==1
    name1=["IsoHMX",'','','','','';"TaIn","TaOut",'Td','waIn','waout','wd'];

name2=["IsoHMX",'','','','','','';"MRC","DCOP","T_ad","RH_ad","T_rg","RH_rg",
"Cycle Time"];


    Range1_1='H:M';
    Range2_1='I:O';
    Range1_2='H3:M3';
    Range2_2='I3:O3';


elseif Mode==2
    name1=["Desiccant wheel with no
heater",'','','','','';"TaIn","TaOut",'Td','waIn','waout','wd'];
    name2=["Desiccant wheel with no
heater",'','','','','','';"MRC","DCOP","T_ad","RH_ad","T_rg","RH_rg","Cycle
Time"];


    Range1_1='O:T';
```

```
    Range2_1='Q:W';
    Range1_2='O3:T3';
    Range2_2='Q3:W3';

else
    name1=["Desiccant wheel with a
heater",'','','','','';"TaIn","TaOut",'Td','waIn','waout','wd'];
    name2=["Desiccant wheel with a
heater",'','','','','','';"MRC","DCOP","T_ad","RH_ad","T_rg","RH_rg","Cycle
Time"];

    Range1_1='V:AA';
    Range2_1='Y:AE';
    Range1_2='V3:AA3';
    Range2_2='Y3:AE3';

end

filename = 'Results.xlsx';

XXXOutputFinal1=[Comp_TaIn,Comp_TaOut,Comp_Td,Comp_waIn, Comp_waOut,Comp_wd];
XXXOutputFinal2=[MRC,DCOP_IsoHMX,T_ad,RH_ad,T_rg,RH_rg,cycle_time];

writematrix(name1,filename,'Sheet',1,'Range',Range1_1)
writematrix(XXXOutputFinal1,filename,'Sheet',1,'Range','H:M')
writematrix(name2,filename,'Sheet',2,'Range',Range2_1)
writematrix(XXXOutputFinal2,filename,'Sheet',2,'Range','H:M')

end
```

Appendix B: Uncertainty Analysis

The method proposed by Kline and McClintock [116] is used to calculate the uncertainty of the experimental study. Based on this method, if f is any function of $x_1,\ldots, x_n$, then the uncertainty of measured f is calculated by the Eq.(98):

$$\delta f = \sqrt{\left(\frac{\partial f}{\partial x_1}\delta x_1\right)^2 + \cdots + \left(\frac{\partial f}{\partial x_n}\delta x_n\right)^2} \tag{98}$$

Based on Eq.(98) the uncertainty of the measured MRC and $DCOP_{IsoHMX}$ are calculated by the following equations:

$$MRC = \dot{m}_a\left(\omega_{a,out} - \omega_{a,in}\right) =>$$

$$\delta MRC = \sqrt{\left(\frac{\partial MRC}{\partial \dot{m}_a}\delta \dot{m}_a\right)^2 + \left(\frac{\partial MRC}{\partial \omega_{a,out}}\delta \omega_{a,out}\right)^2 + \left(\frac{\partial MRC}{\partial \omega_{a,in}}\delta \omega_{a,in}\right)^2} \tag{99}$$

$$DCOP_{IsoHMX} = \frac{h_{ad}\left(\omega_{a,out} - \omega_{a,in}\right)}{c_{p,a}(T_{a,in} - T_{a,out})} =>$$

$$\delta DCOP = \sqrt{\left(\frac{\partial DCOP}{\partial \omega_{a,out}}\delta \omega_{a,out}\right)^2 + \left(\frac{\partial DCOP}{\partial \omega_{a,in}}\delta \omega_{a,in}\right)^2 + \left(\frac{\partial DCOP}{\partial T_{a,in}}\delta T_{a,in}\right)^2 + \left(\frac{\partial DCOP}{\partial T_{a,out}}\delta T_{a,out}\right)^2} \tag{100}$$

Based on the measurement accuracy of the sensors listed in **Table 10**, the calculated uncertainties of the measured MRC and $DCOP_{IsoHMX}$ are around 5% and 6%, respectively.

Appendix C: Experimental data of TGA test

Table 18. TGA results for adsorption

Uptake (kg/kg)	Temperature (℃)	P/Po	logP/Po
0.022288	30.227	6.28E-05	-4.20224
0.017486	29.921	1.07E-04	-3.97006
0.031356	38.16	3.32E-04	-3.47841
0.050003	19.809	6.96E-04	-3.15736
0.055892	14.998	8.00E-04	-3.09674
0.080098	38.975	2.85E-02	-1.54468
0.095621	29.323	4.87E-02	-1.31247
0.121806	19.638	5.10E-02	-1.29235
0.109855	39.037	5.68E-02	-1.24533
0.108664	14.637	5.99E-02	-1.22275
0.13008	9.952	8.12E-02	-1.09055
0.134286	39.056	8.53E-02	-1.06923
0.157291	19.562	8.73E-02	-1.05911
0.140988	29.3	9.71E-02	-1.0128
0.165728	39.052	1.14E-01	-0.94445
0.157315	14.632	1.20E-01	-0.92231
0.214888	19.557	1.31E-01	-0.88322
0.196402	39.028	1.42E-01	-0.84634
0.204405	29.304	1.46E-01	-0.83522
0.22875	9.866	1.63E-01	-0.78762
0.22082	39.023	1.71E-01	-0.76663
0.2548	19.557	1.75E-01	-0.75698
0.227139	14.665	1.79E-01	-0.74712
0.247533	29.295	1.96E-01	-0.70857
0.244926	38.999	2.00E-01	-0.69964
0.292971	19.557	2.19E-01	-0.65993
0.269048	39.018	2.28E-01	-0.6417

0.278984	14.67	2.38E-01	-0.62377
0.289654	29.29	2.44E-01	-0.61199
0.298937	9.876	2.45E-01	-0.61147
0.292504	39.023	2.57E-01	-0.59062
0.328826	19.552	2.63E-01	-0.58018
0.31588	39.023	2.85E-01	-0.54489
0.329004	29.276	2.94E-01	-0.53157
0.328037	14.675	2.98E-01	-0.52605
0.353493	19.533	3.07E-01	-0.51327
0.337579	39.028	3.14E-01	-0.50362
0.353208	9.857	3.26E-01	-0.48614
0.359695	39.018	3.42E-01	-0.46549
0.361589	29.285	3.43E-01	-0.46487
0.380143	19.538	3.51E-01	-0.45496
0.371766	14.689	3.57E-01	-0.44705
0.380611	39.028	3.71E-01	-0.43087
0.389201	29.28	3.92E-01	-0.40679
0.406156	19.533	3.94E-01	-0.40418
0.399678	39.023	3.99E-01	-0.3986
0.403123	9.847	4.10E-01	-0.38736
0.413135	14.689	4.17E-01	-0.37997
0.411652	39.009	4.28E-01	-0.36826
0.421189	19.542	4.38E-01	-0.35864
0.417277	29.276	4.41E-01	-0.35559
0.419143	39.023	4.56E-01	-0.34079
0.428975	14.694	4.76E-01	-0.32239
0.432081	19.538	4.82E-01	-0.31688
0.42913	39.018	4.85E-01	-0.31429
0.446174	29.276	4.90E-01	-0.30995
0.431146	9.861	4.91E-01	-0.30934

0.463557	14.708	5.35E-01	-0.27132
0.477058	29.28	5.39E-01	-0.26854
0.487418	9.866	5.73E-01	-0.24219
0.51656	29.271	5.88E-01	-0.23027
0.511698	14.703	5.96E-01	-0.22499
0.563718	29.285	6.37E-01	-0.19616
0.554768	9.857	6.54E-01	-0.1843
0.561033	14.698	6.55E-01	-0.18387
0.6197	29.28	6.86E-01	-0.16388
0.686413	29.29	7.34E-01	-0.13403
0.646016	9.866	7.36E-01	-0.13292
0.764287	29.295	7.83E-01	-0.10617
0.767951	9.861	8.18E-01	-0.0871
0.865089	29.314	8.32E-01	-0.08003
0.923819	9.88	8.98E-01	-0.04649

Table 19. TGA results for desorption

Uptake (kg/kg)	**Temperature** (℃)	**P/Po**	**logP/Po**
0.865089	29.314	8.32E-01	-0.08003
0.776974	29.29	7.84E-01	-0.10585
0.693017	29.29	7.35E-01	-0.13385
0.625382	29.285	6.86E-01	-0.16381
0.570921	29.28	6.37E-01	-0.19581
0.524437	29.28	5.88E-01	-0.23049
0.482933	29.28	5.39E-01	-0.26839
0.445744	29.285	4.90E-01	-0.3099
0.425974	29.295	4.41E-01	-0.35579
0.41687	29.285	3.92E-01	-0.40683

0.405098	29.314	3.42E-01	-0.46556
0.370469	29.295	2.94E-01	-0.53194
0.329284	29.295	2.45E-01	-0.61131
0.285155	29.304	1.96E-01	-0.70861
0.238999	29.304	1.47E-01	-0.83318
0.19039	29.314	9.77E-02	-1.00996
0.13597	29.304	4.90E-02	-1.31013
0.044848	29.386	1.17E-03	-2.93321
0.42913	39.018	4.85E-01	-0.31429
0.419934	39.013	4.57E-01	-0.34045
0.414307	39.013	4.28E-01	-0.3684
0.408968	39.013	4.00E-01	-0.3983
0.40307	38.999	3.71E-01	-0.4302
0.391	39.013	3.43E-01	-0.46524
0.36983	39.009	3.14E-01	-0.50295
0.346429	39.018	2.85E-01	-0.54459
0.322314	38.989	2.57E-01	-0.58961
0.297573	38.999	2.29E-01	-0.64102
0.272105	39.009	2.00E-01	-0.69939
0.246438	39.023	1.71E-01	-0.76647
0.220166	39.032	1.43E-01	-0.84608
0.193498	39.028	1.14E-01	-0.94346
0.166051	39.018	8.56E-02	-1.06745
0.135844	39.028	5.70E-02	-1.24404
0.099209	39.018	2.86E-02	-1.54303
0.035888	39.023	7.61E-04	-3.11834
0.923819	9.88	8.98E-01	-0.04649
0.811362	9.895	8.17E-01	-0.0878
0.684034	9.899	7.35E-01	-0.13374
0.588534	9.899	6.53E-01	-0.18521

0.51733	9.895	5.72E-01	-0.2426
0.457536	9.885	4.91E-01	-0.30932
0.42502	9.899	4.08E-01	-0.38904
0.410015	9.899	3.26E-01	-0.48626
0.352394	9.899	2.45E-01	-0.61172
0.279018	9.914	1.63E-01	-0.78715
0.191411	9.918	8.15E-02	-1.08905
0.058904	11.23	1.07E-03	-2.97091
0.561033	14.698	6.55E-01	-0.18387
0.513057	14.708	5.95E-01	-0.22525
0.470985	14.703	5.36E-01	-0.27092
0.434237	14.703	4.76E-01	-0.32226
0.421955	14.708	4.17E-01	-0.38017
0.411373	14.708	3.57E-01	-0.447
0.381248	14.713	2.97E-01	-0.52675
0.334584	14.727	2.38E-01	-0.62424
0.28281	14.717	1.78E-01	-0.74894
0.224916	14.727	1.19E-01	-0.92511
0.159823	14.736	5.93E-02	-1.22714
0.055756	15.446	1.26E-03	-2.89859
0.432081	19.538	4.82E-01	-0.31688
0.422133	19.547	4.38E-01	-0.35834
0.41469	19.547	3.94E-01	-0.40404
0.405712	19.533	3.51E-01	-0.45493
0.380162	19.547	3.07E-01	-0.51301
0.346352	19.547	2.63E-01	-0.58027
0.310135	19.552	2.19E-01	-0.65943
0.271174	19.557	1.75E-01	-0.75685
0.229793	19.538	1.31E-01	-0.88155
0.185538	19.547	8.77E-02	-1.05686

0.134814	19.562	4.38E-02	-1.35836
0.050255	20.024	1.10E-03	-2.95755

Appendix D: Optimization MATLAB code

```
%-------------------------------------------------------------------------%
% This code purpose is to optimize IsoHMX                                 %
%                                                                         %
%-------------------------------------------------------------------------%

% Some cleanup %
clc
clear
fclose('all');


%% ----------------------------------------
% Input Parameteres




P_total = 101325;                % [Pa]

%ads
T_1 = 25;
RH_1=0.75;
PsaT1 =  22064000*exp(647.096/(T_1+273.15)*(-7.85951783*(1-
((T_1+273.15)/647.096))+1.84408259*(1-((T_1+273.15)/647.096))^1.5-
11.7866497*(1-((T_1+273.15)/647.096))^3+22.6807411*(1-
((T_1+273.15)/647.096))^3.5-15.9618719* (1-
((T_1+273.15)/647.096))^4+1.80122502*(1-((T_1+273.15)/647.096))^7.5));
w1 = 0.622 * RH_1 * PsaT1 / ( P_total -  RH_1 * PsaT1 )

%reg
T2 = 5;                % [degree C]
```

```
RH2=0.2;
Psat2 =  22064000*exp(647.096/(T2+273.15)*(-7.85951783*(1-
((T2+273.15)/647.096))+1.84408259*(1-((T2+273.15)/647.096))^1.5-
11.7866497*(1-((T2+273.15)/647.096))^3+22.6807411*(1-
((T2+273.15)/647.096))^3.5-15.9618719* (1-
((T2+273.15)/647.096))^4+1.80122502*(1-((T2+273.15)/647.096))^7.5));
w2 = 0.622 * RH2 * Psat2 / ( P_total -  RH2 * Psat2 )


del_T=abs(T1-T2);
del_w=abs(w1-w2);



cp_a = 1009;     % air J/kgK
cp_d=921;        % desiccant J/kgK
cp_s=4181.3;     % substrate J/kgK
rho_a = 1.204;   % kg / m^3        % can be defined as function of temperature
rho_d = 720;     % kg / m^3        %REF NARAYANAN et al.
k_a = 0.0263;    % W/mK
Nu_T = 4.3;
Nu_H = 3.5;
Nu = (Nu_T+Nu_H)/2;
h_ad=3000000; % enthalpy of adsorption kJ/kg

MRC_power=1;
DCOP_power=1/10;
%% ----------------------------------------
% Optimization

lb = [0.2,0.01,0.001,10^5];
ub = [3,0.4,0.01,inf];
A = [];
b = [];
Aeq = [];
beq = [];

FitnessFunction= @(x) objectsFunction(x,MRC_power,DCOP_power) ;
% options = optimoptions(@gamultiobj,'PlotFcn',@gaplotpareto);
```

```
options =
optimoptions("gamultiobj","PlotFcn","gaplotpareto","PopulationSize",100);
[x,fval,exitflag,output] =
gamultiobj(FitnessFunction,4,A,b,Aeq,beq,lb,ub,options)
% x = gamultiobj(FitnessFunction,4)


u_L_H_tovDel(:,1)=x(:,1);
u_L_H_tovDel(:,2)=100*x(:,2);
u_L_H_tovDel(:,3)=1000*x(:,3);
u_L_H_tovDel(:,4)=1/1000*x(:,4);

MRC_DCOP_Result(:,1)=(1./fval(:,1)).^(1/MRC_power)
MRC_DCOP_Result(:,2)=(1./fval(:,2)).^(1/DCOP_power)



function MRC_DCOP= objectsFunction(x,MRC_power,DCOP_power)

    u0=x(1);
    L=x(2);
    H_a=x(3);
    t_over_delta=x(4);

    %----------------------
    T1=25;
    T2=5;
    w1=0.001*14.9;
    w2=0.001*1.1;
    del_T=abs(T1-T2);
    del_w=abs(w1-w2);



    cp_a = 1009;    % air J/kgK
    cp_d=921;       % desiccant J/kgK
    cp_s=4181.3;    % substrate J/kgK
    rho_a = 1.204;  % kg / m^3        % can be defined as function of
temperature
```

```
    rho_d = 720;     % kg / m^3         %REF NARAYANAN et al.
    k_a = 0.0263;    % W/mK
    Nu_T = 4.3;
    Nu_H = 3.5;
    Nu = (Nu_T+Nu_H)/2;
    h_ad=3000000; % enthalpy of adsorption J/kg
    %----------------------

    d_h=4*H_a;
    h = Nu * k_a / d_h;  % convective heat transfer coefficient

    S1= h*L/(u0*rho_a*cp_a*H_a);
    S5_over_omega=h*del_w*2*t_over_delta/(rho_d*cp_a);
    S2_over_S3=h_ad*del_w/(cp_a*del_T);

    A=1-exp(-S1);
    N=A*S5_over_omega/S1;

    MRC=1800*A/N*rho_a*u0*del_w*(1-exp(-N))/(1+exp(-N));
    DCOP=2*S2_over_S3/N *(1-exp(-N))/(1+exp(-N));

    MRC_DCOP(1)=1/(MRC^(MRC_power));
    MRC_DCOP(2)=1/(DCOP^(DCOP_power));

end
```